5. CONTAMINANT FATE AND TRANSPORT

Various modeling activities that supported development of this ABRA are discussed below. These activities included source release modeling, dissolved-phase flow and transport modeling, biotic uptake modeling, and VOC transport modeling. Most of the discussion concerns source release and fate and transport modeling for dissolved-phase contaminants. Transport modeling for VOCs was not conducted for this ABRA; however, the results of the VOC transport modeling from the IRA (Becker et al. 1998) were incorporated in the ABRA. Biotic uptake modeling also is presented for the analysis of human health surface exposure pathways and ecological risk assessment.

Modeling in the ABRA is essentially the same as that implemented in the IRA but with some improvements. The differences compared to the IRA models are identified in the discussions below. In general, modeling has three major components: source release, subsurface transport, and transport to the surface. The source release model (DUST-MS [Sullivan 1992]) produces mass estimates used as inputs to the TETRAD subsurface model for fate and transport simulations (Shook 1995) and as inputs to the DOSTOMAN model (Root 1981) to simulate biotic uptake. Numerous model runs were implemented to define a base case analysis and to assess the sensitivity of the results to select model parameters.

All contaminants, except VOCs, were simulated by using the source release model (Disposal Unit Source Term [DUST-MS]), and the biotic uptake model (DOSTOMAN). The results from previous modeling were used to assess VOCs. Because of their low mobility and short half-lives, Cs-137 and Sr-90 were not identified as groundwater pathway risk drivers in the IRA and were eliminated from subsurface modeling. These contaminants were assessed for biotic uptake and surface exposure pathways only. Twenty-nine contaminants were evaluated in the human health analysis, including the 24 human health COPCs identified in the IRA and five additional contaminants that were modeled because they are decay chain members. The long-lived daughter products were specifically included in the simulations because of the possibility of a remedial action slowing transport, which would allow additional ingrowth and influence risk estimates. No extra simulations were performed specifically for the ecological analysis. Biotic modeling used to assess human health risks for surface exposure pathways also provided the basis for ecological risk assessment. Contaminants and models used in the ABRA are summarized in Table 5-1.

5.1 Source Release Modeling

The source term for the ABRA is defined as the waste buried in the SDA. Conceptually, the source term model is simple. Waste was buried in containers such as drums, boxes, and bags. When the containers fail, the contaminants can be released over time by one of three release mechanisms: washoff, diffusion, or dissolution. The type of release mechanism and the release rates are dependent on the characteristics of the waste. The mass released from the buried waste is available for transport to the subsurface by infiltration or to the surface by biotic uptake.

The DUST-MS source release computer code (Sullivan 1992) was used to estimate the mass available for transport. The source term model predicts release of contaminants from the waste buried in the SDA into the subsurface. Version 1.0 of the DUST-MS code (Sullivan 1993) was selected for the WAG 7 RI/FS (Becker 1997). The IRA (Becker et al. 1998) modeled the distributed failure of containers but did not account for releases limited by solubility. The code was enhanced with capability to simulate container failures distributed in time and releases limited by solubility.

Table 5-1. Contaminants evaluated in the Ancillary Basis for Risk Analysis and the computer models used to assess them.

Contaminant	Computer Models			Note
	DUST-MS	TETRAD	DOSTOMAN	
Ac-227	Yes	Yes	Yes	Contaminant of potential concern
Am-241	Yes	Yes	Yes	Contaminant of potential concern
Am-243	Yes	Yes	Yes	Long-lived parent of Pu-239
C-14	Yes	Yes	Yes	Contaminant of potential concern
Cl-36	Yes	Yes	Yes	Contaminant of potential concern
Cs-137	Yes	No	Yes	Contaminant of potential concern for surface exposure pathways only
I-129	Yes	Yes	Yes	Contaminant of potential concern
Nb-94	Yes	Yes	Yes	Contaminant of potential concern
Np-237	Yes	Yes	Yes	Contaminant of potential concern
Pa-231	Yes	Yes	Yes	Contaminant of potential concern
Pb-210	Yes	Yes	Yes	Contaminant of potential concern
Pu-238	Yes	Yes	Yes	Long-lived parent of U-234
Pu-239	Yes	Yes	Yes	Contaminant of potential concern
Pu-240	Yes	Yes	Yes	Contaminant of potential concern
Ra-226	Yes	Yes	Yes	Contaminant of potential concern
Sr-90	Yes	No	Yes	Contaminant of potential concern for surface exposure pathways only
Tc-99	Yes	Yes	Yes	Contaminant of potential concern
Th-229	Yes	Yes	Yes	Long-lived daughter product of U-233
Th-230	Yes	Yes	Yes	Long-lived daughter product of U-234
Th-232	Yes	Yes	Yes	Long-lived daughter product of U-236
U-233	Yes	Yes	Yes	Contaminant of potential concern
U-234	Yes	Yes	Yes	Contaminant of potential concern
U-235	Yes	Yes	Yes	Contaminant of potential concern
U-236	Yes	Yes	Yes	Contaminant of potential concern
U-238	Yes	Yes	Yes	Contaminant of potential concern
Nitrate	Yes	Yes	Yes	Contaminant of potential concern
Carbon tetrachloride	No	No	No	Contaminant of potential concern-used scaled results from the Interim Risk Assessment (Becker et al. 1998)
Methylene chloride	No	No	No	Contaminant of potential concern-used scaled results from the IRA
Tetrachloroethylene	No	No	No	Contaminant of potential concern-used scaled results from the IRA

Implementation of the source term model is described below. Input parameters include the source term inventory, waste types, infiltration rates, release mechanisms, and release rates. The contaminant grouping and the assignment of SDA contaminants to source areas also are described. The source release model provided mass estimates for total yearly releases from all waste source areas, which were then used as inputs for the subsurface and biotic transport models discussed in the remainder of Section 5.

5.1.1 Source Term Inventory

Annual best-estimate inventories for waste buried in the SDA through 1999 were taken from CIDRA and input into the source term model. Actual disposal quantities were modeled for the base case. Estimates for future disposals in active LLW pits were assessed through sensitivity analyses (see Table 4-1 for the annual disposal inventories for radionuclides and Table 4-2 for nonradionuclides). Total inventories in Tables 4-1 and 4-2 differ from those presented in the IRA for two reasons: (a) the original inventory estimates were modified to reflect the corrections and updates, and (b) this analysis implements best-estimate inventories while the IRA (Becker et al. 1998) considered upper-bound inventories.

Inventories for one COPC (i.e., nitrate) could not be extracted directly from CIDRA because many compounds contain the element nitrogen. Conversion factors used to estimate disposal inventories for nitrate (listed as total nitrogen) are listed in Table 5-2. Conversion factors were taken directly from the MERCK Index (Merck 1989) or developed from the chemical formula and atomic weights of the constituent chemicals. Nitrogen-bearing inventories in CIDRA were multiplied by conversion factors in Table 5-2 to determine the amount of nitrate as total nitrogen buried in the SDA.

Table 5-2. Factors used to convert disposal quantity to amount of contaminant in the total waste stream to nitrate as total nitrogen.

Contaminant	Conversion Factor
Total nitrate (as nitrogen)	—
Aluminum nitrate nonahydrate	0.1972
Ammonia	0.7778
Copper nitrate	0.1489
Mercury nitrate monohydrate	0.0819
Nitric acid	0.2222
Potassium nitrate	0.1386
Sodium nitrate	0.1412
Uranyl nitrate	0.0711

Radioactive decay was the only mechanism considered to affect the source term inventories. As was shown in the IRA, decaying isotopes to the present and then initiating the fate and transport simulations can bias the results low for mobile isotopes with short half-lives. Therefore, inventory estimates for most radionuclides were not adjusted directly to account for radioactive decay. Instead, inventories at the time of disposal were input for each year. The DUST-MS code simulated the inventory changes over time caused by radioactive decay and ingrowth, thus allowing decay and transport to begin at the actual year of disposal.

Inventories for three parent nuclides, Pu-242, Cm-244, and Pu-241, were decayed to the daughter and only the daughters were simulated. In the IRA, risk from Pu-242 was below 1E-12, Cm-244 had a low groundwater risk and is short-lived, and Pu-241 has a short half-life and the risk was 1E-11.

Therefore, all three parent nuclides were decayed to their daughters to minimize the number of isotopes in the subsurface transport simulations.

5.1.2 Container Failure Rates

Distributions to represent failure rates as a function of time for different types of containers such as drums, concrete casks, and metal boxes were developed (Becker et al. 1996; Becker 1997) and implemented in the source term model. Multiple failure rates were assigned to contaminants buried in more than one type of container. For example, if the annual disposal inventory for a particular contaminant included disposals in both drums and cardboard boxes, the relative fraction for each container type was used to model the disposal for that year. For waste streams that were not buried in containers or that were buried in cardboard or wooden boxes, the container failure time in the model was set at zero.

The majority of containers buried in the SDA were 55-gal metal drums. Historical disposal practices included periods when drums were carefully stacked in the SDA and periods when drums were dumped. Drums that were stacked in the SDA provide a barrier to contaminant release until the metal corrodes. Thus, stacked drums fail at a slower rate compared to drums that were dumped into the pits without attempting to maintain their integrity. A separate study was performed to determine the failure rate of metal drums in the SDA using data gathered during earlier waste retrieval efforts (Becker 1997). Failure rate distributions were developed to represent stacked and dumped drums. For stacked drums, a normal distribution with a mean failure time of 22.6 years from the time of disposal and a standard deviation of 9.7 years was developed. For dumped drums the data indicated that 28.5% fail at disposal and that the remaining 71.5% fail in a normal distribution with a mean failure time of 11.7 years from time of disposal and a standard deviation of 5 years. The fraction of a contaminant in drums was modeled with the distributed failure appropriate for the type of drum disposal, whether the drums were stacked or dumped.

The rate of corrosion for carbon steel was used to determine failure time of metal boxes and canisters. Boxes and canisters were considered to fail when one-half of the wall thickness had corroded.

Each waste stream was evaluated for the type of container used. The disposal contents of many waste streams were buried in wood or other readily degradable boxes, and no delay of the contaminant release was assumed for the boxes in the model. Polyethylene bags were not accounted for in the container failure modeling. Calculations by Kudera and Brown (1996) indicated that VOC transport through polyethylene bags is rapid compared to transport through sludge. Therefore, the bags do not limit VOC releases. The 55-gal drums, concrete casks, and metal boxes offer a barrier to contaminant release, which was accounted for in the source term model. Waste streams listed as "O" (i.e., other) in CIDRA, or as a combination of container types without a fractional distribution for each type, were modeled as having no container.

5.1.3 Release Mechanisms and Release Rates

The DUST-MS code is a one-dimensional model that has three contaminant release mechanisms: surface washoff, diffusion, and dissolution. These release mechanisms are described as follows:

- The surface washoff model estimates the release from general laboratory trash and is equivalent to the first-order leach model used in other codes such as GWSCREEN (Rood 1999)

- By applying diffusion coefficients for each waste form, the diffusion model computes the diffusional release from different waste geometries such as VOCs from sludge or cement-encased waste

- The dissolution release model estimates the release caused by general corrosion such as the release of activated metals from the corrosion of the base metal.

Yearly disposal amount of each contaminant was proportioned among the three DUST-MS release mechanisms. The percent of contaminant in a release mechanism was input into the DUST-MS code. Total disposal inventory was analyzed to determine the release mechanism and release rate as a function of the waste stream contents buried in any given year. Table 5-3 contains summary information on the waste streams for each individual contaminant, a brief description of the waste streams, and the release mechanisms identified for use in the modeling of the waste streams.

Because each contaminant has a unique set of information, the disposal amount each year for each contaminant was modeled as a separate waste container. The DUST-MS code was used to compute the sum of the results to provide the total release over the time interval for input into the transport models. A summary of release rate information for the different release models is contained in Table 5-4. The basis for using the individual values is discussed in the following paragraphs.

Waste streams that are primarily metal were modeled either as dissolution release by corrosion of the base metal or as surface washoff of contamination on the metal. For actinides and fission products, metal waste streams were modeled as surface washoff release of contaminants on the base metal. Activation products are integral to the base metal and are released by dissolution as the metal corrodes. Table 5-5 lists the release mechanism for contaminants in metal waste streams.

Concrete casks were not modeled with an assumed failure time. Instead, release of contaminant mass from within the casks was modeled as diffusion out of the cask. Casks were modeled as cylinders with a 15-cm (6-in.) wall thickness. Using this thickness assumption allows the ready release of contamination at the surface of the cask. In addition, a diffusion coefficient of 1.0E-06 cm^2/s was used. A diffusion coefficient of 1.0E–06 cm^2/s is typical for a metal ion in water and does not account for the possible partitioning of the contaminant with the waste form or the porous media that the contaminants must travel through. Any partitioning would slow the contaminant release.

Nagata and Banaee (1996) assessed the metals buried in the SDA and concluded that the majority is a form of stainless steel or inconel (nickel-based alloy). Nagata and Banaee (1996) provided a corrosion rate of 1 mm in 4,500 years (2.22E-05 cm/year) for stainless steel in INEEL soil with a magnesium chloride dust suppressant applied. For beryllium the corrosion rate is based on results of a long-term corrosion and degradation test, Adler Flitton et al. (2001). The measured results from the test were modified to include the effect of the magnesium chloride dust suppressant that was applied to the surface of the SDA. The chloride in the dust suppressant would increase the corrosion rate of the beryllium metal. The beryllium corrosion rate is different from that used in the IRA.

Table 5-3. Waste streams for Waste Area Group 7 contaminants of potential concern and long-lived decay chain members.

Contaminant	Waste Stream Code or Waste Generator	Percent of Total in Waste Stream	Total Inventory (Ci)	Waste Stream Description	Release Mechanism
Ac-227	D&D-ARA-1	3.6	1.82E-08	Low-level waste (LLW) from decontamination and demolition of the Auxiliary Reactor Area (ARA) (primarily contaminated metal and debris)	Surface washoff
	CFA-RWM-1	14.1	7.20E-08	Central Facilities Area (CFA) Sewage Treatment Plant unpainted concrete rubble, drying beds soils, clarifier piping, and trickle filter bricks	Surface washoff
	Test Reactor Area	34.3	1.76E-07	Beryllium blocks	Dissolution
	CFA-690-1	47.5	2.43E-07	Combustibles, animal carcasses, scrap metal, sources, sand, and gravel	Surface washoff
	Miscellaneous	0.6	2.86E-09	Miscellaneous minor streams	Surface washoff
Total Ac-227		**100.0**	**5.12E-07**		
Am-243	Idaho National Engineering and Environmental Laboratory (INEEL)	99.6	1.34E+02	Idaho National Engineering and Environmental Laboratory (INEEL) reactor operations waste	Surface washoff
	Miscellaneous	0.4	~ 0	Miscellaneous minor streams	Surface washoff
Total Am-243		**100.0**	**1.34E+02**		
Am-241	INEEL	2.2	4.01E+03	INEEL reactor operations waste	Surface washoff
	RFO-DOW-12H	2.6	4.85E+03	Dirt, concrete, graphite, ash, and soot	Surface washoff
	RFO-DOW-4H	13.8	2.52E+04	Combustibles: paper, rags, plastic clothing cardboard, wood, and polyethylene bottles (Codes 330, 336, 337, 900, and 970)	Surface washoff
	RFO-DOW-3H	80.0	1.46E+05	Uncemented sludge	Surface washoff

Table 5-3. (continued).

Contaminant	Waste Stream Code or Waste Generator	Percent of Total in Waste Stream	Total Inventory (Ci)	Waste Stream Description	Release Mechanism
	Miscellaneous	1.4	2.56E+03	Miscellaneous minor streams	Surface washoff
Total Am-241		**100.0**	**1.83E+05**		
C-14	ANL-785-1	1.5	7.51E+00	Subassembly LLW from Hot Fuel Examination Facility experiments	Dissolution
	TRA-603-1H	1.6	7.81E+00	Test Reactor Area (TRA) resins	Surface washoff
	Argonne National Laboratory – West (ANL-W)	3.3	1.66E+01	Subassembly hardware	Dissolution
	CPP-603-1H	9.2	4.58E+01	Fuel end pieces	Dissolution
	TRA	18.5	9.26E+01	Beryllium waste	Dissolution
	NRF-616-3H, 4H, 8H	21.3	1.07E+02	Core structural pieces	Dissolution
	TRA	41.7	2.08E+02	Activation products	Dissolution
	Miscellaneous	2.9	1.45E+01	Miscellaneous minor streams	Surface washoff
Total C-14		**100.0**	**5.00E+02**		
Cl-36	NRF-618-8R	9.1	1.01E-01	Structural components from reactor fuel modules (e.g., end boxes) from 1989 to 1993	Surface washoff
	OFF-UBM-1H	31.0	3.43E-01	Ore processing waste	Surface washoff
	TRA	59.9	6.62E-01	Beryllium blocks	Dissolution
Total Cl-36		**100.0**	**1.11E+00**		
Cs-137	INEEL	21.4	1.32E+05	INEEL reactor operations	Surface washoff
	TRA-603-15H	16.9	1.04E+05	Metal	Surface washoff
	ANL-765-2H	14.5	8.94E+04	Subassembly hardware	Surface washoff
	TRA-642-6H	9.8	6.02E+04	Scrap metal	Surface washoff
	TRA-603-1H	7.9	4.86E+04	Resins	Surface washoff

Table 5-3. (continued).

Contaminant	Waste Stream Code or Waste Generator	Percent of Total in Waste Stream	Total Inventory (Ci)	Waste Stream Description	Release Mechanism
	ANL-785-1H	6.9	4.23E+04	Subassembly hardware	Surface washoff
	TRA-603-4H	4.3	2.64E+04	Core and loop components	Surface washoff
	OFF-ATI-1H	4.2	2.56E+04	Fuel	Surface washoff
	TRA-603-9H	3.5	2.20E+04	Fuel	Surface washoff
	ANL-765-1H	1.8	1.10E+04	Dry active waste	Surface washoff
	CPP-633-1H	1.3	7.76E+03	High-efficiency particulate air filters	Surface washoff
	Miscellaneous	7.7	4.75E+04	Miscellaneous minor streams	Surface washoff
Total Cs-137		**100.0**	**6.17E+05**		
I-129	PBF-620-1	1.2	1.90E-03	Miscellaneous scrap	Surface washoff
	Naval Reactors Facility	1.7	2.67E-03	Test specimens	Surface washoff
	INEEL	94.5	1.49E-01	INEEL reactor operations waste	Surface washoff
Total I-129		**100.0**	**1.58E-01**		
Nb-94	TRA	4.0	4.06E+01	Activation products	Dissolution
	CPP-603-1H	4.7	4.74E+01	Fuel end pieces	Dissolution
	NRF-618-12H	1.3	1.31E+01	Core structural components	Dissolution
	INEEL	87.6	8.80E+02	INEEL reactor operations waste	Dissolution
	Miscellaneous	2.3	2.31E+01	Miscellaneous minor streams	Surface washoff
Total Nb-94		**100.0**	**1.00E+03**		
Np-237	TRA-632-1H	1.3	3.42E-02	Core structural pieces	Surface washoff
	TRA-603-9H	4.6	1.22E-01	Expended fuel and ceramic fuel	Surface washoff
	TRA-603-4H	6.6	1.74E-01	Core and loop components	Surface washoff
	TRA-642-6H	15.0	3.96E-01	Core, vessel, and loop components	Surface washoff
	TRA-603-1H	15.6	4.13E-01	Resins	Surface washoff

Table 5-3. (continued).

Contaminant	Waste Stream Code or Waste Generator	Percent of Total in Waste Stream	Total Inventory (Ci)	Waste Stream Description	Release Mechanism
	TRA-603-15H	25.9	6.85E-01	Metal	Surface washoff
	INEEL	28.5	7.54E-01	INEEL reactor operations waste	Surface washoff
	Miscellaneous	2.5	6.61E-02	Miscellaneous minor streams	Surface washoff
Total Np-237		**100.0**	**2.64 E+00**		
Pa-231	D&D-ARA-1	99.0	8.56E-04	The LLW from the decontamination and demolition of the ARA facilities (primarily of contaminated metal and debris)	Surface washoff
	Miscellaneous	1.0	8.44E-06	Miscellaneous minor streams	Surface washoff
Total Pa-231		**100.0**	**8.64E-04**		
Pb-210	WER-CMP-1	5.3	2.70E-08	Compacted waste: combination of glass, plastic, absorbents, cloth, paper, and wood	Surface washoff
	ALE-ALE-1H	94.7	4.83E-07	Building rubble, electric wires, piping, machinery, tracers and sources, glass, gloves, paper, filters, and vermiculite	Surface washoff
Total Pb-210		**100.0**	**5.10E-07**		
Pu-240	RFO-DOW-5H	1.7	2.82E+02	Concrete and brick	Surface washoff
	OFF-LRL-2H	2.7	4.53E+02	Concrete, bricks, and asphalt	Surface washoff
	RFO-DOW-11H	4.5	7.62E+02	Graphite molds	Surface washoff
	RFO-DOW-8H	6.0	1.02E+03	Lead from glovebox gloves and sheeting	
	RFO-DOW-7H	7.1	1.21E+03	Glass, including raschig rings	Surface washoff
	RFO-DOW-4H	7.9	1.35E+03	Combustibles: paper, rags, plastic clothing cardboard, wood, and polyethylene bottles (Codes 330, 336, 337, 900, and 970)	Surface washoff
	RFO-DOW-12H	9.0	1.53E+03	Dirt, concrete, graphite, ash, and soot	Surface washoff
	RFO-DOW-6H	10.4	1.78E+03	Filters	Surface washoff
	RFO-DOW-3H	12.4	2.12E+03	Uncemented sludge	Surface washoff

Table 5-3. (continued).

Contaminant	Waste Stream Code or Waste Generator	Percent of Total in Waste Stream	Total Inventory (Ci)	Waste Stream Description	Release Mechanism
	INEEL	13.8	2.36E+03	INEEL reactor operations waste	Surface washoff
	RFO-DOW-9H	22.5	3.85E+03	Noncombustibles: gloveboxes, equipment, pumps, motors, control panels, and office equipment	Surface washoff
	Miscellaneous	2.0	3.42E+02	Miscellaneous minor streams	Surface washoff
Total Pu-240		**100.0**	**1.71E+04**		
Pu-239	RFO-DOW-13H	1.1	7.31E+02	Resins	Surface washoff
	RFO-DOW-5H	1.9	1.25E+03	Concrete and brick	Surface washoff
	INEEL	2.0	1.29E+03	INEEL reactor operations waste	Surface washoff
	RFO-DOW-11H	5.2	3.37E+03	Graphite molds	Surface washoff
	RFO-DOW-8H	7.0	4.53E+03	Lead from glovebox gloves and sheeting	Surface washoff
	RFO-DOW-7H	8.3	5.37E+03	Glass: including raschig rings	Surface washoff
	RFO-DOW-4H	9.2	5.96E+03	Combustibles: paper, rags, plastic clothing cardboard, wood, and polyethylene bottles (Codes 330, 336, 337, 900, and 970)	Surface washoff
	RFO-DOW-12H	10.5	6.79E+03	Dirt, concrete, graphite, ash, and soot	Surface washoff
	RFO-DOW-6H	12.2	7.90E+03	Filters	Surface washoff
	RFO-DOW-3H	14.5	9.40E+03	Uncemented sludge	Surface washoff
	RFO-DOW-9H	26.3	1.70E+04	Noncombustibles: gloveboxes, equipment, pumps, motors, control panels, and office equipment	Surface washoff
	Miscellaneous	1.9	1.23E+03	Miscellaneous minor streams	Surface washoff
Total Pu-239			**6.49E+04**		
Pu-238	RFO-DOW-4H	1.0	1.74E+02	Combustibles: paper, rags, plastic clothing cardboard, wood, and polyethylene bottles (Codes 330, 336, 337, 900, and 970)	Surface washoff

Table 5-3. (continued).

Contaminant	Waste Stream Code or Waste Generator	Percent of Total in Waste Stream	Total Inventory (Ci)	Waste Stream Description	Release Mechanism
	RFO-DOW-12H	1.2	1.99E+02	Dirt, concrete, graphite, ash, and soot	Surface washoff
	RFO-DOW-6H	1.4	2.32E+02	Filters	Surface washoff
	RFO-DOW-3H	1.6	2.75E+02	Uncemented sludge	Surface washoff
	TRA-603-9H	2.9	4.95E+02	Expended fuel and ceramic fuel	Surface washoff
	RFO-DOW-9H	2.9	5.00E+02	Noncombustibles: gloveboxes, equipment, pumps, motors, control panels, and office equipment	Surface washoff
	INEEL	85.3	1.46E+04	INEEL reactor operations waste	Surface washoff
	Miscellaneous	3.8	6.50E+02	Miscellaneous minor streams	Surface washoff
Total Pu-238		**100.0**	**1.71E+04**		
Ra-226	ALE-ALE-1H	1.7	9.93E-01	Building rubble, electric wires, piping, machinery, tracers and sources, glass, gloves, paper, filters, and vermiculite	Surface washoff
	TAN-640-1H	1.7	1.00E+00	Radium-beryllium neutron source	Surface washoff
	ALE-317-2R	1.8	1.10E+00	Combustibles	Surface washoff
	TRA-603-22H	2.1	1.25E+00	Combustibles	Surface washoff
	TRA-603-8H	2.1	1.25E+00	Two Ra-226 sources	Surface washoff
	OFF-DPG-1H	2.8	1.67E+00	Biological waste	Surface washoff
	OFF-AEF-1H	5.6	3.33E+00	Wipes, gloves, glassware, and dry activated waste embedded in concrete	Surface washoff
	OFF-ISC-1H	8.3	5.00E+00	Magnesium-thorium scrap, sources, and miscellaneous laboratory equipment	Surface washoff
	OFF-USN-1H	72.3	4.33E+01	Animal carcasses, waste-paper towels, glassware, tools, and laboratory items	Surface washoff
	Miscellaneous	1.7	1.02E+00	Miscellaneous minor streams	Surface washoff
Total Ra-226		**100.0**	**6.00E+01**		

Table 5-3. (continued).

Contaminant	Waste Stream Code or Waste Generator	Percent of Total in Waste Stream	Total Inventory (Ci)	Waste Stream Description	Release Mechanism
Sr-90	INEEL	60.3	3.89E+05	INEEL reactor operations waste	Dissolution
	ANL-765-2H	21.6	1.39E+05	Subassembly hardware	Dissolution
	ANL-785-1H	10.1	6.60E+04	Subassembly hardware	Dissolution
	ANL-765-1H	2.3	1.48E+04	Dry active waste	Dissolution
	CPP-601-1H	1.5	9.85E+03	Leached Vycor glass	Surface washoff
	CPP-601-3H	1.0	4.00E+03	Dissolved fuel specimens	Surface washoff
	Miscellaneous	3.4	2.19E+04	Miscellaneous minor streams	Surface washoff
Total Sr-90		**100.0**	**6.44E+05**		
Tc-99	D&D-ARA-1	1.1	6.42E-01	LLW from the decontamination and demolition of the ARA facilities (primarily contaminated.	Surface washoff
	NRF	2.6	1.56E+00	Test specimens	Surface washoff
	ANL metal	2.9	1.75E+00	Subassembly hardware	Surface washoff
	INEEL	89.9	5.44E+01	INEEL reactor operations waste	Surface washoff
	Miscellaneous	3.5	2.12E+00	Miscellaneous minor streams	Surface washoff
Total Tc-99		**100.0**	**6.05E+01**		
Th-232	TAN-607-2	1.1	1.41E-02	Test Area North (TAN) Hot Shop noncompactable waste	Surface washoff
	OFF-GDA-1H	1.5	2.00E-02	Fuel fabrication item, laboratory equipment, activated metal, and irradiated fuel	Surface washoff
	TRA-603-9H	1.5	2.01E-02	Expended fuel and ceramic fuel	Surface washoff
	OFF-UBM-1H	93.5	1.26E+00	Ore processing waste	Surface washoff
	Miscellaneous	2.5	3.36E-02	Miscellaneous minor streams	Surface washoff
Total Th-232		**100.0**	**1.34E+00**		

Table 5-3. (continued).

Contaminant	Waste Stream Code or Waste Generator	Percent of Total in Waste Stream	Total Inventory (Ci)	Waste Stream Description	Release Mechanism
Th-230	TAN-607-2	7.5	2.34E-03	TAN Hot Shop noncompactable waste	Surface washoff
	D&D-ARA-1	34.8	1.09E-02	The LLW from the decontamination and demolition of the ARA facilities (primarily of contaminated metal and debris)	Surface washoff
	WMC-WMC-1H	57.1	1.79E-02	Soil, pond sediment, scrap metal, and equipment	Surface washoff
Total Th-230		**100.0**	**3.13E-02**		
Th-229	TRA	3.9	2.69E-07	Beryllium blocks	Surface washoff
	WER-CMP-1	37.1	2.52E-06	Compacted waste: combination of glass, plastic, absorbents, cloth, paper, and wood	Surface washoff
	CPP-ALL-1	58.8	4.01E-06	Contaminated structural materials (metal, concrete, bricks, soil, gravel, wood, and plastics) and concreted ash processed at the Waste Experimental Reduction Facility	Surface washoff
	Miscellaneous	0.1	6.81E-06	Miscellaneous minor streams	Surface washoff
Total Th-229		**100.0**	**6.81E-06**		
U-233	SMC-628-1	1.5	2.21E-02	Nonacidic evaporator sludge	Surface washoff
	SMC-990-1	1.8	2.74E-02	Depleted uranium-contaminated material (metals, glass, and gravel)	Surface washoff
	SMC-628-2	19.9	3.01E-01	Unsolidified slag	Surface washoff
	RFO-DOW-19H	35.9	5.40E-01	Miscellaneous scrap	Surface washoff
	ARA-626-1H	39.8	6.00E-01	Fuel scrap, waste from disassembly of facilities and hot cell waste	Surface washoff
	Miscellaneous	1.1	1.66E-02	Miscellaneous minor streams	Surface washoff
Total U-233		**100.0**	**1.51E+00**		
U-234	ALE-317-2R	1.1	7.10E-01	Combustibles	Surface washoff
	TRA-603-15H	1.6	1.11E+00	Metal	Surface washoff

Table 5-3. (continued).

Contaminant	Waste Stream Code or Waste Generator	Percent of Total in Waste Stream	Total Inventory (Ci)	Waste Stream Description	Release Mechanism
	ANL-704-1R	1.8	1.21E+00	Contact-handled fuel fabrication waste	Surface washoff
	OFF-CSM-1H	1.9	1.30E+00	Magnesium fluoride slag and miscellaneous laboratory waste	Surface washoff
	ANL-752-1R	2.0	1.33E+00	Contact-handled waste	Surface washoff
	TAN-607-2	2.7	1.83E+00	TAN Hot Shop noncompactable waste	Surface washoff
	OFF-GEC-1H	4.4	2.95E+00	Core, vessel, and loop components	Surface washoff
	ANL-EBRI-1H	5.0	3.36E+00	Miscellaneous combustibles and core, vessel, and loop components	Surface washoff
	OFF-ATI-1H	5.4	3.64E+00	Irradiated fuel from research	Surface washoff
	PDA-RFO-1A	6.9	4.64E+00	Inorganic salts, depleted uranium, and sewage sludge	Surface washoff
	CPP-601-3H	7.0	4.70E+00	Dissolved fuel specimens	Surface washoff
	RFO-DOW-16H	21.5	1.45E+01	Depleted uranium	Surface washoff
	RFO-DOW-18H	31.9	2.15E+01	Enriched uranium	Surface washoff
	Miscellaneous	6.9	4.65E+00	Miscellaneous minor streams	Surface washoff
Total U-234		**100.0**	**6.74E+01**		
U-235	ANL-752-1R	1.0	5.60E-02	Contact-handled waste	Surface washoff
	OFF-GDA-1H	1.3	7.00E-02	Fuel fabrication item, laboratory equipment, activated metal, and irradiated fuel	Surface washoff
	OFF-CSM-1H	1.4	8.00E-02	Magnesium fluoride slag and miscellaneous laboratory waste	Surface washoff
	ANL-EBRI-1H	2.0	1.10E-01	Miscellaneous combustibles and core, vessel, and loop components	Surface washoff
	OFF-ATI-1H	2.1	1.14E-01	Irradiated fuel from research	Surface washoff
	INEEL	2.3	1.28E-01	INEEL reactor operations waste	Surface washoff
	CPP-601-3H	2.7	1.50E-01	Dissolved fuel specimens	Surface washoff

Table 5-3. (continued).

Contaminant	Waste Stream Code or Waste Generator	Percent of Total in Waste Stream	Total Inventory (Ci)	Waste Stream Description	Release Mechanism
	OFF-GEC-1H	2.8	1.57E-01	Core, vessel, and loop components	Surface washoff
	WAG-WG7-02	3.3	1.80E-01	Acid Pit in situ stabilization treatability study	Surface washoff
	PDA-RFO-1A	5.9	3.25E-01	Inorganic salts, depleted uranium, and sewage sludge	Surface washoff
	TRA-603-6H	7.3	4.02E-01	Core, vessel, and loop components	Surface washoff
	TRA-603-15H	9.7	5.35E-01	Metal	Surface washoff
	RFO-DOW-18H	13.4	7.44E-01	Enriched uranium	Surface washoff
	TRA-603-16H	14.1	7.80E-01	Combustibles	Surface washoff
	RFO-DOW-16H	19.5	1.08E+00	Depleted uranium	Surface washoff
	Miscellaneous	11.3	6.26E-01	Miscellaneous minor streams	Surface washoff
Total U-235		**100.0**	**5.54E+00**		
U-236	SMC-628-2	1.5	4.37E-02	Unsolidified slag	Surface washoff
	NRF	1.8	5.29E-02	Test specimens	Surface washoff
	RFO-DOW-18H	2.8	8.04E-02	Enriched uranium	Surface washoff
	TRA-603-9H	2.8	8.11E-02	Expended fuel and ceramic fuel	Surface washoff
	TRA-603-4H	3.7	1.07E-01	Core and loop components	Surface washoff
	TRA-642-6H	8.5	2.44E-01	Core, vessel, and loop components	Surface washoff
	TRA-603-1H	9.4	2.70E-01	Resins	Surface washoff
	TRA-603-15H	14.7	4.22E-01	Metal	Surface washoff
	INEEL	20.4	5.83E-01	INEEL reactor operations waste	Surface washoff
	RFO-DOW-16H	31.5	9.03E-01	Depleted uranium	Surface washoff
	Miscellaneous	2.6	7.44E-02	Miscellaneous minor streams	Surface washoff
Total U-236		**100.0**	**2.86E+00**		

Table 5-3. (continued).

Contaminant	Waste Stream Code or Waste Generator	Percent of Total in Waste Stream	Total Inventory (Ci)	Waste Stream Description	Release Mechanism
U-238	INEEL	1.1	1.30E+00	INEEL reactor operations waste	Surface washoff
	ALE-ALE-1H	1.1	1.32E+00	Building rubble, electric wires, piping, machinery, tracers and sources, glass, gloves, paper, filters, and vermiculite	Surface washoff
	OFF-CSM-1H	1.1	1.32E+00	Magnesium fluoride slag and miscellaneous laboratory waste	Surface washoff
	ARA-627-1H	1.4	1.64E+00	Fuel scrap, waste from disassembly of facilities, and hot cell waste	Surface washoff
	SMC-628-2	2.0	2.31E+00	Unsolidified slag	Surface washoff
	PDA-RFO-1A	21.2	2.49E+01	Inorganic salts, depleted uranium, and sewage sludge	Surface washoff
	RFO-DOW-16H	65.0	7.62E+01	Depleted uranium	Surface washoff
	Miscellaneous	7.0	8.20E+00	Miscellaneous minor streams	Surface washoff
Total U-238		**100.0**	**1.17E+02**		
Nitrate	CPP-601-4H	11.0	1.13E+08	Acidic aqueous liquid	Surface washoff
	PDA-RFO-1A	53.0	5.46E+08	Nitrate salts Rocky Flats Plant (RFP) sludge	Surface washoff
	RFO-DOW-17H	36.0	3.71E+08	Nitrate salts in sludge	Surface washoff
Total Nitrate (as nitrogen)		**100.0**	**1.03E+09**		
Carbon tetrachloride	RFO-DOW-4H	2.5	2.05E+07	Paper, rags, and plastic	Vapor diffusion
	RFO-DOW-15H	96.8	7.94E+08	Organic sludge	Vapor diffusion
	Miscellaneous	0.7	5.74E+06	Miscellaneous minor streams	Vapor diffusion
Total carbon tetrachloride		**100**	**8.20E+08**		

Table 5-3. (continued).

Contaminant	Waste Stream Code or Waste Generator	Percent of Total in Waste Stream	Total Inventory (Ci)	Waste Stream Description	Release Mechanism
Methylene chloride	RFO-DOW-12H	9.3	1.30E+06	Dirt, sand, concrete, ashes, and soot	Vapor diffusion
	RFO-DOW-9H	18.3	2.56E+06	Equipment (drill presses, lathes, and pumps)	Vapor diffusion
	RFO-DOW-4H	20.3	2.84E+06	Paper, rags, and plastic	Vapor diffusion
	RFO-DOW-3H	51.2	7.16E+06	Uncemented sludge	Vapor diffusion
	Miscellaneous	1.0	1.40E+05	Miscellaneous minor streams	Vapor diffusion
Total methylene chloride		**100.0**	**1.40E+07**		
Tetrachloroethylene	RFO-DOW-15H	100.0	9.80E+07	Organic sludge	Vapor diffusion
Total tetrachloroethylene		**100.0**	**9.8E+07**		

Table 5-4. Summary of release types and release rate coefficients applied in the source release modeling.

Release Type	Release Rate Coefficient	Reference
Container failure rate	Site-specific values	See Section 5.1.2
Corrosion of carbon steel	1 mm in 450 to 680 years	Nagata and Banaee (1996)
Corrosion of stainless steel	1 mm in 4,500 years (1.19E-05/year)	Adler Flitton et al. (2001)
Beryllium corrosion	1 mm in 39.37 years (2.65E-03/year)	Adler Flitton et al. (2001)
Metal corrosion	Contaminant solubility	Dicke (1997) (see Section 5.2)
Resin dissolution	Surface washoff model was used	Dicke (1997) (see Section 5.2)
Surface washoff	Soil-to-water partition coefficients	Dicke (1997) (see Section 5.2)
Volatile organic compound diffusion	2E-03 cm^2/second (soil) to 5E-09 cm^2/second (saturated saltstone) 1.5E-08 cm^2/second is recommended	Kudera and Brown (1996)

Table 5-5. Waste stream release mechanisms for actinides, activation products, and fission products.

Type of Contaminant	Release Mechanism	Contaminants
Actinides	Surface washoff	Am-241, Am-243, Np-237, Pu-238, Pu-239, Pu-240, U-233, U-234, U-235, U-236, and U-238
Activation products	Dissolution	C-14, Nb-94, and Tc-99
Fission products	Surface washoff	Cs-137, I-129, and Sr-90

Geometry used for the steel pieces also was modified from the IRA. Review of available data showed the surface-area-to-volume ratio for typical INEEL-type reactors to be 0.535/cm (Oztunali and Roles 1985). Combining the corrosion rate and geometry data provided a fractional release from stainless steel of 1.19E-05/year. Similarly, the corrosion rate of beryllium blocks was based on the long-term corrosion and degradation test (Adler Flitton et al. 2001). As for stainless steel, measured beryllium corrosion was modified to account for chloride in the dust suppressant. The corrosion rate of the beryllium blocks used was 1 mm in 39.37 years (2.54E-03 cm/year). The surface-area-to-volume ratio of the beryllium blocks is 1.043/cm. Combining geometry data with the corrosion rate provides a fractional release from the beryllium blocks of 2.65E-03/year.

The above discussion applies to integral contamination of steels. Release of other metals (e.g., lead) into the subsurface is dependent on chemical properties of soil water and solubility of that metal in INEEL pore water conditions. Soil water has a high pH, causing many contaminants to have a low solubility (Dicke 1997). To simulate release of metals (e.g., lead), the surface washoff release model was used with the appropriate contaminant-specific solubility limit for INEEL soil water chemistry.

Sludge buried at the SDA contains VOCs, radioactive contaminants, and other hazardous constituents. Release of VOCs from sludge is through vapor diffusion (Kudera and Brown 1996). As shown in Table 5-4, release rates can vary by several orders of magnitude. The value used in the IRA

(Becker et al. 1998) was 2E-06 cm^2/second. Release of metals and radioactive contaminants from sludge occurs through leaching, which was modeled with the surface washoff release model.

A surface washoff release mechanism was assumed for waste streams that are generic laboratory trash. The surface washoff release mechanism provides the most rapid release rates. Similarly, contaminants identified as surface contamination of a base material (e.g., anticontamination clothing) were modeled with the surface washoff release model. The surface washoff model applies a partition coefficient to determine the release. The soil-to-water partition coefficient was used as a first approximation.

The surface washoff release model was used to simulate the release from resins. For activation and fission products, using surface washoff release generates a higher release rate, which is appropriate because these contaminants are generally mobile (low K_d). Resin would sorb the contaminant better than soil.

5.1.4 Contaminant Grouping for Modeling

Release and subsurface transport were simulated for 24 contaminants, which were grouped into seven groups of contaminants for fate and transport simulation. This grouping was used in source term simulations to provide a consistent set of inputs for the biotic uptake model (DOSTOMAN) and the subsurface model (TETRAD). Members of a decay chain are assigned to the same group. Isotopes in the chain with a half-life of more than 1 year were included explicitly in the simulations, while contaminants with shorter half-lives were assumed to be in equilibrium with long-lived parents. Grouping for the COPCs and long-lived decay chain members is defined in Table 5-6 as Groups 1 through 5. Some of the long-lived daughter products were not identified as COPCs in the IRA (Becker et al. 1998) but were included here to confirm that they pose no unacceptable risk and to assess sensitivity and uncertainty. Some of the ABRA sensitivity cases reduce the release of the parent nuclide and thus increase the ingrowth of the daughter in the waste zone.

Table 5-6. Contaminant grouping for simulations implemented for the Pre-Draft Remedial Investigation/Baseline Risk Assessment.

Simulation Group	Contaminants in the Group	Description	Basis[a]
Group 1	Am-241, Np-237, U-233, and Th-229	Pu-241 decay chain	Neptunium series beginning at Pu-241 created by nuclear reactions.
Group 2	Pu-239, U-235, Pa-231, Ac-227, and Am-243	Am-243 and Pu-239 decay chain	Am-243 to Pu-239, both created by nuclear reactions, to actinium series initiated by U-235.
Group 3	Pu-240, U-236, and Th-232	Pu-240 decay chain	Pu-240 to U-236 created by nuclear reactions to thorium series initiated by Th-232.
Group 4	Pu-238, U-234, Th-230, Ra-226, and Pb-210	Pu-238 decay chain	Pu-238 created by nuclear reactions to U-234 to mid-uranium series.
Group 5	U-238, U-234, Th-230, Ra-226, and Pb-210	U-238 decay chain	Uranium series initiated by U-238.
Group 6	Nitrate	Toxic chemicals	Contained primarily in Rocky Flats Plant waste.
Group 7	Tc-99, I-129, C-14, Nb-94, and Cl-36	Fission and activation products	Created by nuclear reactions.

a. Shleien (1992).

5.1.5 Simulated Source Areas

In the ABRA modeling, distribution of waste in the SDA was substantially refined relative to the IRA. At the time of the IRA, data were insufficient to proportion waste into individual pits or trenches; however, information on the shipping records was subsequently input into WasteOScope database (INEEL 2002a, 2002b). Use of WasteOScope has facilitated modeling of the distribution of the contaminant mass to specific source areas in the SDA based on actual disposal records. The SDA was divided into 13 source areas for modeling contaminant release and transport. These source areas are listed in Table 5-7, which also includes a brief description of the disposals composing them. Each source area is represented in the subsurface model grid as illustrated in Figure 5-1. Note that the pits are individually modeled (except for Pits 1 and 2, which are adjoining), whereas the trenches and soil vaults are modeled together. Because DUST-MS is a one-dimensional model, multiple simulations were implemented for each contaminant group to simulate the release from each source area individually. Results were then combined for input into the subsurface transport and biotic uptake simulations.

Table 5-7. Source areas in the Subsurface Disposal Area implemented in the source release model.

Source Area	Description[a]	Area (ft^2)	Open	Closed
1	Trenches 1–10	120,960	July 8, 1952	February 7, 1958
2	Pits 1 and 2	103,338	November 1, 1957	July 1, 1963
3	Pit 3	41,830	December 15, 1961	January 3, 1963
4	Pit 4	111,732	January 3, 1963	September 26, 1967
5	Pit 5	108,754	June 18, 1963	December 22, 1966
6	Pit 6	54,984	May 18, 1967	October 22, 1968
7	Pit 8	31,294	March 6, 1967	November 30, 1969
8	Pit 9	45,541	November 8, 1967	June 9, 1969
9	Pit 10	111,732	June 7, 1968	July 8, 1971
10	Pad A[b]	32,160	September 26, 1972	November 17, 1978
11	Low-level waste Pits 17 through 20[c,d]	97,051	June 25, 1975	December 31, 1999[e]
12	Projected low-level waste Pits 17 through 20	36,000	January 1, 2000	Projected to 2010[e]
13	All soil vault rows[c]	2,849	March 2, 1977	April 15, 1995

a. Pit 7 had only five disposals and was not assigned to a source area. The acid pit was not assigned to a source area because it contains no contaminants of potential concern and was eliminated from further evaluation (DOE-ID 1998).

b. Pad A waste includes part of the waste that was originally disposed of in Pits 11 and 12. Residual inventory in Pits 11 and 12 were assigned to the Pad A source area.

c. Trenches 11 through 58 were not explicitly modeled. The inventories in Trenches 11 through 58 were partitioned between the soil vaults and the active low-level waste (LLW) pit, depending on the waste stream.

d. Pits 13 through 16 received LLW from on-Site generators and the inventories were assigned to the LLW pit.

e. The LLW disposal operation is still active. Actual disposals in Pits 17 through 20 were implemented in the model for Source Area 11. Projected disposals were evaluated in Source Area 12.

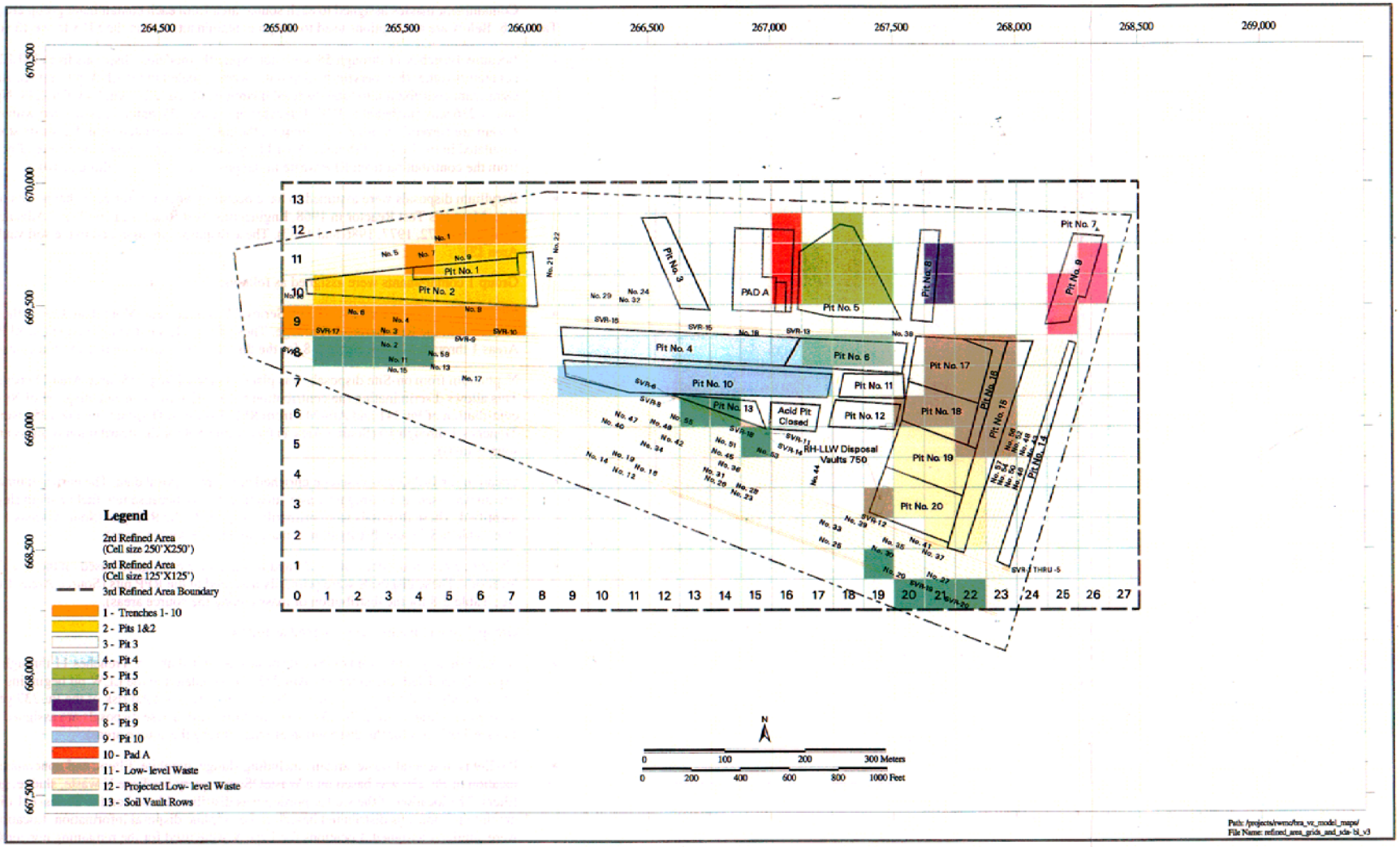

Figure 5-1. The 13 source areas simulated in the source release model and specifically represented in the subsurface model domain.

Contaminant masses assigned to each source area from each contaminant group are given in Table 5-8. Below are assumptions used to assign contaminants within the SDA to the 13 source areas.

- Because Trenches 11 through 58 were not explicitly modeled, disposals from INEEL waste generators (other than beryllium disposals) were modeled in the LLW pit (Source Area 11). A significant contribution to total disposal quantities for Ac-227, Am-243, Cm-244, Np-237, Pu-238, and U-236 was attributed to INEEL reactor operations. Inventories associated with this waste stream are currently in review. Therefore, the fraction associated with that waste stream was simulated in the LLW pit (Source Area 11) so that the contribution could be readily distinguished from the contribution from RFP waste in the pits (Source Areas 1 through 10).

- Beryllium disposals were assumed to have occurred when reactor core changeouts occurred (i.e., Materials Test Reactor in 1968, Engineering Test Reactor in 1970, and Advanced Test Reactor in 1972, 1977, 1986 and 1987). These disposals are assigned to the soil vault rows (Source Area 13).

Group 1 contaminants were assigned as follows:

- Locations for Am-241 were based on Series-741 sludge data. More than 80% of the Am-241 was contained in the RFP Series-741 sludge. These disposals are divided among the RFP pits (Source Areas 1 through 10) (see Table 5-8 for the distribution of mass among the source areas).

- Neptunium from on-Site disposals was placed in the LLW pit (Source Area 11) beginning in 1958. This allows discriminating the contribution to total risk from on-Site disposal of Np-237 from the contribution of Pu-241 and Am-241 from RFP disposals. Disposals before 1958 went into Trenches 1 through 10 (Source Area 1) (see Table 5-8 for the distribution of mass among the source areas).

- Location for U-233 was based on enriched uranium disposal data. The enriched uranium waste stream was used as a surrogate waste stream identifier because few fuel or scrap shipments were identified. These disposals were primarily assigned to the RFP pits (Source Areas 1 through 10) (see Table 5-8 for the distribution of mass among the source areas).

- Th-229 comes from decay of U-233 and locations were assigned based on the U-233 disposal locations. These disposals were primarily assigned to the RFP pits (Source Areas 1 through 10) (see Table 5-8 for the distribution of mass among the source areas).

Group 2 contaminants were assigned as follows:

- Am-243 mainly came from on-Site disposals. As noted above, Trenches 11 through 58 were not explicitly modeled; therefore, the Am-243 was simulated in the LLW pit beginning in 1958. This approach allowed determining the relative contribution to total risk of the Pu-239 generated by ingrowth separately from Pu-239 disposals from RFP. These disposals are assigned to Source Area 11 (see Table 5-8 for the distribution of mass among the source areas).

- Pu-239 is in several waste streams including sludge, graphite, filters, and noncombustibles. The location of Pu-239 was based on a WasteOScope query for Type V waste, sludge, graphite, and filters. The location of the sludge portion was distributed based on the Series-741 disposals. The graphite portion was distributed based on the graphite disposal information. Locations for filters were similarly assigned. Locations for Type V were used for the remaining noncombustible mass. These disposals are assigned to the RFP pits (Source Areas 1 through 10) (see Table 5-8 for the distribution of mass among the source areas).

Table 5-8. Mass (in grams) disposed of in the 13 simulated source areas by simulation groups for the Subsurface Disposal Area modeling.

Simulation Group	Isotope	Total	Source Area 1	Source Area 2	Source Area 3	Source Area 4	Source Area 5	Source Area 6	Source Area 7	Source Area 8	Source Area 9	Source Area 10	Source Area 11	Source Area 12	Source Area 13
1	Am-241	5.32E+04	2.07E+03	1.43E+04	1.92E+03	1.18E+04	8.65E+03	2.65E+03	0.00E+00	3.00E+03	6.28E+03	2.56E+03	2.62E-01	0.00E+00	3.45E+01
	Np-237	3.75E+03	1.16E+02	0.00E+00	0.00E+00	0.00E+00	0.00E+00	0.00E+00	0.00E+00	0.00E+00	0.00E+00	0.00E+00	3.63E+03	0.00E+00	0.00E+00
	U-233	1.56E+02	8.51E-06	8.00E-06	0.00E+00	3.19E+01	3.36E-06	2.41E+01	0.00E+00	5.68E-08	6.22E+01	9.98E-01	3.69E+01	0.00E+00	2.12E-02
	Th-229	3.20E-05	4.81E-11	4.52E-11	0.00E+00	1.16E-11	1.90E-11	5.13E-12	0.00E+00	3.21E-13	5.90E-07	2.17E-07	3.07E-05	0.00E+00	4.56E-07
2	Am-243	6.74E+02	3.53E-03	0.00E+00	0.00E+00	0.00E+00	0.00E+00	0.00E+00	0.00E+00	0.00E+00	0.00E+00	0.00E+00	6.74E+02	0.00E+00	0.00E+00
	Pu-239	1.04E+06	9.81E+04	2.36E+05	4.52E+04	1.87E+05	2.76E+05	4.07E+04	0.00E+00	1.42E+04	1.40E+05	7.83E+03	7.78E+01	0.00E+00	0.00E+00
	U-235	2.56E+06	2.15E+05	5.81E+05	0.00E+00	1.98E+05	4.68E+05	3.4,6E+04	0.00E+00	2.41E+03	3.74E+05	4.35E+05	1.38E+05	0.00E+00	1.15E+05
	Pa-231	2.08E-02	5.90E-07	5.55E-07	0.00E+00	1.43E-07	2.33E-07	6.29E-08	0.00E+00	3.93E-09	8.54E-05	3.27E-05	2.07E-02	0.00E+00	3.19E-05
	Ac-227	7.08E-09	0.00E+00	0.00E+00	0.00E+00	0.00E+00	0.00E+00	0.00E+00	0.00E+00	0.00E+00	0.00E+00	0.00E+00	7.08E-09	0.00E+00	0.00E+00
3	Pu-240	7.53E+04	5.99E+03	1.4,7E+04	3.29E+03	1.16E+04	1.75E+04	2.19E+03	0.00E+00	5.86E+02	8.39E+03	7.68E+02	1.03E+04	0.00E+00	0.00E+00
	U-236	4.42E+04	8.35E+03	4.16E+03	4.09E+02	1.39E+03	1.32E+03	5.25E+02	0.00E+00	0.00E+00	1.17E+03	9.91E+02	2.59E+04	0.00E+00	0.00E+00
	Th-232	1.23E+07	1.52E-06	5.35E+06	5.33E+06	4.87E+05	8.82E+05	2.74E+01	9.19E+00	2.76E+01	2.04E+03	1.15E+03	2.36E+05	0.00E+00	7.09E+03
4	Pu-238	9.99E+02	1.05E+01	2.67E+01	6.45E+00	2.95E+01	4.70E+01	2.91E+00	0.00E+00	0.00E+00	1.4,7E+01	1.42E+00	8.59E+02	0.00E+00	0.00E+00
	U-234	0.00E+00	0.00E+00	0.00E+00	0.00E+00	0.00E+00	0.00E+00	0.00E+00	0.00E+00	0.00E+00	0.00E+00	0.00E+00	0.00E+00	0.00E+00	0.00E+00
	Th-230	0.00E+00	0.00E+00	0.00E+00	0.00E+00	0.00E+00	0.00E+00	0.00E+00	0.00E+00	0.00E+00	0.00E+00	0.00E+00	0.00E+00	0.00E+00	0.00E+00
	Ra-226	0.00E+00	0.00E+00	0.00E+00	0.00E+00	0.00E+00	0.00E+00	0.00E+00	0.00E+00	0.00E+00	0.00E+00	0.00E+00	0.00E+00	0.00E+00	0.00E+00
	Pb-210	0.00E+00	0.00E+00	0.00E+00	0.00E+00	0.00E+00	0.00E+00	0.00E+00	0.00E+00	0.00E+00	0.00E+00	0.00E+00	0.00E+00	0.00E+00	0.00E+00
5	U-238	3.4,8E+08	6.31E+07	5.39E+07	1.11E+07	3.23E+07	2.4,8E+07	1.25E+07	0.00E+00	4.84E+05	2.61E+07	1.01E+08	2.32E+07	0.00E+00	0.00E+00
	U-234	1.08E+04	9.69E+02	2.80E+03	1.24E+03	6.80E+02	6.54E+02	2.05E+02	1.82E+02	6.58E+02	1.10E+03	1.21E+03	4.82E+02	0.00E+00	6.25E+02
	Th-230	1.55E+00	3.53E-08	3.68E-08	8.4,8E-09	1.41E-08	1.34E-08	4.24E-09	3.15E-08	1.25E-07	6.10E-07	1.4,8E-01	6.64E-01	0.00E+00	7.38E-01
	Ra-226	6.06E+01	3.68E-13	2.75E+01	2.69E+01	1.33E-02	1.09E-02	2.18E-02	1.28E-02	4.40E-02	8.31E-02	3.78E+00	8.00E-02	0.00E+00	2.13E+00
	Pb-210	6.68E-09	6.4,7E-16	6.72E-16	1.55E-16	2.59E-16	2.4,6E-16	7.76E-17	1.40E-13	5.60E-13	2.82E-12	1.42E-12	6.67E-09	0.00E+00	5.76E-12
6	Nitrate	1.03E+09	2.66E+07	2.84E+07	8.37E+06	4.08E+07	1.23E+07	9.59E+07	0.00E+00	5.55E+06	2.43E+08	5.70E+08	0.00E+00	0.00E+00	0.00E+00
7	Tc-99	3.56E+03	6.01E+02	0.00E+00	0.00E+00	0.00E+00	0.00E+00	0.00E+00	0.00E+00	0.00E+00	0.00E+00	0.00E+00	2.96E+03	0.00E+00	0.00E+00
	I-129	8.94E+02	8.84E+01	0.00E+00	0.00E+00	0.00E+00	0.00E+00	0.00E+00	0.00E+00	0.00E+00	0.00E+00	0.00E+00	8.06E+02	0.00E+00	0.00E+00
	C-14	1.12E+02	9.96E+00	0.00E+00	0.00E+00	0.00E+00	0.00E+00	0.00E+00	0.00E+00	0.00E+00	0.00E+00	0.00E+00	8.57E+01	0.00E+00	1.64E+01
	Cl-36	3.35E+01	9.26E-06	0.00E+00	9.52E+00	0.00E+00	0.00E+00	0.00E+00	0.00E+00	0.00E+00	0.00E+00	0.00E+00	2.40E+01	0.00E+00	0.00E+00
	Nb-94	5.36E+03	2.38E+02	0.00E+00	0.00E+00	0.00E+00	0.00E+00	0.00E+00	0.00E+00	0.00E+00	0.00E+00	0.00E+00	5.12E+03	0.00E+00	0.00E+00

- Location of U-235 was based on disposal data for enriched uranium. These disposals are primarily assigned to the RFP pits (Source Areas 1 through 10) (see Table 5-8 for the distribution of mass among the source areas).

- Location of Pa-231 was based on disposal data for enriched uranium. These disposals are primarily assigned to the RFP pits (Source Areas 1 through 10) (see Table 5-8 for the distribution of mass among the source areas).

- Location of Ac-227 disposals was assumed to be in the LLW pit. These disposals are assigned to Source Area 11 (see Table 5-8 for the distribution of mass among the source areas).

Group 3 contaminants were assigned as follows:

- The portion of the Pu-240 generated by INEEL reactor operations was disposed of in the LLW pit (Source Area 11) for disposals after 1958. The RFP portion of Pu-240 was proportioned with a methodology similar to the Pu-239 in Group 2 above. The fraction of the waste in the various RFP waste streams was used to determine distribution of masses into the various RFP pits (Source Areas 1 through 10) (see Table 5-8 for the distribution of mass among the source areas).

- Because U-236 has on-Site contributions, locations were determined using the same approach applied for plutonium. All waste was assumed to have been placed in trenches (Source Area 1) through 1958. The U-236 was divided between the RFP waste in pits (Source Areas 2 through 10) and on-Site waste in the LLW pit (Source Area 11) (see Table 5-8 for the distribution of mass among the source areas).

- Th-232 is assumed to come primarily from decay of U-236 so disposals are proportioned in source areas based on the U-236 distribution.

Group 4 contaminants were assigned as follows:

- Waste was proportioned similar to plutonium waste in Groups 2 and 3 because significant contributions of Pu-238 may have been received from the INEEL reactor operations. The on-Site portion of the Pu-238 was disposed of in the LLW pit (Source Area 11) for disposals after 1958. The RFP portion of Pu-238 proportioned with a methodology similar to the Pu-239 in Group 2 above (see Table 5-8 for the distribution of mass among the source areas).

- Disposal inventories of U-234 and its daughters (i.e., Th-230, Ra-226, and Pb-210) are included in Group 5; therefore, inventory was zero for Group 3 to allow discriminating the relative contribution to total risk from the uranium disposals and the U-234 ingrowth from Pu-238.

Group 5 contaminants were assigned as follows:

- The bulk of U-238 and U-234 was in roaster oxide. Disposal data for roaster oxide exist for 1966 through 1969. Before 1961, all waste was disposed of in the open pit or trench. From 1962 to 1965, mass was proportioned equally in the open pits. All uranium waste from 1970 to 1978 was disposed of on Pad A. Uranium waste disposal after 1978 was assigned to the LLW pit. Because the majority of the uranium disposals are from RFP, these disposals were assigned to Source Areas 1 through 11 (see Table 5-8 for the distribution of mass among the source areas).

- Inventories of Th-230, Ra-226 and Pb-210 are assumed to come largely from ingrowth from the uranium decay chain and are proportioned in the pits and trenches in the same manner as U-238.

Group 6 contaminants were assigned as follows:

- Nitrates were primarily in the Series-745 sludge. The Series-745 data were used for disposals from 1967 through 1978. Disposal before 1967 were proportioned into Pits 1 through 10. Waste disposal beginning in 1979 was assigned to the LLW pit. These disposals were proportioned between Source Areas 1 through 11 (see Table 5-8 for the distribution of mass among the source areas).

Group 7 contaminants were assigned as follows:

- The amount of Tc-99 in beryllium blocks is small. It was modeled as surface washoff rather than dissolution because part of the Tc-99 is in activated metal and DUST-MS cannot handle two separate corrosion rates in a single year. Therefore, the Tc-99 was assigned to Trenches 1 through 10 for disposals before 1960 (Source Area 1) and in the LLW pit for disposals after 1960 (Source Area 11) (see Table 5-8 for distribution of mass among the source areas).

- I-129 comes from on-Site generators. Disposals of I-129 before 1960 were in Trenches 1 through 10 (Source Area 1) and disposals after 1960 were placed in the LLW pit (Source Area 11). Distribution of mass among the source areas is shown in Table 5-8.

- C-14 consists of several waste types: beryllium blocks, activated metal, and other trash. Before 1960, the C-14 was disposed of in Trenches 1 through 10 (i.e., Source Area 1). Disposals after 1960 were segregated to evaluate the effect of the C-14 in the beryllium blocks and to be able to account for the different corrosion rate of beryllium compared to stainless steel. The C-14 disposed in the beryllium blocks was disposed of in the SVRs (i.e., Source Area 13) and the C-14 in activated metal and other trash was put into the LLW pit (i.e., Source Area 11) because Trenches 11 through 58 were not explicitly modeled.

- Most of the Cl-36 is contained in the beryllium blocks that were disposed of in the SVRs (Source Area 13). Disposals for off-Site waste were in Pit 3 (Source Area 3) and in trenches before 1961 (Source Area 1). The remainder was assigned to the LLW pit (Source Area 11) because the later trenches, Trenches 11 through 58, were not modeled explicitly (see Table 5-8 for distribution of mass among the source areas).

- Nb-94 came from on-Site generators. Because none of the Nb-94 is in the beryllium blocks, Nb-94 disposals were modeled as in the trenches (Source Area 1) or LLW pit (Source Area 11). The LLW pit was used rather than the soil vault rows to allow consistency with other contaminants in the group that simulated the contribution from the beryllium blocks in the SVRs (see Table 5-8 for the distribution of mass among the source areas).

Based on these assumptions, the mass disposed of in each of the 13 source areas is listed by simulation group in Table 5-8.

5.1.6 Infiltration Rates

Site-specific infiltration rates were developed for the SDA. The infiltration rate assigned to each of the 13 source areas was based on the assignment of infiltration in the subsurface flow and transport model. Infiltration rates applied to the grid blocks of the subsurface flow and transport model along with the 13 source areas are presented in Figure 5-2. Infiltration assigned in the subsurface model was averaged over the grid blocks representing the source areas. The resulting averages are shown at the bottom of Figure 5-2.

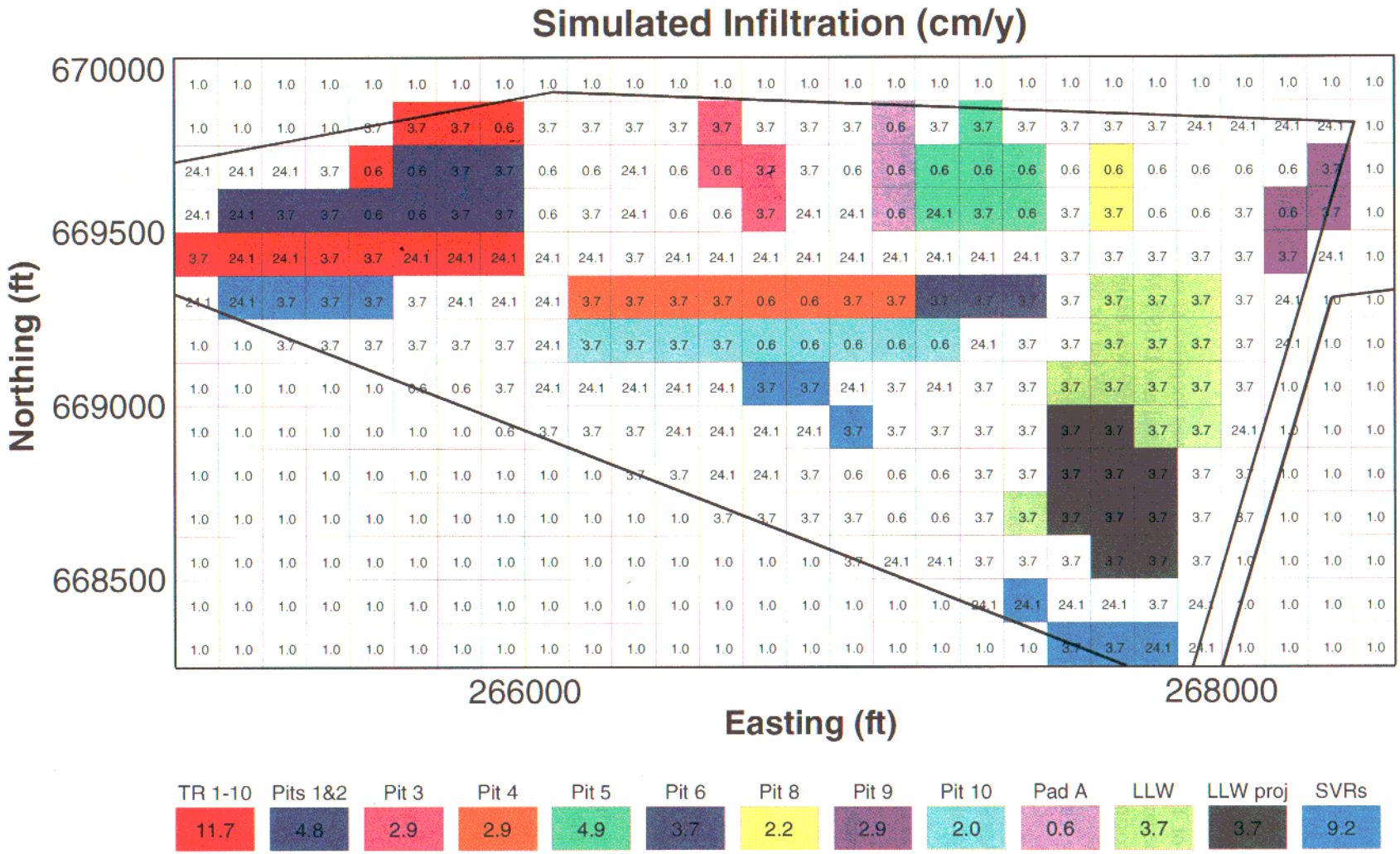

Figure 5-2. Infiltration rates assigned in the subsurface flow model and averages used for the 13 source areas simulated in the source release model.

5.1.7 Source Term Model Calibration

Monitoring data from in and immediately proximal to the buried waste are required to calibrate the source term model. Data taken from directly beneath the waste are limited and time histories have not been developed. Therefore, available data are insufficient to attempt source term model calibration.

Several different types of probes were installed in the waste as described in Section 3.6. Continued monitoring and evaluation of the data could allow validation of the values used in the ABRA source release modeling and provide data sets for calibrating any future source release modeling.

5.2 Dissolved-Phase Transport Modeling

Contaminant fate and transport simulations performed for dissolved or aqueous phase COPCs are discussed in this section. Volatile organic compound modeling is addressed in Section 5.3. The model developed and implemented to represent movement of water and contaminants in the subsurface for this ABRA was derived from the model presented in Magnuson and Sondrup (1998), which was used to support development of the IRA (Becker et al. 1998). The model originally developed by Magnuson and Sondrup (1998) for the IRA will be referred to as the IRA model. The IRA model was improved to represent the current best interpretation of water movement and contaminant transport in the subsurface. The ABRA numerical model described in this section was developed and implemented to represent movement of water and contaminants after they are released from their disposal locations. This section presents the conceptual model, improvements compared to the IRA model, the basis for parameters of the numerical model, and results of the numerical model in terms of moisture distributions and resulting contaminant concentrations.

5.2.1 Dissolved-Phase Flow and Transport Conceptual Model

The general conceptual flow model treated water movement as though subsurface sediments consisted of a heterogeneous, isotropic, porous medium. Net infiltration of meteoric water into the subsurface was described in the model by three constant rates representing areas of low, medium, and high infiltration. Surficial sediments and sedimentary interbeds were simulated with varying thicknesses and upper-surface elevations. Only the three uppermost interbeds were considered in the conceptual model. These were the A-B, B-C, and C-D interbeds. Interbeds deeper than the C-D interbed, though present in reality, were not included in the ABRA simulations.

Flow in the fractured basalt portion of the subsurface was considered as occurring only in the fracture network, to emulate an anisotropic medium with a low effective porosity and a high permeability. The basalt matrix itself was not considered to affect flow or transport.

The effect of water migrating laterally at depth in the vadose zone from either Spreading Area A or B, or from the Big Lost River was included in the conceptual model. No attempt was made to discern the source. Rather, based on the 1999 USGS tracer test (Nimmo et al. 2002), the influence of this additional spreading-area water was limited to the western half of the SDA. A steady-state spreading area influence was modeled; however, in reality, the effect would vary temporally, depending on the magnitude of surface water flows in the Big Lost River and discharges to the spreading areas. Variation caused by changing the steady-state magnitude of the spreading area influence in the vadose zone model was assessed in sensitivity cases.

Movement of water and contaminants within the aquifer was considered controlled by the regional flow in the aquifer. Because of the long time durations of hundreds to thousands of years simulated in the ABRA, movement of water within the SRPA was considered steady state.

Locally, groundwater flow was affected by a region of low permeability in the aquifer. This region has been identified in wells immediately south of the SDA. This low-permeability region may extend underneath the SDA, as evidenced by the extremely slow decline in concentration of a tracer injected directly into aquifer Well M17S. This extremely slow decline is indicative of low velocities at that location. Low velocities in the aquifer have an impact on model results. As contaminants enter the aquifer from the vadose zone, less dilution occurs in grid blocks with low aquifer velocities and simulated contaminant concentrations are higher than they would be if the aquifer velocity were greater.

Processes that were considered for dissolved-phase transport include advection, dispersion, diffusion, radioactive chain decay and ingrowth, and adsorption in the sediment portions of the simulation domain.

In the fractured basalt portion of the simulation, no sorption was assumed. Sorption in surficial and interbed sediments was assumed to follow linear reversible isotherms that could be described by use of partition coefficients (K_ds). Sediment K_ds were assigned based on best-estimate values rather than conservative screening values. A set of best-estimate K_ds developed by Dicke (1997) was the primary source used in this application. Revised values for C-14 were included based on additional RWMC-specific work conducted since 1997 (Dicke 1998). Facilitated transport mechanisms (e.g., colloidal transport) may affect contaminant migration in the SDA subsurface. Studies have been conducted that show very small fractions of the plutonium and americium may move in a facilitated manner at the SDA (Grossman et al. 2001) (see Section 3.7). Facilitated transport was included conceptually in sensitivity studies. In the baseline case, facilitated transport was not included in the conceptual model and its implementation.

Single isolated detections of contaminants have occurred at the SDA during monitoring of subsurface contaminants. Though these isolated detections may be indicative of contaminant transport, it is not feasible with the current modeling approach to try to emulate each one. Instead, the subsurface transport model attempts to mimic the large-scale overall behavior of contaminants in the subsurface. This approach directs the model to emulate contaminants that are consistently present in a distributed manner in the subsurface.

Concentrations of contaminants in the aquifer near the SDA are not attributed to facilities in the general upgradient direction relative to flow in the aquifer. This interpretation is based on analyses of time histories of contaminant-monitoring results in the upgradient well-monitoring network. The implication of this aspect of the conceptual model is that if contaminants are in the aquifer near the SDA, then the contamination originated in the SDA and was derived from leaching and migration of contaminants from the buried waste.

5.2.2 Predecessor Model, the Interim Risk Assessment

Though other attempts have been made to simulate flow and transport of specific contaminants in the subsurface of the SDA, the primary previous modeling study was the comprehensive model developed by Magnuson and Sondrup (1998) for the IRA. That model represented the first attempt to simulate flow and transport through the entire vadose zone and aquifer domains for an extensive suite of contaminants of potential concern. The IRA model attempted to include calibration to vadose zone perched water behavior and an interpreted contribution to nitrate concentrations in the aquifer. Results of that calibration were termed limited in their degree of success in emulating observed behavior. Attempts to improve calibration were hindered by the paucity of vadose zone monitoring data that could be used to demonstrate transport of a nonsorbing contaminant. The IRA model was used to make a series of 10,000-year predictive simulations for 52 contaminants. Results of that modeling formed the basis for risk estimates in the IRA and were used to screen contaminants for the ABRA.

The IRA model was slightly revised for the ABRA by Sondrup (1998) to improve simulation of VOCs (see Section 5.4). The IRA model also has been used by Waste Management to update both the LLW Radiological Performance Assessment (Case et al. 2000) and the Composite Analysis (McCarthy et al. 2000). The IRA model development, implementation, and results have undergone extensive review by Fabryka-Martin, Gee, and Flint (1999) and the USGS (1998). Though the reviews are generally complimentary of the IRA model, none of these reviews concluded that the IRA model was in a satisfactory state to make conclusive predictions of the fate and transport of contaminants in the subsurface. Of these reviews, the USGS effort (which is currently in progress) was by far the most extensive. The main comments from the USGS about modeling flow and transport of radionuclides at the RWMC are listed below:

- The modeling performed for the IRA cannot necessarily be shown to be conservative.
- Spatial variability of hydrologic and transport properties of the sedimentary interbeds should be evaluated and the impact of including this spatial variability into the modeling should be assessed.
- Impacts of additional sources of vadose zone water from the Big Lost River system on predicted contaminant concentrations should be evaluated.
- Selected K_d values used in the IRA cannot be shown to be conservative because they do not account for (a) colloidal transport, (b) the enhanced mobility fraction observed in column studies, (c) variations in mineralogy, (d) nonlinearity of isotherms, and (e) fluctuations in pore water chemistry. Furthermore, K_d values taken from the literature cannot be shown to be representative of the SDA.

Modeling presented in Section 5 responds to each of these observations, particularly to the second and third bullets above.

5.2.3 Overview of Improvements to the Interim Risk Assessment Model

Improvements on the IRA model that have been made in large part in response to review comments are summarized below.

5.2.3.1 Vadose Zone and Aquifer Domain Separation. The IRA model had both the vadose zone and the aquifer included into a single simulation domain to enable simulating off-gassing of volatile contaminants as they migrated within the aquifer. While this approach was convenient because it eliminated the need for an interface to take water and contaminants from the bottom of the vadose zone model and assign them as boundary conditions at the top of a saturated zone model, the single domain was computationally inefficient because of the larger scale required to include the INEEL southern boundary in the simulation domain. This inefficiency resulted in an excessively large number of grid blocks in portions of the vadose zone distant from the SDA that were not of interest.

By separating the vadose zone and aquifer into two domains, increased discretization could be achieved in the representation for the vadose zone with emphasis on the surficial sediments. The smallest horizontal grid used to represent surface sediments were square grid blocks that were 38.1 m (125 ft) on a side. By comparison, the smallest grid blocks in the IRA model were 62.5 m (205 ft) on a side. This increased discretization allowed improved representation of the release of different waste streams into the subsurface.

5.2.3.2 Conformable Gridding in the Vadose Zone Model. The IRA model had a rigidly structured three-dimensional grid where the vertical dimension of each grid in a horizontal slice of the

model was the same. This structure precluded accurately representing the elevation of the lithologic contacts between interbed sediments and basalts in the simulation domain. In the ABRA model, the grid blocks had variable vertical dimensions to better emulate the actual lithologic surfaces. This conformable grid also had a variable upper surface elevation. The IRA model treated the upper surface as perfectly flat.

5.2.3.3 Improved Linkage Between Source Release and Vadose Zone Models. The current model is similar to the IRA model and relies on an external simulation of the release of contaminants from their burial locations. The IRA source model applied one overall average infiltration rate of 8.5 cm/year (3.3 in./year) to calculate the release of contaminants. However, the IRA subsurface model included spatially varying infiltration across the surface of the SDA. In the current model, the spatially varying infiltration rates were partially incorporated into the source term model. The assigned infiltration rates for the grid blocks representing a waste stream were averaged together to determine a more consistent estimate of the amount of water going through that portion of the model. This resulted in 13 infiltration rates being used in the source term model instead of one (see Figure 5-2). The effect of this improvement was tested in a sensitivity analysis.

5.2.3.4 Additions to Lithologic Database and Spatial Variability Assessment. Twenty-two wells at 13 locations have been drilled and completed since the IRA model was developed. Most of these wells were drilled in response to the USGS review of the IRA modeling. Lithologic information from these additional wells was used to further interpret local lithology. The IRA model included a spatial variability assessment that was used to krige lithologic contacts and assign material properties in the simulation grid. The spatial variability assessment was upgraded for the current model and the final kriged results were validated in Leecaster (2002).

5.2.3.5 Aquifer Model Calibration. Water levels and flow directions for the aquifer simulations were recalibrated with the additional data collected after the development of the IRA model. Complete details of aquifer model development and calibration are contained in Whitmire (2001).

Recalibration of the aquifer model was necessary to take advantage of seven additional water-level data from aquifer monitoring wells that were not present for the calibration of the IRA model. The additional aquifer wells were designated M11S, M12S, M13S, M14S, M15S, M16S, and M17S. Deviation (i.e., corrected water) level data were used from two time periods in calendar year 2000. An optimal set of aquifer permeabilities were selected that minimized differences between measured and simulated water levels. This optimized set of parameters was used in predictive modeling for the ABRA. As part of this aquifer calibration effort, kriged permeability distributions based on single well pump-test results were tested. However, the short spatial correlation range and limited data points did not result in an accurate prediction of water levels.

The effect of transient influences from the spreading areas also was investigated. Simulation results indicated that, when additional water representing recharge from the spreading areas was input into the aquifer, the magnitude of southeasterly groundwater-flow velocities beneath the eastern portion of the SDA increased; however, the directions changed only slightly.

The flatness of the water table coupled with an apparent low-permeability region to the south-southwest of the SDA precludes accurate determination of groundwater-flow directions. The IRA hypothesis that the flow velocities immediately under the SDA are slow is consistent with new evidence. The ongoing tracer test in Well M17S immediately beneath the SDA has been showing a very slow dilution of tracers introduced directly into the well, which is indicative of slow movement.

This hypothesis also is consistent with the interpretation by Roback et al. (2001) that the RWMC is in a low-permeability region that extends southerly from the Lost River Range onto the INEEL.

Additional water levels collected during the ongoing WAG 7 quarterly monitoring program will be a key part of conclusively determining direction and timing of aquifer flow velocities in the SDA region.

5.2.3.6 Contaminant Data. The IRA model was primarily based on monitoring data collected before April 1995. Additional contaminant monitoring data were available from previously existing wells and new vadose zone and aquifer wells for use in developing the current model. As discussed in Section 4, the data from the monitoring network do not indicate consistent trends in the vadose zone or aquifer. The generally sporadic monitoring results could not be used as a basis for calibrating a numerical simulation.

5.2.3.7 Hydrologic and Transport Data. Interbed core samples from the 22 wells that were drilled in 1999 were collected for analysis of hydrologic and transport properties. These analyses generated an order of magnitude improvement in the size of the data set available for spatial variability analyses, especially for hydrologic properties. Correlation ranges for the data were determined and used to predict spatially variable properties for the B-C and C-D interbeds. Including these spatially variably hydrologic properties was necessary to address the USGS criticism of the IRA that disregarding spatial variability in interbed properties neglected the possibility of fast migration pathways through the interbeds.

Tensiometers were installed at each location where a suction lysimeter was installed in the B-C and C-D interbeds. Matric potential data from the tensiometer network can be used to (a) guide timing of sampling activities, (b) determine the vertical extent of transient infiltration events at the surface, and (c) determine timing and extent of the influence of discharges to spreading areas in the vadose zone beneath the SDA.

Transport property analyses on approximately 60 interbed cores included sorption isotherms for uranium and neptunium; particle size distributions; surface area; exchangeable cations and anions; clay mineralogy; and extractable silica, iron, manganese, and aluminum. Comparison of partition coefficients from the sorption isotherms to the values from Dicke (1997) support the conclusion that the partition coefficients selected for simulating transport of uranium and neptunium are physically plausible and conservative because they are on the extreme lower end of the measured partition coefficient distributions. Sorption isotherms measured from the core samples were decidedly nonlinear. Partition coefficients with linear isotherms were used in the simulations. Comparisons of the linear values to the nonlinear values also demonstrated that linear values were conservative with respect to enhancing transport over the range of simulated concentrations.

5.2.4 Baseline Model Development and Description

Development and parameterization of models used to simulate flow and transport in the subsurface are described in this section, which also includes a complete list of assumptions. The vadose zone model is described first, followed by the aquifer model.

5.2.4.1 Assumptions. This section lists all assumptions that resulted from the conceptual model (discussed above) or were necessary to develop the subsurface model. Assumptions are divided into flow and transport categories. Most of these assumptions were the same as those used in developing the IRA model. *Assumptions that were modified are italicized.* These assumptions were applied only to dissolved-phase subsurface flow and transport modeling. Assumptions relative to source term modeling and VOC modeling are included in Sections 5.1 and 5.4, respectively.

5.2.4.1.1 Flow Modeling Assumptions

- Infiltration was spatially variable inside the SDA and was greater than the infiltration that occurs outside the SDA because of disturbed soil profiles with reduced vegetation.
- The infiltration description of Martian (1995) was adequate for the ABRA model and, beginning in 1952, was implemented as though it was effective across the SDA.
- The background infiltration rate outside the SDA through undisturbed vegetated sediments was 1 cm/year (0.4 in./year).
- Initial conditions obtained from simulating a background infiltration rate of 1 cm/year (0.4 in./year) for 100,000 days (approximately 274 years) were adequate for representing the vadose zone beneath the SDA.
- The amount of water entering the SDA from the three historical floods was adequately estimated by Vigil (1988).
- Duration of infiltration from each of the historical flooding events was 10 days.
- Infiltration patterns at the SDA will remain the same indefinitely into the future.
- The high infiltration rate assigned over parts of the SDA by Martian (1995) was sufficient to account for occasional flooding of the SDA that may occur in the future.
- The surficial sediments and sedimentary interbeds have spatially variable lithologic surfaces and thicknesses that influence water and contaminant movement.
- Interbeds below the C-D interbed are thin and discontinuous and do not significantly affect flow and transport near the SDA.
- Hydrologic properties in the surficial sediments and A-B interbed were homogeneous. *Hydrologic properties in the B-C and C-D interbeds were heterogeneous and varied spatially.*
- Waste had the same hydrologic properties as the surficial sediments.
- Flow in the fractured porous basalts was controlled by the fracture network and could be adequately represented as a high-permeability, low-porosity equivalent-porous continuum using a Darcian description.
- The field-scale hydraulic properties for fractured basalts were adequately described by the inverse modeling performed by Magnuson (1995) for the large-scale infiltration test.
- *A steady-state influence in the vadose zone model occurred because of Big Lost River water discharges to the spreading areas. The ABRA model implements additional water entering the simulation domain just above the C-D interbed and includes enough water to affect the western portion of the C-D interbed beneath the SDA.*
- *Spreading area influence on the vadose zone began in 1965, as that was the year when the first significant flows in the Big Lost River occurred after the diversion dam was constructed in 1958 (Wood 1989).*

- Water movement in the aquifer was steady-state. Possible influences of discharges from the Big Lost River to the spreading areas do not influence flow in the aquifer in the immediate vicinity of the SDA.

- *Water levels corrected for borehole deviations from FY 2001 were adequate for calibrating the SRPA model and are representative of long-term steady-state conditions.*

- A region of low permeability exists in the aquifer southwest of the SDA.

- The effective depth of the SRPA is 76 m (250 ft) (Robertson 1974)

5.2.4.1.2 Transport Modeling Assumptions

- Field-measured concentrations of COPCs are generally representative and valid based on data quality requirements associated with sampling activities. Single isolated detections of contaminants are anomalous and not representative because they are not consistently present.

- Advection, dispersion, diffusion, sorption, and radioactive decay are the only processes that influence dissolved-phase contaminant movement in the subsurface beneath the SDA.

- A linear equilibrium reversible partition coefficient is representative of all geochemical processes that occur between contaminants dissolved in water and sediments.

- Partition coefficients are homogenous in the interbeds.

- *Sorption does not occur in fractured basalt portions of the vadose zone and aquifer.*

- There were no upgradient influences from other INEEL facilities on aquifer contaminant concentrations near the SDA, with the exception of nitrate, which had an estimated local background concentration of 0.7 mg/L.

5.2.4.2 Simulation Code. The TETRAD code (Vinsome and Shook 1993), Version 12.7, was used to simulate flow and transport for the ABRA. The TETRAD code has complete multiphase, multicomponent simulation capabilities and can mimic the behavior of any number of components in aqueous, gaseous, and oleic phases. The ABRA modeling was limited to dissolved phase aqueous transport using the TETRAD block-centered finite-difference approach and local grid refinement. Though modeling was not performed in the ABRA for VOCs, the IRA VOC modeling results were adapted for use in the ABRA as discussed in Section 5.3.

Dual-permeability simulation capabilities used to simulate transport in both aqueous and gaseous phases in the IRA model were not applied in this modeling exercise. Instead, as discussed in Section 5.3, the results of the vapor phase modeling for the IRA were linearly scaled.

A limitation of using TETRAD is that it treats dissolved-phase contaminants as a separate water component and tracks their movement as if the contaminants were a portion of the total water mass. When contaminants are added into a model representation, they can potentially increase total water in the system. For cases in which contaminant concentration is very low, such as for dissolved radionuclides, the contaminant mass must be scaled upwards from one to 10 orders of magnitude to result in a mole fraction large enough to provide satisfactory mass balance tracking while still maintaining a small enough mole fraction as to not affect the water pressure field. This method effectively limits the valid range of a transport solution to a region around the center of mass of a propagating contaminant front and a limited

portion of the leading and trailing tails of the distribution that are above the specified convergence criterion. Additional complications are introduced when a contaminant sorbs because removal of its related water mass can affect the simulated pressure field. When a decay chain is simulated, all the members of the decay chain must be equivalently scaled.

5.2.4.3 Vadose Zone Flow Model

5.2.4.3.1 Horizontal Domain Extent and Discretization—Two domains were considered for simulating vadose zone flow and transport (see Figure 5-3). An initial attempt was made to use a vadose zone domain that included the spreading areas, which would have allowed spreading area fluxes to be input at their actual locations at the surface. This initial attempt was unsuccessful because the number of grid blocks became too great and increased the computational burden to the point where the simulation was not feasible.

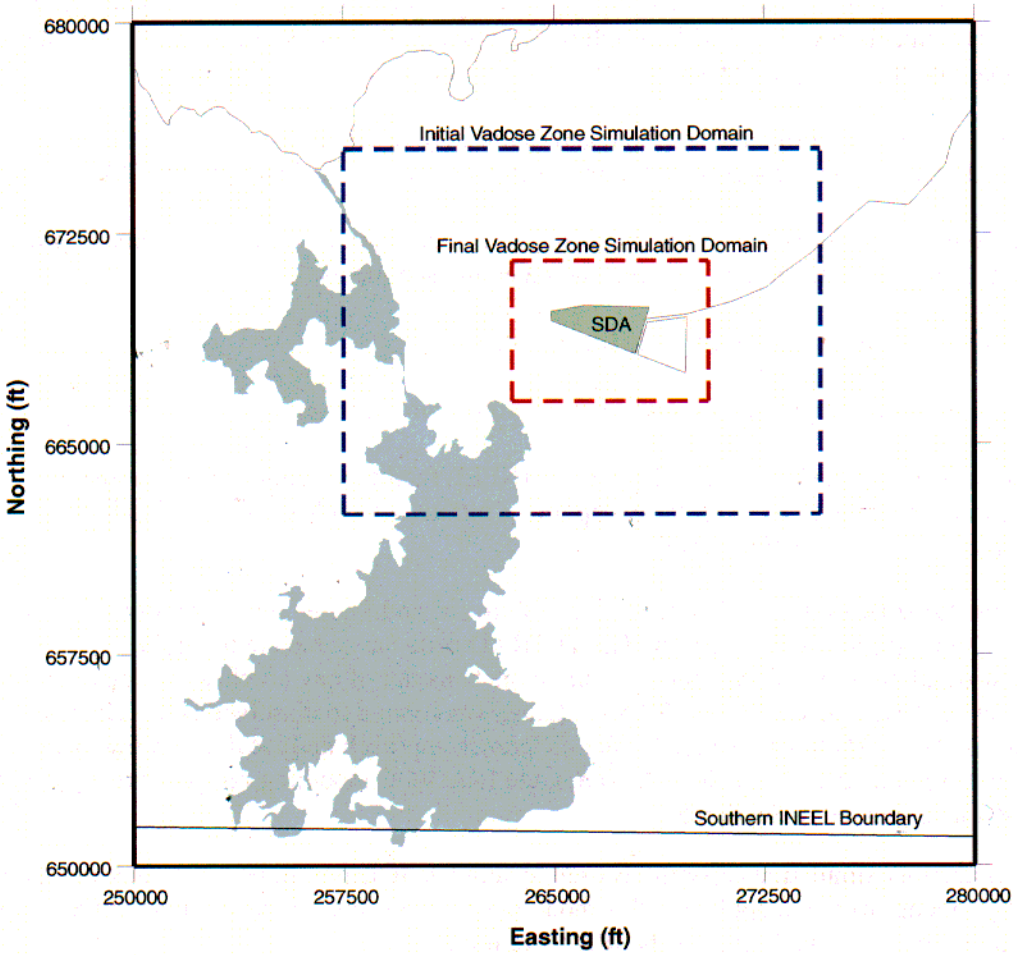

Figure 5-3. Horizontal domains considered for simulation of vadose zone flow and transport.

Horizontal gridding for the final vadose zone domain is shown in Figure 5-4. The upper part of the figure shows just the domain. Two concentric levels of refinement are used to obtain adequate grid resolution in the SDA. The largest horizontal grids are 152.4 m (500 ft) on a side and the smallest grid blocks are 38.1 m (125 ft) on a side. The lower part of the figure shows the same domain with well locations superimposed on the grid. Selection of the grid domain required a balance between the objectives of maximizing the extent of the domain so that outlying wells such as Wells M7S, M15S, and M16S could be included while still obtaining sufficient resolution in the SDA. As shown in Figure 5-4,

some outlying wells were not encompassed in the vadose zone simulation domain. The final domain extent was adequate to simulate transport without undue influence from the horizontal no-flux boundaries, causing elevated simulated concentrations at the boundaries.

5.2.4.3.2 Lithologic Assignment—With the addition of the 22 wells drilled in 1999, 118 wells currently exist in the SDA region from which lithologic information could be used for interpreting lithology. These wells are shown in Table 5-9. The table shows the upper surface and thickness for the surficial sediments and the A-B, B-C, and C-D interbeds. Interbeds deeper than the C-D interbed were not simulated. The lithologic data were derived from the USGS database developed by Anderson et al. (1996) with additions for wells drilled in 1999. An entry of a "-" symbol in Table 5-9 indicates that either the interbed was absent or lithologic information could not be extracted from the data. The latter is the case, for example, in Well I-1D where no attempt was made to obtain the depth of the A-B and B-C interbeds because the well was drilled to obtain lithologic information for the C-D interbed. An entry with a ">" symbol following it indicates partial penetration of an interbed. Three wells (i.e., Wells 6E, 7E, and DE1) were drilled but did not have information available for the lithologic spatial analysis and are not included in the table.

An extensive spatial variability assessment was performed on this data set (Leecaster 2002) using Splus Version 1.5 (MathSoft 2000). The first stage of this stepwise analysis consisted of calculations and modeling to determine the best empirical variograms for raw data and residuals followed by directional variogram analysis to investigate statistical anisotropy, variogram clouds, and models of resulting isotropic data. The next stage was to predict the upper elevations and thicknesses of the surficial sediments, and the A-B, B-C, and C-D interbeds for each of the base and refined grids in the model domain. The three spatial models used to predict values for the base and refined grids were inverse distance weighting, simple kriging, and universal kriging. Cross validation was performed to assess the fit of the models for the variogram modeling and the kriging predictions. Results were selected based on the model that was most accurate and plausible. The statistical testing performed in this analysis included testing different methods for handling cases of partial penetration and gaps.

Table 5-10 gives the final fitted variograms and interpolation method used for each of the lithologic variables. The final fitted variograms for all the lithologic variables used a spherical form. These fitted variograms were used to krige the upper surfaces and thicknesses for the surficial sediments and the A-B, B-C, and C-D interbeds onto the base grid and each of the refined grids.

Figures 5-5, 5-6, 5-7, and 5-8 show examples of kriged surfaces for lithologic contacts and thicknesses. The well locations and lithologic elevation or thickness also are shown. The kriged surfaces were used in developing the vertical conformable grids discussed in the next subsection. One advantage of kriging is the ability to estimate uncertainty in the results. The uncertainty in the elevation of the surficial sediments is included in Figure 5-5. A complete set of kriging standard error plots are included in Leecaster (2002), and generally shows greater uncertainty at distance from the measurement locations. Estimates were kriged for grid block centroids, which means that for a grid block containing a well showing an interbed gap, the kriged result may not show that same gap. Where gaps were statistically significant, they persisted through the kriging as evidenced in the thickness of the A-B interbed (see Figure 5-6). Where gaps were less consistent, such as in the B-C interbed thickness plot, the gaps influenced the kriged surfaces but no gaps persisted into the kriged results (see Figure 5-7).

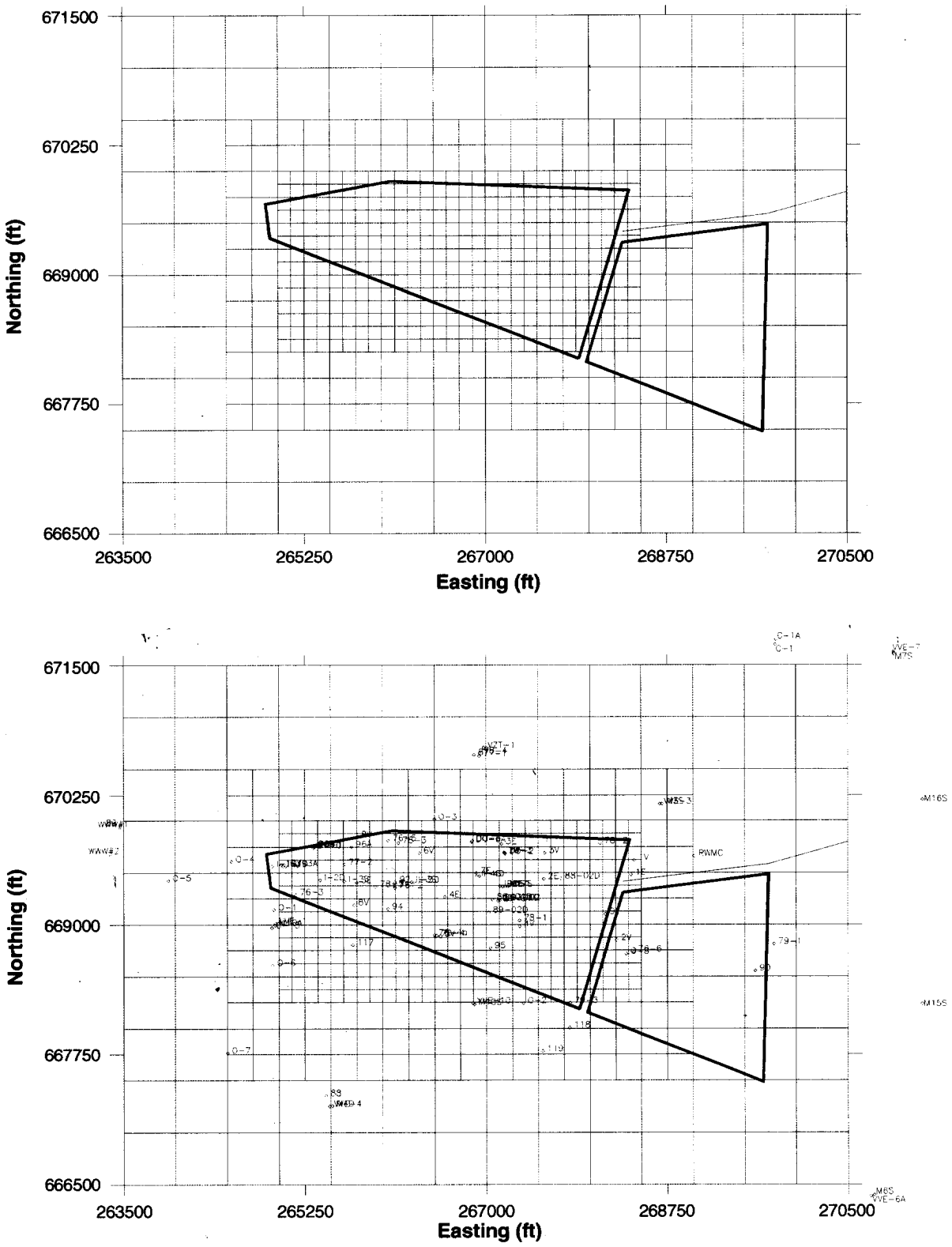

Figure 5-4. Horizontal discretization for the vadose zone model domain.

Table 5-9. Lithologic data used for FY 2001 vadose zone model for the Subsurface Disposal Area baseline risk assessment.

Common Well Name	Northing (ft)	Easting (ft)	Surface Elevation (ft amsl)	Thickness (ft)	A-B Interbed Elevation (ft amsl)	Thickness (ft)	B-C Interbed Elevation (ft amsl)	Thickness (ft)	C-D Interbed Elevation (ft amsl)	Thickness (ft)
76-1	669749	265343	5,009	7	4,983	9	4,921	0	4,790	9>
76-2	669352	266118	5,010	12	4,989	4	4,924	0	4,789	32>
76-3	669286	265161	5,010	18	4,988	3	4,917	26	4,790	20>
76-4	668889	266520	5,011	7	4,995	7	4,915	4	—	—
76-4a	668896	266495	5,011	2	4,995	8	4,915	3	4,790	33>
76-5	669808	266055	5,011	11	5,000	0	4,918	17	4,791	20
76-6	668734	268426	5,011	4	5,007	0	4,913	4	4,783	6
77-1	670623	266933	5,017	4	4,977	8	4,919	6	4,789	22
77-2	669579	265633	5,014	18	4,986	3	—	—	—	—
78-1	669037	267319	5,010	15	4,995	0	—	—	—	—
78-2	669782	268099	5,007	2	4,989	5	4,914	7	4,784	30>
78-3	669788	266151	5,011	4	4,999	0	4,919	0	4,786	23>
78-4	670650	266935	5,018	2	4,976	5	4,920	7	4,790	20
78-5	669365	265931	5,010	12	4,998	0	4,915	28	4,790	30>
79-1	668807	269783	5,010	5	5,005	0	4,897	28	4,785	5
79-2	669692	267171	5,011	13	4,987	3	4,913	4	—	—
79-3	668243	267807	5,008	13	4,995	0	4,909	4	4,780	29
88-02D	669441	267717	5,006	6	4,981	3	4,912	8	—	—
88-01D	669240	267059	5,008	18	4,990	0	4,907	4	4,781	5>
89-01D	669233	267132	5,009	22	4,987	0	4,908	7	4,781	14>
89-02D	669114	267021	5,011	16	4,995	0	4,910	9	4,780	7

Table 5-9. (continued).

Common Well Name	Northing (ft)	Easting (ft)	Surface Elevation (ft amsl)	Thickness (ft)	A-B Interbed Elevation (ft amsl)	Thickness (ft)	B-C Interbed Elevation (ft amsl)	Thickness (ft)	C-D Interbed Elevation (ft amsl)	Thickness (ft)
93-01	669228	267112	5,009	20	4,989	0	4,903	4	4,781	10>
93-02	669234	267197	5,009	29	4,980	0	4,902	6	4,779	8>
USGS-9	654492	258101	5,032	9	5,000	0	4,878	38	—	0
USGS-86	667053	243371	5,081	14	—	0	—	0	—	0
USGS-87	670635	266881	5,016	3	4,975	5	4,920	0	4,787	15
USGS-88	667356	265453	5,020	5	5,015	0	4,917	11	4,789	33
USGS-89	669957	263286	5,029	10	4,985	0	4,932	14	4,798	14
USGS-90	668552	269602	5,010	5	5,005	0	4,906	22	4,763	5
USGS-91	669100	268150	5,006	9	4,997	0	4,910	15	4,777	19
USGS-92	669408	266121	5,008	19	4,989	0	4,922	5	4,790	28
USGS-93	669566	265067	5,010	13	4,997	0	4,914	12	4,792	11
USGS-93A	669566	265179	5,010	11	4,999	0	4,916	13	4,793	9
USGS-94	669150	266050	5,008	12	4,996	0	4,915	18	4,788	26
USGS-95	668770	267038	5,008	23	4,985	0	4,912	16	4,786	12
USGS-96	669750	265700	5,009	13	4,978	4	4,912	27	4,790	10
USGS-96B	669754	265337	5,009	14	4,977	5	4,911	28	4,791	11>
USGS-105	651355	277395	5,090	15	5,075	0	—	0	—	0
USGS-106	669059	280994	5,017	3	5,014	0	4,886	22	—	0
USGS-108	650807	285611	5,033	7	5,026	0	4,844	82	4,715	0
USGS-109	651255	265736	5,045	1	5,044	0	4,873	12	—	0
USGS-117	668800	265711	5,012	14	4,998	0	4,915	5	4,789	28

Table 5-9. (continued).

Common Well Name	Northing (ft)	Easting (ft)	Surface Elevation (ft amsl)	Thickness (ft)	A-B Interbed Elevation (ft amsl)	Thickness (ft)	B-C Interbed Elevation (ft amsl)	Thickness (ft)	C-D Interbed Elevation (ft amsl)	Thickness (ft)
USGS-118	668007	267802	5,013	14	4,999	0	4,910	11	4,791	28
USGS-119	667780	267541	5,031	3	5,028	0	4,919	5	4,783	19
USGS-120	665237	264542	5,042	12	5,030	0	4,911	40	4,790	14
DO-2	669683	267180	5,012	15	4,984	3	4,914	5	4,789	12>
DO-6	669806	266863	5,012	3	4,973	9	4,925	0	—	—
DO-6A	669796	266860	5,012	2	4,971	9>	—	—	—	—
D-10	669739	265331	5,009	9	4,981	9	4,916	2	4,791	11
D-15	668966	264930	5,011	2	4,980	4	4,917	18	4,793	20
RWMC	669659	269011	5,005	7	4,998	0	4,909	6	4,786	17
TW-1	669689	267177	5,010	14	4,977	0	4,913	5	4,789	17>
Test Well	665238	264743	5,042	3	5,039	0	4,912	10	4,788	20
WWW#1	669941	263210	5,036	5	4,992	11	4,931	16	4,805	21
WWW#2	669689	263116	5,036	3	5,001	10	4,933	18>	—	—
VZT-1	670702	266975	5,018	4	4,975	7	4,918	18	—	—
C-1	671675	269780	5,029	2	4,993	2	4,909	5	4,799	10
C-1A	671707	269792	5,029	4	4,993	0	4,911	4	4,799	12
Rif-Ran	685752	282883	4,967	9	4,958	20	4,849	0	4,821	0
HWY-3	687065	277159	4,981	21	4,960	14	4,835	0	4,816	0
EBR-I	674268	276993	5,024	11	5,013	0	4,900	24	4,788	5
A11A31	662517	268728	5,065	3	5,062	0	4,892	66	4,782	35
OW-1	665336	264794	5,042	5	5,037	0	4,915	30	4,787	14

Table 5-9. (continued).

Common Well Name	Northing (ft)	Easting (ft)	Surface Elevation (ft amsl)	Thickness (ft)	A-B Interbed Elevation (ft amsl)	Thickness (ft)	B-C Interbed Elevation (ft amsl)	Thickness (ft)	C-D Interbed Elevation (ft amsl)	Thickness (ft)
OW-2	664910	264932	5,044	7	5,037	0	4,910	42	4,784	4
NA89-1	669083	259758	5,045	2	4,995	0	4,931	17	4,821	8
NA89-2	675154	257588	5,059	12	5,014	0	4,863	4	—	—
NA89-3	665178	264344	5,038	1	5,037	0	4,909	4,6	—	—
M1SA	668992	264962	5,011	7	4,980	5	4,917	20	4,790	20
M3S	670165	268700	5,016	5	4,989	3	4,910	15	4,792	3
M4D	667255	265510	5,023	8	5,015	0	4,914	29	4,787	28
M6S	666379	270722	5,066	7	5,059	0	4,900	10	4,74,6	18
M7S	671588	270921	5,005	9	4,996	0	4,908	6	4,782	0
M10S	668227	266882	5,022	6	5,016	0	4,910	24	4,789	27
VVE-1	669009	264964	5,011	8	4,980	6	4,917	22	4,792	23>
VVE-3	670163	268676	5,015	6	4,987	4	4,909	14	4,792	10>
VVE-4	667253	265486	5,022	8	5,000	15	4,916	31	4,787	23>
VVE-6A	666368	270684	5,066	4	5,062	0	4,903	14	—	—
VVE-7	671608	270919	5,004	14	4,990	0	4,887	11	4,784	7>
VVE-10	668241	266869	5,021	6	5,015	0	4,908	24	4,781	18>
1E	669475	268396	5,006	15	4,991	0	4,907	7>	—	—
1V	669619	268429	5,006	9	4,997	0	4,911	7	—	—
2E	669438	267553	5,008	15	4,979	3	4,912	3>	—	—
2V	668845	268259	5,006	7	4,999	0	4,910	9	4,767	3>
3E	669775	267147	5,012	5	5,007	0	4,913	3	—	—

Table 5-9. (continued).

Common Well Name	Northing (ft)	Easting (ft)	Surface Elevation (ft amsl)	Thickness (ft)	A-B Interbed Elevation (ft amsl)	Thickness (ft)	B-C Interbed Elevation (ft amsl)	Thickness (ft)	C-D Interbed Elevation (ft amsl)	Thickness (ft)
3V	669690	267564	5,009	17	4,982	4	4,910	4	4,787	2>
4E	669265	266600	5,014	23	4,991	0	4,913	4>	—	—
4V	668980	267320	5,012	10	5,002	0	4,908	13	4,781	4>
5E	669403	265750	5,013	21	4,992	0	4,916	4>	—	—
5V	668885	266555	5,011	9	4,992	7	4,913	3	—	—
6V	669688	266352	5,017	10	4,986	7	4,926	4	4,793	2>
7V	669370	266113	5,009	15	4,987	7	4,925	10	4,786	5>
8V	669190	265723	5,012	21	4,991	0	4,914	37	4,786	1>
9V	669845	265754	5,014	20	4,994	0	4,913	20	4,786	1>
10V	669572	265022	5,013	10	4,993	9	4,916	14	4,789	5>
M11S	675132	274247	4,994	10	4,984	0	4,903	5	4,787	23
M12S	677145	280877	4,975	8	4,967	0	4,911	2	4,783	12
M13S	672953	276945	5,027	16	5,011	0	4,894	12	4,781	0
M14S	674610	266413	5,032	7	5,025	0	4,904	0	4,824	0
M15S	668207	271193	5,019	18	5,001	0	4,889	27	4,789	15
M16S	670185	271201	5,004	18	4,986	0	4,886	10	4,807	12
M17S	669364	267183	5,012	23	4,989	0	4,911	10	4,784	22
I-1S	669563	264936	5,013	8	5,005	0	4,913	11	—	—
I-1D	669563	265041	—	—	—	—	—	—	4,790	20
I-2S	669413	265632	5,014	18	4,996	0	4,911	11	—	—
I-2D	669427	265396	—	—	—	—	—	—	4,791	1

Table 5-9. (continued).

Common Well Name	Northing (ft)	Easting (ft)	Surface Elevation (ft amsl)	Thickness (ft)	A-B Interbed Elevation (ft amsl)	Thickness (ft)	B-C Interbed Elevation (ft amsl)	Thickness (ft)	C-D Interbed Elevation (ft amsl)	Thickness (ft)
I-3S	669406	266280	5,012	16	4,985	2	4,914	4	—	—
I-3D	669405	266304	—	—	—	—	—	—	4,787	11>
I-4S	669462	266907	5,009	15	4,994	0	4,912	2	—	—
I-4D	669462	266932	—	—	—	—	—	—	4,787	16>
I-5S	669366	267132	5,012	32	4,980	0	4,913	6>	—	—
O-1	669140	264952	5,011	8	4,979	1	4,917	18	4,790	15>
O-2	668242	267356	5,014	5	5,009	0	4,907	18	4,771	7
O-3	670011	266496	5,010	8	4,975	9	4,919	12	4,789	15>
O-4	669607	264543	5,014	11	4,970	7	4,909	18	4,789	19>
O-5	669423	263931	5,021	2	4,976	6	4,916	23	4,789	26
O-6	668606	264939	5,013	10	4,982	6	4,905	14	4,789	26>
O-7	667762	264503	5,033	4	5,006	6	4,915	34	4,788	4>
O-8	668715	268351	5,010	8	5,002	0	4,910	0	4,777	1>

amsl (above mean sea level)

- indicates that either the interbed was absent or lithologic information could not be extracted from the data.

> indicates partial penetration of an interbed.

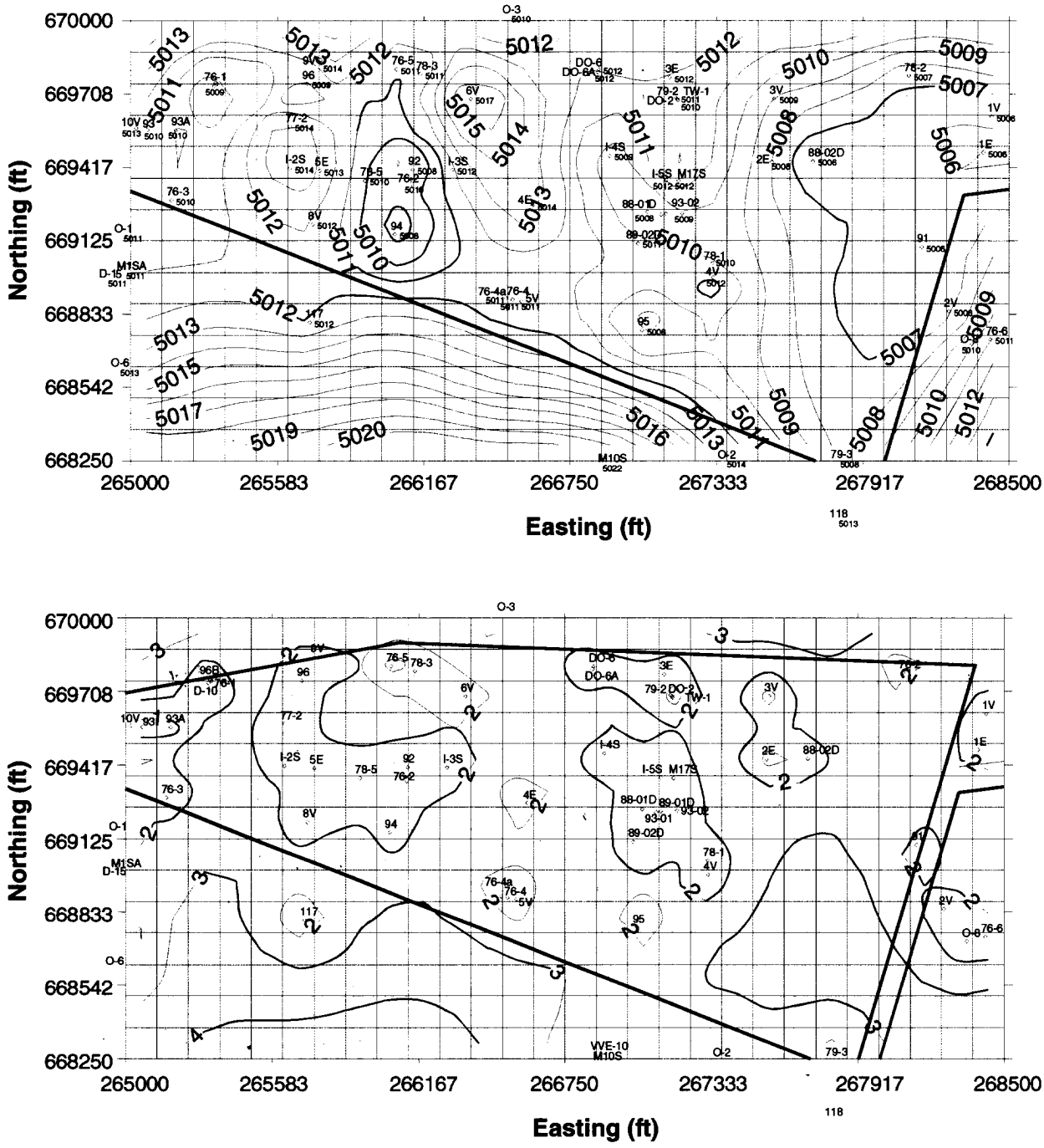

Figure 5-5. The top plot shows the final kriged results for elevations (ft amsl) of surficial sediments for the second level of grid refinement. The bottom plot shows uncertainty (standard error) in the elevations of surficial sediments for the same grid.

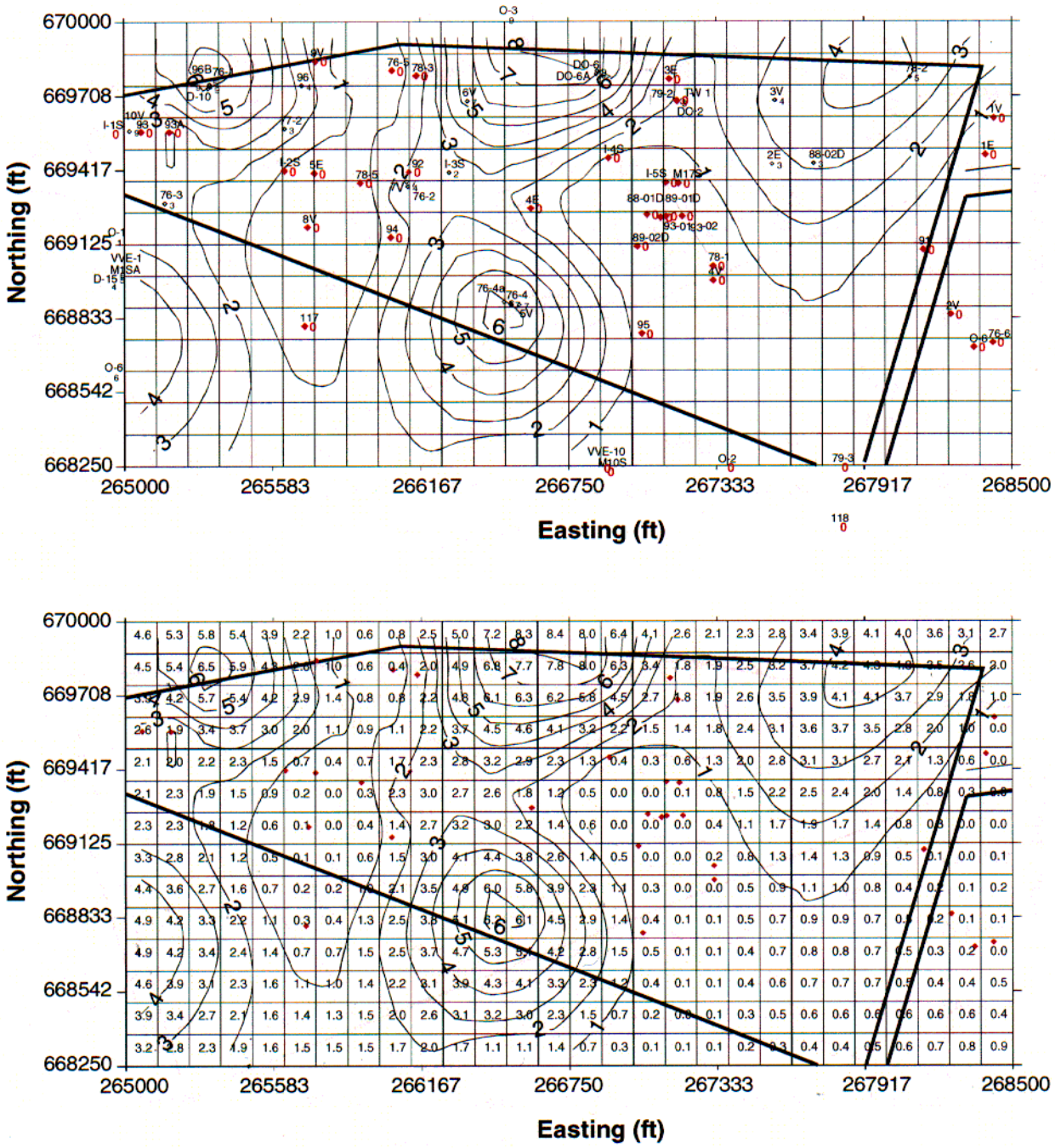

Figure 5-6. Kriged results for the A-B interbed thickness (ft) on the second level of grid refinement. Colored markers indicate locations of zero thickness. The lower plot has only colored markers for zero thickness locations and the matrix of kriging results are superimposed. Note the persistence of locations with zero thickness into the kriging results.

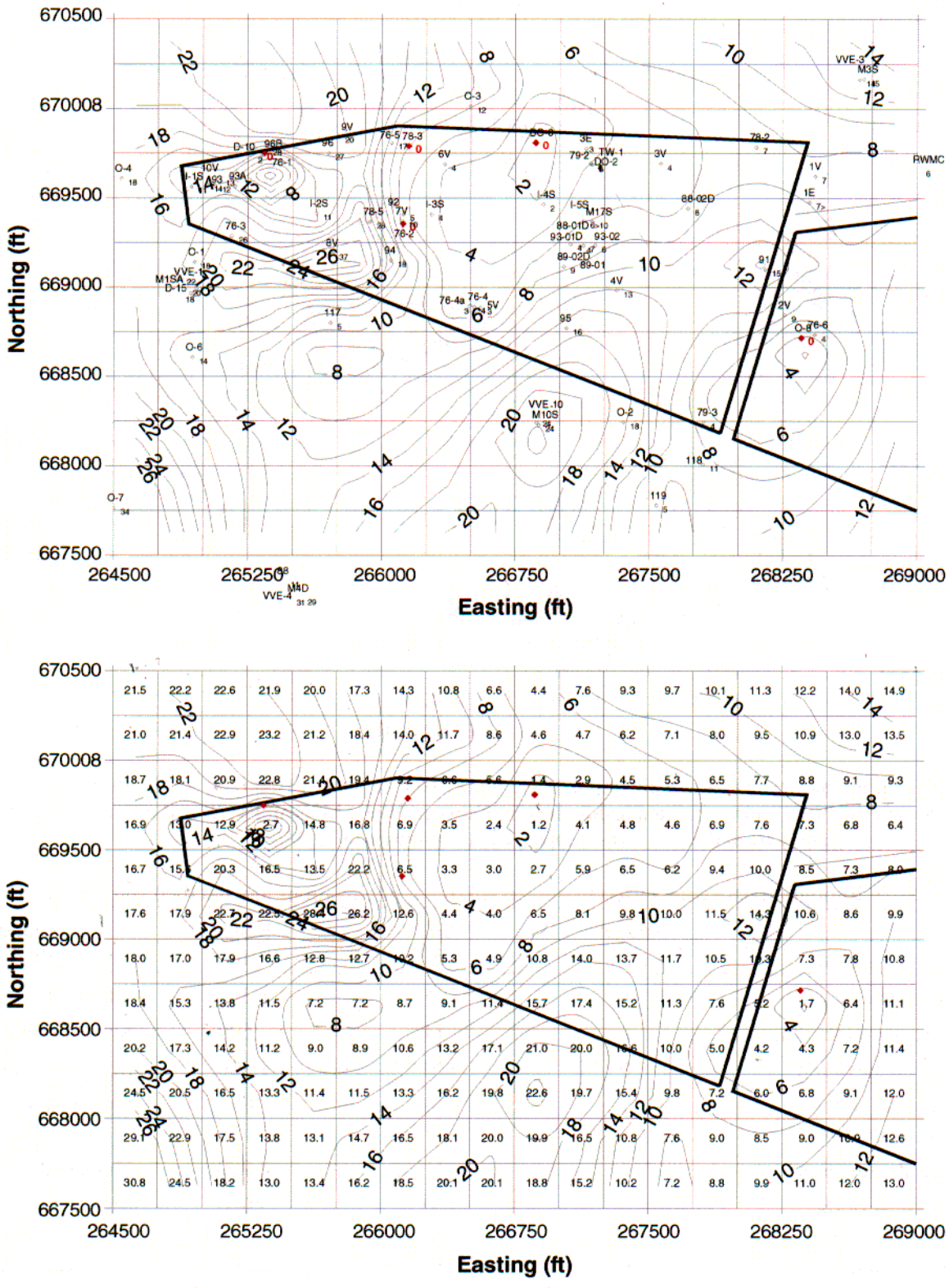

Figure 5-7. Kriged results for the B-C interbed thickness (ft) on the first level of grid refinement. Colored markers indicate locations of zero thickness. The lower plot has only colored markers for zero thickness locations and the matrix of kriging results are superimposed. Note the lack of persistence of locations with zero thickness into kriging results.

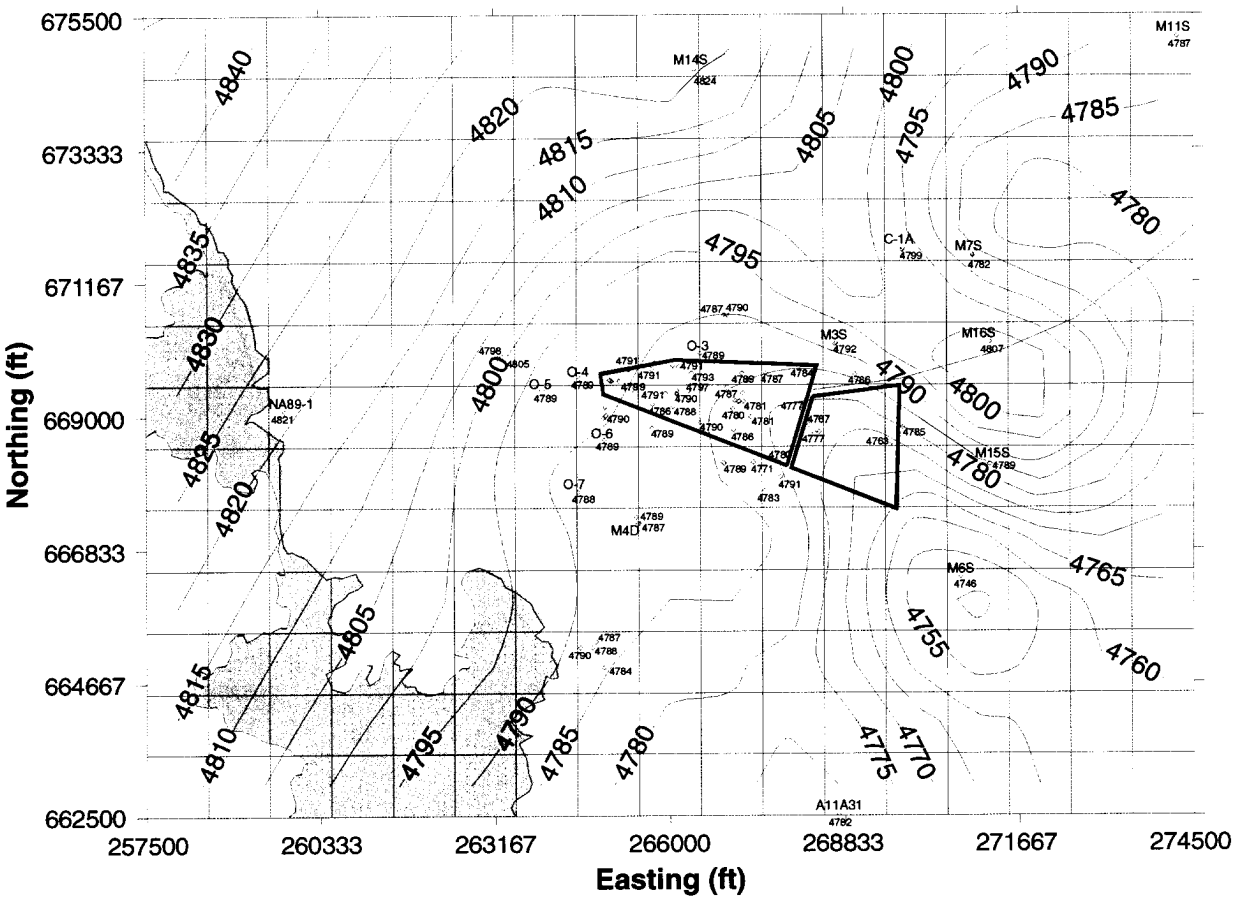

Figure 5-8. Kriged results for the elevation of the top surface of the C-D interbed for the initial vadose zone base grid. Note an interpolated saddle feature between Wells M3S and M7S and a trough feature leading southeasterly from the Subsurface Disposal Area toward Well M6S.

Table 5-10. Variogram parameters used in universal kriging of elevations and interbed soil thickness.

Variable	Nugget[a] (ft^2)	Sill[a] (ft^2)	Range (ft)	Interpolation Method
Surface elevation	0	25	1,300	Universal kriging
Surficial soil thickness	5	44	600	Simple kriging
A basalt elevation	0	170	1,800	Simple kriging
Thickness of the A-B interbed soil	1	4	850	Universal kriging
B basalt elevation	5	31	2,900	Universal kriging
Thickness of the B-C interbed soil	0	120	3,000	Simple kriging
C basalt elevation	0	45	2,200	Universal kriging
Thickness of the C-D interbed soil	40	50	700	Universal kriging

a. Nuggets and sills are fitting parameters that describe irreducible local variance and overall population variance (Leecaster 2002).

The last plot in this sequence (see Figure 5-8) shows kriging results for the elevation of the top of the C-D interbed for the initial vadose zone domain. Though this domain was not used in the simulations contained in this report, the figure is included because of the interesting feature near Well M7S to the northeast of the SDA. A saddle feature in the upper surface of the C-D interbed was interpolated between Wells M7S and M3S. This topologic feature, if it really exists at the SDA, may enhance the movement of contaminants that move in the vapor phase after they are present in sufficient concentrations to begin diffusing or advecting in the gaseous phase over the saddle, thus aiding the movement of such contaminants in a northeasterly direction from the SDA. Also visible in this plot is a trough feature or depression leading southeasterly from the SDA toward Well M6S. Elevated concentrations of chromium and nitrate in Well M6S (discussed in Sections 5.2.4.6) may result from preferential migration aided by the presence of this trough.

5.2.4.3.3 Vertical Conformable Gridding—The next step in development of the ABRA vadose zone model was vertical discretization of the base simulation domain. The kriged lithologic surfaces were used in conjunction with the horizontally discretized domains to create a conformable vertical grid. Minimum vertical grid size, maximum vertical grid size, and a geometric factor for increasing vertically adjacent grid blocks were assigned a priori for each lithologic unit in the base vadose zone domain. Minimum grid size was 0.5 m (1.6 ft) for each of the sediment and basalt units, except for the A-B interbed where a minimum grid size of 0.4 m (1 ft) was assigned. The geometric factor for the ratio between successive vertical grid blocks was a maximum of 1.5, which is a commonly used ratio to ensure numerical accuracy. Maximum vertical grid block size was 3 m (9.8 ft) in the sediment units and 10 m (33 ft) in the basalts. Logic for adjusting vertical grid block sizes was applied vertically at each horizontal grid block location to allow for an optimum match of the grid block interfaces to the kriged surface elevations. By having the same minimum grid block size specified for both sediment features and basalt features, uniformity of grid block sizes was ensured across lithologic interfaces. The total number of vertical grid blocks was determined through this process and resulted in 72 vertical grid blocks at each horizontal location for the base vadose zone simulation domain. The upper surface of the vadose zone simulation domain was variable and was determined from the kriged elevation for the surficial sediments. The lower surface of the vadose zone simulation domain was arbitrarily assigned as a flat plane. The lowest level of the vadose zone simulation domain was inadvertently assigned an elevation that was actually 27.5 m (90 ft) above the aquifer. This truncated vadose zone domain resulted in slightly decreased water and contaminant travel times through the vadose zone domain because water and contaminant movement in the fractured basalt portion were assigned values to make water movement very fast. Also, there was no intention to include interbeds in this lowest 27.5 m (90 ft). Therefore, the truncation of the vadose zone domain and slight decrease in water and contaminant travel times through the vadose zone domain was insignificant.

The logic for vertical grid discretization was different for the refined areas. Vertical discretization for the base domain was not further adjusted based on the kriged elevations in the refined grids. Rather, the kriged elevations for the refined grids were compared to the conformable vertical discretization determined from the base grid and then, as necessary, the material properties assigned in the refined domains were adjusted. This process resulted in smooth-appearing grid interfaces in the base domain and some degree of stair-stepping in the refined grids. This can be seen in Figures 5-9, 5-10, and 5-11, which show three-dimensional views of the resulting grids starting with the base grid and ending with the second-level grid refinement. These three-dimensional views are distorted both horizontally and vertically because the software (Visual Numerics 1996) that produces them projects onto a cube. The outline of the SDA is shown in each case projected just above the cube. The vertical extent shown in each figure is indicated in the captions.

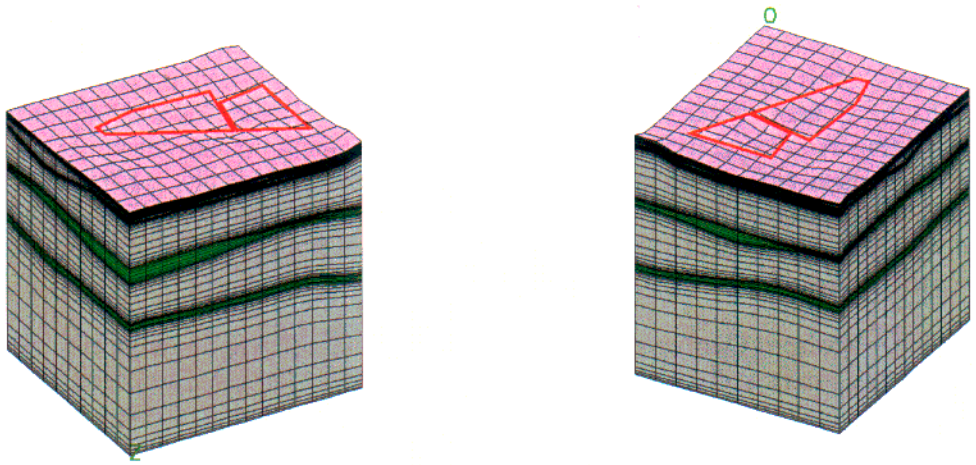

Figure 5-9. Southwest and northeast views of base grid beneath the Subsurface Disposal Area showing vertical conformable gridding. The vertical extent shows the entire vadose zone simulation domain. Interbed grids are shaded green and fractured basalt grids are shaded gray.

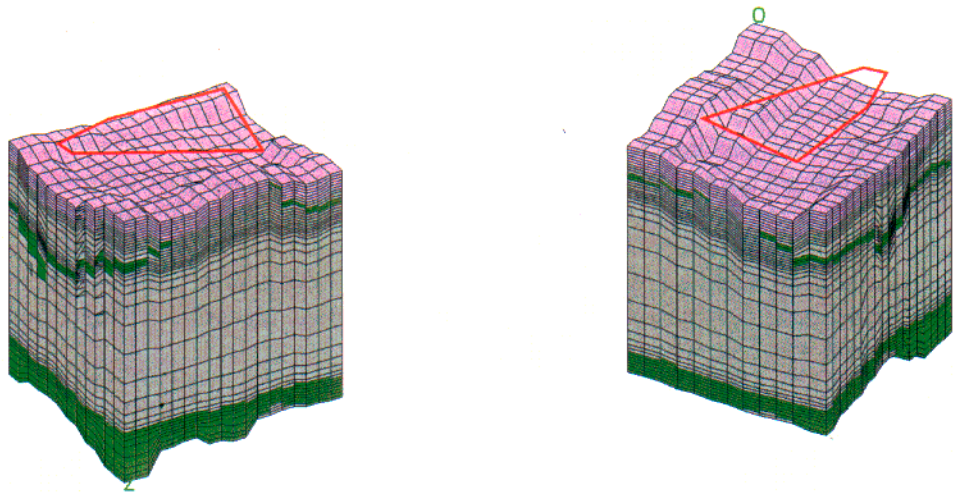

Figure 5-10. Southwest and northeast views of first-level refined grid showing vertical conformable gridding. The first level of grid refinement extended to the base of the B-C interbed beneath the Subsurface Disposal Area.

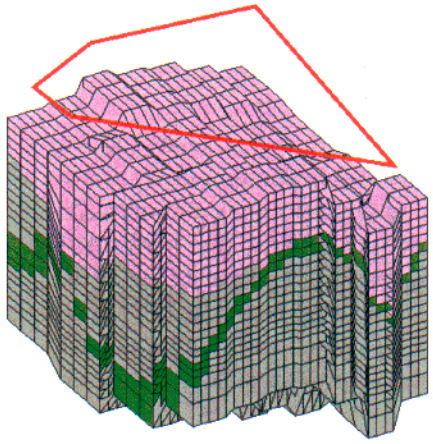

Figure 5-11. Southwest view of the second-level refined grid showing vertical conformable gridding. The second level of grid refinement extended to the base of the A-B interbed beneath the Subsurface Disposal Area. Note the A-B interbed merging with the surficial sediments.

5.2.4.3.4 Hydrologic Property Assignment—Hydrologic properties for porosity and permeability for the surficial sediments, the A-B interbed, and the fractured basalt were assigned the same properties as the IRA model (see Table 5-11) because no new information was available for these units.

Table 5-11. Parameterization of hydrologic properties and source of parameters for surficial sediments, A-B interbed, and fractured basalt.

Parameter	Permeability	Porosity
Surficial sediments	680 milliDarcy (mD), isotropic. Average of calibrated properties in Martian (1995).	0.50 cm^3/cm^3 (Martian 1995)
A-B interbed	4 mD. Waste Area Group 3 modeling in Rodriguez et al. (1997).	0.57 cm^3/cm^3 (Magnuson and McElroy 1993)
Fractured basalt	300 mD vertical and 9,000 mD horizontal in Magnuson (1995).	0.05 cm^3/cm^3 (Magnuson 1995)

The moisture characteristic curve (also known as the water release curve or theta-psi curve) for all of the sediment features was based on the empirical relationship determined by van Genuchten (1980). The parameters assigned for the van Genuchten curve were taken from the GWSCREEN (Rood 1999) default values that were based on the average of four SDA surficial sediment samples that were hydraulically characterized and reported in Baca et al. (1992). The values for residual moisture content, van Genuchten alpha, and van Genuchten N were 0.142 cm^3/cm^3, 1.066 m^{-1}, and 1.523 (dimensionless), respectively. This was a slightly different approach from that used in the IRA model and was used to obtain numerical convergence. The moisture characteristic curves used in the IRA model were tested with the new conformable grid; however, a stable solution could not be obtained.

The moisture characteristic curve used for the fractured basalts was the same as that used for the IRA model. Sensitivity simulations performed to investigate the appropriateness of this moisture characteristic curve are discussed below.

A major difference between the IRA model and the model used to make the simulations presented in this report was the use of spatially variable permeabilities and porosities for the B-C and C-D interbeds. The spatial variability analyses used to krige porosity and permeability onto the simulation grids are contained in Leecaster (2002). A process similar to that performed for the lithology analysis (discussed above) was also performed for the porosity and permeability of the B-C and C-D interbeds. The data set consisted of 112 samples, the majority coming from the 1999 drilling activities. Scale issues associated with using core sample results applied to much larger areas are acknowledged but not addressed in this modeling exercise. These 112 samples represented 32 site locations, 17 in the B-C interbed and 24 in the C-D interbed. Some of the sites were for the same well. The porosity data from multiple depths across an individual interbed were arithmetically averaged. Likewise, the permeability data were combined by harmonic averaging because the primary flow direction was interpreted to be vertical across the layers. Figures 5-12 and 5-13 show the kriged porosity and permeabilities for the B-C and C-D interbeds, respectively. Only the most refined grid for each interbed is shown, which is the base grid for the C-D interbed and the first level of grid refinement for the B-C interbed. Standard errors for the kriging results are presented in Leecaster (2002).

Similar to the IRA model, a low permeability of 1 milliDarcy (mD) and a low porosity of 0.05 were assigned to the top grid block representing both the B-C and C-D interbeds. This was accomplished by identifying the uppermost grid block representing each interbed in the grid with the greatest level of refinement, and then assigning the low porosity and low permeability value to that grid block. This low permeability feature is considered representative of either a low permeability sedimentary feature at the top of the interbeds or a low permeability feature caused by fine sediments infilling fractures in the basalts immediately above the interbed. Inclusion of this low permeability, low porosity feature was necessary to create conditions close to saturation at locations within the interbeds and to facilitate spreading of water from where it was applied at depth above the C-D interbed to include the effect of spreading-area water. The latter topic is discussed below.

5.2.4.3.5 Boundary and Initial Conditions—Boundary conditions for the vadose zone model primarily consist of assigning surface water fluxes. Two types of water fluxes were imposed on the simulation domain representing steady-state conditions and historical flooding conditions. No additional information existed by which to assign background infiltration inside the SDA; therefore, the fluxes were assigned in a manner to mimic the infiltration pattern of the IRA model as close as possible with a constraint to maintain an overall average of 8.5 cm/year (3.3 in./year) inside the SDA (see Figure 5-14). The same low, medium, and high infiltration rates of 0.64 cm/year (0.25 in./year), 3.68 cm/year (1.45 in./year), and 24.1 cm/year (9.48 in./year) from the IRA model were used. The original assignment in the IRA model was based on interpretations of neutron moisture monitoring and surface topography made in Martian (1995). Outside the SDA, surface infiltration was assigned the same rate of 1 cm/year (0.4 in./year) based on Cecil et al (1992).

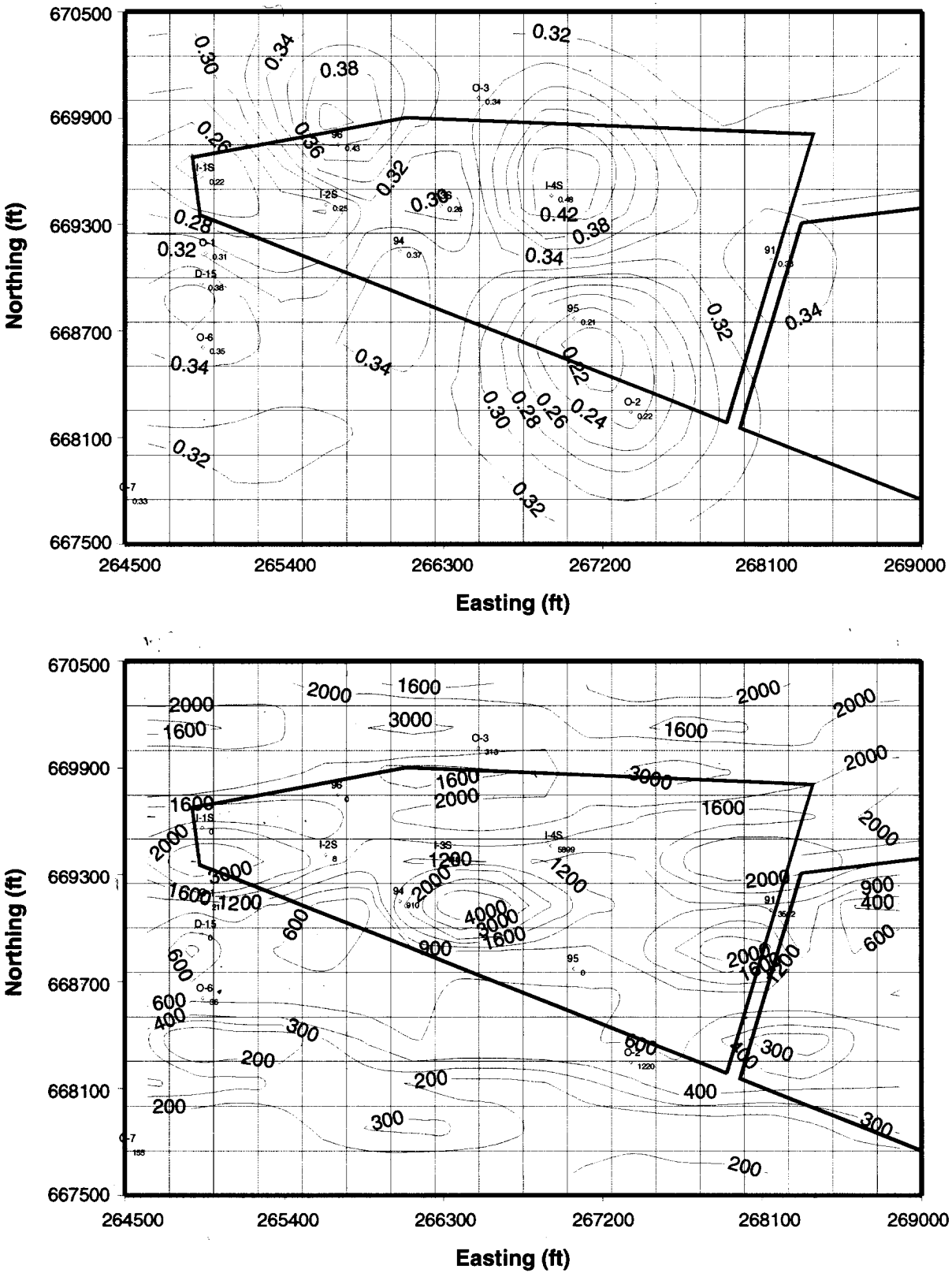

Figure 5-12. Kriged porosity and permeability (mD) for the B-C interbed.

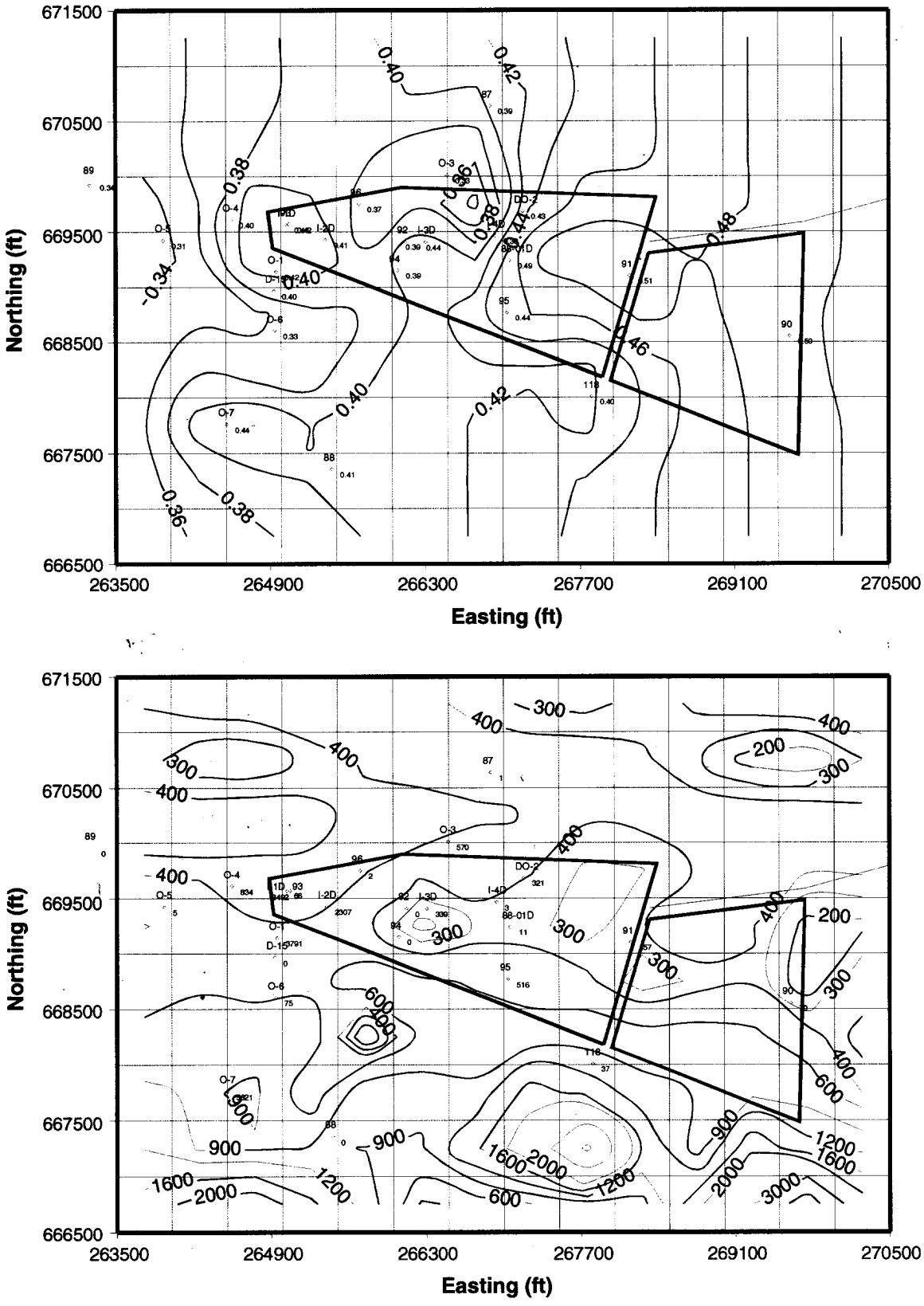

Figure 5-13. Kriged porosity and permeability (mD) for the C-D interbed.

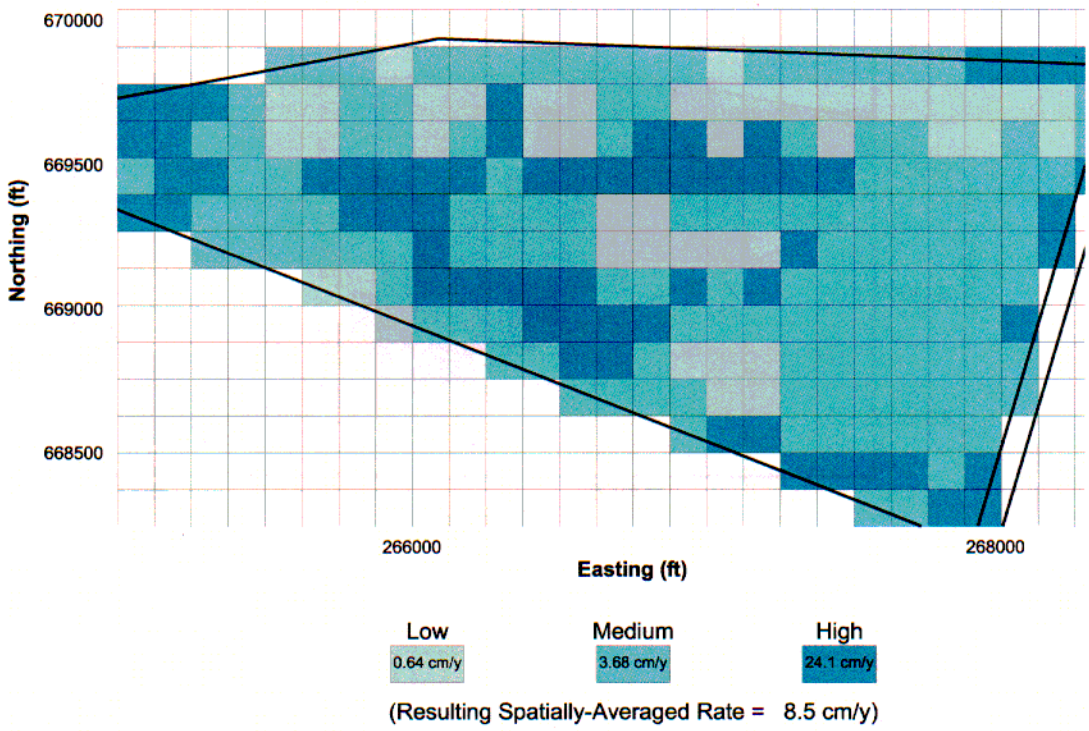

Figure 5-14. Spatially variable infiltration assignment for model domain inside the Subsurface Disposal Area.

Three historical flooding events have occurred at the SDA and also were included in the ABRA model, essentially using the same method as the IRA model but with slight differences caused by gridding. Figure 5-15 shows the locations where additional water was imposed at the surface for the 1962, 1969, and 1982 floods, respectively. Estimates of the amount of water that entered the SDA for each of the floods were taken from Vigil (1988) and are shown in Table 5-12. Each flood was assumed to last for 10 days.

Table 5-12. Historical flooding volumes and application rates at the Subsurface Disposal Area.

Year	Estimated Volume (acre-ft)	Infiltration Rate (m/day)
1962	30	2.26×10^{-2}
1969	20	1.68×10^{-2}
1982	8.3	1.24×10^{-2}

The lower boundary of the model domain was assigned a water table condition. Lateral boundaries were all assigned as no-flow boundaries. The addition of an assumed water source from the spreading areas is discussed below.

Initial conditions for all simulations were obtained by assigning an initial water saturation of 50% to the entire simulation domain. Then the simulation was run for 100,000 days (approximately 270 years) to let the system come into equilibrium. Water saturation in the C-D interbed was monitored to determine whether equilibrium had been obtained. After the first 20,000 days (approximately 55 years), the change in the saturation was negligible.

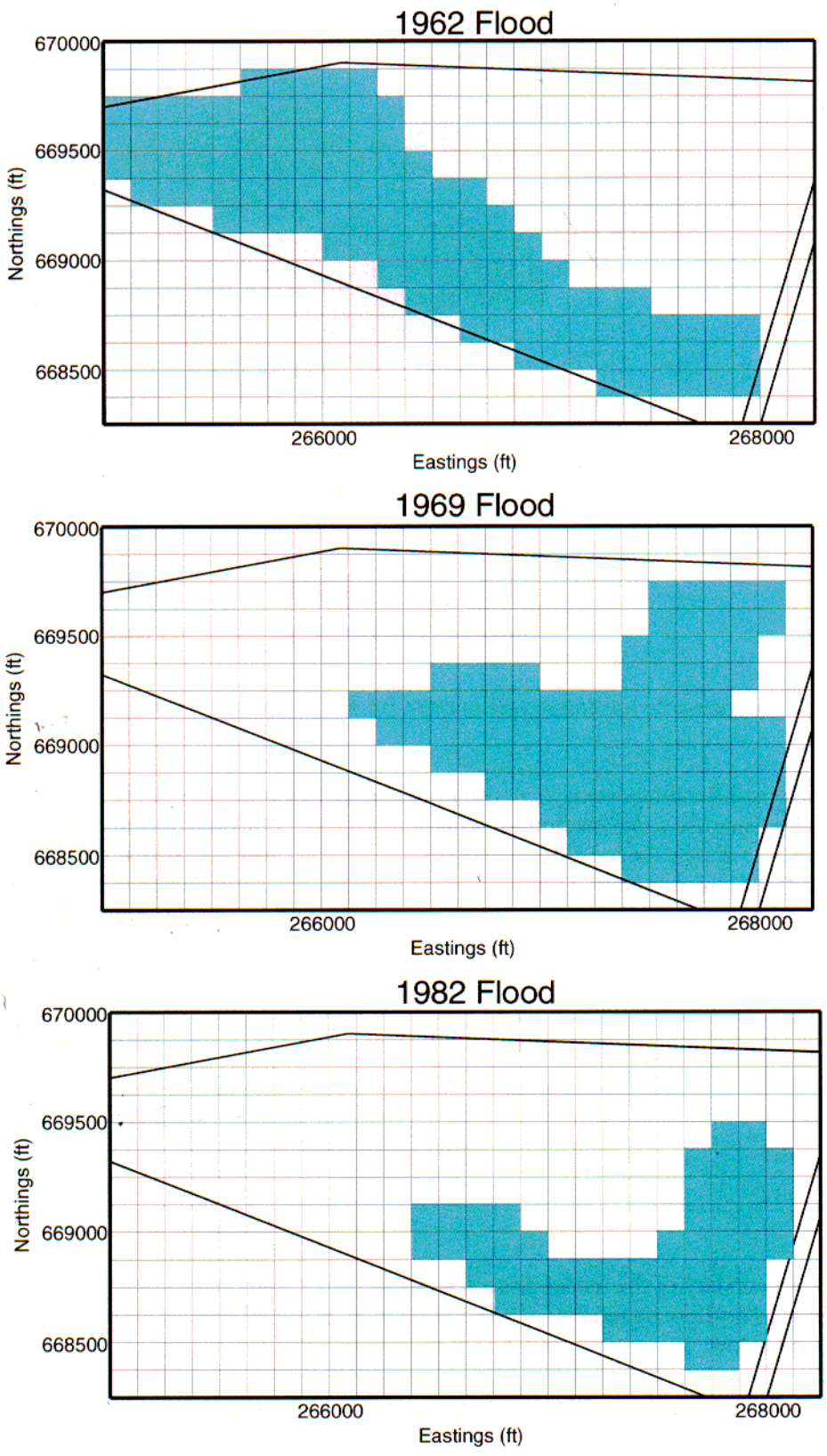

Figure 5-15. Locations of additional water supplied by the 1962, 1969, and 1982 flooding events at the Subsurface Disposal Area.

5.2.4.3.6 Development Simulations—Simulations performed as part of the development of the ABRA model are discussed in this section.

5.2.4.3.7 Wetting Front Advancement at Well 76-5—The simulations presented in this section tested the appropriateness of the moisture characteristic curve used to represent the fractured basalt in the ABRA model. This same curve was used in the IRA model and in other modeling studies at the INEEL (Rodriguez et al. 1997). The use of this moisture characteristic curve has not been further investigated since it was introduced in Magnuson (1995). The testing summarized in this section provided evidence of the conservatism in the ABRA model caused by the moisture characteristic curve assigned for the fractured basalts.

A set of nested advanced tensiometers installed in Well 76-5 inside the SDA at depths of 6.7, 9.4, and 11.6 m (22, 31, and 38 ft) show changes in measured tension at each depth as a series of wetting fronts migrated downward during the period from February to April of 1999 (see Figure 5-16). The shallowest tensiometer is emplaced within fractured basalt (see Figure 5-17) and shows the influence of infiltrating water that appears to be three separate infiltration events, likely caused by snow melting at land surface. The middle tensiometer, at a depth of 9.4 m (31 ft), was emplaced within a thin interbed of approximately 15 cm (0.5 ft) thickness. The deeper tensiometer is located in fractured basalt beneath the thin interbed and shows some degree of damping of the infiltration fronts.

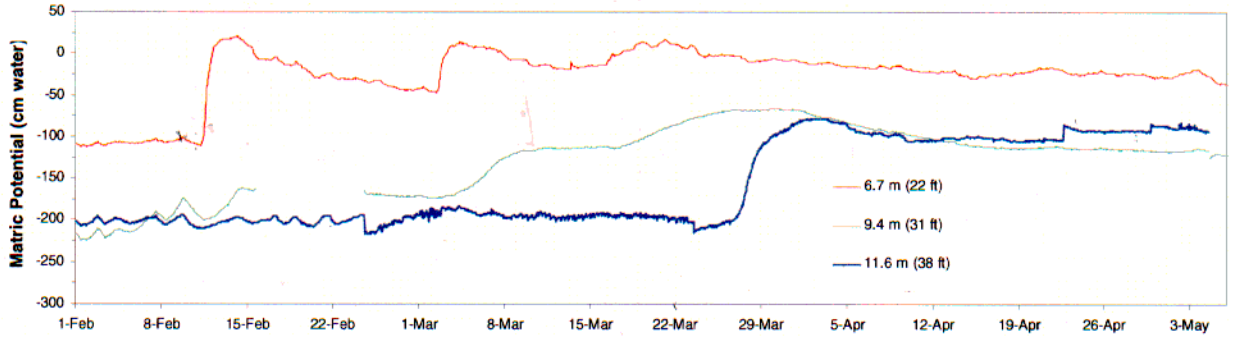

Figure 5-16. Tensiometric monitoring results in Well 76-5 during the winter and spring of 1999.

Three one-dimensional TETRAD simulations were implemented to compare simulated matric potentials to tensiometric monitoring data from Well 76-5. Figure 5-17 shows the one-dimensional simulation grid juxtaposed with a well construction and instrumentation diagram for Well 76-5. The sediment moisture characteristic curve in each run was parameterized the same as that used for the ABRA model described above in Section 5.2.4.3.4. The first run applied the Corey-type fractured-basalt moisture characteristic curve implemented for the ABRA modeling. The second run applied a Corey-type moisture characteristic curve for the fractured basalt with lower capillary pressures. The third run simulated a fractured basalt van Genuchten moisture characteristic curve that partially mimics the ABRA Corey-type curve. The parameter values for the fractured basalt residual moisture content, van Genuchten alpha, and van Genuchten N were 0.001, 1.066 m^{-1}, and 1.523, respectively. The three moisture characteristic curves are shown in Figure 5-18. Initial conditions were obtained by imposing a background flux of 1 cm/year (0.4 in./year) of water for 100,000 days. Three pulses of water (related to melting events at the surface) were imposed at the top boundary by prescribing a first-type boundary condition consisting of saturated conditions for one day per melting event.

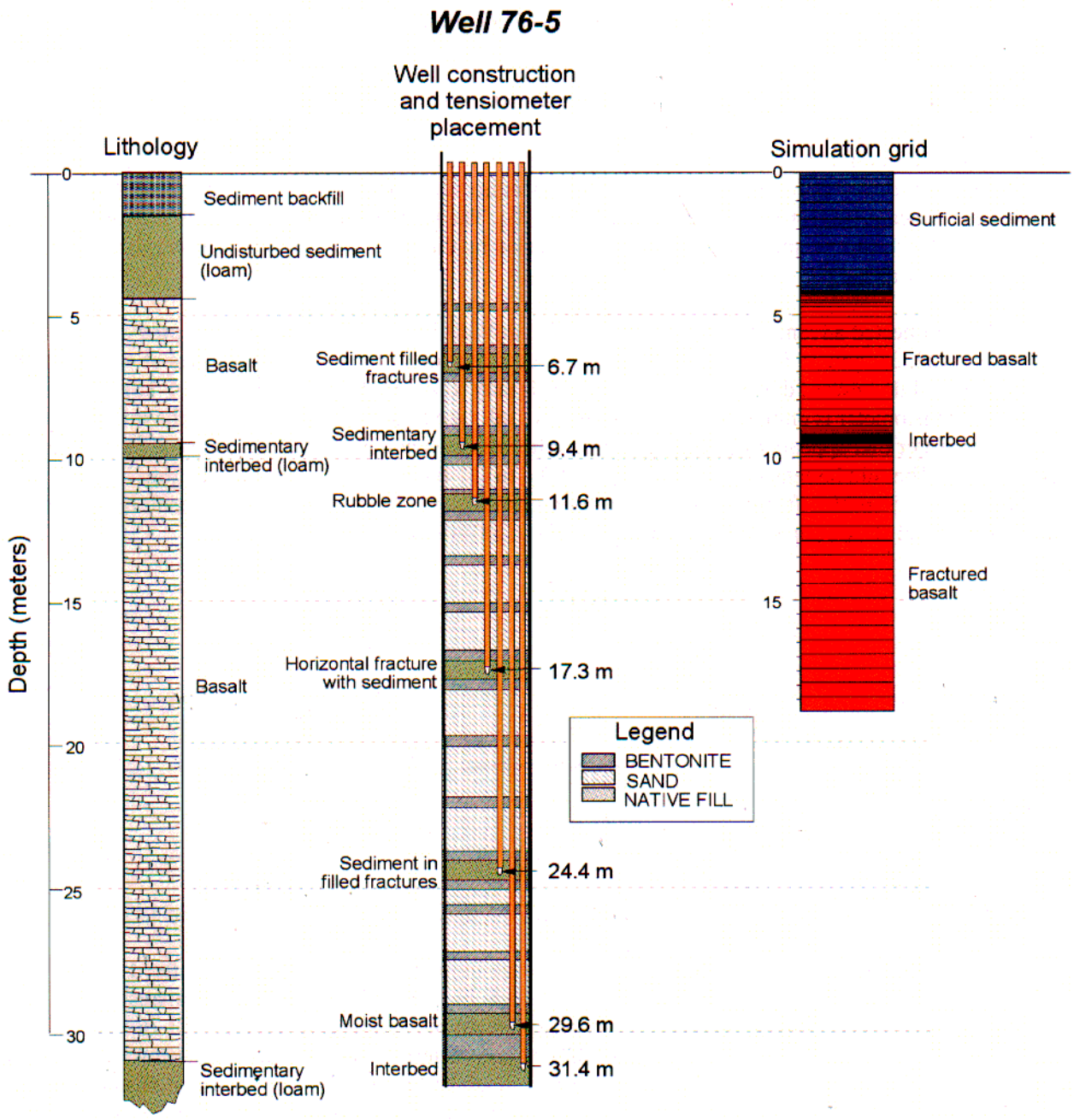

Figure 5-17. Simulation grid for Well 76-1 with lithology and tensiometer monitoring locations.

The simulated matric potentials at equivalent depths for each of the three moisture characteristic curves are shown in Figure 5-19. Although there was considerable difference between the results, each simulation successfully mimicked some of the observed matric potential behavior. The results with the van Genuchten curve showed the lowest tensions (capillary pressures), which are more feasible in fractures than tensions indicated by either of the results from the Corey-type curves. The alternate Corey-type curve resulted from a desire to run the ABRA simulations without the resulting extremely high capillary pressures. However, numerical convergence could not be obtained when the alternate Corey-type curve was implemented in the full three-dimensional ABRA simulation.

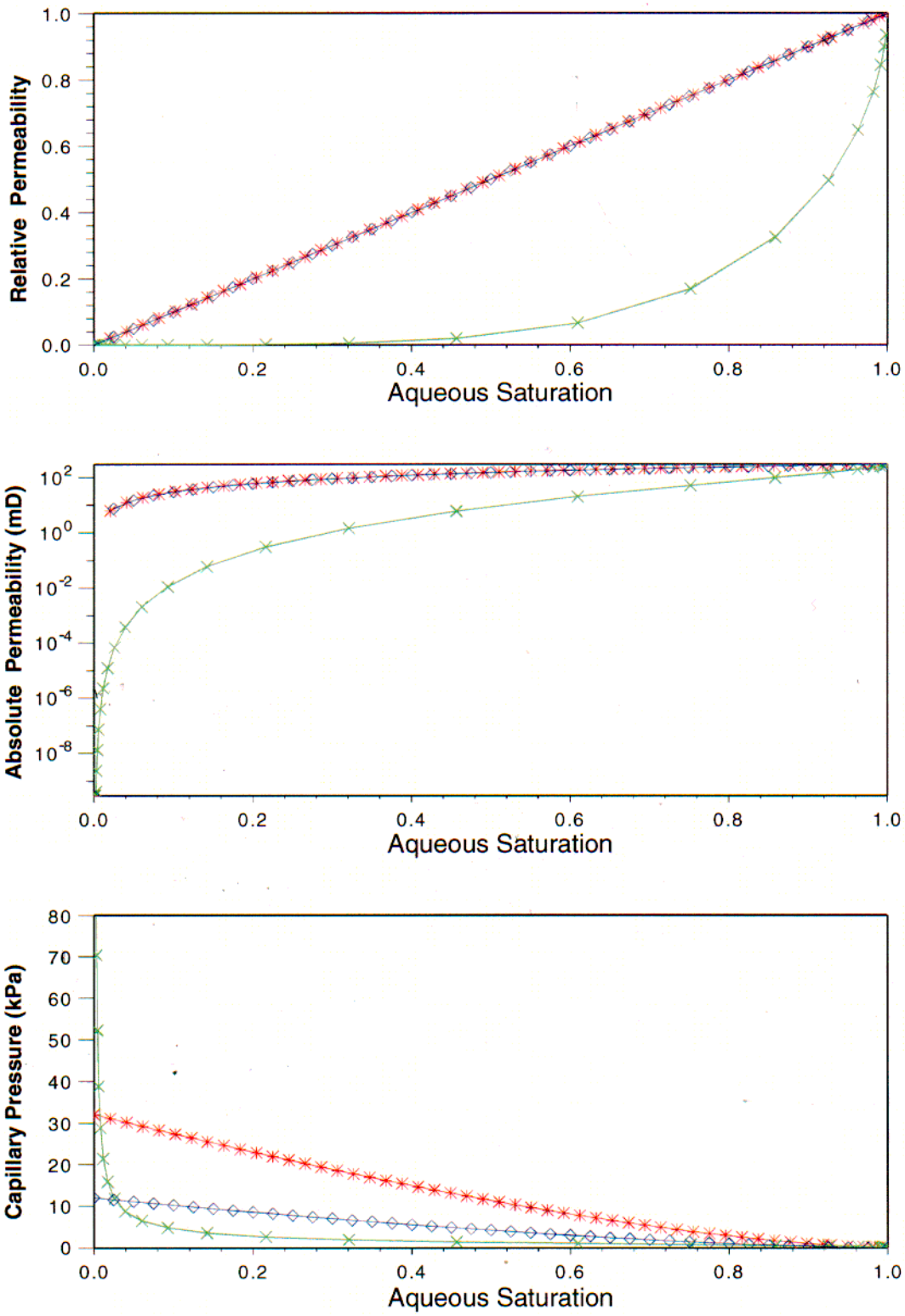

Figure 5-18. Three moisture characteristic curves used in Well 76-5 infiltration simulation. The red asterisks represent the Corey-type moisture characteristic curve used in the ABRA simulations. The other two curves are an alternate Corey-type curve (blue diamonds) and a van Genuchten curve (green Xs).

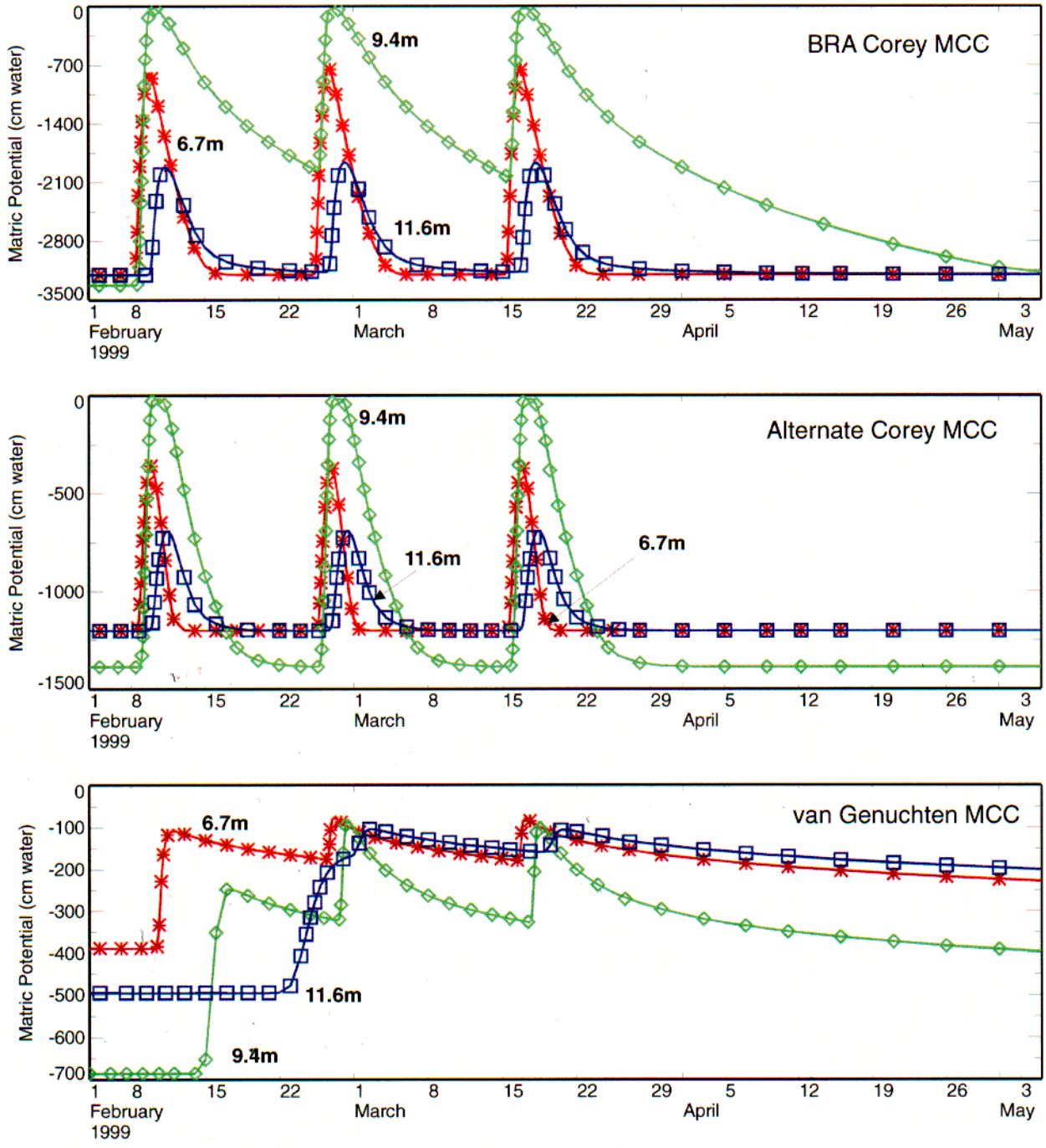

Figure 5-19. Simulated matric potentials for the three moisture characteristic curves.

Using the van Genuchten curve, simulation results better matched the compounding behavior observed in the monitoring results where the second and third fronts resulted in increasingly wetter conditions at depth because the moisture accumulated from the earlier wetting events had not drained out of the system. Using either of the Corey-type simulations, the wetting front propagates more completely through the simulation domain for each wetting event.

To compare the three simulations, the resulting water flux at a depth of 11.6 m (38 ft) is shown for each simulation in Figure 5-20. Similar to what was seen in the matric potential results, fluxes with either of the Corey-type curves are much more compressed in time, yielding higher values and quicker penetration to depths greater than those observed in the field tensiometric monitoring. Therefore, the Corey-type curve for the fractured basalts used in the IRA model is demonstrably conservative with respect to maximizing water and contaminant movement downward through the fractured basalt. This same conservative Corey-type curve was applied in the ABRA modeling. Note that the use of first-type boundaries at the surface to impose the melting events does not require that the cumulative water flux down through the system to this depth be the same for each of the three simulations.

An alternative suite of simulations was performed to investigate the effect of using second-type prescribed fluxes as the upper boundary condition representing each melting event. The amount of water applied for each event was 2.54 cm (1 in.) over a 1-day duration. Results shown in Figure 5-21 were similar to those using first-type conditions because the Corey-type curves both allowed much faster propagation of water fronts down through the system. The time axis in Figure 5-21 was extended the full length of the 200-day simulation period to allow the flux curve resulting from the van Genuchten curve to be partially seen on the plot.

5.2.4.3.8 Spreading Area Influence in the Vadose Zone—The base case model for the ABRA includes the influence of water entering the domain in the vadose zone at the C-D interbed from the spreading areas. The decision to include spreading area effects resulted from the tracer test conducted by the USGS in 1999 (Nimmo et al. 2002). In that test, perched water sampled from Well 92 in the vadose zone beneath the SDA yielded a tracer within 90 days after it was applied in the spreading areas during a period when water was diverted from the Big Lost River to both Spreading Areas A and B. In the implementation for the ABRA model, the additional water that entered the simulation domain was assumed to be located just above the C-D interbed and to affect only the western portion of the C-D interbed beneath the SDA.

To mimic these effects, the initial vadose zone domain was defined to include the spreading areas. When simulations with the resulting grid from that domain were impractical, it was necessary to use a smaller domain, which did not include the spreading areas. To implement the additional spreading-area water into the simulation it was necessary to assign an amount of water, a location to apply the water, and a duration for the application. The latter is not important in the use of the ABRA model for long-term predictive simulations because they consider only a steady-state influence at depth.

A series of transient simulations was made in which additional water was added above the C-D interbed at two different locations. These simulations used the model developed above as the starting point. One of the locations, chosen to mimic Spreading Area A, was defined as two grid blocks along the central portion of the western simulation boundary. The other location represented Spreading Area B and was defined as three grid blocks along the southern boundary of the domain beginning in the extreme southwestern corner. The approximate length of time that water was present in the spreading areas in 1999 was 60 days (Nimmo et al. 2002). Amounts of water representing 0.04, 0.08, 0.2 and 0.4 % of the water discharged to Spreading Area A in 1999 were applied over 60 days to the first location. Similarly, amounts of water representing 0.02, 0.05, 0.1 and 0.2 % of the water discharged to Spreading Area B in 1999 were applied at the second location.

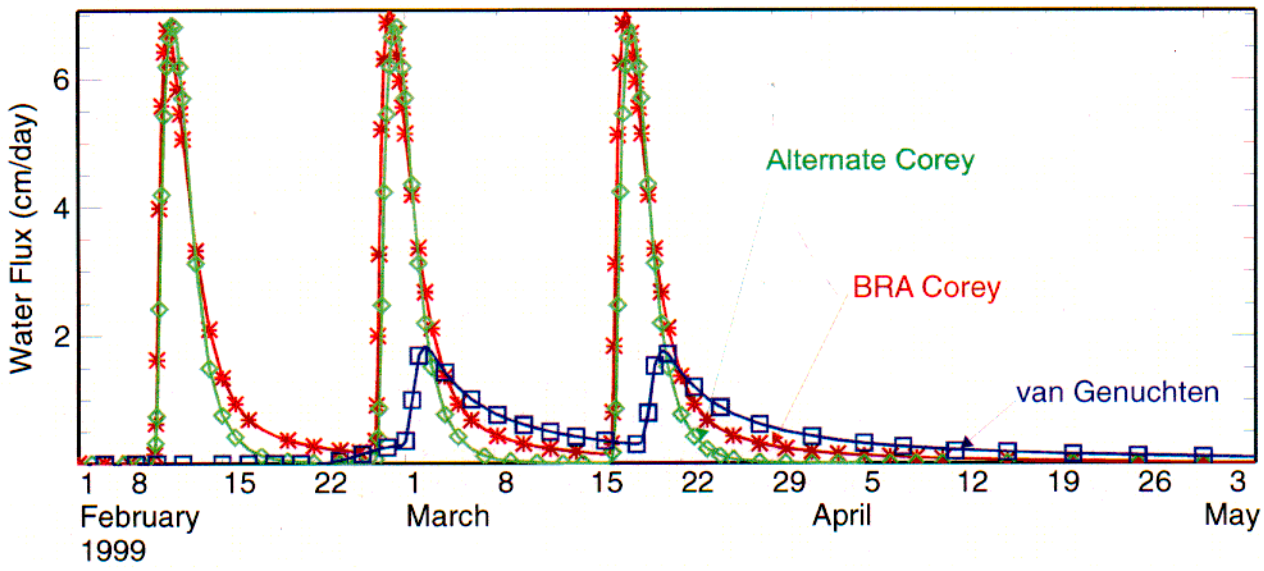

Figure 5-20. Simulated water fluxes at 11.6-m (38-ft) depth beneath a thin interbed for the three moisture characteristic curves using first-type prescribed saturation conditions for melting events.

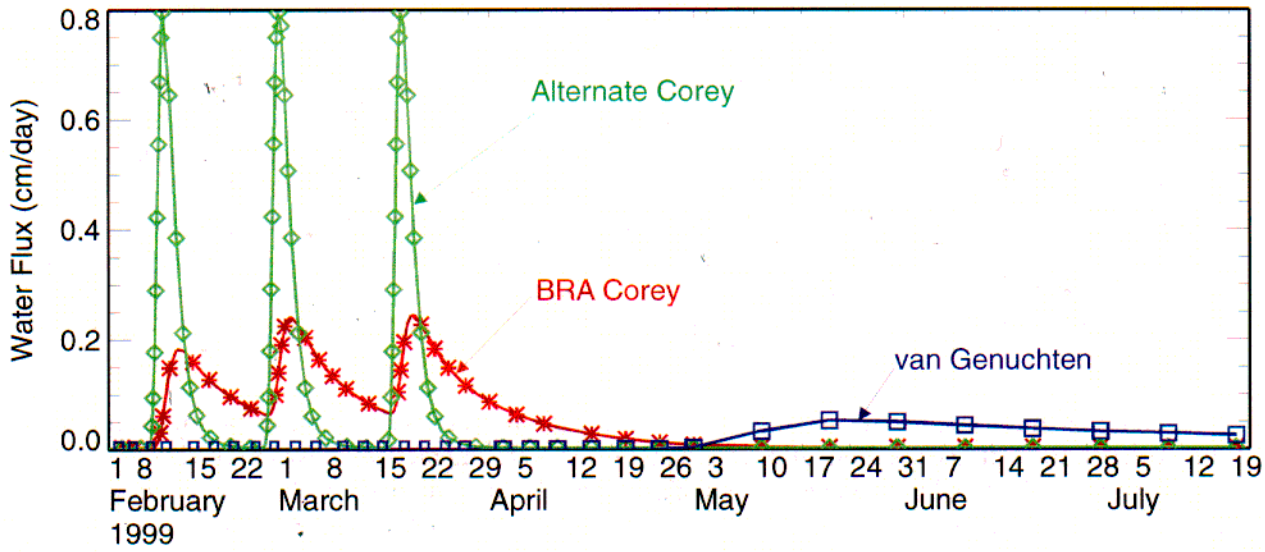

Figure 5-21. Simulated water fluxes at 11.6-m (38-ft) depth for the three moisture characteristic curves using second-type prescribed flux conditions for the melting events.

The varying slope of the C-D interbed had a large influence on the simulation results. The location chosen to represent Spreading Area A was slightly upgradient from the SDA compared to the location for Spreading Area B, which was off gradient. This resulted in Spreading Area A water easily reaching Well 92 within 90 days, while the larger amounts of water applied at the Spreading Area B location never advanced to the location of Well 92. Figures 5-22 and 5-23 show the simulation results at 90 days for each case. The contour lines show the relative fraction of water from the spreading areas compared to total water present. Well 92 is in the west-central portion of the SDA and is just touched by the 0.01 isoline. This 1% concentration is approximately the same as the tracer concentration observed in Well 92 compared to the input concentration in the spreading areas (Nimmo et al. 2002). Though not conclusive, comparison of these simulation results implies that Spreading Area A is the source of water affecting the vadose zone beneath the SDA. The location that was used to represent Spreading Area A was chosen for use in the steady-state ABRA simulations. By choosing the Spreading Area A location, an influence from spreading-area water beneath the SDA is reflected in the simulation, regardless of whether the actual influence is from Spreading Area A or B.

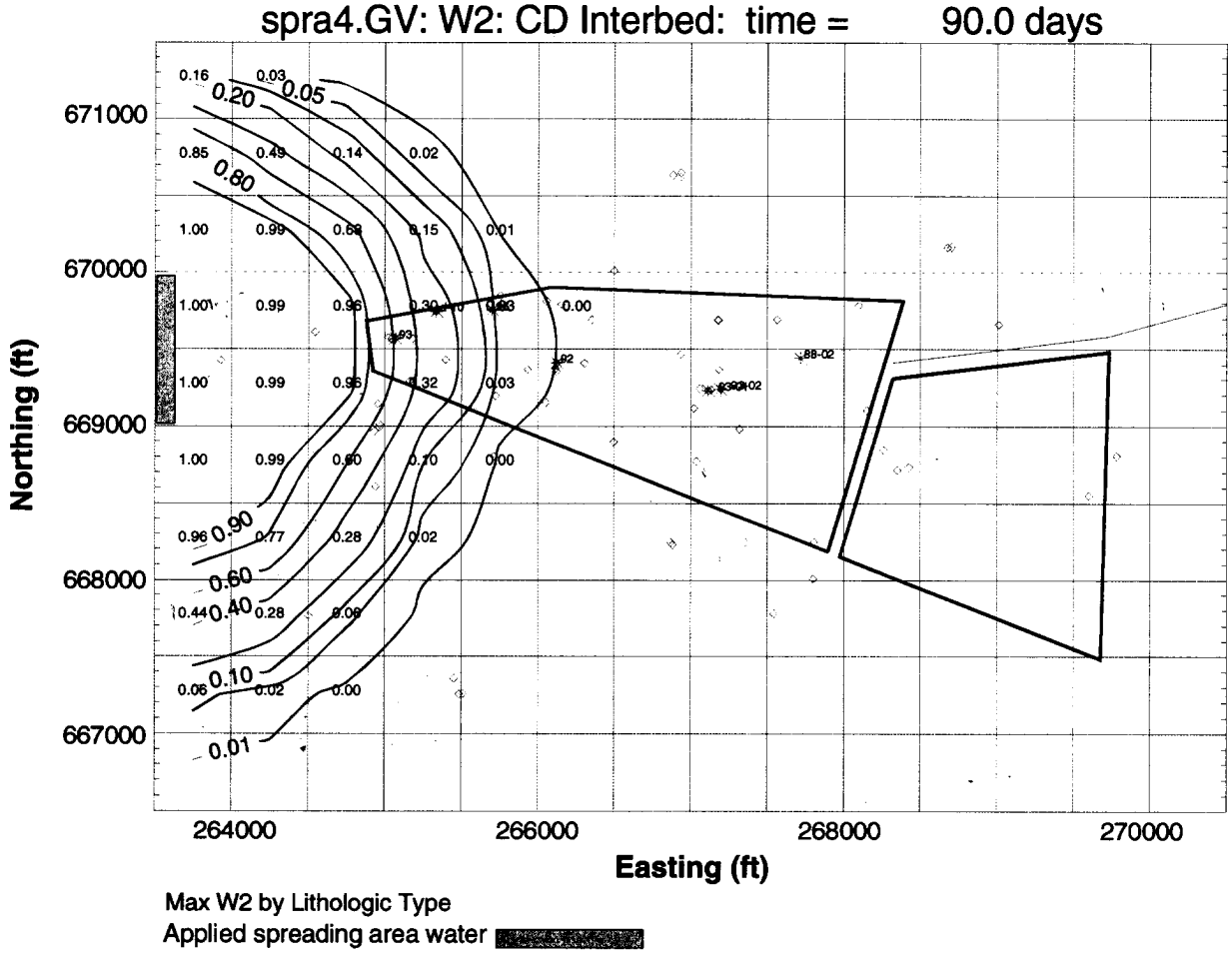

Figure 5-22. Transient simulation results with water applied at Spreading Area A.

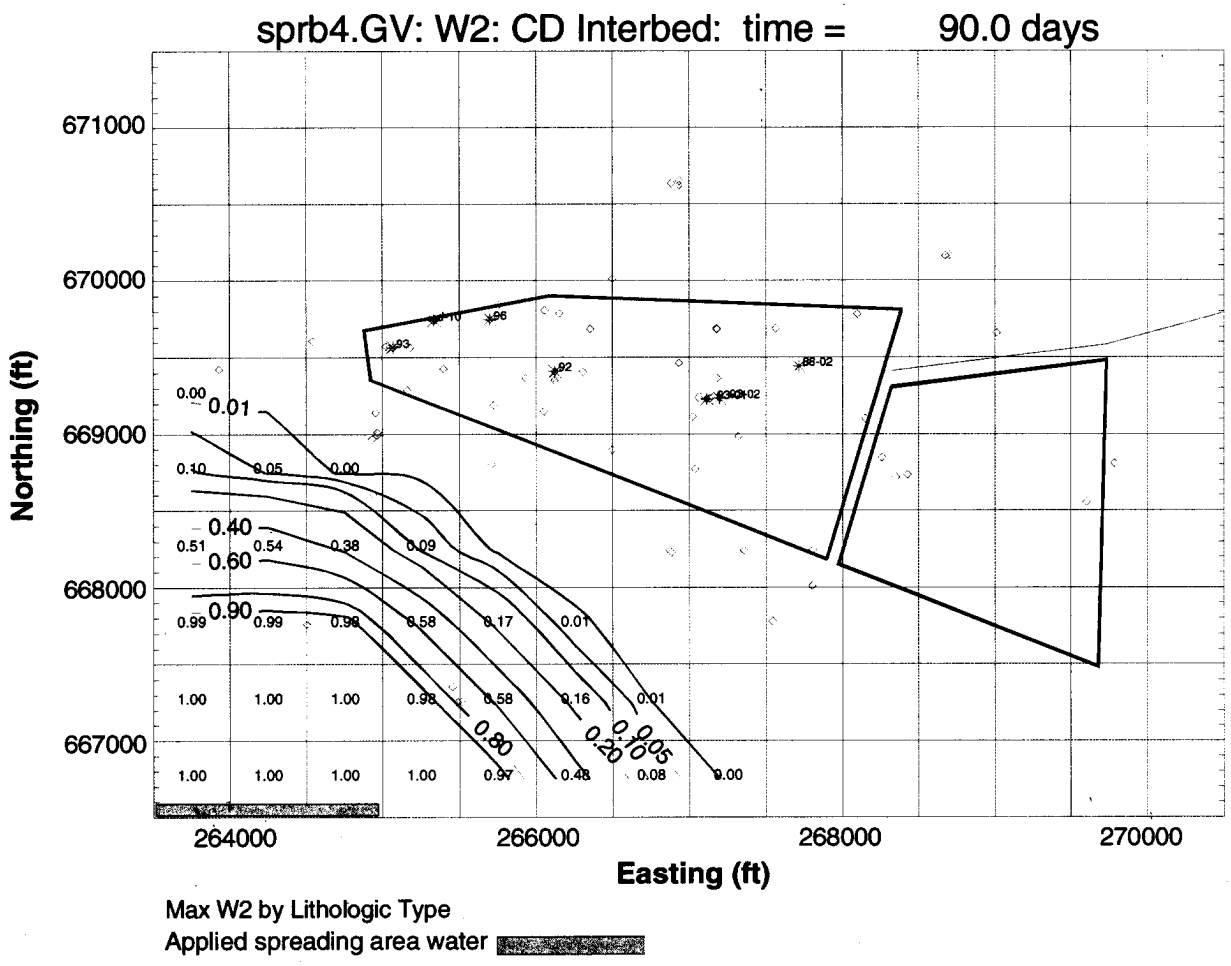

Figure 5-23. Transient simulation results with water applied at Spreading Area B.

The next series of simulation results (Figures 5-24, 5-25, 5-26, 5-27, and 5-28) indicates the sensitivity of the modeling results to the magnitude of applied spreading-area water volumes. Amounts of 1, 2, 3, 4, and 8 acre-ft of water per day in perpetuity were evaluated. Simulations were run for 10,000 days to obtain steady-state conditions. Results shown in the figures depict relative presence of spreading-area water within the C-D interbed. As greater amounts of water are added at the western boundary, the spreading-area water spreads farther eastward because the simulated upper surface of the C-D interbed slopes east-southeast. Horizontal no-flux boundaries also impact solutions by keeping water within the simulation domain, as can be seen in the refraction of the isolines, especially along the northern boundary. In general, good modeling practice proscribes having the boundary condition influence the simulation results. However, in this case the proximity of the boundaries helps achieve the goal described earlier in this subsection of obtaining a spreading area influence under the western portion of the SDA.

Simulation with an additional 1 acre-ft (1,233 m^3) per day applied at the western boundary was selected for further use in the ABRA model. The 0.01 isoline bisects the SDA west to east, indicating that all locations west of this line exhibit some impact from the spreading-area water. The spreading area influence in the base case is implemented at the beginning of 1965 when the first significant flows in the Big Lost River occurred since it was constructed in 1958 (Wood 1989). The history of diversions from the Big Lost River to the spreading areas is presented in Figure 5-29.

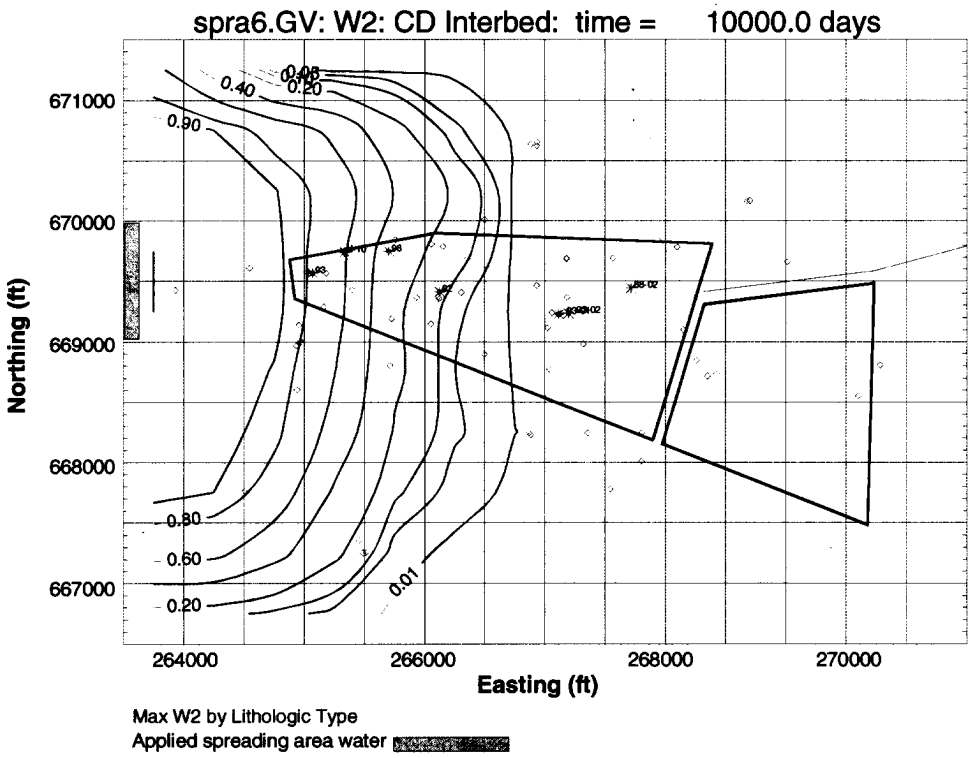

Figure 5-24. Relative presence of spreading-area water with 1 acre-ft/day steady-state application. (This simulation was selected for the baseline risk assessment base case.)

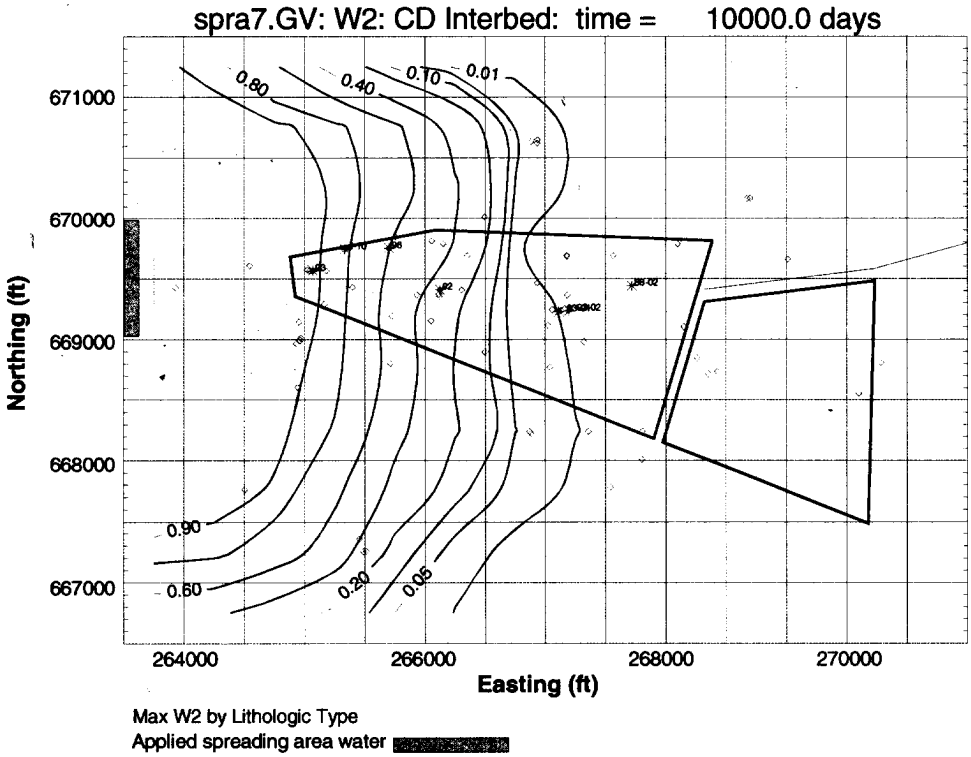

Figure 5-25. Relative presence of spreading-area water with 2 acre-ft/day steady-state application.

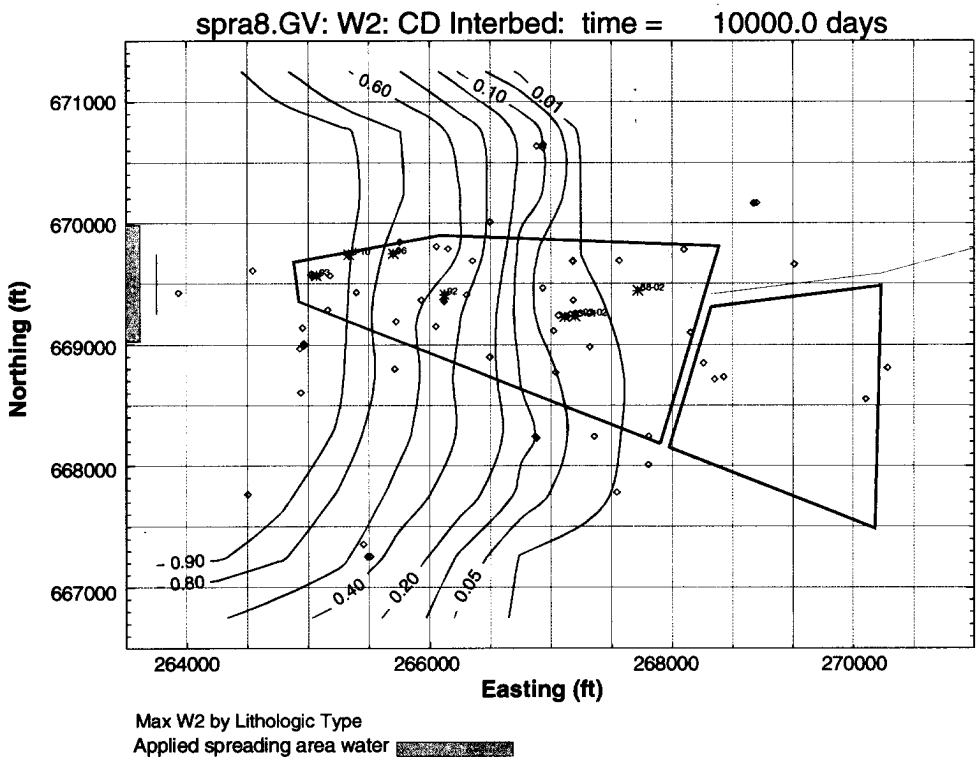

Figure 5-26. Relative presence of spreading-area water with 3 acre-ft/day steady-state application.

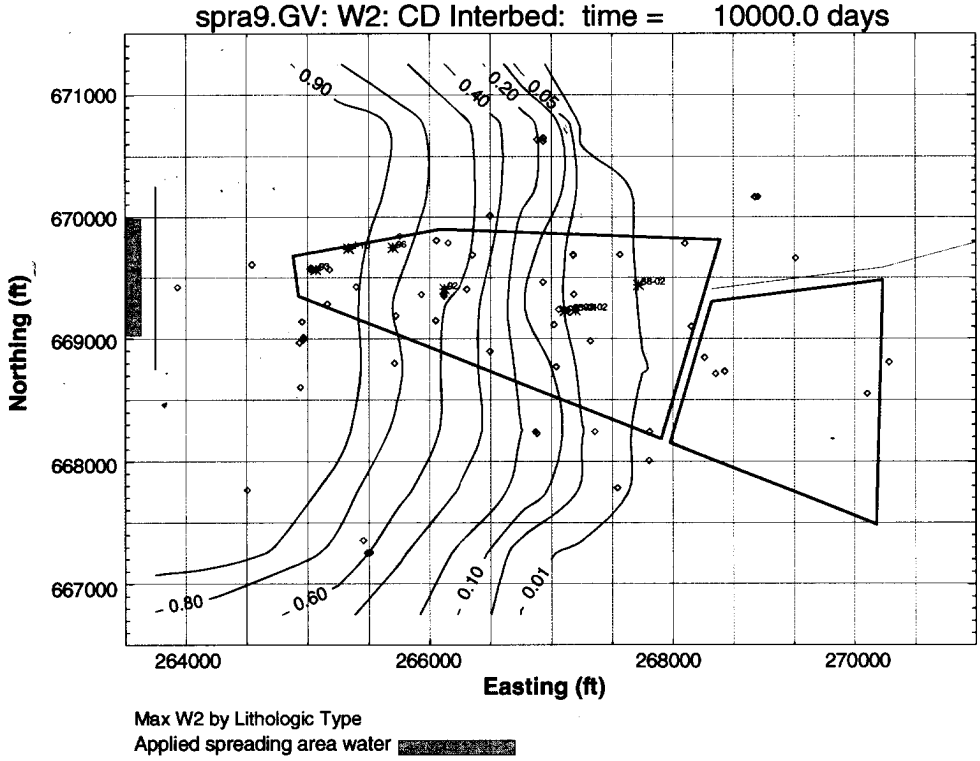

Figure 5-27. Relative presence of spreading-area water with 4 acre-ft/day steady-state application. (This simulation was selected for the sensitivity evaluation of twice the spreading area effect.)

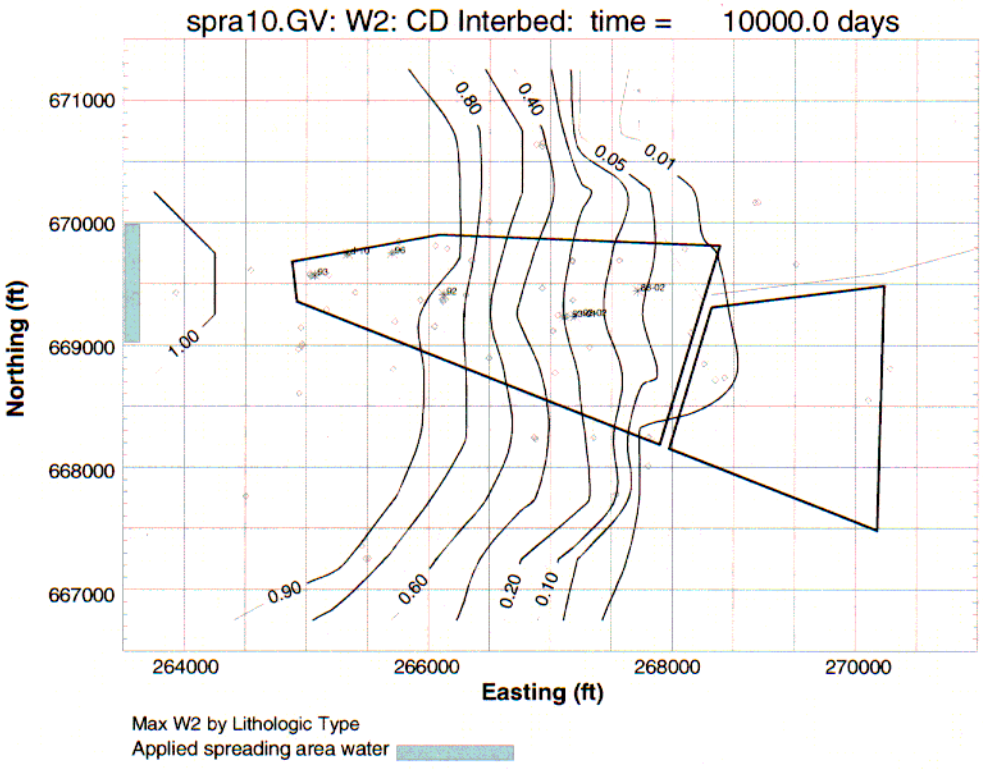

Figure 5-28. Relative presence of spreading-area water with 8 acre-ft/day steady-state application.

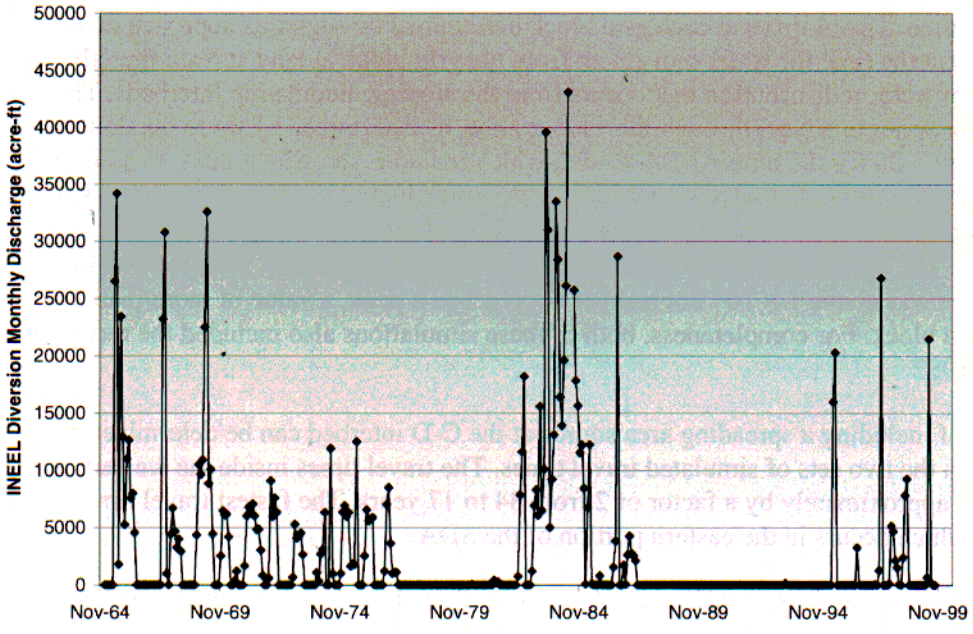

Figure 5-29. Historical diversion of Big Lost River water to the spreading areas from 1965 through 1999.

Historical data were obtained from the USGS web site (http://water.usgs.gov/id/nwis) (USGS 2001). The overall average monthly diversion for the data in the figure is 3,000 acre-ft/month, which equates to 100 acre-ft/day. The 1 acre-ft/day amount of water applied in the ABRA simulations represents 1% of the overall average diversion, which is a reasonable proportion to apply to ensure an impact beneath the SDA in the model.

One scenario evaluated below in the sensitivity analyses involved investigating the effect of twice the impact of spreading-area water on predicted contaminant migration. Rather than simply doubling the amount of water applied, the simulation with 4× the amount of water was selected because it showed an impact over nearly all the SDA, which effectively doubled the impacted area.

5.2.4.3.9 Vadose Zone Water Travel Times—This section provides a discussion of simulated water travel times through the vadose zone. Because no incontrovertible evidence exists to demonstrate required time to reach the aquifer from the SDA surface, model calibration is indirect and uncertain at best. Best-available knowledge based on site-specific information on infiltration, lithology, and hydrologic properties was used to assign parameters in the model, and the water travel time through the vadose zone was a simulation result. Because the simulated vadose zone water travel times impact dissolved-phase transport of mobile contaminants, these resulting vadose zone water travel times are of interest and are presented in this section. A comparison also is made to the vadose zone water travel times that resulted from the IRA model.

Travel times for the ABRA model were determined using the same method as was used for the IRA model. Starting from an equilibrium condition in 1952, the spatially distributed infiltration at land surface inside the SDA was applied as a separate nonsorbing tracer component for the first 1,000 days. At each grid block location at the bottom of the vadose zone simulation domain, the breakthrough curve for the tracer component was evaluated to determine the peak value. The time corresponding to this peak value was then decreased by 500 days, the midpoint of the initial application pulse, to determine the vadose zone water travel time. Travel times at each grid block determined through this approach do not necessarily represent the time for water movement from the grid block at land surface directly above each location because of water redistribution that occurs from the sloping, undulating interbeds. The travel times (in years) for water to advect through the vadose zone, as determined by these breakthrough curves, are shown in Figure 5-30 for the base ABRA model, which includes spreading areas. In addition, travel times are shown for a simulation that does not include the spreading areas. If the maximum value was less than a relative fraction of 1×10^{-6}, the travel time to that grid block was not determined and is represented by the symbol: **. The simulation was truncated at 100,000 days (272 years); therefore, if the breakthrough curve was above 1×10^{-6} but had yet not reached a peak, a value of more than 272 years is shown for that grid block. For completeness, both of these simulations also included the three floods of 1962, 1969, and 1982.

The effect of including a spreading area source at the C-D interbed can be determined from the difference between the two sets of simulated travel times. The travel times inside the western portion of the SDA decrease approximately by a factor of 2 from 34 to 17 years. The fastest travel time in either case is 14 years, which occurs in the eastern portion of the SDA.

For comparison to the current ABRA model, Figure 5-31 shows the simulated travel times from the IRA model, for which the fastest water travel time through the vadose zone was 23 years. Therefore, the revisions to the IRA model implemented in this ABRA model result in shorter simulated water travel times through the vadose zone. The extremely long 210-year vadose zone water travel time in the west-central portion of the SDA from the IRA model is completely absent in the ABRA modeling results.

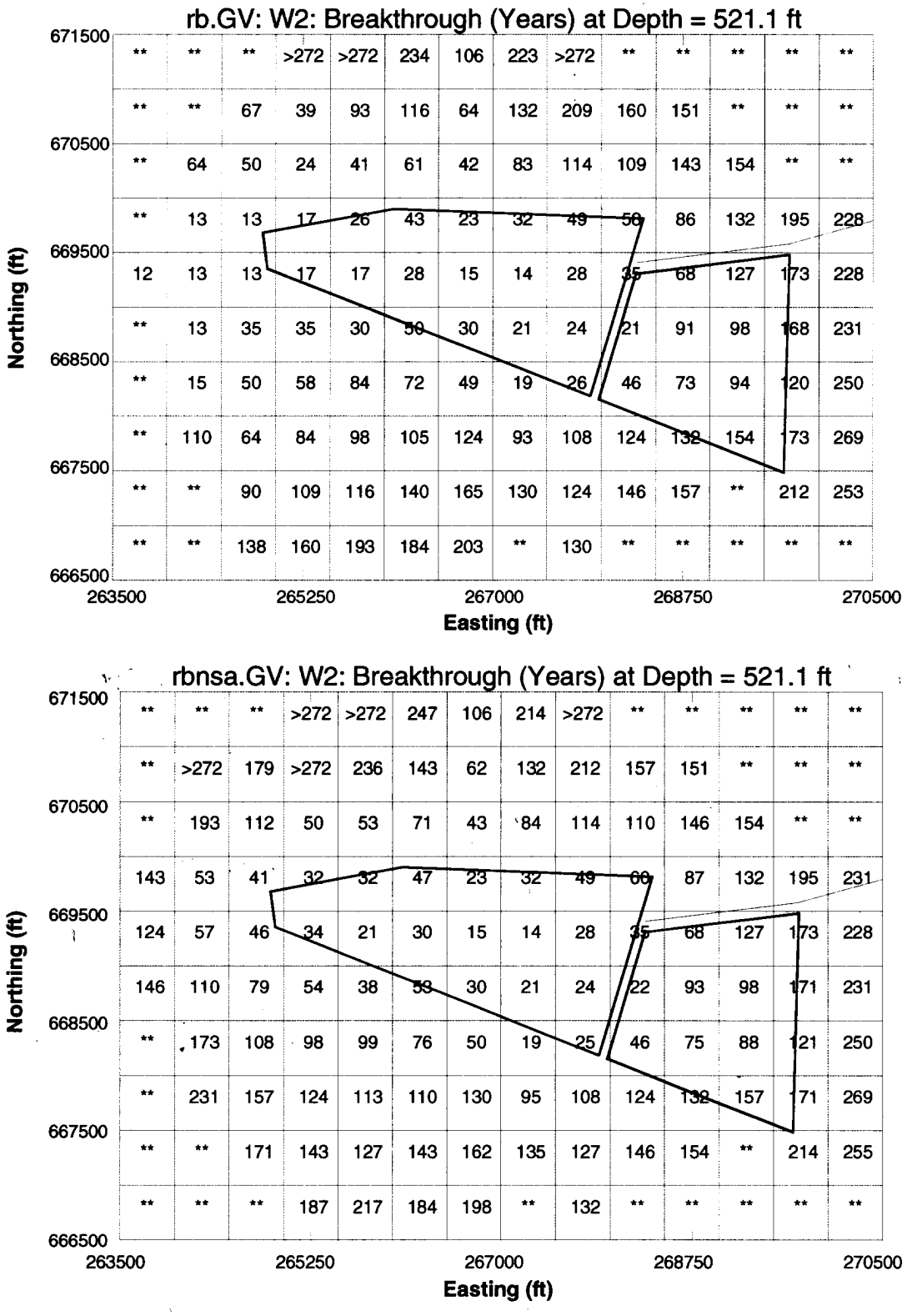

Figure 5-30. Water travel times in years through the vadose zone for the Ancillary Basis for Risk Analysis simulation (top) and for a case without an assumed spreading area influence (bottom).

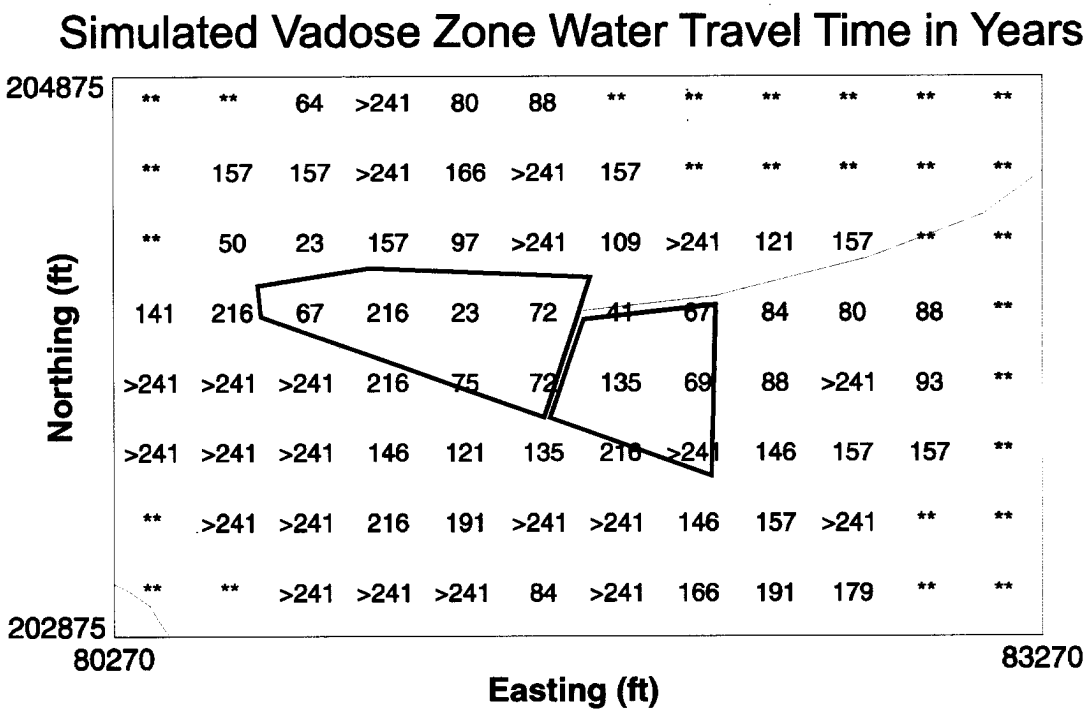

Figure 5-31. Simulated water travel times from the Interim Risk Assessment model.

Primary causes for reducing vadose zone water travel time were: (a) including the spatially variable hydrologic properties in the B-C and C-D interbeds, (b) the additional grid refinement in the ABRA model, and (c) using the conformable gridding approach that more closely matches the lithologic contacts between the sedimentary and fractured basalt portions of the subsurface. The application of spatially variable infiltration inside the SDA is essentially the same between models.

5.2.4.3.10 Vadose Zone Interbed Moisture Contents—The last topic presented in the development of the vadose zone transport model is the simulation results for moisture content in the interbeds. Figure 5-32 shows the maximum water saturation for the most refined grid in calendar year 2001 for the B-C and C-D interbeds, respectively. All locations where perched water has been detected are shown in orange for comparison. The simulation results for calendar year 2001 reflect steady-state saturations well after the 1982 flood.

The areas of elevated moisture content partially mimic the distribution of known perched water locations. Less apparent is the control exerted by the presence or absence of the A-B interbed. The regions in the B-C interbed where the moisture content is elevated generally correspond to where the A-B interbed is absent or is very thin. This same behavior persists down into the C-D interbed, but is less obvious because of the influence of the additional water added in the simulation to represent a spreading area influence.

In the simulation results, the location containing Well 92 is still in a region of lower water content. Perched water has been observed continuously in this well since it was drilled in 1992. The proximity of the simulated elevated saturation region immediately to the west of Well 92 (see the lower plot in Figure 5-32) implies that the continuous presence of water in Well 92 could be attributed to spreading area influences.

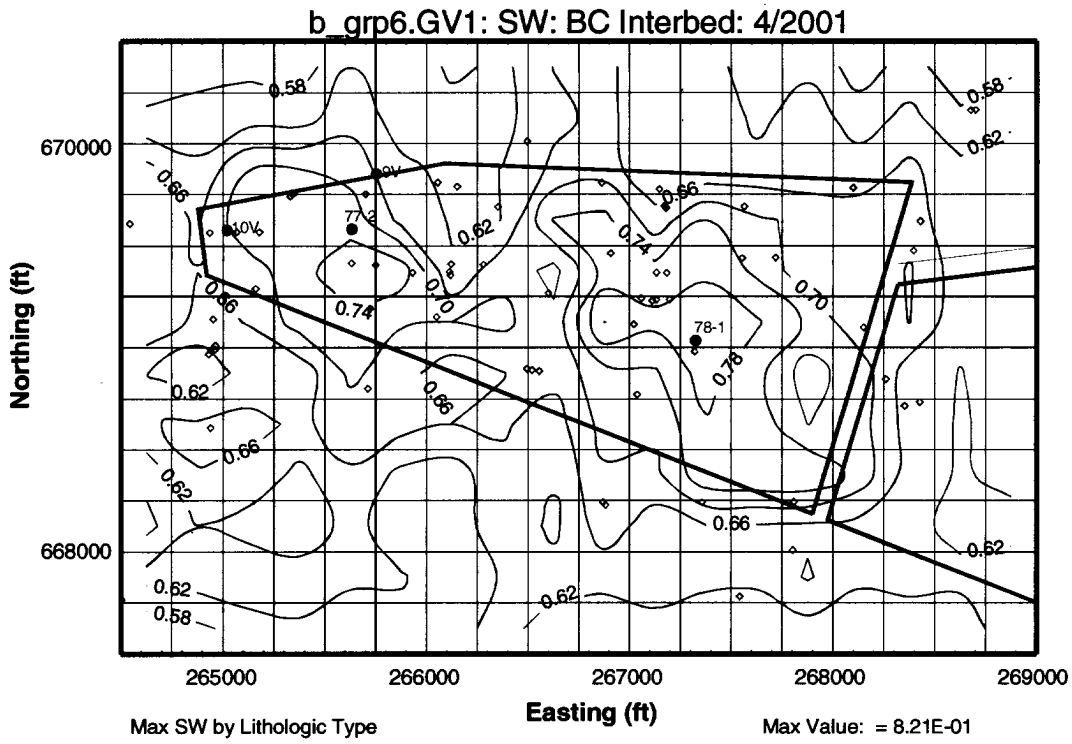

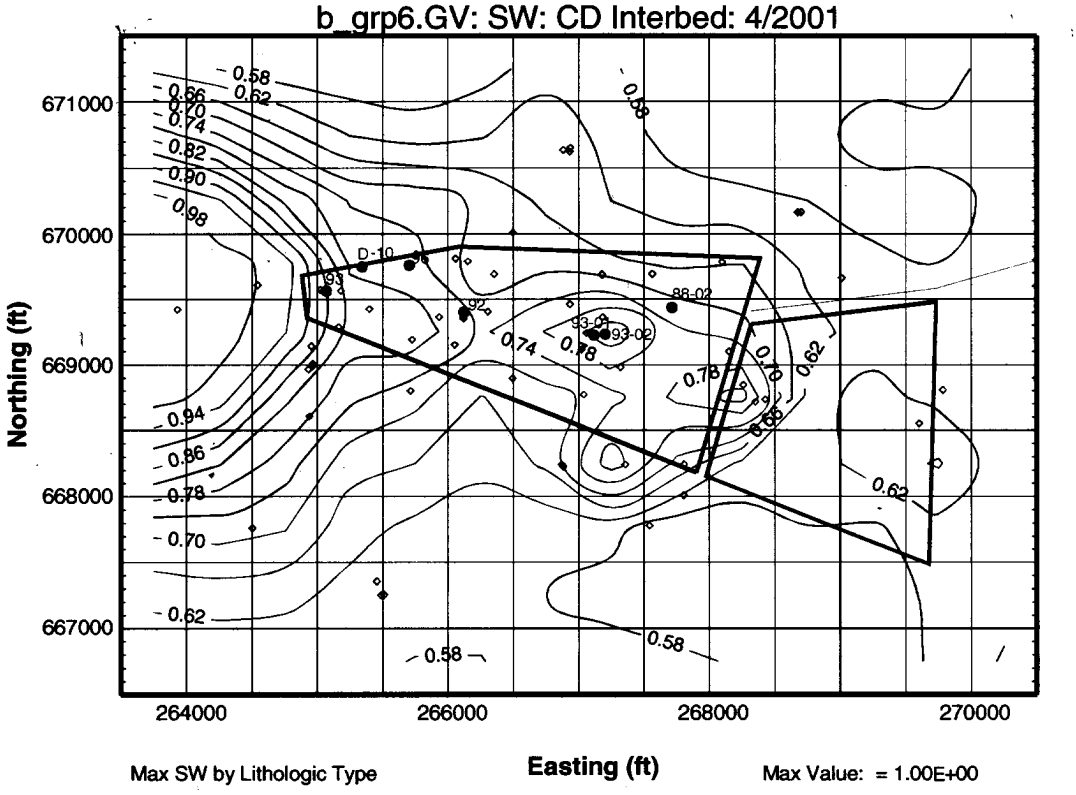

Figure 5-32. The upper plot shows the maximum simulated water saturation in the B-C interbed in calendar year 2001 and the lower plot shows the maximum simulated water saturation in the C-D interbed in calendar year 2001.

5.2.4.4 Vadose Zone Transport Model. This section describes development and implementation of the transport model for the vadose zone. Overall, there were very few changes in this portion of the ABRA model from that implemented in the IRA model.

5.2.4.4.1 Interface from Source Release Model into Vadose Zone Model—Similar to the IRA model, the vadose zone model implements the temporal source term release (described above) spatially. In addition, the release is distributed vertically at each assigned location based on the number of grid blocks within the surficial sediments. Once released, the contaminants are allowed to migrate with the simulated water movement.

5.2.4.4.2 Partition Coefficient—Sorption was considered to follow linear, reversible isotherms that could be described by use of K_ds, also known as distribution coefficients. A K_d lumps all possible geochemical interactions into a single parameter. Since sorption was assumed to not occur within the fractured basalt portions of either the vadose zone or the aquifer, only sediment K_d values were necessary in the ABRA model.

Consistent with the approach recommended in Hull (2001), sediment K_ds were assigned based on best-estimated values rather than conservative screening values. The set of best-estimate K_ds developed by Dicke (1997) was once again the primary source used in this application. Dicke (1997) placed primary reliance on site-specific measured K_ds as opposed to using literature values. Values measured on sediments from the SDA were given priority as opposed to K_ds measured on sediments from elsewhere on the INEEL. This approach is consistent with the guidance contained in EPA (1999), which includes the following statement in the introduction to Volume 1:

> It is important to note that soil scientists and geochemists knowledgeable of sorption processes in natural environments have long known that generic or default partition coefficient values found in the literature can result in significant errors when used to predict the absolute impacts of contaminant migration or site-remediation options. Accordingly, one of the major recommendations of this report is that for site-specific calculations, partition coefficient values measured at site-specific conditions are absolutely essential.

Table 5-13 gives the K_ds used in the ABRA model. A K_d value of 0.1 mL/g was used for C-14 based on additional site-specific work (Dicke 1998). For comparison, the K_d used for C-14 in the IRA model was 5 mL/g. One additional contaminant that was not a COPC, chromium, was also simulated, and it was assigned a K_d value of 0.1 mL/g based on Dicke (1997).

Table 5-13. Best-estimate site-specific K_ds used in the baseline risk assessment model.

Contaminant of Potential Concern	K_d (mL/g)	Contaminant of Potential Concern	K_d (mL/g)	Contaminant of Potential Concern	K_d (mL/g)
Actinium	400	Niobium	500	Radium	575
Americium	450	Neptunium	8	Technetium	0
Carbon	0.1	Protactinium	8	Thorium	500
Chlorine	0	Lead	270	Uranium	6
Iodine	0.1	Plutonium	5,100	Nitrate	0

Linear isotherms were assumed for the ABRA model for all COPCs. Results determined on SDA soil (Grossman et al. 2001) clearly demonstrate that the isotherms for uranium and neptunium were nonlinear. An example of a laboratory result and fitted isotherms for sample 7DS00501 is provided

in Figure 5-33. The fitted nonlinear isotherm crosses the linear isotherm (K_d approach) at concentrations greater than 250 pCi/mL. It can be argued that using a linear isotherm is conservative as long as simulated concentrations are less than this crossover point. For example, at a concentration of 100 pCi/mL, the adsorbed concentration for the linear case is ~10,000 pCi/g, while concentrations for nonlinear cases are ~17,000 pCi/g. Nonlinear isotherms thus take more of a sorbing contaminant out of solution for concentrations less than the crossover point. Results from all the other samples that were analyzed for uranium and neptunium isotherms were similar with crossover points approximately equal to 250 pCi/mL.

Maximum simulated concentrations in this modeling effort logically occurred in the most refined simulation domain closest to the source. For Np-237 and U-238, these concentrations were 20 and 100 pCi/mL, respectively. These concentrations are to the left of the crossover point of the linear and nonlinear curves on Figure 5-33. Therefore, using a linear isotherm (K_d approach) is conservative in the ABRA model. For completeness, from the Section 4 discussion, the maximum observed uranium isotope concentrations are on the order of 0.08 pCi/mL, which is also well within the portion of the isotherm where using a linear isotherm is conservative compared to nonlinear isotherms. Neptunium-237 has not been detected in subsurface sampling.

Cumulative frequency distribution of site-specific measured K_ds for uranium and neptunium is shown in Figures 5-34 and 5-35, respectively. These two distributions are based on the K_ds in Table 3-22. The best-estimated K_d values from Dicke (1997) of 6 and 8 mL/g for uranium and neptunium (see Table 5-13), respectively, were used in the ABRA. These values are within the distributions, thus validating their representativeness when compared to site-specific measurements. Because they are at the low end of the site-specific measured values, they also are demonstrably conservative with respect to maximizing the likelihood of contaminant migration predicted with the ABRA model.

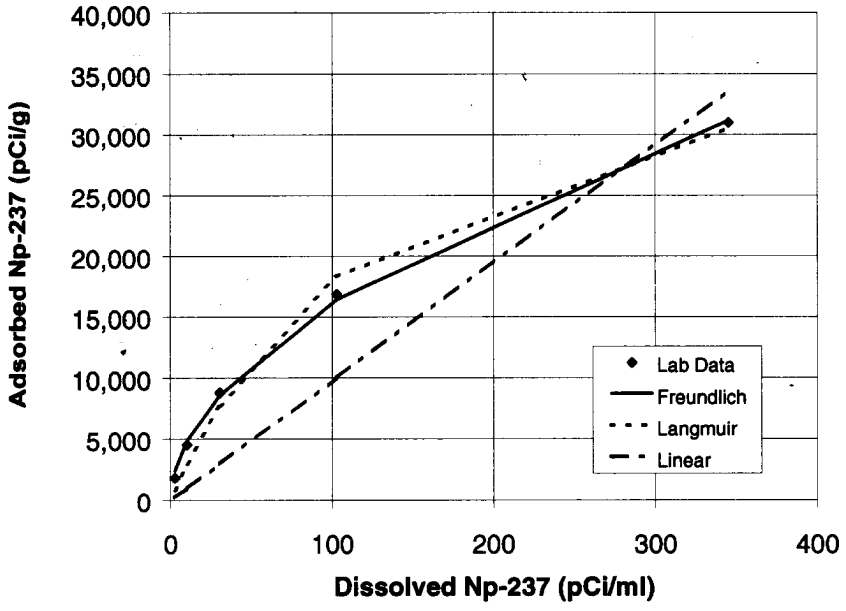

Figure 5-33. Fitted linear and nonlinear isotherms for neptunium for sample 7DS00501.

U Kd (ml/g)	Frequency	Cumulative %
< 3	0	0
3 – 5	0	0
5 – 8	2	14
8 – 13	3	36
13 – 20	6	79
20 – 32	2	93
32 – 50	1	100
> 50	0	100

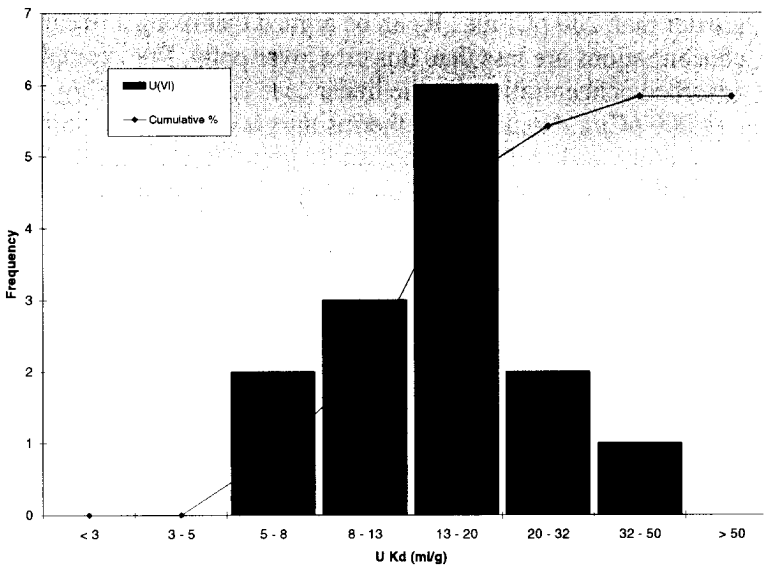

Figure 5-34. Cumulative frequency distribution of uranium K_d values measured on Subsurface Disposal Area sedimentary interbed samples.

Np Kd (ml/g)	Frequency	Cumulative %
< 5	0	0
5 – 10	1	7
10 – 20	2	21
20 – 40	7	71
40 – 80	1	79
80 – 160	3	100
> 160	0	100

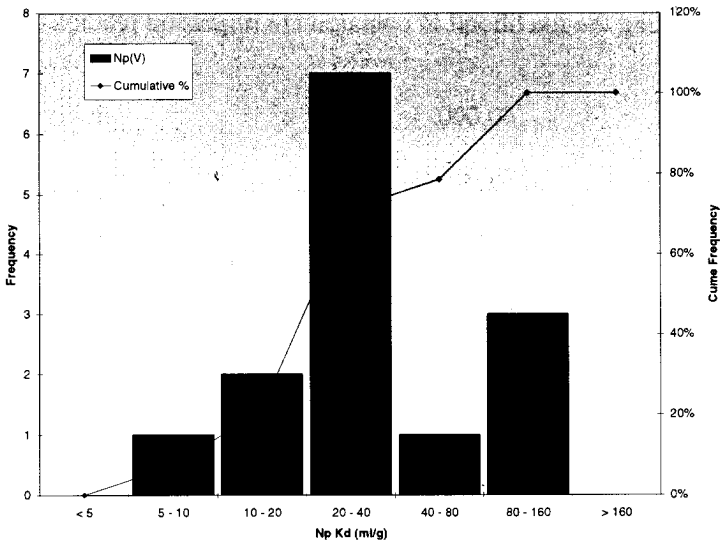

Figure 5-35. Cumulative frequency distribution of neptunium K_d values measured on Subsurface Disposal Area sedimentary interbed samples.

Plutonium behavior in the subsurface at the SDA has continued to receive scrutiny since vadose zone investigations started in the early 1970s. For the base case estimates in the ABRA, the plutonium K_d of 5,100 mL/g is assigned based on the best-available, site-specific data. The assigned value is from the low end of the measured K_d values for plutonium(IV), which is the predominant state (Hull 2001). Figure 5-36 shows the cumulative frequency distribution for measured plutonium K_d values, including both plutonium(IV) and plutonium(VI). The topic of facilitated transport of plutonium is addressed below.

Plutonium K_d (mL/g)	Frequency	Cumulative %
<100	0	0
100 to 250	2	13
250 to 500	1	19
500 to 1,000	1	25
1,000 to 2,500	1	31
2,500 to 5,000	3	50
5,000 to 10,000	6	88
10,000 to 25,000	2	100
>25,000	0	100

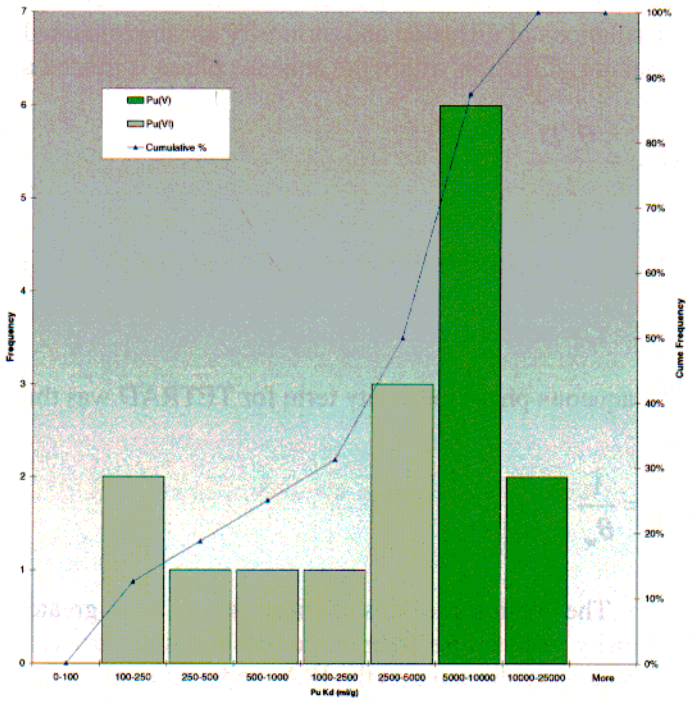

Figure 5-36. Cumulative frequency distribution of plutonium K_d values measured on Idaho National Engineering and Environmental Laboratory soil and sedimentary interbed materials by Newman and Dunnivant (1995).

5.2.4.4.3 Other Transport Parameters—A variety of additional parameters were required in order to implement the vadose zone transport model. These were the particle density, diffusion coefficients, tortuosity, and half-lives. The particle density was assigned the typical value for sediments of 2,700 kg/m^3 (Freeze and Cherry 1979). This was the same value that was assigned in the IRA model. Since sorption was assumed not to occur in the fractured basalt, the grain density assigned for that portion of the simulation domain did not matter.

Diffusion of contaminants within the aqueous phase was assigned the common literature value of 1×10^{-5} cm^2/s (Freeze and Cherry 1979). This was the same value that was assigned in the IRA model. The restriction of diffusion caused by tortuosity also was included based on a relationship from Lerman (1988) used to describe diffusion as follows:

$$D = D_o \theta_w^2 . \qquad (5\text{-}1)$$

where

D = diffusion in the porous medium (length^2/time)

D_o = free-water diffusion coefficient (length^2/time)

θ_w = volumetric moisture content (unitless).

In any numerical simulation exercise, correct implementation of diffusion is important. Various formulations of diffusion and tortuosity are implemented in different simulators. In the TETRAD simulator, diffusion within the aqueous phase is treated as

$$D_{eff} = \frac{\theta_w D_o}{\tau_w} \tag{5-2}$$

where D_{eff} = effective diffusion coefficient (length^2/time)

τ_w = aqueous-phase tortuosity.

The aqueous-phase tortuosity term for TETRAD was then calculated as

$$\tau_w = \frac{1}{\theta_w} \tag{5-3}$$

The end result of this application is to have greater tortuosities assigned for drier conditions. Single tortuosity values were assigned for each sedimentary feature and for the fractured basalt; the values assigned were the same as the IRA model and are given in Table 5-14. The fractured basalt has a very low simulated moisture content, less than 0.01, and therefore was assigned the highest aqueous-phase tortuosity.

Table 5-14. Aqueous-phase tortuosities for the baseline risk assessment model.

Material	TETRAD Tortuosity (Dimensionless)
Surficial sediments	3.4
A-B interbed	5.3
B-C interbed	3.8
C-D interbed	2.1
Fractured basalt	133

Longitudinal and transverse dispersivities of 5.0 and 0.5 m, respectively, were assigned in the vadose zone transport model. The longitudinal value is the same as the IRA model and was originally based on inverse modeling from the Large-Scale Infiltration Test (Magnuson 1995). The IRA model used a value of 0.0 m for the transverse dispersion in the vadose zone. The ABRA model assigned the value 0.5 m by using the modeling rule-of-thumb that the transverse dispersion is one-tenth of the longitudinal dispersion (Freeze and Cherry 1979). The 5.0 m longitudinal value is smaller than would be assigned using the general rule of thumb that the dispersivity should be approximately 1/10th of the domain size (Gelhar 1986). In the absence of calibration data, such as the breakthrough of a nonsorbing contaminant, there is no basis to substantially adjust the dispersivities from those used in the IRA model. Ideally, higher concentrations would result for pulses of mobile contaminants because the simulated front would remain sharper because of the lower dispersivity. For a long slow release, such as a solubility-limited release of a lower-mobility contaminant, the lower dispersivity would ideally result in slightly later first-arrival. However, because dispersion control was not used in the TETRAD simulation, the relative contribution of numerical dispersion compared to simulated dispersion is unknown.

Half-lives for each radioactive COPC were assigned based on literature values (GE 1989) and were the same as those used in the IRA model.

5.2.4.4.4 Interface from Vadose Zone Model into Aquifer Model—Because of the separation of the vadose zone and aquifer domains, it was necessary to take the mass of water and contaminants emanating from the vadose zone simulation domain and transfer them into the top of the aquifer simulation domain as a boundary condition. This was done on a grid-block-by-grid-block basis; therefore, no spatial averaging was necessary. Refinement was used in the aquifer domain to establish a one-to-one correspondence between grid blocks in each domain. The complete time-history of the flux of water and contaminants from the vadose zone model was transferred into the aquifer model.

5.2.4.5 Aquifer Flow Model. Water levels and flow directions for aquifer simulations were recalibrated with additional data collected after the development of the IRA model. Complete details of aquifer model development and calibration are contained in Whitmire (2001).

Calibration of the aquifer model was necessary to take advantage of additional water level data from aquifer monitoring wells that were not present for the calibration of the IRA model. The additional seven aquifer wells were M11S, M12S, M13S, M14S, M15S, M16S, and M17S. Deviation-corrected water level data from the March and April measurements and the October and November measurements in 2000 were used. Figure 5-37 is the water table map that was developed using data collected in March and April of 2000. Superimposed on the figure is the base aquifer simulation domain, which used grid blocks 305 m (1,000 ft) on a side. Open circles indicate locations where data were used in creating the water table map. Prescribed boundary conditions for the aquifer simulation were interpolated onto the outer edge of each external grid block based on this water table map. Figure 5-38 illustrates just the aquifer simulation domain with the one level of refinement that was used to match the vadose zone model in the vicinity of the SDA.

The thickness of the aquifer model was kept the same as in the IRA model, namely 76 m (250 ft). This thickness was again discretized using seven vertical grid blocks varying in size from 8 m (26 ft) at the top to 18 m (59 ft) at the bottom. The 76 m (250 ft) thickness originated from generalizations of Robertson, Schoen, and Barraclough (1974) on the depth to which contaminants were detected in plumes in the southern part of the INEEL. This aquifer thickness was first implemented in simulations by Robertson (1974). Recent estimates of effective aquifer thickness show that it varies across the INEEL and is approximately 150 m (490 ft) in Well C1A, immediately northeast of the SDA (Arnett and Smith 2001). The effect of retaining the thinner aquifer in the ABRA simulations is conservative in that there is less aquifer thickness is available for contaminant dispersion. Thus, the resulting estimates of contaminant concentrations are higher than for a larger effective aquifer thickness.

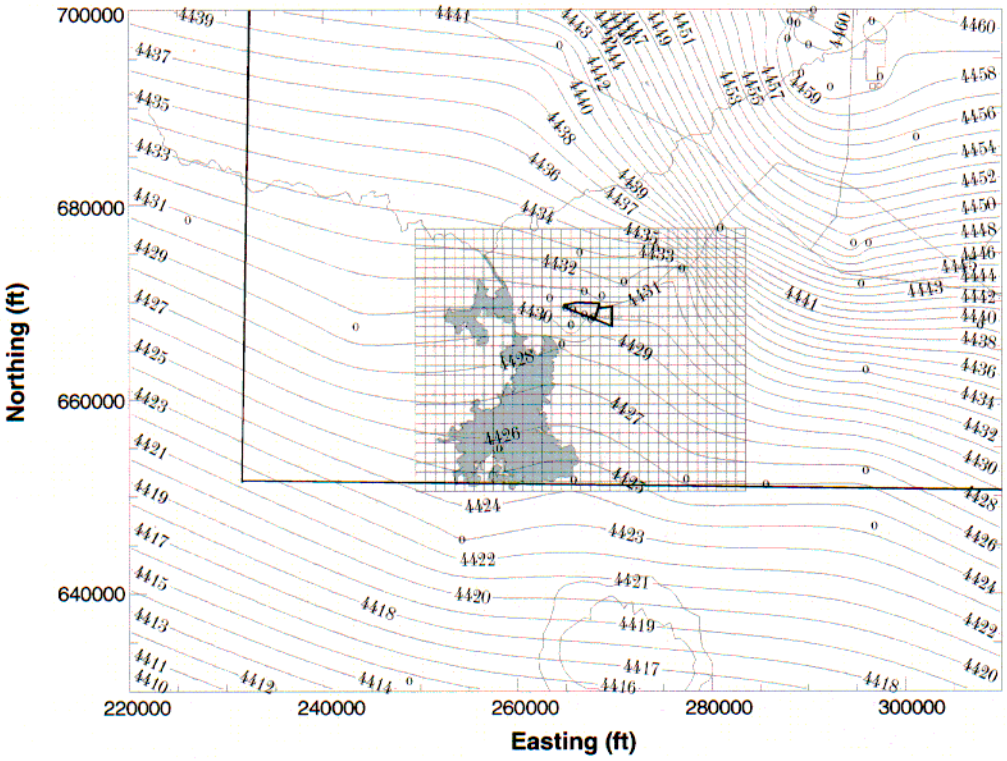

Figure 5-37. Water table map generated with deviation-corrected data from March and April 2000. Also shown is the base aquifer simulation domain.

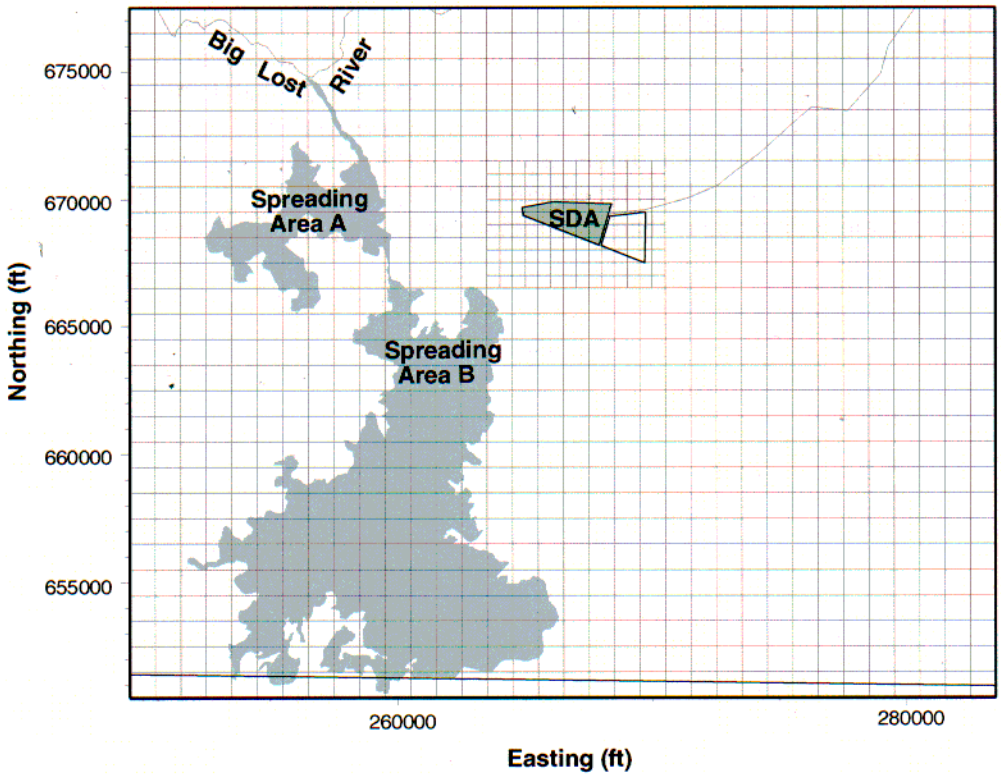

Figure 5-38. Aquifer simulation domain with one level of refinement to match vadose zone model.

Simulated hydraulic heads were compared with values measured from wells across the southern portion of the INEEL. The final optimized simulation results are shown in Figure 5-39 for the base and refined simulation domains. The small localized mound in the refined area is a result of additional water flux being applied inside the refined area from the vadose zone simulation. These heads were optimized through manual trial-and-error by trying different permeability distributions across the aquifer simulation domain. It is recognized that this does not result in a unique solution. The root mean squared error of the residuals, or difference between observed and simulated water levels, was used to judge between results of different attempts to simulate water levels in the aquifer. The value was calculated using

$$RMS = \sqrt{\frac{\sum_{i=1}^{n} (\text{Residuals})_i^2}{n}} \tag{5-4}$$

where

RMS =

Residuals

n = number of locations at which observed water level measurements were available.

The root mean squared error for the optimal fit shown in Figure 5-39 was RMS=0.899 ft. The optimal set of aquifer permeabilities that minimized the root-mean-squared-error differences between measured and simulated water levels is shown in Figure 5-40. The measured water level at Well M13S (close to the EBR-1 facility) exerted the greatest impact in terms of changing the simulated water levels from the IRA model. This optimized set of aquifer permeabilities was used in predictive modeling for the ABRA. The final optimized aquifer permeability set was a combination of the permeabilities and distribution used in the IRA model and the permeabilities and distribution from the WAG 10 model (McCarthy et al. 1995). A difference from the IRA model was that no vertical variation in aquifer permeability was included.

Resulting relative average linear groundwater velocities (also known as seepage or pore velocities) in the uppermost layer are shown in a vector plot in Figure 5-41 for the base and refined domain. Results for successively deeper model layers are essentially identical, given no vertical permeability contrasts in the model. The size of the vectors from each grid point is drawn on a scale relative to the maximum velocity in the model. The bottom plot in the figure is for the refined grid and has velocities in meters per year overlaid at each grid block. The dominant influence of the low-permeability zone to the south and southwest of the SDA can be seen in the results, especially in the refined grid. Water movement is effectively blocked by the low-permeability region and has to diverge around the low-permeability zone. This divergence results in simulated westward velocities just to the northwest of the SDA and simulated southeastward velocities beneath the eastern half of the SDA.

As part of this aquifer calibration effort, kriged permeability distributions based on single-well pump-test results were tested. Kriged aquifer permeability distributions were taken from Leecaster (2002). However, short spatial correlation range and limited data points restricted the accuracy of the kriged aquifer permeabilities and did not result in an accurate prediction of water levels. These results are not shown in this section but are contained in Whitmire (2001).

Possible influences on aquifer velocities from Big Lost River water discharged to the spreading areas were also investigated. Two methods were used to apply additional water in the aquifer simulation and are shown in Figure 5-42. The period from December 1982 through June 1985 was selected for

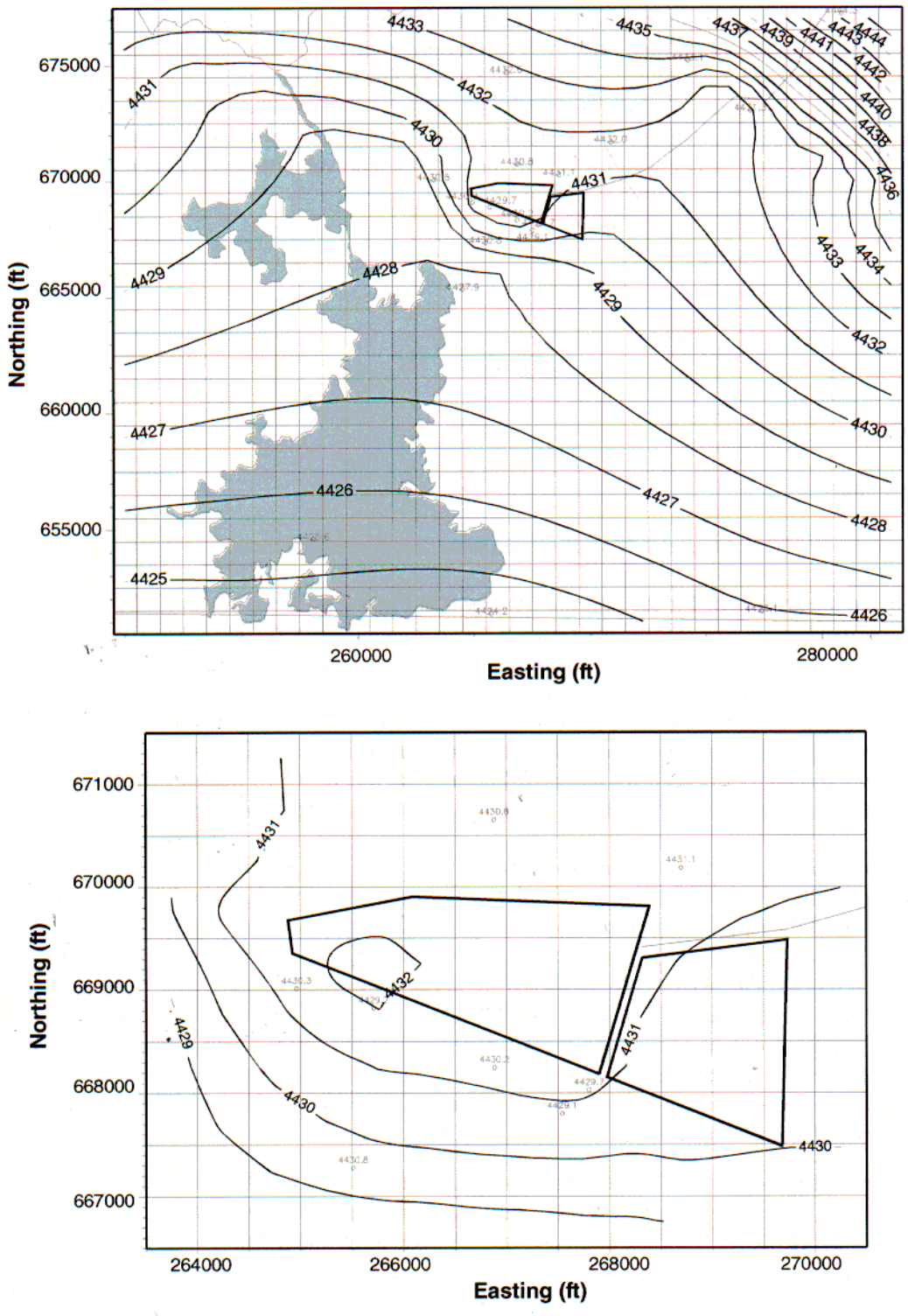

Figure 5-39. Best-fitted simulated water levels for base and refined grid.

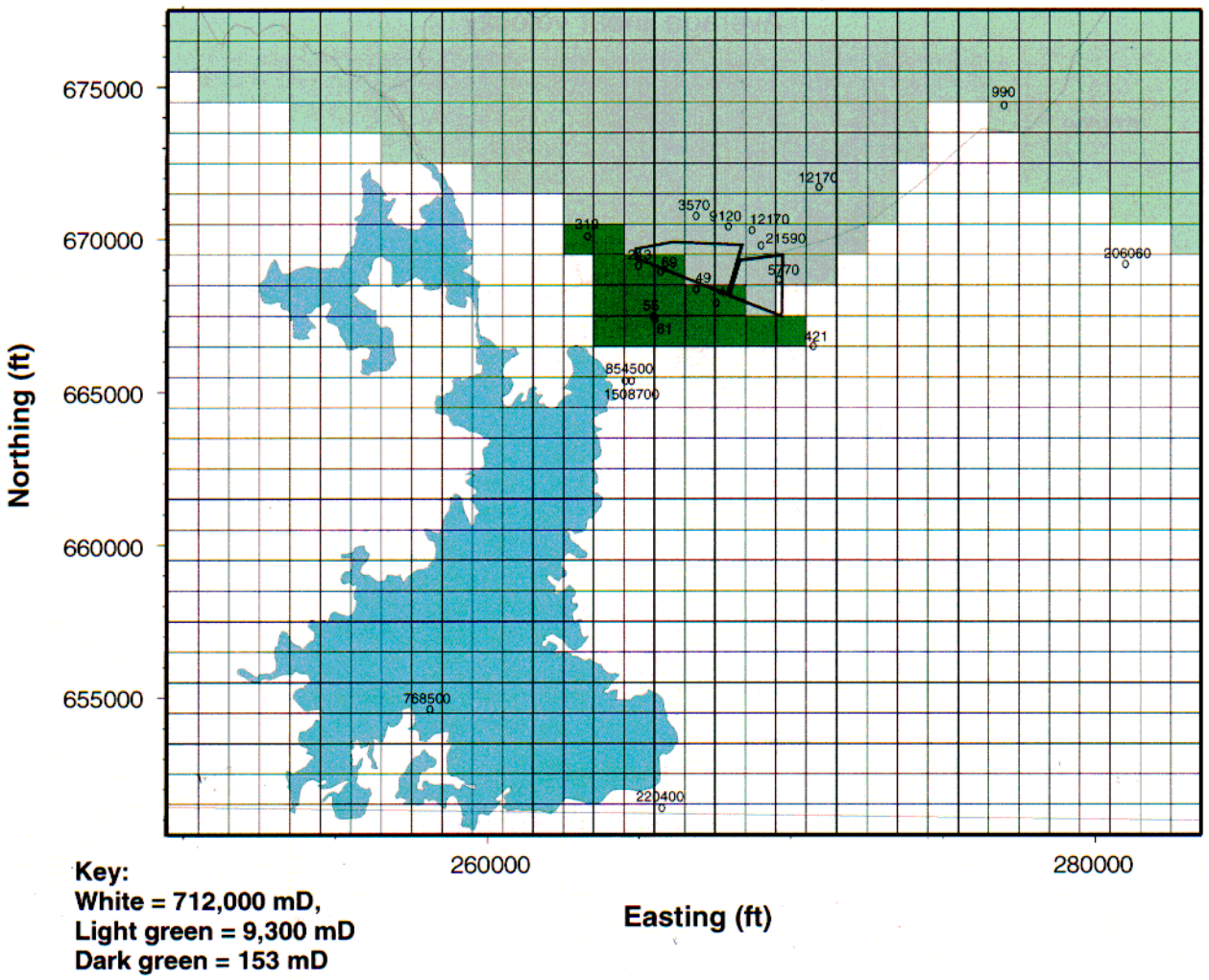

Figure 5-40. Final aquifer permeability set used for the baseline risk assessment model.

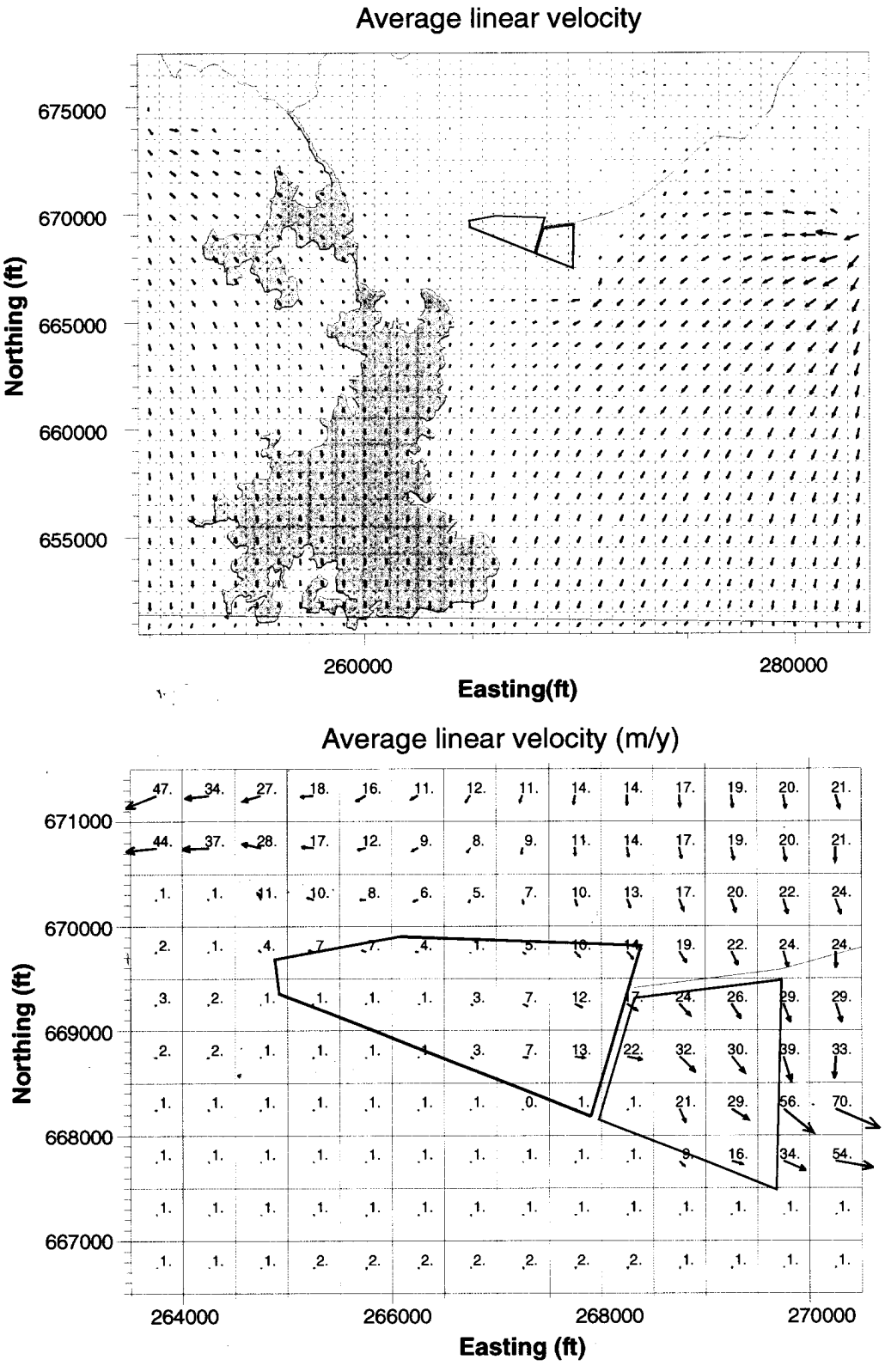

Figure 5-41. Simulated groundwater average linear velocities (m/year) for the base and refined simulation domains.

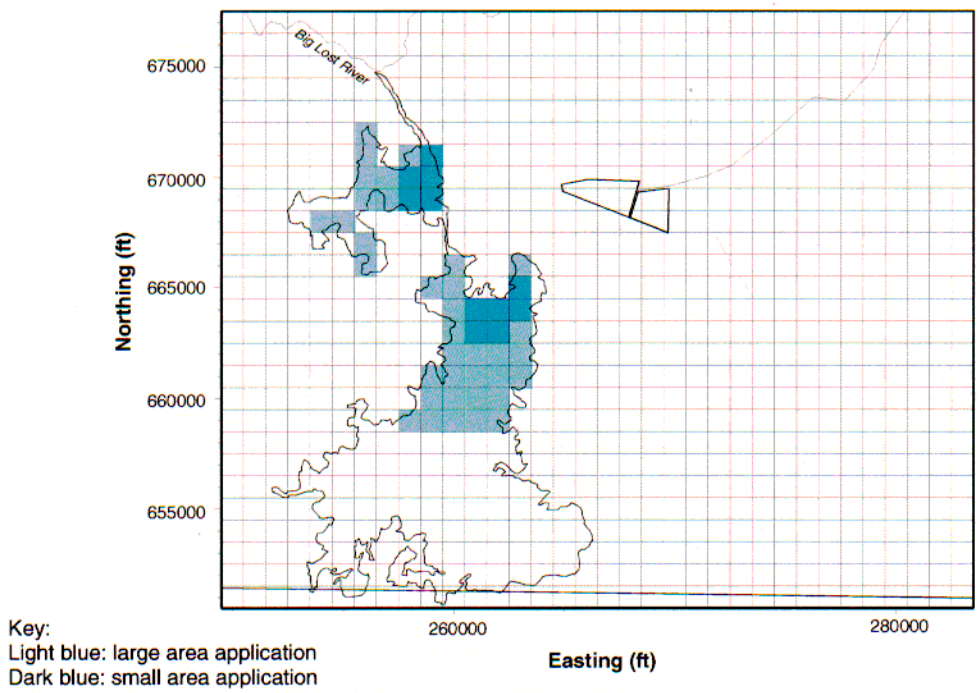

Figure 5-42. Large and small area application regions for spreading area water into the aquifer simulation domain.

simulation because water was diverted continuously to the spreading areas during this period. Average amounts of water discharged to both Spreading Areas A and B were determined based on the gauging results (see Figure 5-29) which show an overall approximate diversion from the river of 16,300 acre-ft/month during this period. In one scenario, this average discharge to the spreading areas was applied over 47 grid blocks to emulate the effect of the entire area of Spreading Areas A and B being filled. This was termed the "large area application." In the second method, the same amount of water was applied over just 11 grid blocks and was termed the "small area application." These water fluxes are applied directly to the top of the aquifer model as if the water transit through the vadose zone was instantaneous and no water was lost either to storage within the vadose zone or to evaporation. Though the modeling for these spreading area simulations was originally performed in Whitmire (2001), the spreading area impact results presented in this section are somewhat different because an implementation error was discovered that resulted in significantly less water being applied than was intended. In this section, the intended fluxes shown in Table 5-15 are applied continuously throughout the period in a step-wise fashion.

Table 5-15. Water fluxes (m/day) applied in spreading area simulations.

Water Flux	Spreading Area A	Spreading Area B
Large area application	0.29	0.97
Small area application	0.091	0.19

Simulated water levels for November 1984, near the end of the application of the spreading-area water, are shown for both cases in Figures 5-43 and 5-44. The same March 2000 water level measurements are still included on these figures for reference. In each case a substantial groundwater mound results. The simulated rise in water levels is partly substantiated by the water level measurements from that period (Wood 1989). Table 5-16 shows measured water level rises in four SDA-vicinity wells

during the period 1982 to 1985 based on the hydrographs presented in Wood (1989). The simulated mound is in part limited by the first-type boundaries prescribed at the perimeter of the model. Ideally, the boundary conditions should not impact this simulation and partially limit the results. Well 88 is included in the table, though its rise is considered abnormal (Wood 1989).

Table 5-16. Measured and simulated rises in water level for wells in the vicinity of the Radioactive Waste Management Complex during 1982 to 1985 spreading area diversions.

Well	Measured Gross Water Level Rise (ft)	Ancillary Basis for Risk Analysis Model Water Level (ft)	Large Area Application Water Level (ft)	Large Area Application Water Level Rise (ft)	Small Area Application Water Level (ft)	Small Area Application Rise in Water Level Rise (ft)
USGS-87	11	4,431.5	4,436	4.5	4,437.5	6
USGS-89	20	4,429	4,440	11	4,444	15
USGS-90	12	4,430.5	4,434.5	4	4,435.5	5
USGS-88	80	4,429.5	4,439.5	10	4,443	13.5

Rises in the simulated water level, based on comparing the large and small spreading area application simulations to the ABRA model, are shown in Table 5-16 for comparison to the measured rise in water level. Though the simulated rises are less than the observed rises, they show similar characteristics. Simulation could possibly be improved by (a) more closely matching actual discharges to the spreading areas instead of using an averaged step-function, and by (b) either moving simulation boundaries farther away so they do not impact the results or by modifying boundaries temporally to reflect regional changes in water levels.

The resulting velocity distribution in the refined portion of the aquifer grid for these two spreading area impact simulations is shown in Figure 5-45. Comparing velocities shown previously in Figure 5-41 for the ABRA aquifer simulation shows the increase in the magnitudes of groundwater flow velocity beneath the eastern portion of the SDA when additional water was input into the aquifer at the spreading areas; however, directions shift only slightly and still generally trend southeast. As expected, flow velocity magnitudes increase more when input from the spreading areas is concentrated into a smaller region. In both cases, westward velocities are reversed northwest of the SDA.

In summary, relative to the aquifer flow model calibration, the flatness of the water table coupled with an apparent low permeability region to the south-southwest of the SDA precludes accurate determination of groundwater flow directions. The IRA hypothesis that the flow velocities immediately under the SDA are slow is consistent with new evidence. Before the IRA model, water velocity beneath the SDA was treated as if it were the same as the regional aquifer, with average linear velocities of 0.15 to 4.6 m/day (0.5 to 15 ft/day) (Maheras et al. 1994). The ongoing tracer test in Well M17S immediately beneath the SDA has been showing a very slow dilution of tracers introduced directly into the well, indicating slow water movement within the aquifer at that location (see Section 2.3.3). This hypothesis is also consistent with the interpretation by Roback et al. (2001) that the RWMC is in a low-permeability region extending southerly from the Lost River Range onto the INEEL. Additional water levels collected during the ongoing WAG 7 quarterly monitoring program will be a key part of conclusively determining the direction and timing of aquifer flow velocities in the SDA region. The use of isobaric techniques may be beneficial in making more accurate quarterly water level measurements in a manner uninfluenced by atmospheric pressure fluctuations.

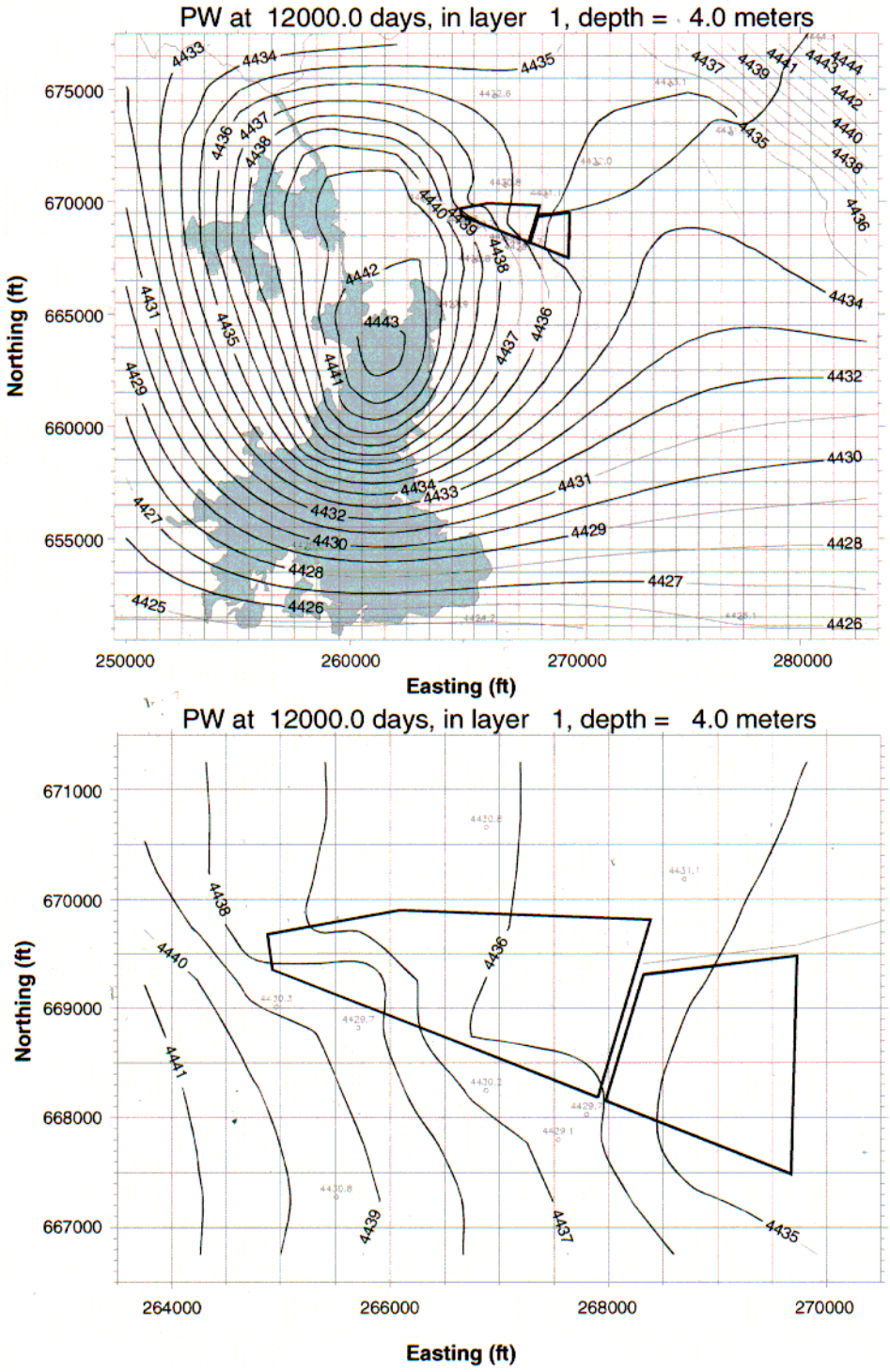

Figure 5-43. Simulated water levels for the base and refined aquifer domain for the large area application of spreading-area water.

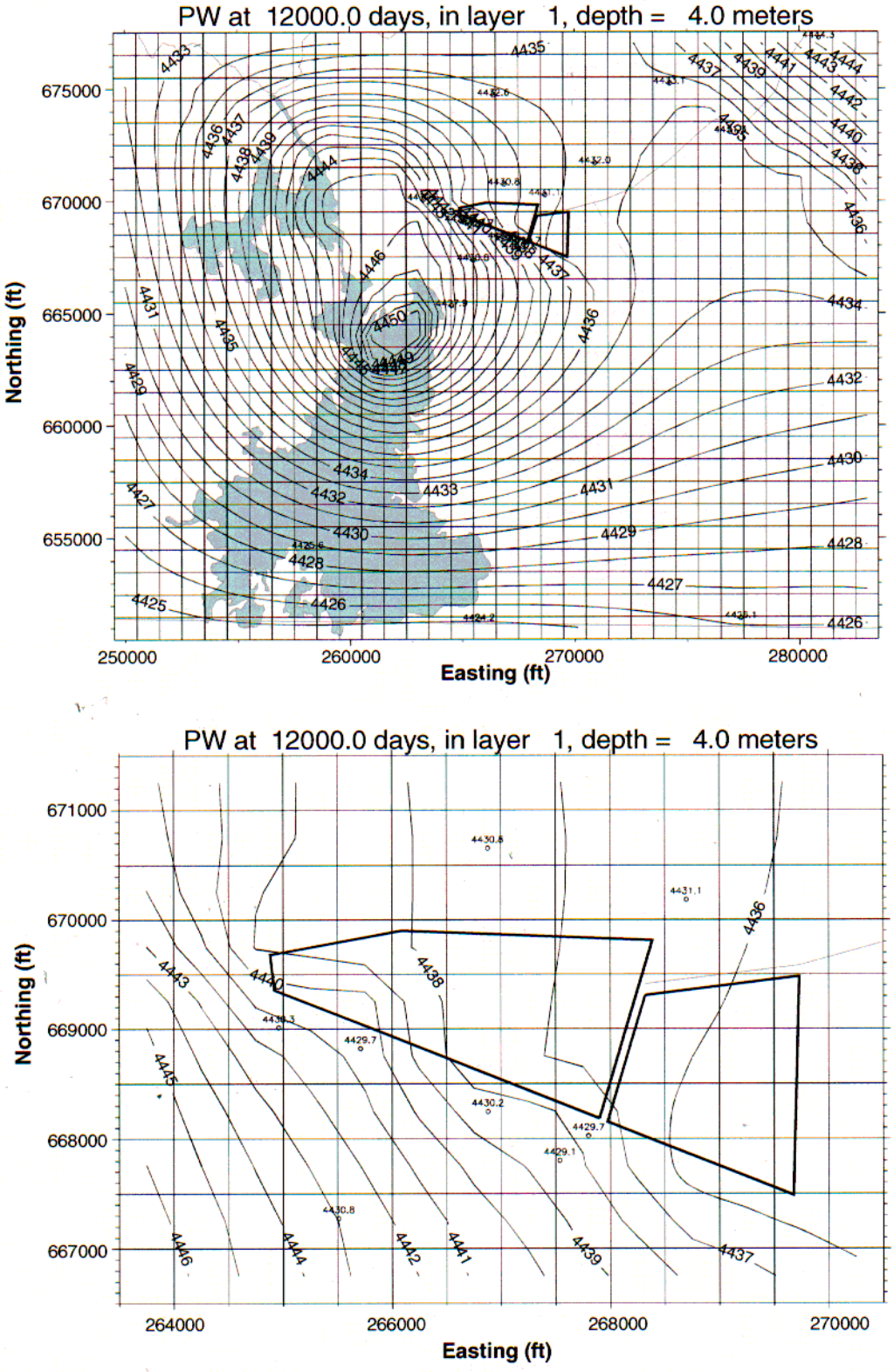

Figure 5-44. Simulated water levels for the base and refined aquifer domain for the small area application of spreading-area water.

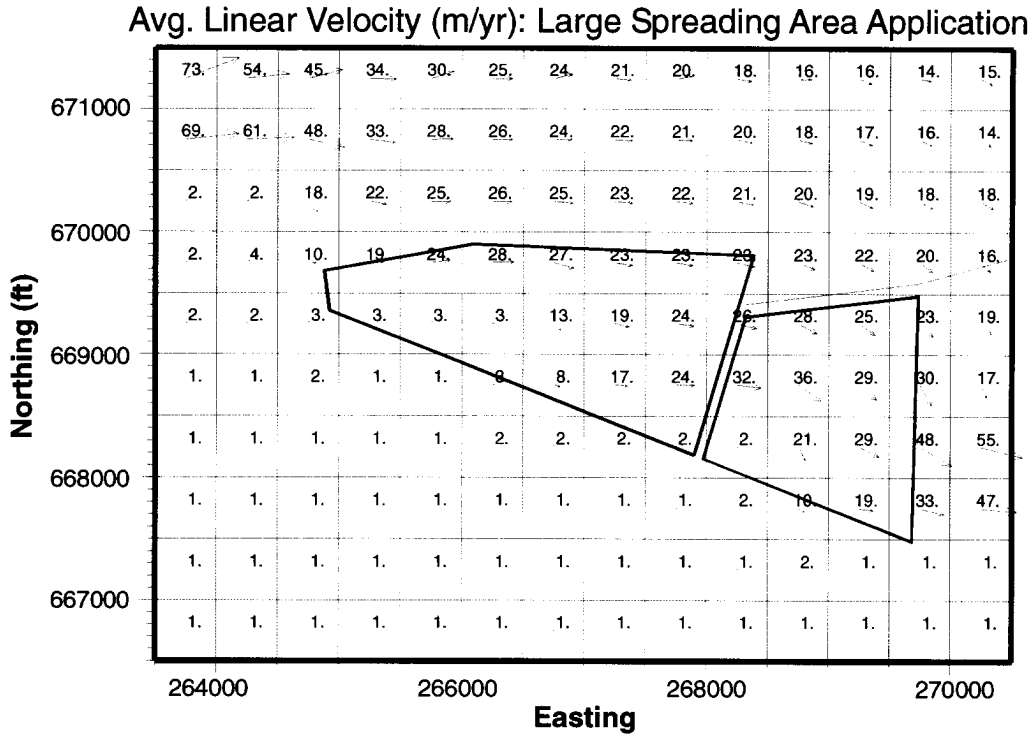

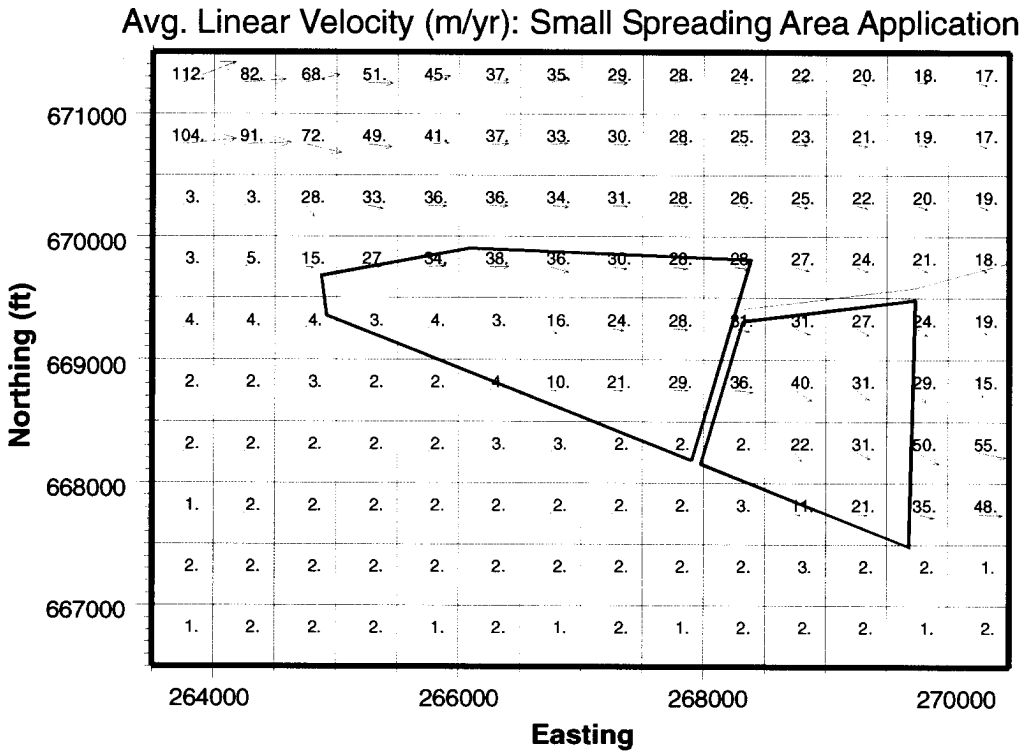

Figure 5-45. Simulated groundwater average linear velocities (m/year) in the refined simulation domain with additional water applied at the spreading areas.

5.2.4.6 Aquifer Transport Model. Simulating transport in the aquifer model was straightforward compared to the vadose zone. The flux of water and contaminants from the vadose zone model was applied as an upper boundary condition in the refined portion of the model. The remainder of the upper surface of the model was treated as a no-flux area, as was the bottom surface of the model. Contaminants could advect out external boundaries.

Because it was assumed that sorption did not occur within the fractured basalts, and only fractured basalts were simulated in the aquifer portion of the model, no K_d values were necessary in the aquifer portion of the model. Diffusion was included and was parameterized the same as in the vadose zone model. Tortuosity was assigned using the same approach as in the vadose zone model (i.e., following the approach in Lerman [1988]). Dispersion was parameterized differently in the aquifer model than in the vadose zone model. Longitudinal and transverse dispersivities of 9 and 4 m (30 and 13 ft) were assigned, respectively. These values were the same as those used in the IRA model. Similar to the vadose zone model, assigned dispersivities are small relative to the 1/10th domain size general rule of thumb. However, because dispersion control was not used in the TETRAD simulation, the relative contribution of numerical dispersion compared to simulated dispersion is unknown.

In the remainder of this section are comparisons of simulated and observed nitrate and chromium concentrations. These two contaminants are chosen for scrutiny because they offer the most insight into how the model results compare to data. Both contaminants are conservative in that they do not adsorb and, thus, avoid the complication of assigning a K_d.

5.2.4.6.1 Comparison of Simulated and Observed Nitrate Concentrations—This section shows comparisons of simulated results and monitoring results for nitrate as elemental nitrogen. Emphasis is on aquifer results because that is where the longest-term monitoring has occurred. Both time history and contour plots are presented to show spatial resolution. Nitrate is a ubiquitous chemical in groundwater; background concentrations must be considered even though it is assumed for the ABRA modeling that contaminant concentrations in the vicinity of the SDA are not influenced by upgradient sources. The local background concentration was previously estimated as 0.7 mg/L (Burgess 1996). For the time history plots shown in Figure 5-46, the simulation results are added to this background concentration. Time history plots are all shown with a consistent time axis and a consistent concentration axis. The value selected for the maximum on the concentration scale was the maximum observed in field monitoring data. In some cases, predicted values extend above the concentration axis.

These same 16 time histories, with an additional time history for Well 120, are shown again in Figure 5-47 superimposed onto a plan-view map showing their locations with respect to the SDA. As can be seen in the figure, nitrate is sometimes over predicted and sometimes under predicted. Ignoring for the moment the complexity of flow and transport in the vadose zone, nitrate monitoring results in Figure 5-47 highlight what is obviously a complex flow system in the aquifer. Monitoring data for nitrate are not spatially consistent. It is tempting to interpret an influence in aquifer nitrate monitoring results from the Big Lost River water that is discharged into the spreading areas. This could explain elevated concentrations of nitrate above the interpreted local background in Wells 89, M1S, and 88, which are closer to the spreading areas. Concentration of nitrate in Well M4D differs from that in Well 88 but that can be explained by the screened interval being much deeper in Well M4D and, therefore, Well M4D samples were obtained from a different portion of the aquifer. However, by this logic, Well 120 should also show elevated nitrate concentrations above the local background and it does not. Wells M10S and 119 show slightly increased concentrations of nitrate, which may be caused by migration of nitrate disposed of in the SDA. Well M17S, located directly beneath the SDA, has shown no elevated nitrate concentrations in its short monitoring history. Wells 87, M3S, the RWMC Production Well, M7S, M16S, 90, and M15S all show nitrate concentrations consistent with the estimated local background concentration of 0.7 mg/L. Well M6S, located approximately 914 m (3,000 ft) to the southeast of the

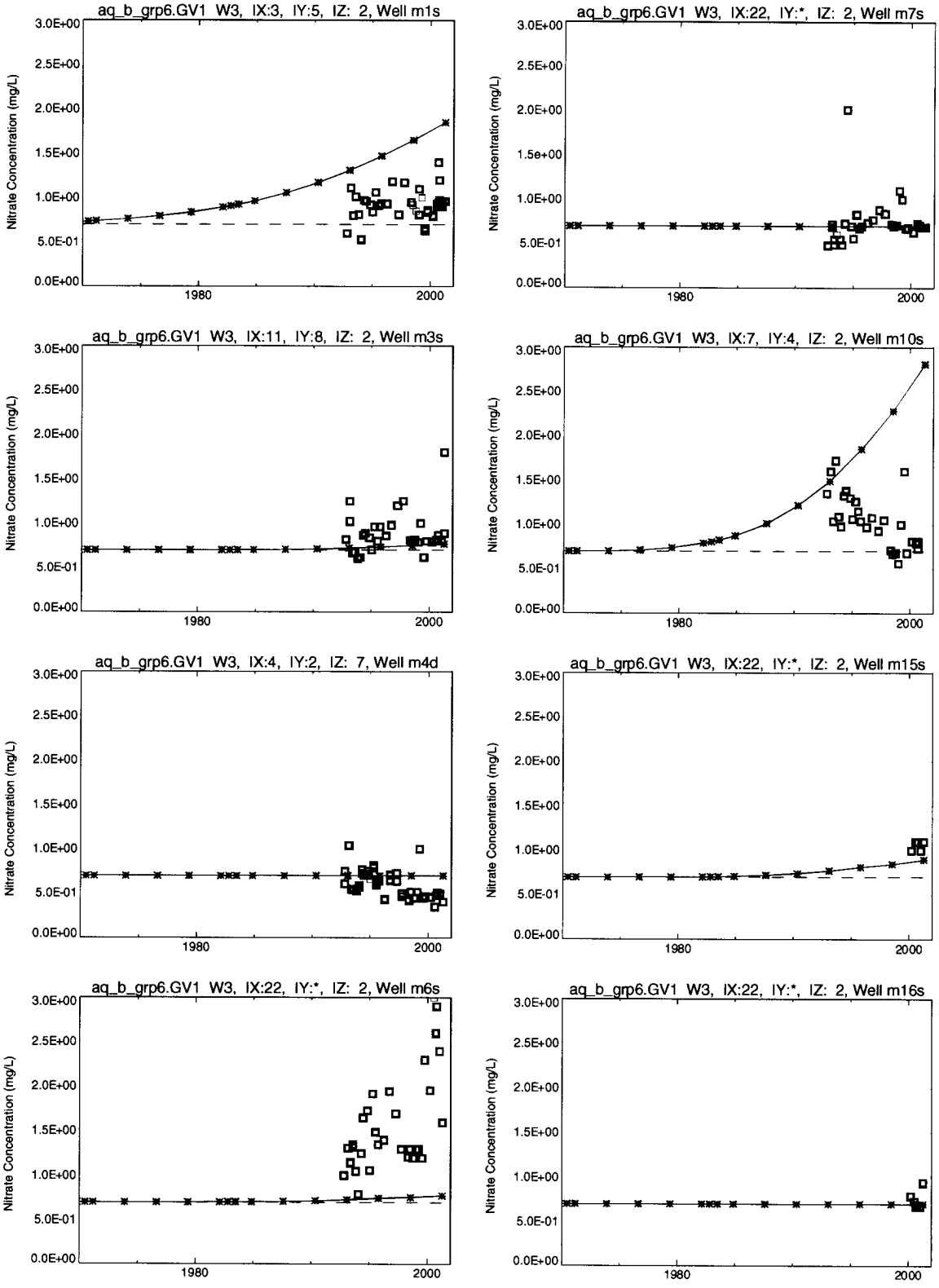

Figure 5-46. Comparison of simulated and observed nitrate (as N) concentration time histories for aquifer monitoring wells in the vicinity of the Subsurface Disposal Area.

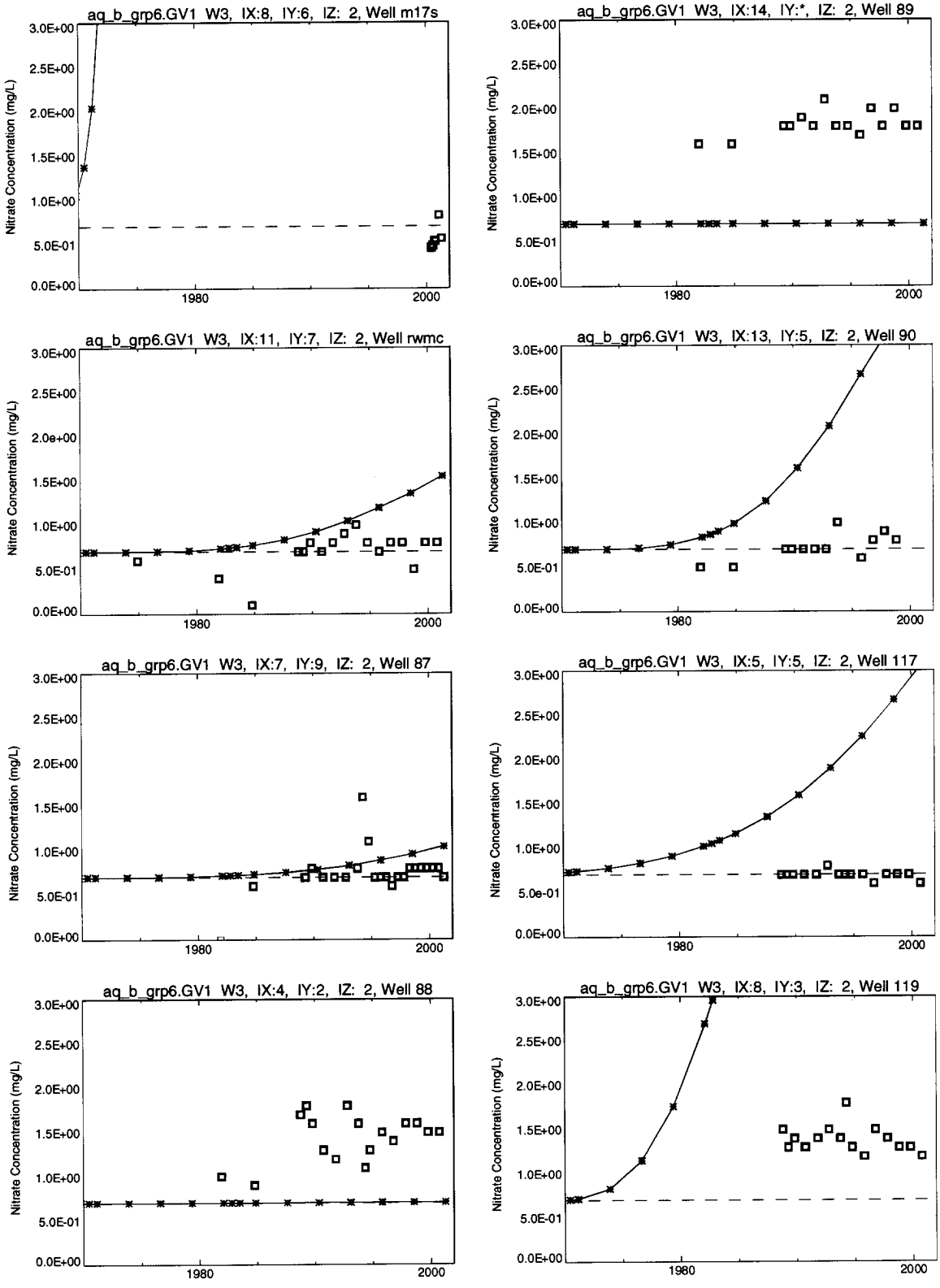

Figure 5-46. (continued).

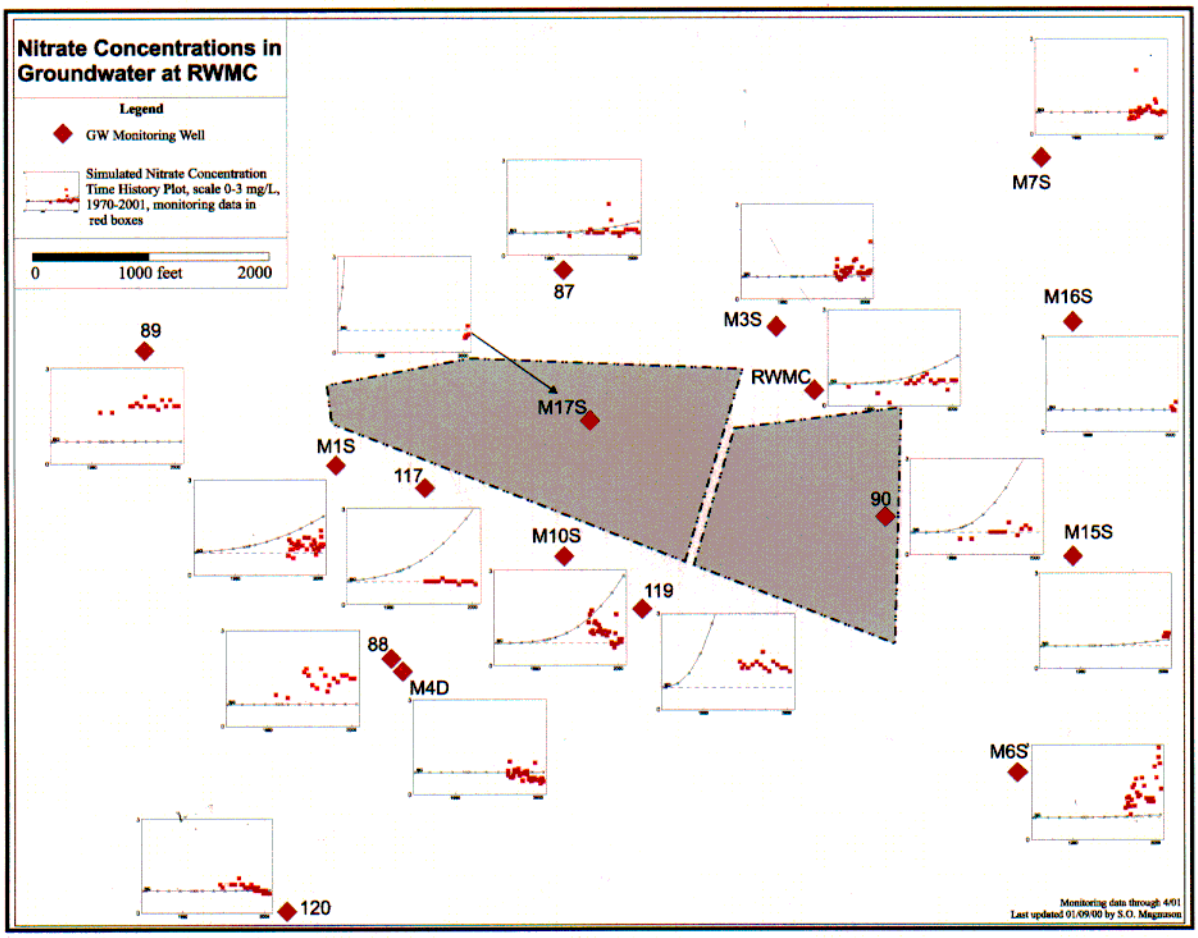

Figure 5-47. Simulated and observed nitrate concentrations superimposed onto monitoring locations in the vicinity of the Radioactive Waste Management Complex.

SDA, also shows elevated concentrations and the most likely increasing trend that can be identified in any RWMC vicinity wells. Most of these monitoring data are consistent with the conceptual model of the aquifer flow system being dominated by a low-permeability region to the south and southwest of the SDA that directs flow eastward around the low permeability system. Well 117 data are contradictory, which may be caused by very low formation permeability at this location limiting communication with the nitrate contaminant plume and resulting in elevated concentrations at Wells M10S and 119. A contour plot of the simulated nitrate concentrations in calendar year 2001 is shown in Figure 5-48 for both the base and refined aquifer simulation domain. The estimated local background of 0.7 mg/L is not added to the simulation results in this figure. The simulated results are similar to those predicted for nitrate in the IRA model (Magnuson and Sondrup 1998).

In comparing simulation results to monitoring results, concentrations are over predicted in Wells M1S, 117, M10S, and 119 immediately south of the SDA; in Well M17S inside the SDA; and in Well 90 and the RWMC Production Well east of the SDA. Concentrations are under predicted in Well M6S to the southeast of the SDA. The observed high nitrate concentrations at the Well M6S aquifer monitoring location are the only monitoring results that appear to show an increasing trend. An eastward component exists in the simulated aquifer water velocities under the eastern portion of the RWMC that results in the simulated nitrate concentrations increasing at the grid block representing Well M6S. However, the simulated concentrations had just barely begun increasing by calendar year 2001. Other factors also contribute to the under prediction at the location of Well M6S. This location is just outside

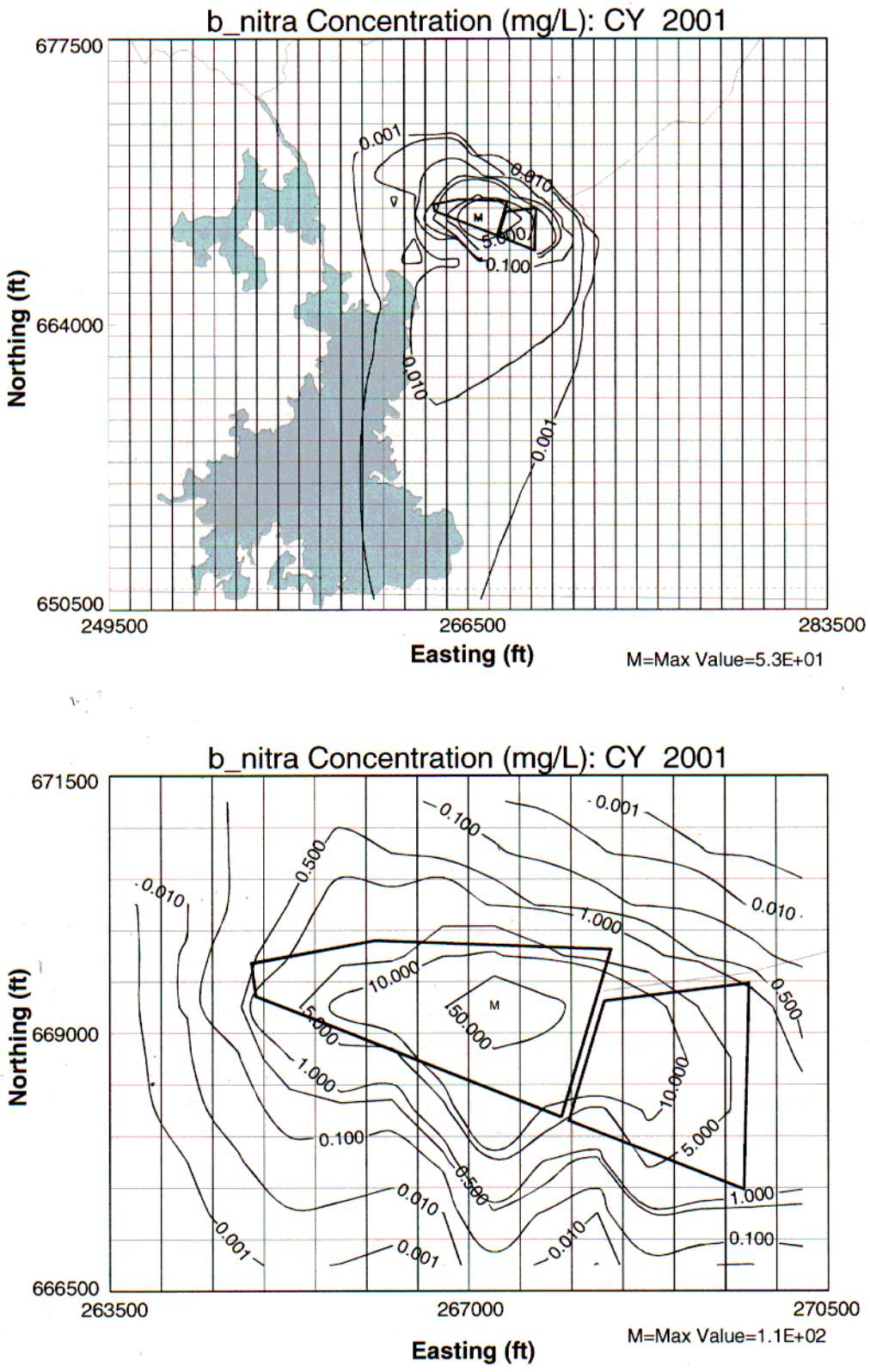

Figure 5-48. Simulated aquifer nitrate concentrations for calendar year 2001.

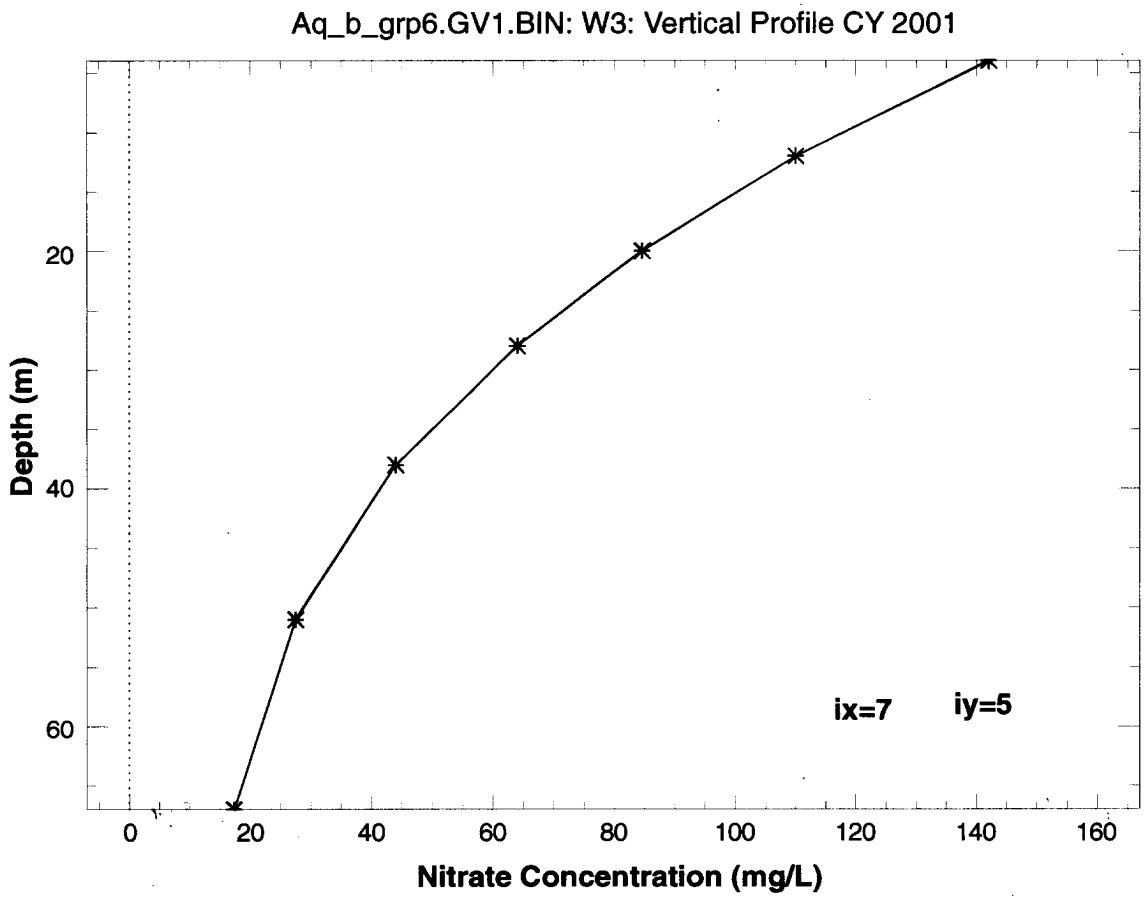

Figure 5-49. Simulated aquifer nitrate concentration profile beneath the Subsurface Disposal Area for calendar year 2001.

the area of grid refinement, so the concentrations are averaged over a grid block volume four times as large. In addition, the low-permeability region is simulated as if it extends almost to the M6S location. This causes simulated contaminants to continue to migrate eastward around this location.

A vertical profile of simulated nitrate concentrations in calendar year 2001 is shown in Figure 5-49. The concentrations decrease throughout the profile at each of the seven grid blocks representing the aquifer. As discussed below, concentrations used for determining risk are taken from the second grid block down, based on the typical screened interval in wells.

Calibration of simulated nitrate concentrations to the observed aquifer nitrate concentrations was not attempted for these simulations. Rather, simulations for both the vadose zone and the aquifer were developed based on best-available information. The only calibration consisted of optimizing agreement between the simulated and observed aquifer water levels. Simulations were then run once in a forward mode. With the exception of Well M6S, simulated concentrations at all locations are either over predicted when compared to measured values, or match measured values as long as the estimated background concentration of 0.7 mg/L is assumed. Except for the under prediction at Well M6S, it would be possible to make a claim of conservatism for the transport model. Well M6S is located farthest southeast of the SDA and, therefore, the well most likely to be affected by an upgradient facility influence, if such an influence exists.

Obviously, the system is more complex than has been represented in the model. However, the model does provide a foundation for explaining most of the observed behavior and, thus, meets the goal of general representability. There is, however, substantial uncertainty associated with the results because of what is not explained by the model. This discussion has focused on the subsurface flow and transport model and does not address the lack of calibration for the source term model (see Section 5.1). Results of the subsurface model are highly sensitive to the source-term inputs.

5.2.4.6.2 Comparison of Simulated and Observed Chromium Concentrations—

Chromium is another contaminant that was buried in the SDA for which transport was simulated. In these transport simulations, chromium was assumed to remain in the mobile hexavalent state. Though chromium is not considered as a COPC in the ABRA, an examination of how the subsurface model predictions for chromium compare to measured values is useful. Time histories of simulated chromium concentrations are compared to observed aquifer concentrations in Figure 5-50. The monitored concentrations are inferred to represent hexavalent chromium also. The time history plots are all scaled consistently to the maximum observed field value, which was just under 100 μg/L in Well M3S. Similar to the time history plots for nitrate concentrations, the simulated chromium concentrations are added onto the estimated regional background concentration of 2.5 μg/L for the Snake River Plain Aquifer (Orr, Cecil, and Knobel 1991). Only simulated chromium concentrations for Well M17S begin to be discernable above background for the 1970 to calendar year 2001 timeframe presented in Figure 5-50. The maximum simulated chromium concentration anywhere in the aquifer through calendar year 2001 is 3.7 μg/L, including background. This is approximately an order of magnitude greater than the maximum simulated chromium concentration through the same period for the IRA model. Both models under predict observed values.

Field data for chromium are all greater than the reported background value, which gives rise to several interpretations. Elevated chromium concentrations could indicate that either the local background is greater than indicated in Orr, Knobel, and Cecil (1991) or that the SDA may be contributing to elevated chromium concentrations in these monitoring wells. Conversely, elevated chromium concentrations could imply that the interpretation is incorrect that SDA-vicinity aquifer concentrations are not affected by upgradient facilities such as the TRA.

5.2.5 Base Case Simulations for the Baseline Risk Assessment

The model developed for the ABRA was run for each COPC. This section presents concentration results from those simulations and makes comparisons to observed values. Results are presented graphically as time history comparisons to field monitoring results at grid locations representing SDA aquifer monitoring wells (Figures 5-51 through 5-57). In contrast to results presented previously for nitrate and chromium, no background concentration is added to these simulation results. Local background concentrations are zero for the COPCs presented in Figures 5-51 through 5-57, based either on evaluations in Section 4 or in Orr, Cecil, and Knobel (1991). Results also are presented below in a table comparing simulated maximums through calendar year 2001 to observed values. Refer to Figure 5-47 when locating wells indicated in the figures. Monitoring results for radionuclide COPCs that represent 3σ detections or greater are included as blue diamonds on the time history plots along with a whisker-style indication of their associated 1σ uncertainties. In cases where analyses were performed but no COPCs were detected, nondetects are plotted in red at the extreme lower bound of the plot. Simulation results are portrayed as a continuous line with black asterisks. Simulation results representing all wells, except Well M4D, are taken from the second slice down in the aquifer model. Well M4D is unique in that it is screened much deeper, so simulated concentrations from deeper in the model are used. The second slice of grid blocks was from a depth of 8 to 16 m (26 to 52 ft) in the aquifer domain and is similar to

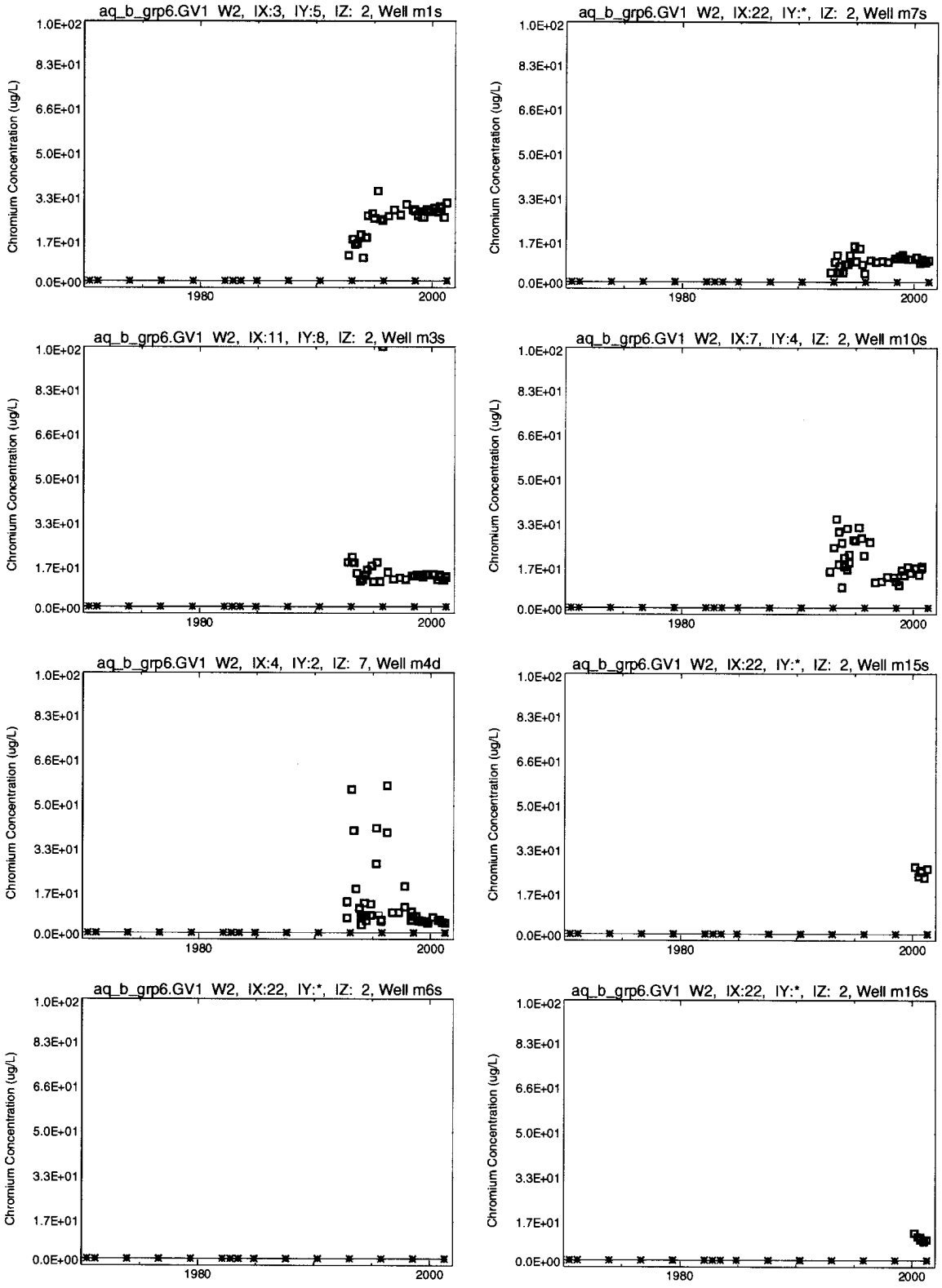

Figure 5-50. Comparison of simulated and observed chromium concentration time histories for aquifer monitoring wells in the vicinity of the Subsurface Disposal Area.

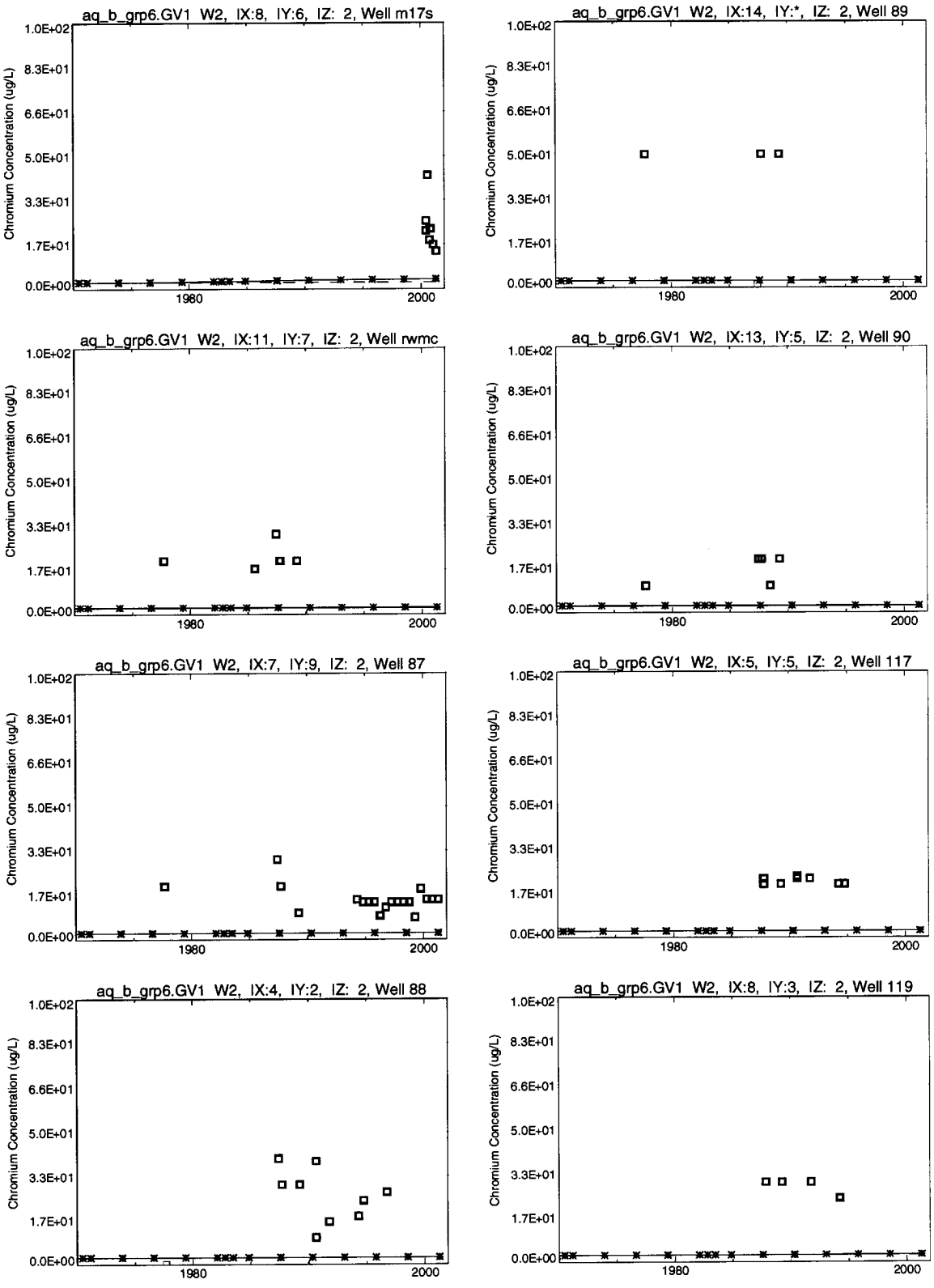

Figure 5-50. (continued).

most of the screened intervals in the monitoring wells. As such, simulated concentrations represent concentrations at a depth of 12 m (39 ft) below the water table.

Results in Figures 5-51 through 5-57 highlight the erratic nature of detections compared to the majority of nondetect results. Sporadic detections include low-level actinide concentrations that are just at instrument detection limits and may be false-positives.

Table 5-17 lists maximum simulated concentration anywhere in the aquifer through calendar year 2001 for chromium and all human health COPCs and their long-lived decay-chain progeny. No background concentrations are added to any of the simulated results. Almost all of the simulated peak values in Table 5-17 occur during calendar year 2001, indicating that concentrations were still increasing at that time. Two exceptions were Pu-238, which was simulated to not be in the aquifer anywhere at any concentration, and Cl-36, which peaked earlier in 1994. For comparison, the corresponding maximum simulated chromium concentrations through 1995 from the IRA model are given in the third column of the table. Estimated background concentrations from Knobel, Orr, and Cecil (1992) are shown in the fourth column of the table. Uranium isotopes were estimated from proportioning the total uranium background concentration of 3 μg/L contained in Knobel, Orr, and Cecil (1992) into the respective isotopes in accordance with their known specific activity and isotopic abundance (weight percent) known to exist in nature. The last two columns present the range of observed values taken from the nature and extent discussion in Section 4 along with comments concerning some of those values. Observed values from earlier than 1987 are not presented in Table 5-17. Numerous COPCs do not have corresponding analyses, as indicated in the table.

Changes in simulated values between the ABRA model and the IRA model result primarily from the following: (a) differences in the use of best-estimate and revised inventories, (b) different source release rates for activation and fission products attributable to changes in the assigned corrosion rates, (c) use of smaller partition coefficients for C-14, (d) differences in simulated water travel times through the vadose zone caused by including spatially variable hydrologic properties for the B-C and C-D interbeds, and (e) the conformable gridding approach. Regarding the latter, using a conformable grid most likely resulted in less numerical dispersion because of improved uniformity of grid sizes across lithologic interfaces. Less numerical dispersion would result in lower simulated concentrations for those contaminants that strongly adsorb, such as Am-241 and the plutonium isotopes, because a contaminant would not be artificially "smeared" ahead of its advective front.

In comparing simulated results from the ABRA model to the range of observed 3σ detections or the background concentrations, several patterns emerge. Simulated aquifer concentrations for fission products (i.e., Tc-99 and I-129) and the activation products (i.e., C-14 and Cl-36) are all over predicted to varying degrees compared to observed monitoring results. This over prediction is thought to be more likely caused by inadequacies in the source release model than in the subsurface flow and transport model. Monitoring results for U-234, U-235, and U-238 are similar to reported background values. Simulated uranium isotope values are slightly less than observed values or background values, indicating that simulated anthropogenic uranium is migrating but has not reached the aquifer in high enough concentrations to be detected yet. All other contaminants are predicted to be either not in the aquifer yet or to be present at concentrations below detectable levels. If it is assumed that background concentrations for anthropogenic radioisotopes are zero for those contaminants not explicitly identified in Knobel, Orr, and Cecil (1992), then model results are in agreement with nondetections for this last group of contaminants. This statement disregards sporadic detections of plutonium isotopes and Am-241 as anomalies. At a minimum, for this latter set of contaminants, model results are not in conflict with observed results.

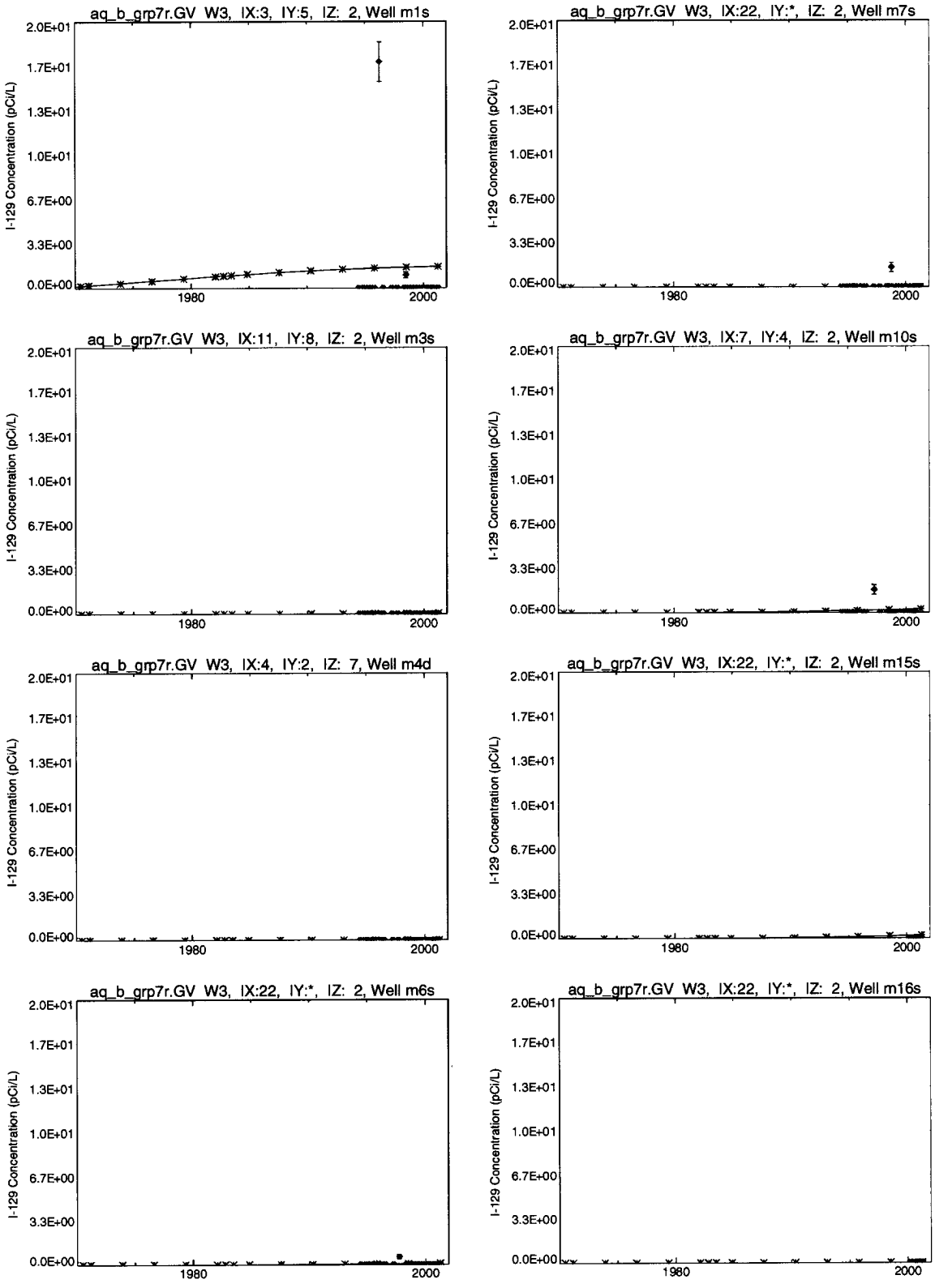

Figure 5-51. Comparison of simulated and observed I-129 concentration time histories for aquifer monitoring wells in the vicinity of the Subsurface Disposal Area.

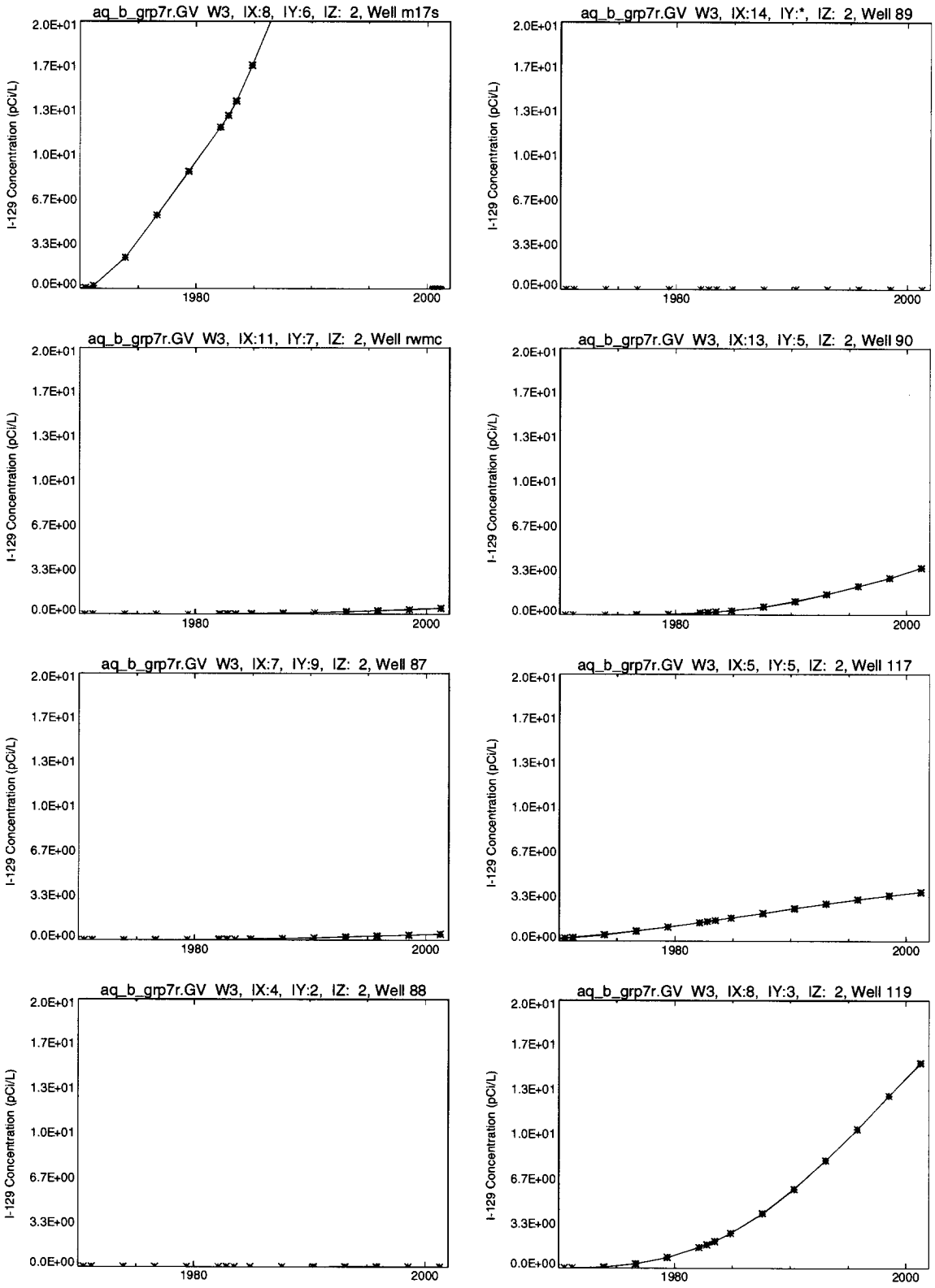

Figure 5-51. (continued).

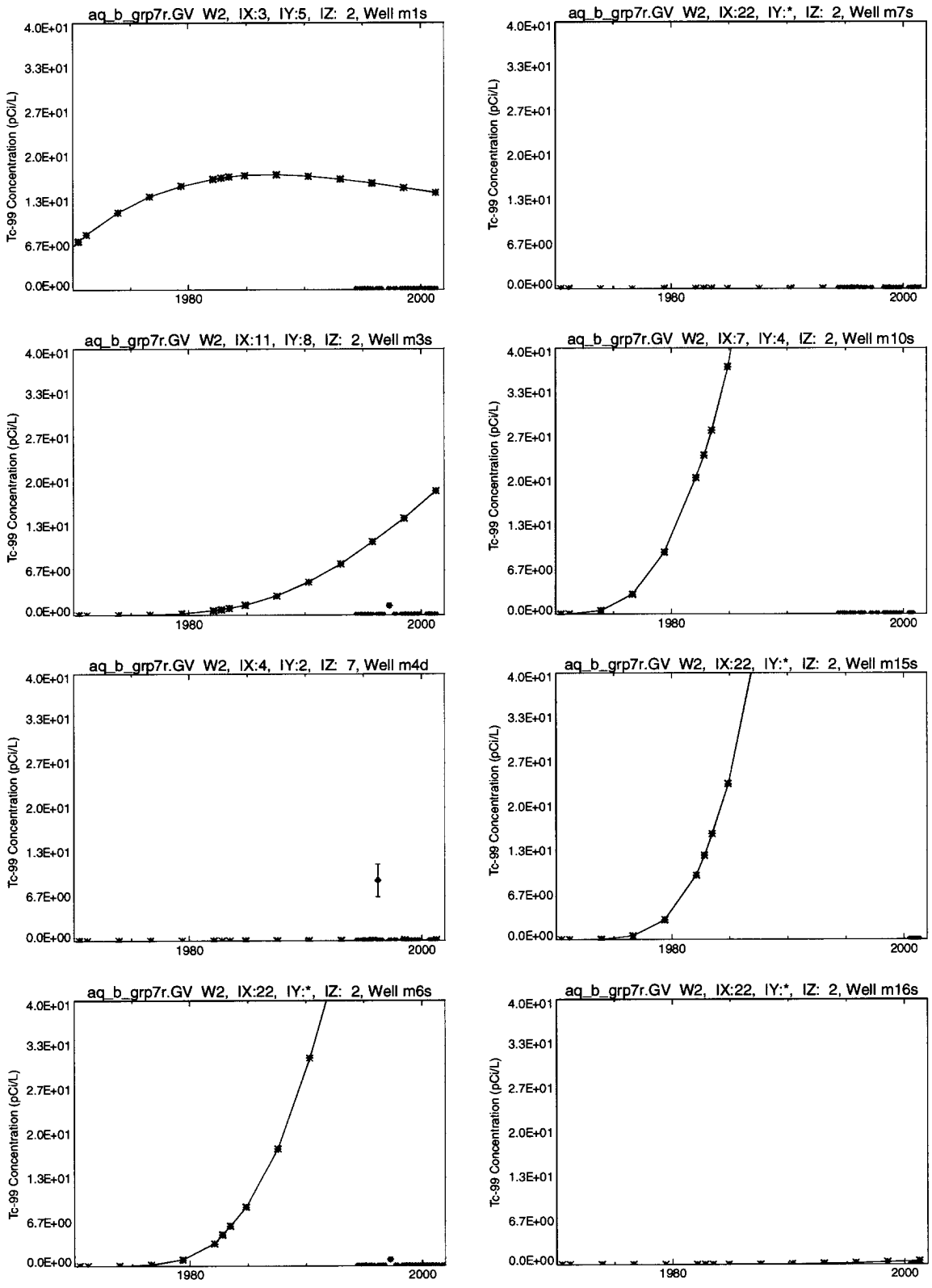

Figure 5-52. Comparison of simulated and observed technetium-99 concentration time histories for aquifer monitoring wells in the vicinity of the Subsurface Disposal Area.

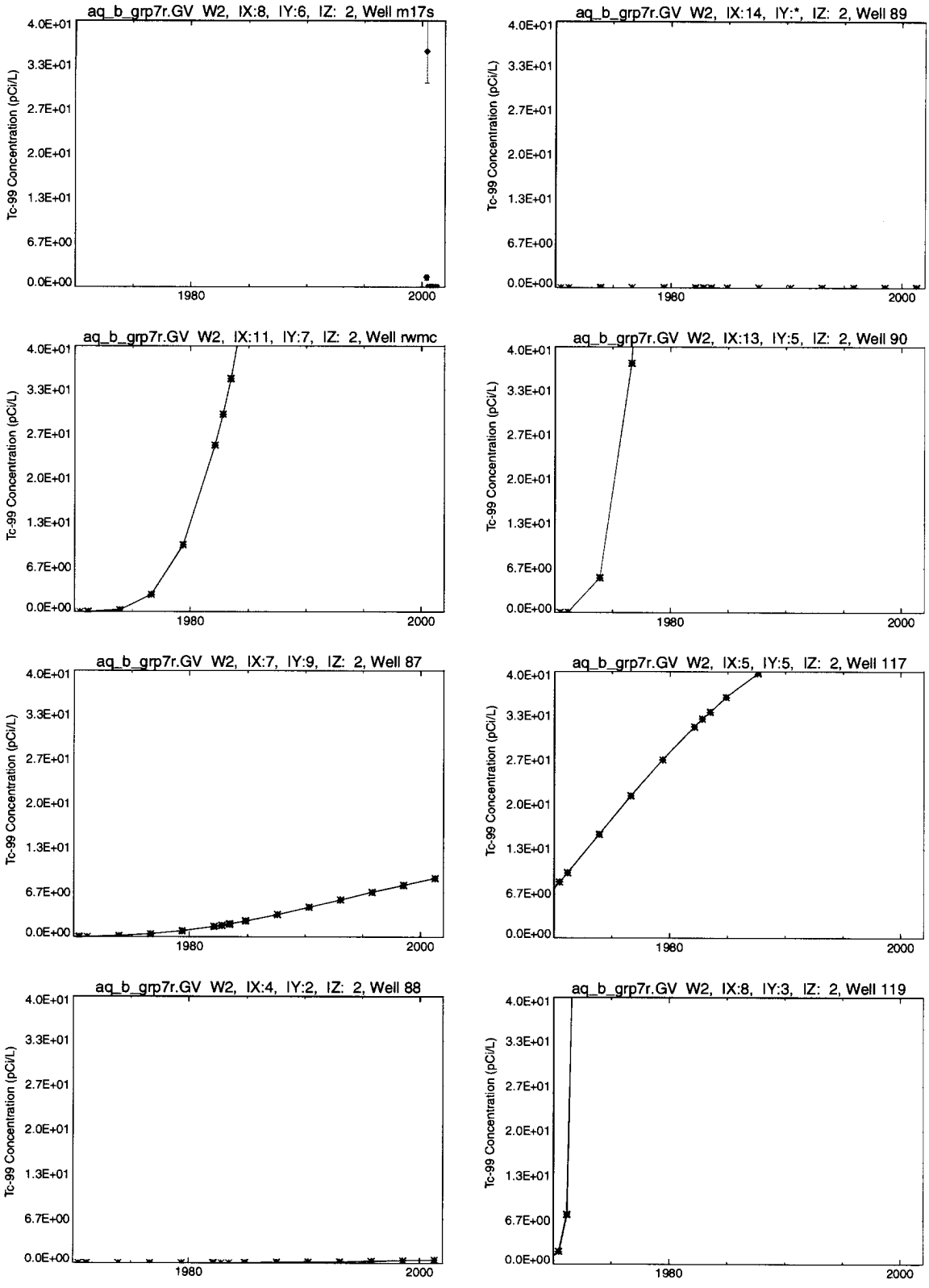

Figure 5-52. (continued).

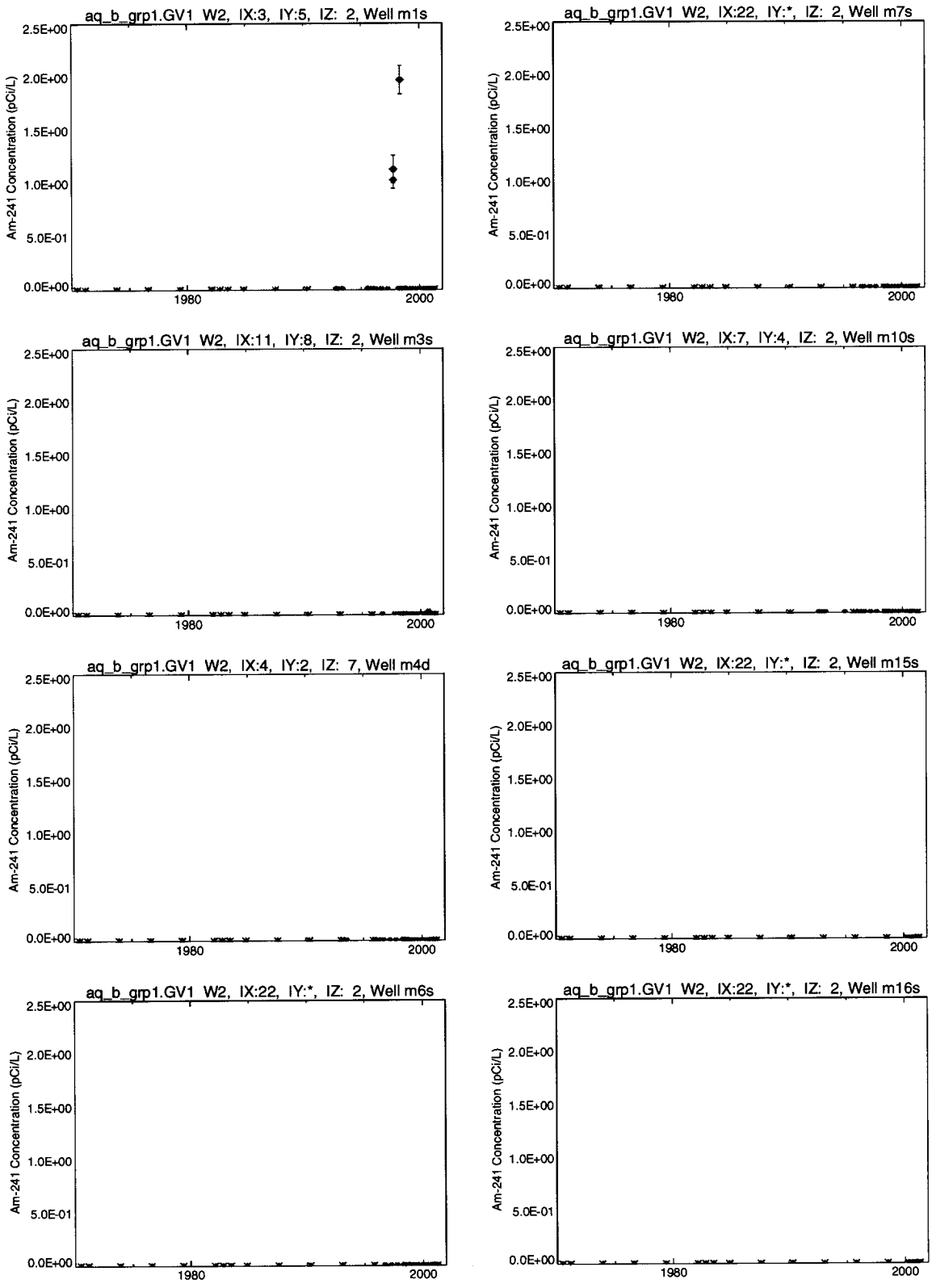

Figure 5-53. Comparison of simulated and observed Am-241 concentration time histories for aquifer monitoring wells in the vicinity of the Subsurface Disposal Area.

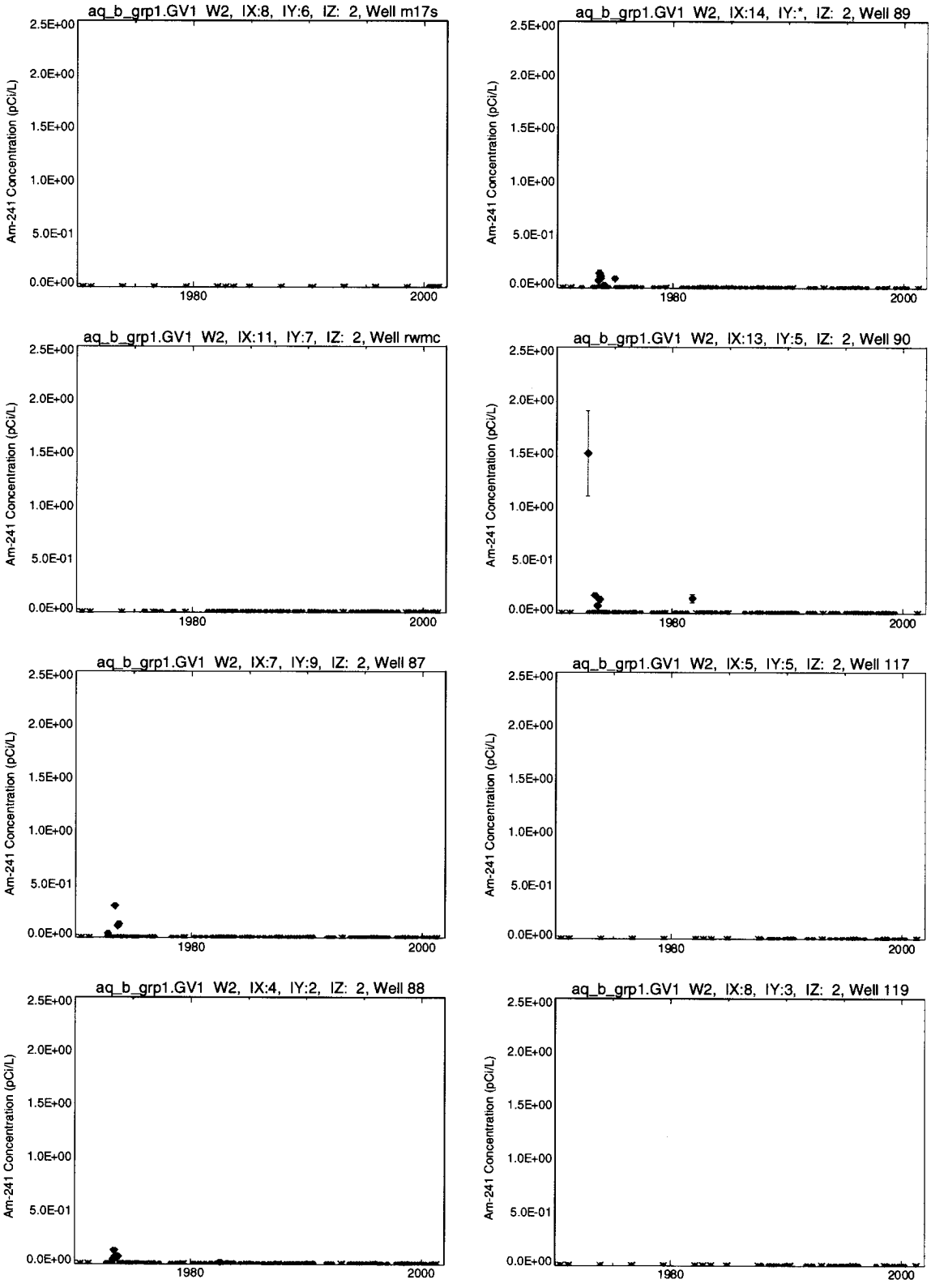

Figure 5-53. (continued).

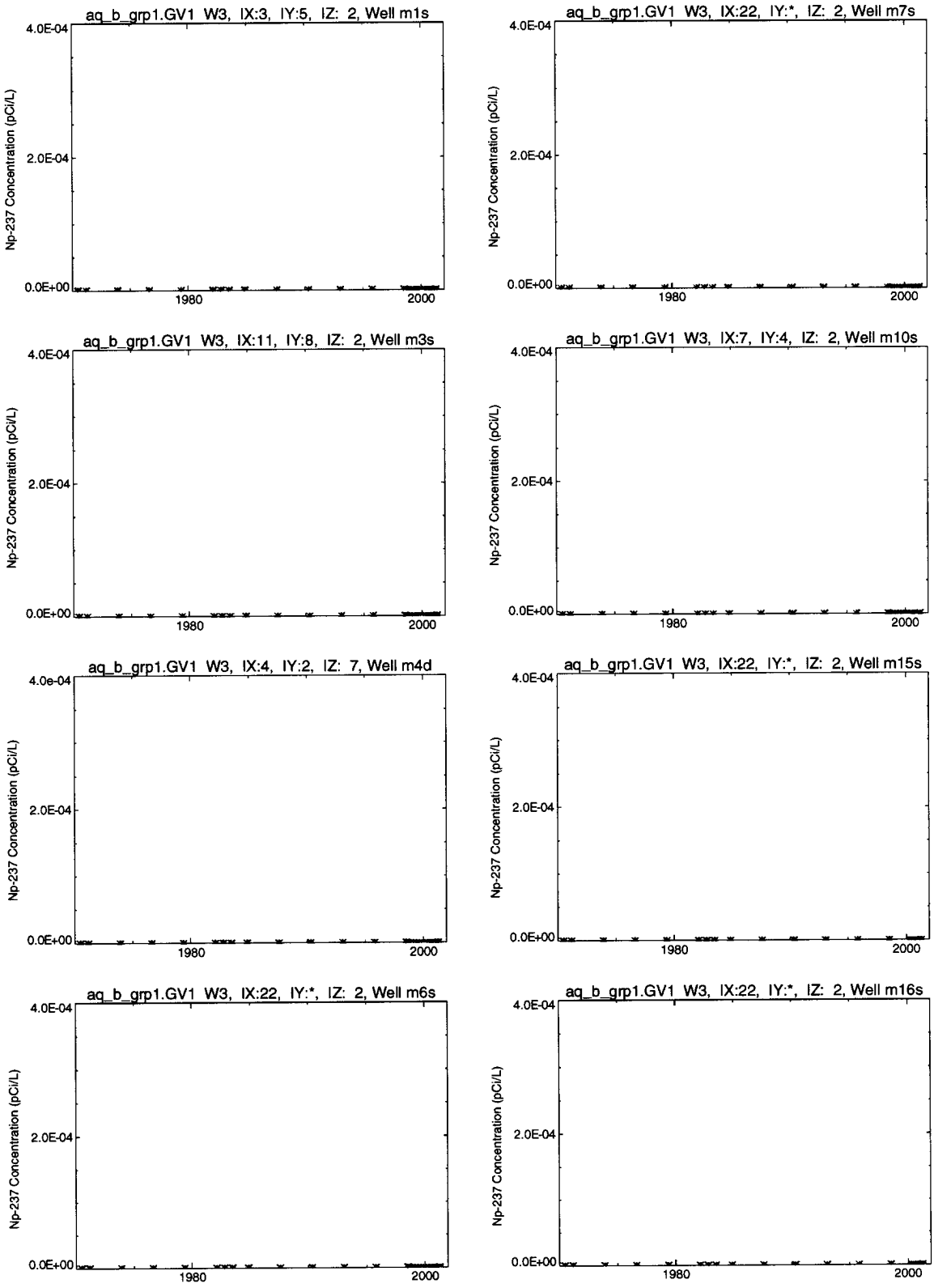

Figure 5-54. Comparison of simulated and observed Np-237 concentration time histories for aquifer monitoring wells in the vicinity of the Subsurface Disposal Area.

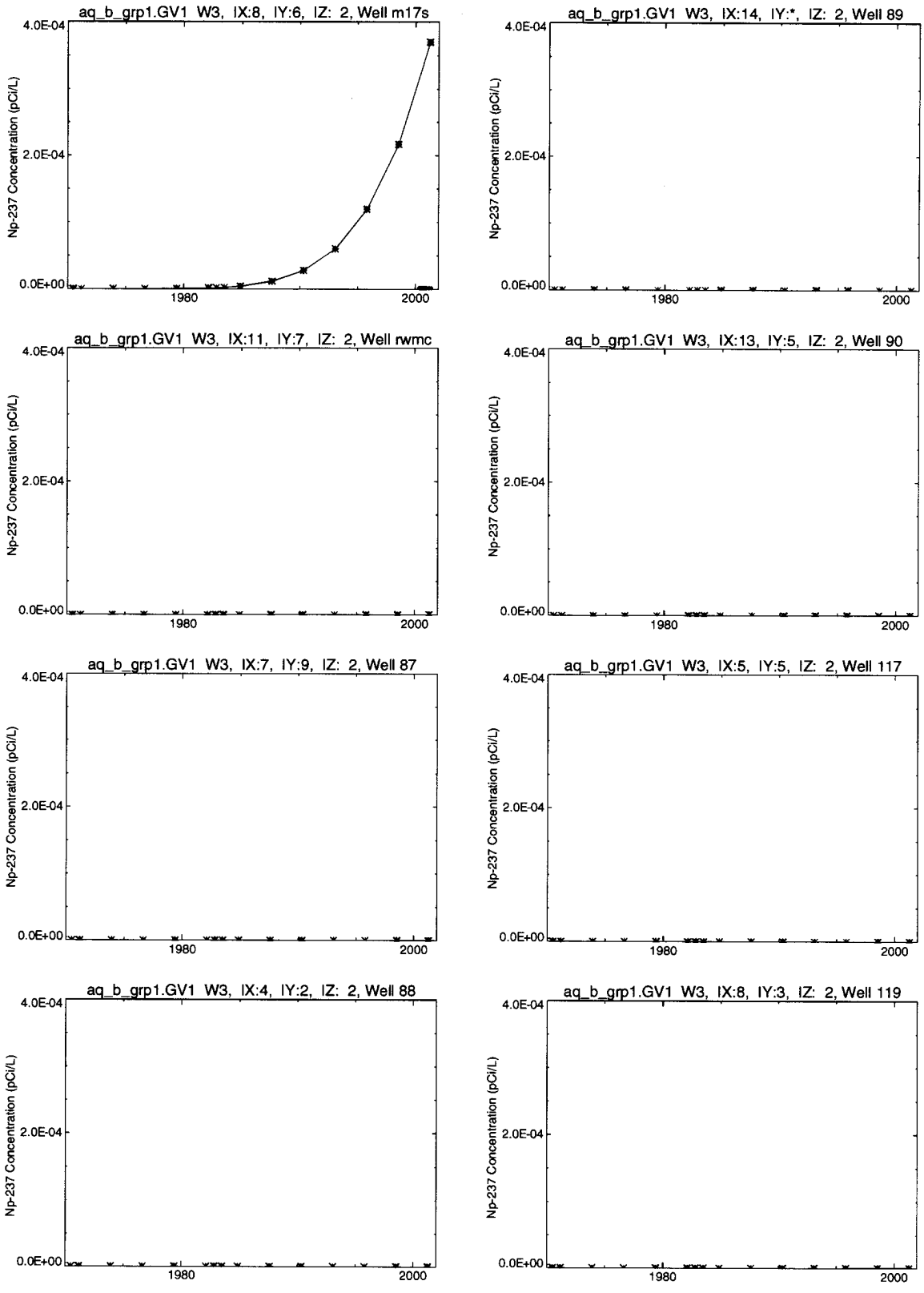

Figure 5-54. (continued).

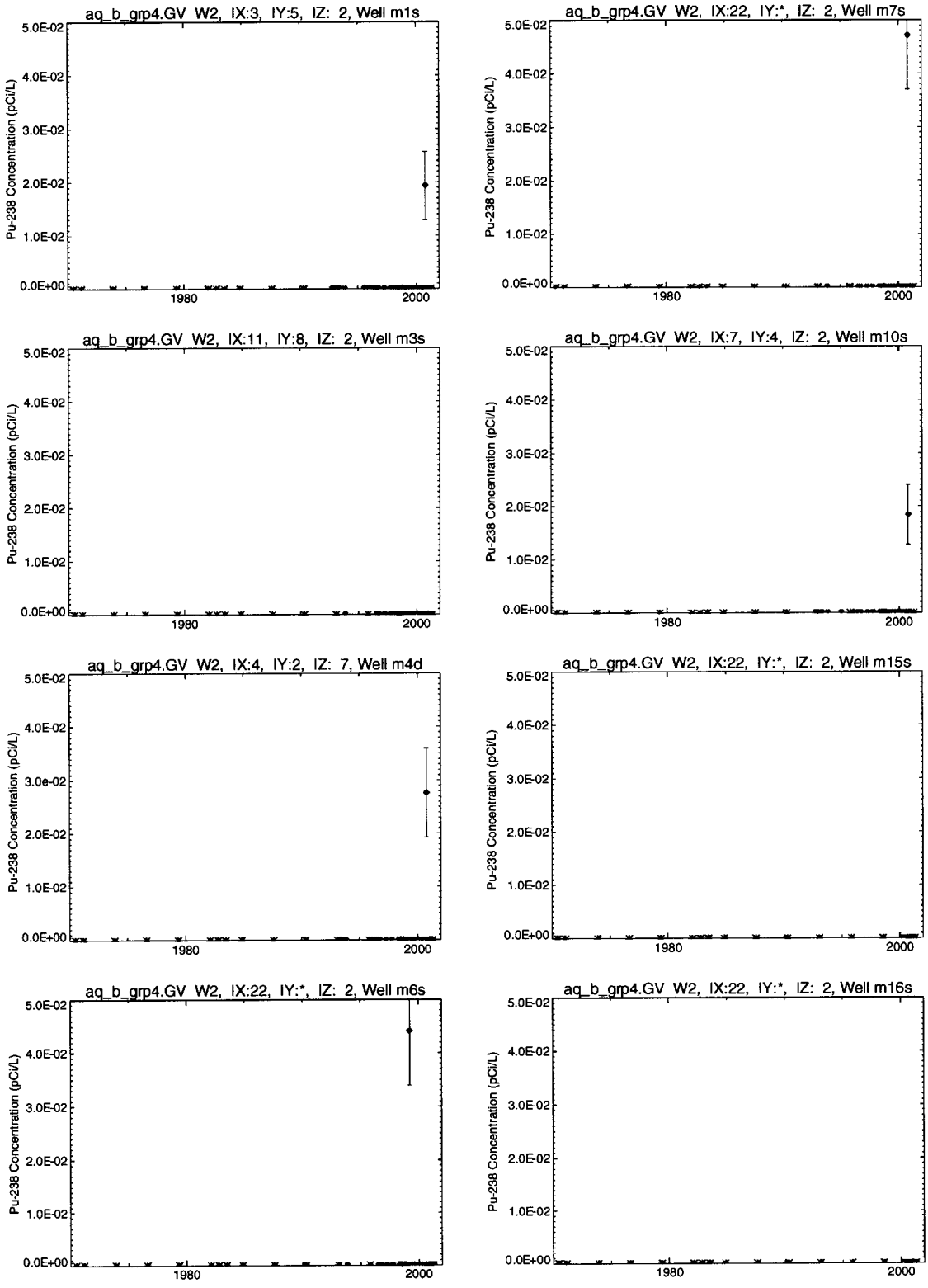

Figure 5-55. Comparison of simulated and observed Pu-238 concentration time histories for aquifer monitoring wells in the vicinity of the Subsurface Disposal Area.

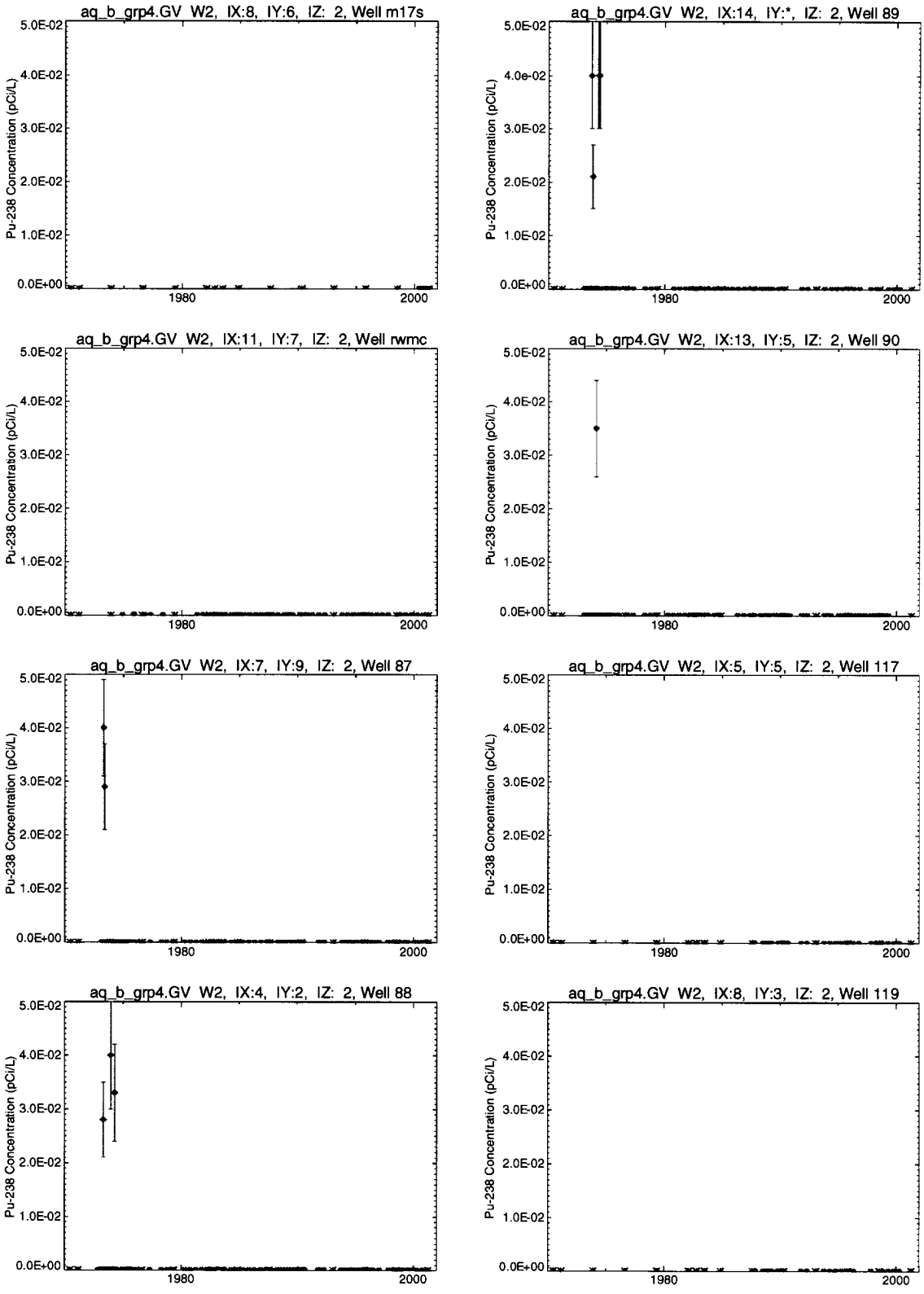

Figure 5-55. (continued).

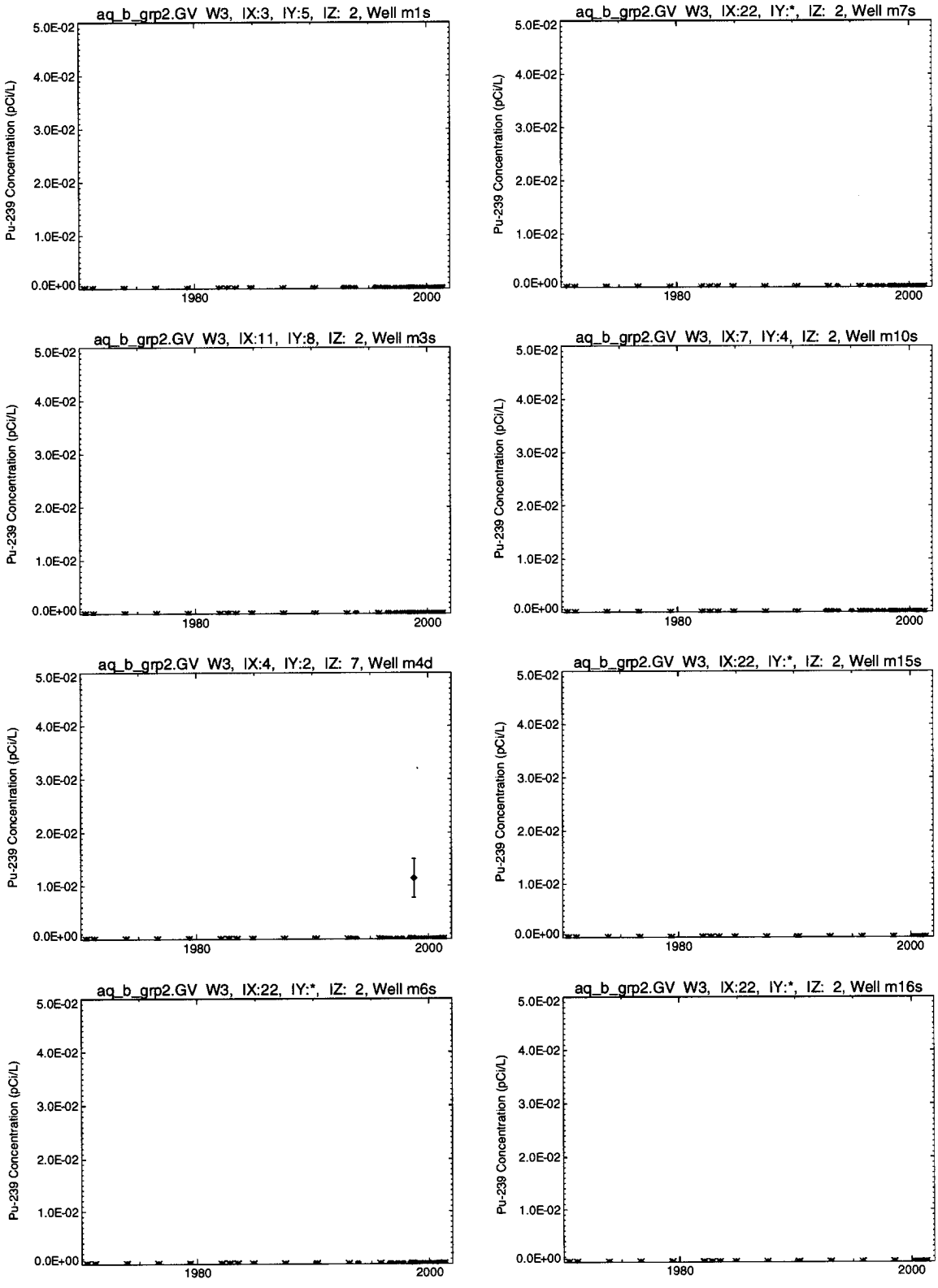

Figure 5-56. Comparison of simulated and observed Pu-239 and Pu-240 concentration time histories for aquifer monitoring wells in the vicinity of the Subsurface Disposal Area.

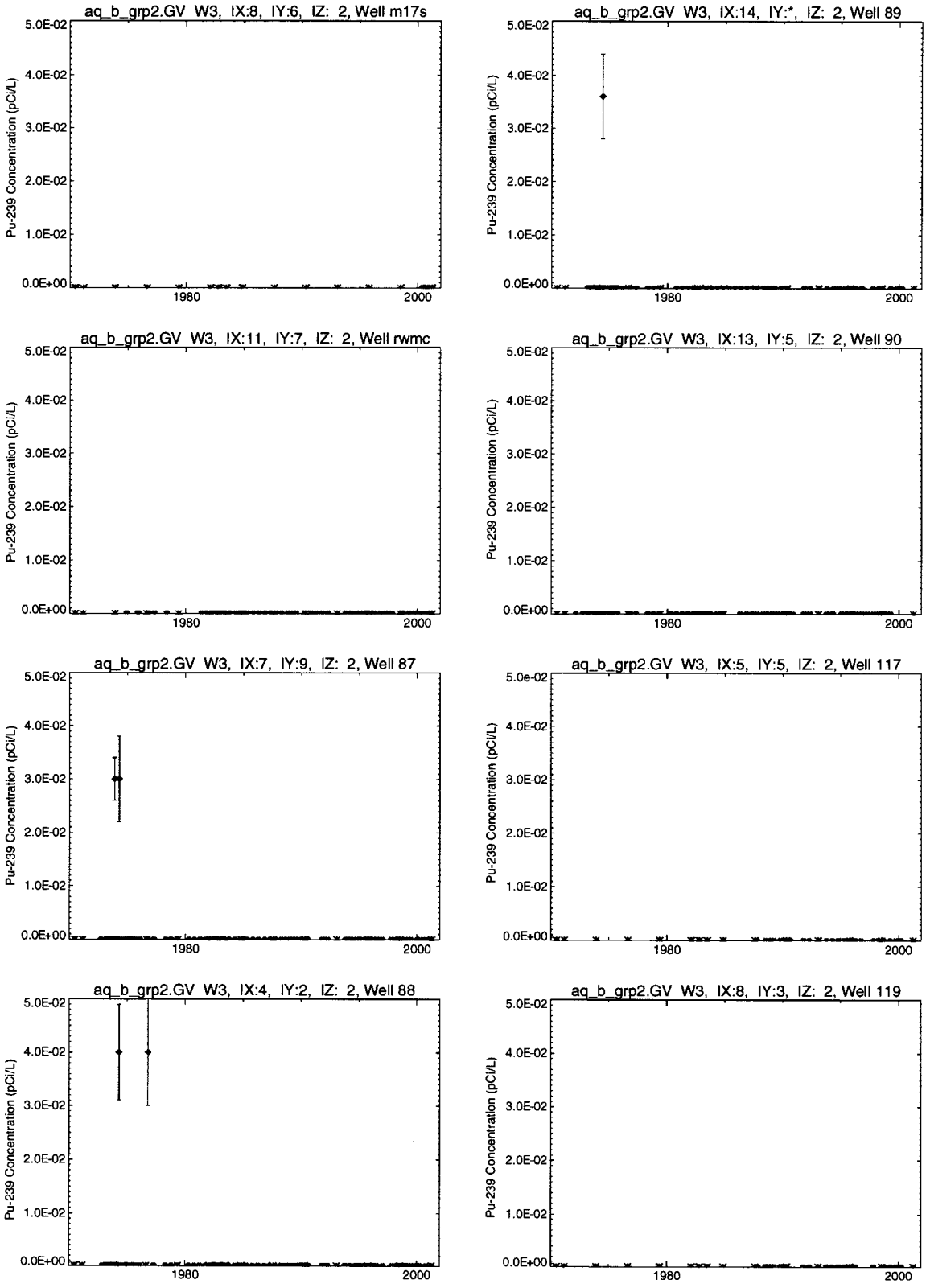

Figure 5-56. (continued).

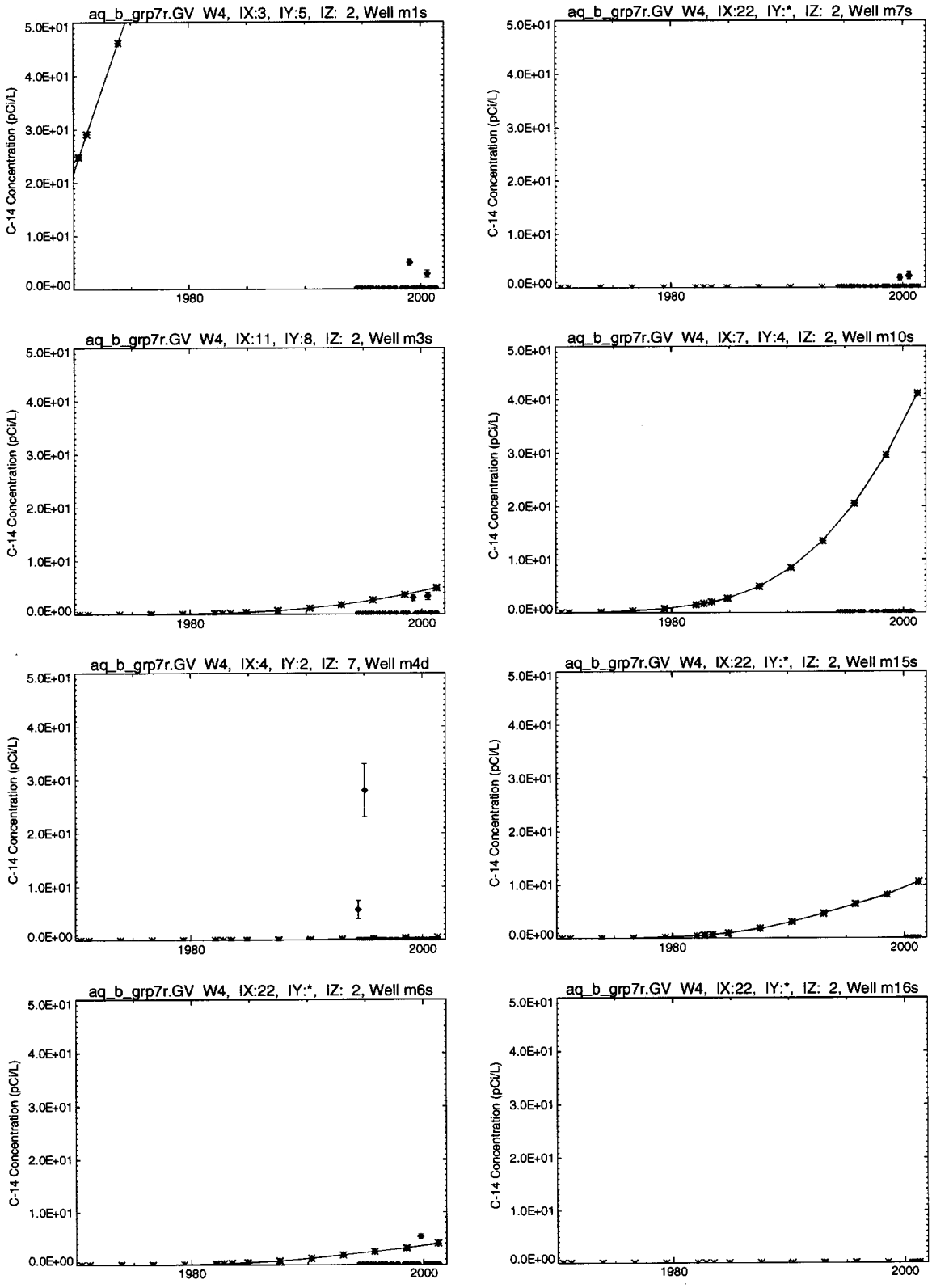

Figure 5-57. Comparison of simulated and observed C-14 concentration time histories for aquifer monitoring wells in the vicinity of the Subsurface Disposal Area.

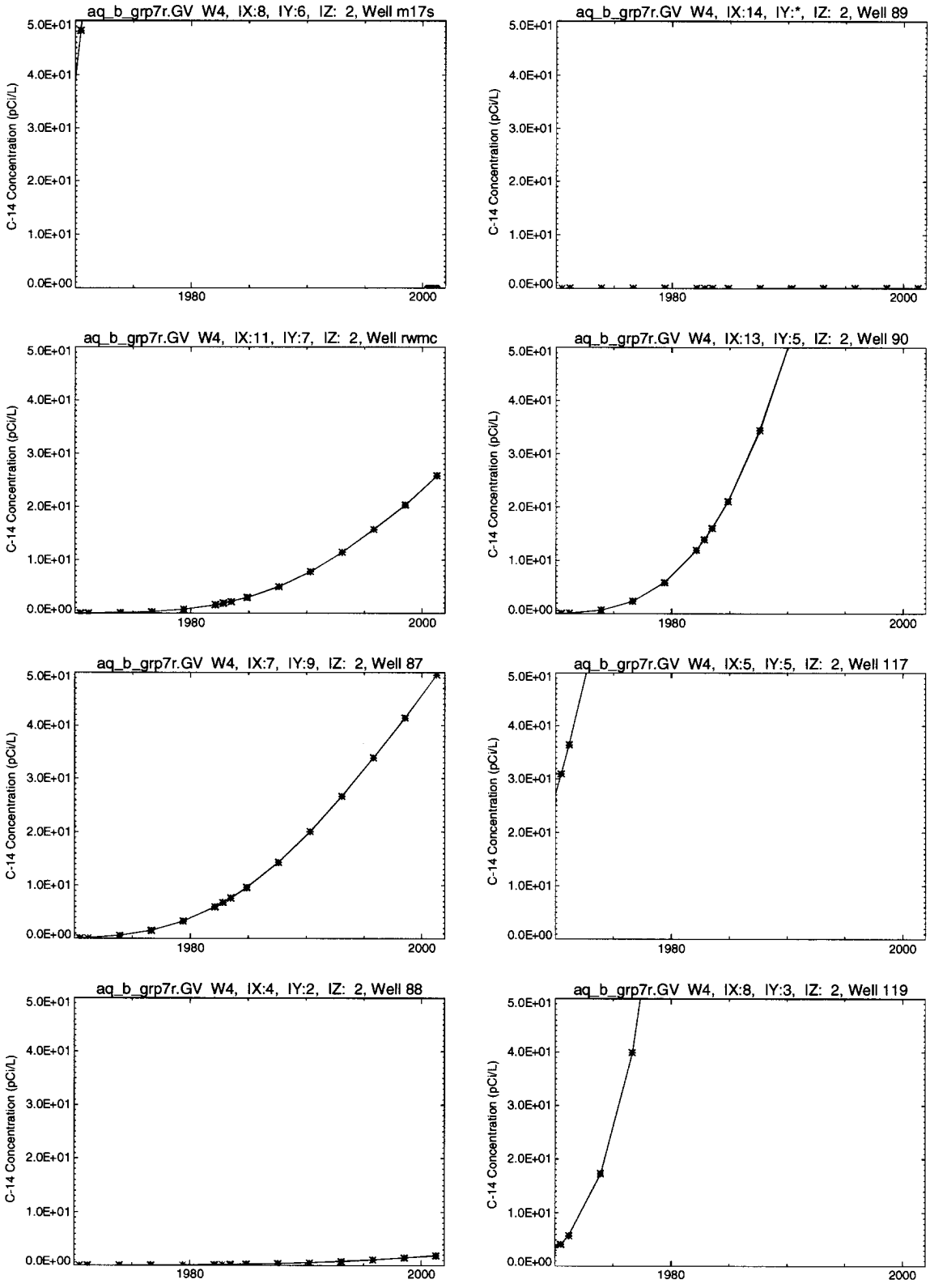

Figure 5-57. (continued).

Table 5-17. Comparison of model concentrations and observed concentrations with no adjustments for background concentrations.

Contaminant of Potential Concern[a]	Baseline Risk Assessment Model Maximum Simulated Concentration at 12-m Depth through Year 2001 (pCi/L)	Interim Risk Assessment Model Maximum Simulated Concentration at 12-m Depth through Year 1995 (pCi/L)	Background Concentrations (Orr, Cecil, and Knobel 1992) (pCi/L)[b]	Range of Observed 1σ Concentrations in Subsurface Disposal Area Vicinity Wells Since 1987 (pCi/L or μg/L)[c]	Comments on Observed 3σ Concentrations[c]
Ac-227	5E-07	6E-08	NA	No analyses[d]	None
Am-241	9E-17	1E-06	0	0.026 to 1.97	None
Am-243	7E-24	2E-11	0	No analyses	None
C-14	3E+03	5 E+00	NA	1.8 to 28.0	Analysis began in 1994.
Cl-l36	3E+02	1E+00	NA	All nondetects	Analyses for Cl-36 began in year 2001. Cl-36 analysis will be done annually.
I-129	5E+01	4E+00	0	0.59 to 17.0	None
Nb-94	1E-23	1E-14	NA	No analyses	None
Np-237	4E-04	8E-04	NA	All nondetects	None
Pa-231	7E-06	1E-06	NA	No analyses	None
Pb-210	3E-10	4E-08	NA	No analyses	None
Pu-238	0	1E-12	0	0.018 to 0.37	NA
Pu-239	5E-28	2E-11	0	0.094 to 4.3	None
Pu-240	3E-30	7E-12	0	0.094 to 4.3	None
Ra-226	4E-09	1E-08	0.0 to 0.1	4.0 to 5.4	Gamma spectroscopy results with inadequate sensitivity. Values shown are near detection limits, use with caution.
Tc-99	4E+04	5E+01	NA	0.97 to 35.4	None
Th-229	1E-06	4E-08	NA	No analyses	None
Th-230	3E-06	8E-7	NA	No analyses	None
Th-232	6E-13	1E-11	NA	No analyses	None
U-233	4E-03	3E-04	0.	No analyses	NA
U-234	1E-01	5E-02	1.1	1.0 to 1.84	None

Table 5-17. (continued).

Contaminant of Potential Concern[a]	Baseline Risk Assessment Model Maximum Simulated Concentration at 12-m Depth through Year 2001 (pCi/L)	Interim Risk Assessment Model Maximum Simulated Concentration at 12-m Depth through Year 1995 (pCi/L)	Background Concentrations (Orr, Cecil, and Knobel 1992) (pCi/L)[b]	Range of Observed 1σ Concentrations in Subsurface Disposal Area Vicinity Wells Since 1987 (pCi/L or µg/L)[c]	Comments on Observed 3σ Concentrations[c]
U-235	2E-02	3E-03	0.05	0.003 to 0.18	Gamma spectroscopy results with inadequate sensitivity. Values shown are near detection limits, use with caution.
U-236	4E-03	2E-03	0.	No analyses	None
U-238	3E-01	4E-02	1.1	0.21 to 0.88	Gamma spectroscopy results with inadequate sensitivity. Values shown are near detection limits, use with caution.
Nitrate (as N)	1E+02 mg/L	1.4E+01 mg/L	1.0 to 2.0 mg/L	0.28 to 2.9 mg/L	None
Chromium	1E+00 µg/L	1E-01µg/L	2.0 to 3.0 µg/L	5.5 to 99.6 µg/L	Most other high chromium values were approximately 40 to 60 pCi/L

a. Observed values from earlier than 1987 are not presented in this table.

b. NA = information not available on background concentrations.

c. The range of observed values is taken from the nature and extent discussion in Section 4.

d. See the respective contaminant discussions in Section 4 regarding lack of analysis.

5.2.6 Baseline Risk Assessment Sensitivity Simulations

This section discusses the implementation of the simulations for the ABRA sensitivity analyses. Results, when presented, are in terms of water travel times and concentrations. Risk results are presented in Section 6. Often, these sensitivity simulations test assumptions used in the model and, as such, the simulations represent an assessment of conceptual uncertainty. For each sensitivity simulation of this type, the entire suite of potential contaminants was simulated. Other sensitivity simulations tested contaminant-specific parameters assigned in the model, and only those contaminants directly affected were evaluated.

5.2.6.1 Upper-Bound Inventories. A simulation suite was performed in which the upper-bound inventories were used instead of the best estimates. The only difference in the subsurface flow and transport models was that a different source term was supplied. Differences in risks are discussed in Section 6.

5.2.6.2 B-C Interbed Gaps. The method used to create the interbed upper surfaces and interbed thicknesses resulted from a consistent statistical approach that was based on all lithologic data available. The use of geostatistics to incorporate spatial variability was implemented and robustly tested by Leecaster (2002). For the ABRA model, kriging results were used without imposing any bias into them. In contrast, the kriging results for the IRA model were modified to enforce gaps in the interbeds in grid block locations containing wells that showed an interbed was missing at that location.

To determine the effect of including gaps, a simulation suite was performed where gaps were enforced in the model for three locations having a grid block that contained a well where the B-C interbed was known to be absent. These interbed gaps were created in the model by modifying the hydrologic properties of the entire interbed at that location so that it consisted of fractured basalt instead of sediment. Locations that had B-C interbed gaps superimposed in the first level of grid refinement are shown in Figure 5-58. No gaps were simulated in the C-D interbed because the one location where a gap has been observed is in Well M7S. Well M7S is located outside the base vadose zone simulation domain. In two out of three locations where the gaps were superimposed in the B-C interbed, other wells that had nonzero thicknesses were present in the grid block.

The effect on predicted risks of including these gaps is discussed in Section 6. Simulated water travel times in the vadose zone, with gaps included in the B-C interbed, are shown in Figure 5-59. Note that travel times are only determined for the base vadose zone domain grid, while the gaps are superimposed in the first level of refinement grid. By comparing travel times in Figure 5-59 to those shown previously for the base simulation (see Figure 5-30), the primary simulated impact is along the northern edge of the SDA, where water travel times are reduced anywhere from 2 to 8 years. Inclusion of the gap to the east of the SDA within the TSA facility causes, at most, a 2-year reduction in water travel time in the vadose zone.

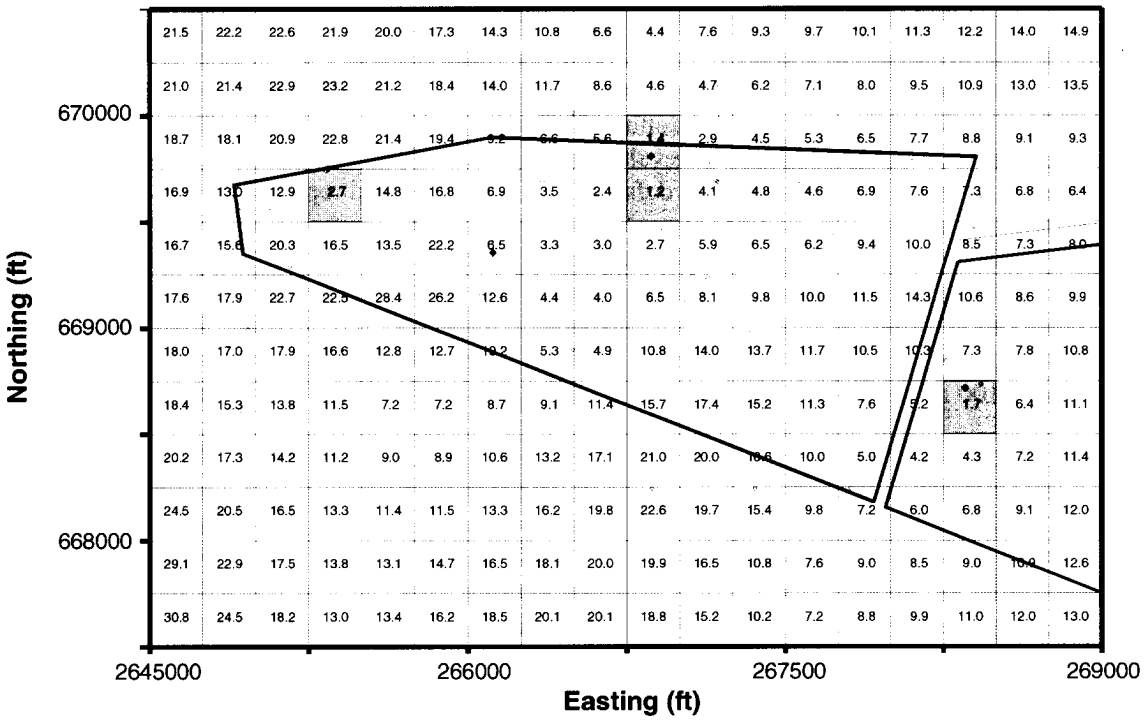

Figure 5-58. The B-C interbed kriged thicknesses with shaded locations where gaps were superimposed.

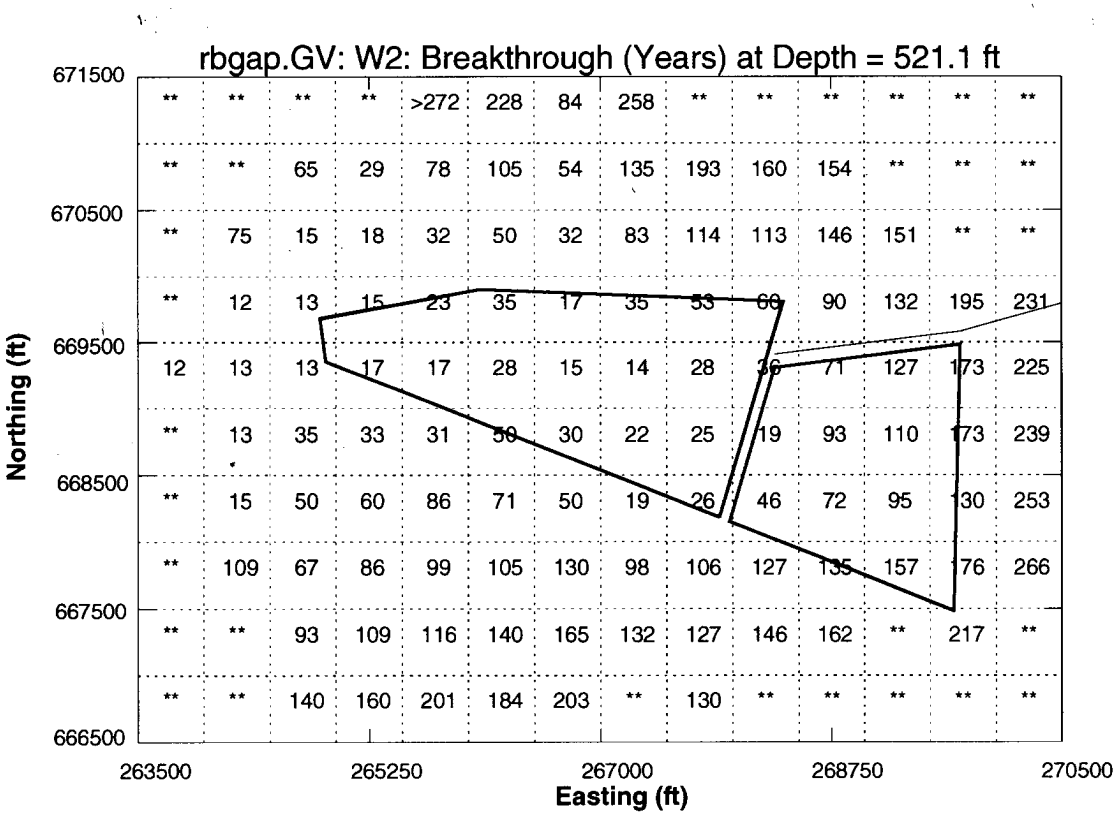

Figure 5-59. Simulated vadose zone water travel times when gaps are included in the B-C interbed.

5.2.6.3 Plutonium Partition Coefficients. The plutonium K_d used in the ABRA model and in the IRA model has been carefully examined. The 5,100-mL/g value selected for the base ABRA simulation was selected as the best site-specific value available. To test the effect of the assigned K_d, a series of simulations was performed in which the plutonium K_d was varied consistently in both the source model and in the vadose zone transport model. The values assigned were 22, 320, and 1,700 mL/g. The 22-mL/g value was taken from the Track 2 screening default (DOE-ID 1994) and represents the extreme low end of measured plutonium K_ds. The value is actually an average of four crushed Hanford basalt samples. The second two values are taken from EPA guidance (see Appendix G of EPA 1999), which was based on work by Glover, Miner, and Polzer (1976) and Miner, Evans, and Polzer (1982). These latter two values were measured on Polatis-type soil taken from unspecified locations on the INEEL. Polatis soil is described as loess over lava. The selected range represents approximately an order of magnitude of changes from 5,100 mL/g down to 22 mL/g and provides a broad spectrum of possible behavior.

Both Pu-238 and Pu-239 were simulated in this sensitivity analysis. The Pu-240 was not simulated, because results would be similar to Pu-239. Comparisons of maximum simulated aquifer concentrations are given in Table 5-18. The maximum values are for the period beginning in 1952 and ending in calendar year 2001. Also shown are the maximum observed Pu-238 and Pu-239 aquifer concentrations from sampling activities since 1987. Decreasing K_d for plutonium isotopes increases resulting simulated concentrations, as shown in Table 5-18. However, even the maximum concentration from the K_d = 22 mL/g simulation is not quite high enough to be detected with normal quarterly sampling conducted by WAG 7 because the instrument detection limit for the analyses is approximately 0.02 pCi/L.

Table 5-18. Maximum 12-m (39-ft) depth simulated Pu-238 and Pu-239 aquifer concentrations (pCi/L) through calendar year 2001 for the base simulation and plutonium K_d sensitivity simulations.

Contaminant of Potential Concern	Baseline Risk Assessment K_d = 5,100 mL/g	K_d = 1,700 mL/g	K_d = 320 mL/g	K_d = 22 mL/g	Range of Observed 3σ Concentrations in the Subsurface Disposal Area Vicinity Wells Since 1987
Pu-238	0	1×10^{-25}	4×10^{-17}	4×10^{-4}	1.8E-02 to 3.7E-01
Pu-239	5×10^{-28}	2×10^{-24}	1×10^{-15}	1×10^{-2}	9.4E-02 to 4.3E+00

Comparison of simulated Pu-238 and Pu-239 soil concentrations in the B-C interbed are presented in Figures 5-60 and 5-61 and Table 5-19. Soil concentrations are determined from simulated aqueous concentrations using the K_d. Contour levels in the figures are for every other order of magnitude beginning at 1×10^{-19} Ci/g up through the maximum value. Two locations with elevated simulated concentrations of Pu-238 and Pu-239 are shown in Figures 5-60 and 5-61. As expected, the simulated soil concentrations increase with decreasing K_ds. The one location that actinides are generally accepted as being detected at depth is for the triad of wells (i.e., Wells 79-2, DO-2, and TW1) located just northeast of Pit 5. This well location is included in the region of elevated soil concentrations in the figures. Locations near this well triad have yielded interbed samples that do not indicate similar concentrations. Comparing these sampling results to the simulation results in Figures 5-60 and 5-61 indicates that broad-spread elevated actinide soil concentrations predicted with the lowest plutonium K_d of 22 mL/g are not reasonable. However, the simulation results from the mid-range K_ds of 1,700 and 320 mL/g do not contradict the sampling results because they show maximums lower than observed values.

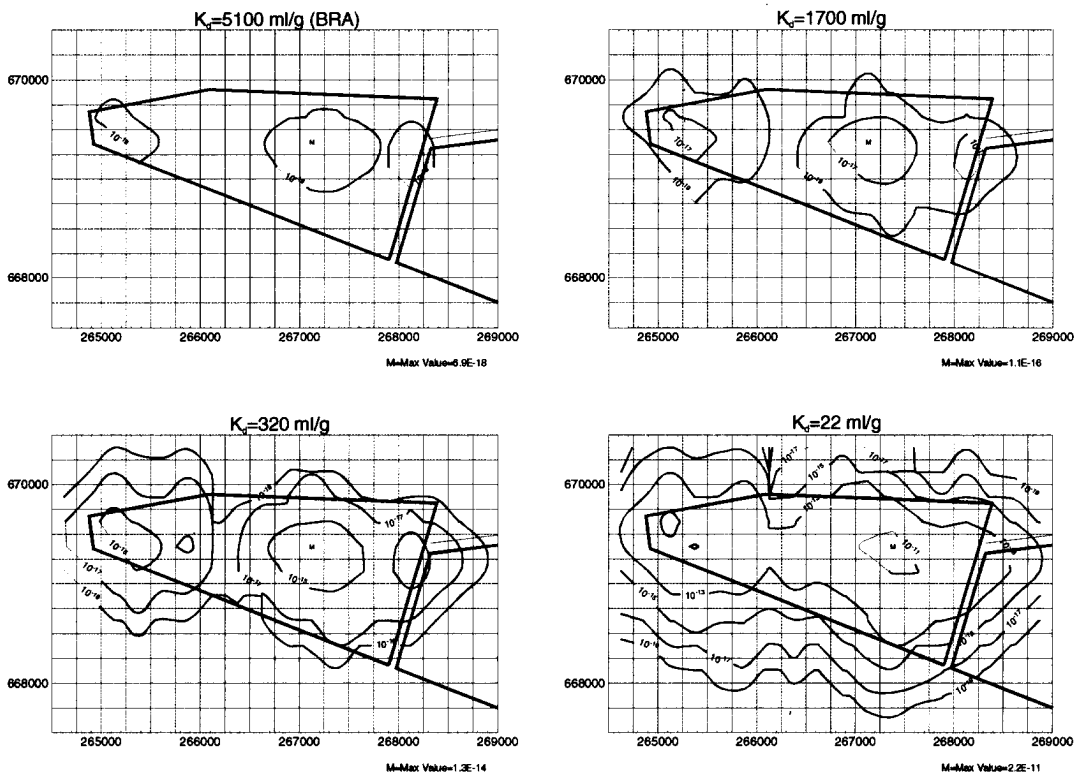

Figure 5-60. Comparison of simulated Pu-238 B-C interbed soil concentrations (Ci/g) for the base simulation to the Pu-238 K_d sensitivity simulations.

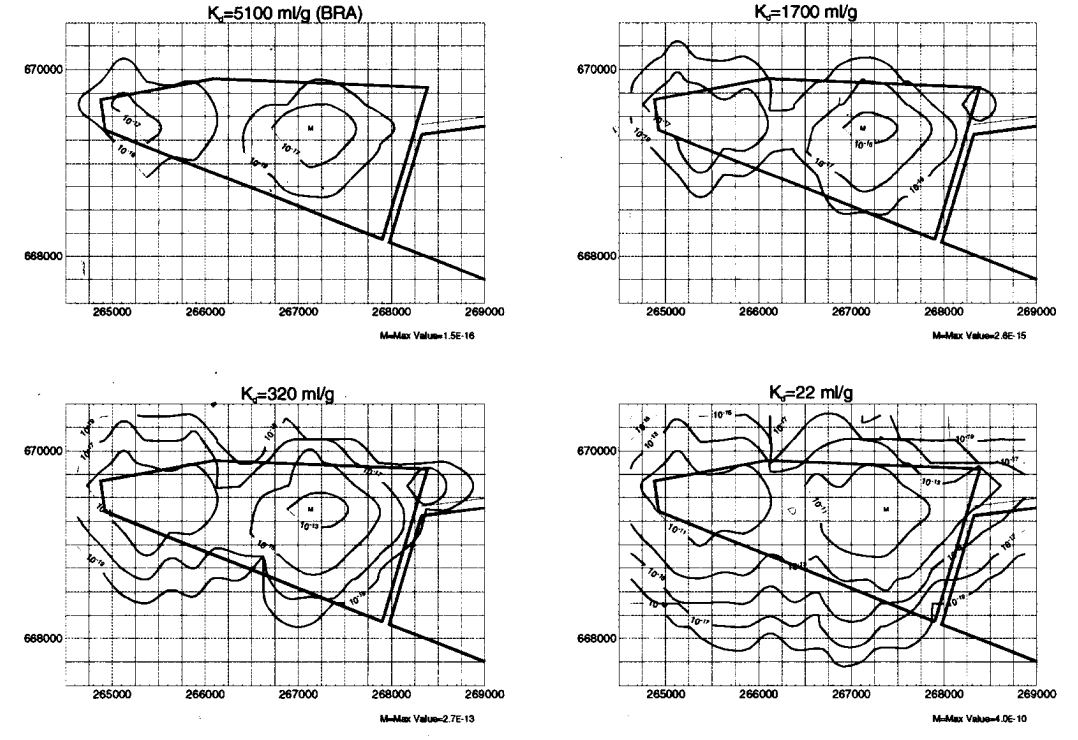

Figure 5-61. Comparison of simulated Pu-239 B-C interbed soil concentrations (Ci/g) for the base simulation and the Pu-238 K_d sensitivity simulations.

Table 5-19. Simulated maximum Pu-238 and Pu-239 B-C interbed soil concentrations (Ci/g) through calendar year 2001 for the base simulation and plutonium K_d sensitivity simulations.

Contaminant of Potential Concern	Base Simulation K_d = 5,100 mL/g	K_d = 1,700 mL/g	K_d = 320 mL/g	K_d = 22 mL/g	Maximum Sampling Results
Pu-238	7×10^{-18}	1×10^{-16}	1×10^{-14}	2×10^{-11}	1×10^{-13}
Pu-239	2×10^{-16}	3×10^{-15}	3×10^{-13}	4×10^{-10}	1×10^{-12}

5.2.6.4 Plutonium Mobile Fractions. Studies on actinide mobility have indicated a potential small mobile fraction of plutonium (Grossman et al. 2001). A series of sensitivity simulations was conducted to test the effect of a small mobile fraction. Both Pu-238 and Pu-239 were simulated in the same manner as for the K_d sensitivity simulations. The source term model was used to release fractions of 1×10^{-6}, 1×10^{-4}, and 1×10^{-2} of the total mass disposed of each year. This range of fractions was very broad and provides a spectrum of possible results. It was necessary to assign a small K_d value of 0.1 mL/g in the sediments and interbeds in the vadose zone model to allow some plutonium to adsorb onto the soil for comparison between predicted and observed soil concentrations in the interbeds.

Table 5-20 shows the maximum simulated aquifer concentrations for Pu-238 and Pu-239 for the plutonium mobile fraction. These values are all at least two orders of magnitude greater than the maximum observed concentrations. A contour plot of simulated aquifer concentrations at the 12-m (39-ft) depth for the smallest mobile fraction simulation is shown in Figure 5-62. Even with the 1×10^{-6} fractional release, the predicted aquifer concentrations at the current time in most of the locations sampled with aquifer wells would be greater than 0.1 pCi/L. Because most of the sample results are nondetects and the detects are generally just at the instrument detection limit of 0.01 to 0.02 pCi/L, these mobile fraction simulations do not mimic concentrations observed in the aquifer. Therefore, if a small mobile fraction does exist, it must be considerably smaller than the 1×10^{-6} fractional release modeled in this analysis. Otherwise, it should be much easier to detect plutonium in the aquifer.

Table 5-20. Maximum 12-m (39-ft) depth simulated Pu-238 and Pu-239 aquifer concentrations (pCi/L) through calendar year 2001 for the base simulation and the plutonium mobile fraction sensitivity simulations.

Contaminants of Potential Concern	Baseline Risk Assessment, No Mobile Fraction	Mobile Fraction 1×10^{-6}/year	Mobile Fraction 1×10^{-4}/year	Mobile Fraction 1×10^{-2}/year	Range of Observed 3σ Concentrations in the Subsurface Disposal Area Vicinity Wells Since 1987
Pu-238	0	$8 \times 10^{+1}$	$8 \times 10^{+3}$	$8 \times 10^{+5}$	0.018 to 0.37
Pu-239	5×10^{-28}	$4 \times 10^{+2}$	$4 \times 10^{+4}$	$4 \times 10^{+6}$	0.094 to 4.3

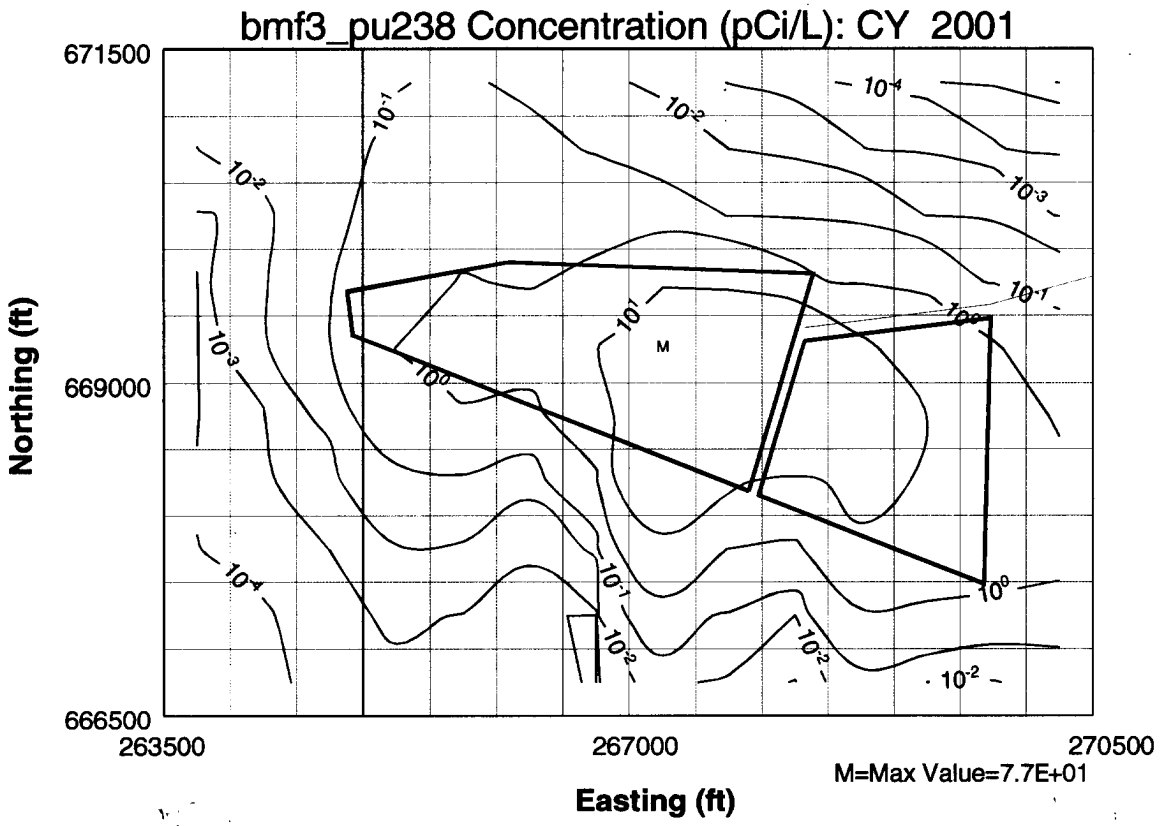

Figure 5-62. Simulated 12-m (39-ft) depth Pu-238 and Pu-239 aquifer concentrations (pCi/L) at calendar year 2001 for the simulation with a 1 x 10^{-6} mobile fraction.

Table 5-21 shows maximum simulated plutonium soil concentrations in the B-C interbed for comparison to those presented previously in Table 5-19 for plutonium K_d sensitivity simulations. Simulated interbed plutonium soil concentrations are approximately 1 to 7 orders of magnitude greater than results for the K_d sensitivity simulations. Except for the 1×10^{-6} mobile fraction, the results also significantly over predict the maximum observed B-C interbed soil concentrations. Contour plots of the interbed soil concentrations are not included because they look similar to those for the K_d sensitivity results but with higher concentrations.

The conclusion from the interbed results for the mobile fraction is slightly different than that for the aquifer. Aquifer results precluded any of the simulated mobile fractions as being plausible, while the lowest mobile fraction does not, at least, contradict the observed interbed soil concentrations.

Table 5-21. Simulated maximum Pu-238 and Pu-239 B-C interbed soil concentrations (Ci/g) through calendar year 2001 for the base simulation and the plutonium mobile fraction sensitivity simulations.

Contaminants of Potential Concern	Base Simulation No Mobile Fraction	Mobile Fraction 1E-06/year	Mobile Fraction 1E-04/year	Mobile Fraction 1E-02/year	Maximum Sampling Results
Pu-238	7E-18	3E-13	3E-11	3E-09	1E-13
Pu-239	2E-16	3E-13	3E-11	3E-09	1E-12

5.2.6.5 Uranium Solubility. This sensitivity study was limited to changes in the source term release. No changes were required in the subsurface flow and transport models. Results are discussed in terms of risk in Section 6.

5.2.6.6 Neptunium Solubility. This sensitivity study was limited to changes in the source term release. No changes were required in the subsurface flow and transport models. Results are discussed in terms of risk in Section 6.

5.2.6.7 Spreading Area Influence. Two different simulations were implemented to test the effects of including additional water from the spreading areas. The implementation of these two simulations was discussed in Section 5.2.4.5. One simulation set had no additional water added at depth, and one had four times as much water added so that the whole region of the C-D interbed beneath the SDA was affected by spreading-area water. For each of these cases, the entire suite of COPCs was simulated. These cases represent conceptual uncertainty bounds on the possible effects of the additional spreading-area water in the vadose zone. The case without the spreading area influence is the most comparable to the IRA model because that model also did not include any effect from the spreading area.

In both simulation sets, the amount of water exiting the bottom of the vadose zone was also input into the aquifer model along with contaminant masses. Additional spreading-area water entering from the vadose zone, coupled with the low-permeability region, results in dilution of simulated concentrations in the extreme western part of the refined portion of the aquifer.

5.2.6.8 Uniform Subsurface Disposal Area Infiltration Rates. Water infiltration rates are assigned at the upper boundary of the vadose zone simulation domain. These amounts of water also are input into the source term model and impact the contaminant release. Two simulation sets were performed to investigate the sensitivity of the simulated flow and transport to these assigned infiltration rates. Both simulation results are presented in terms of risk in Section 6.

In the first set, a uniform infiltration rate of 8.5 cm/year (3.3 in./year) was assigned instead of the spatially varying rate that was used in the ABRA simulation. This uniform infiltration rate was assigned beginning in 1952. This simulation tested the impact of the detailed spatially variable infiltration assignment and included the three historical transient flooding events. The discussion of the impact on risk is included in Section 6. Figure 5-63 shows the simulated vadose zone water travel times with a uniform 8.5 cm/year (3.3 in./year) infiltration rate inside the SDA. These travel times are slightly longer than the ABRA simulated vadose zone water travel times discussed previously. The ABRA travel times ranged from 14 to 30 years at grid blocks contained entirely within the SDA boundary. By comparison, with the 8.5-cm/year (3.3-in./year) uniform infiltration rate, the travel times for the same grid blocks range from 17 to 38 years.

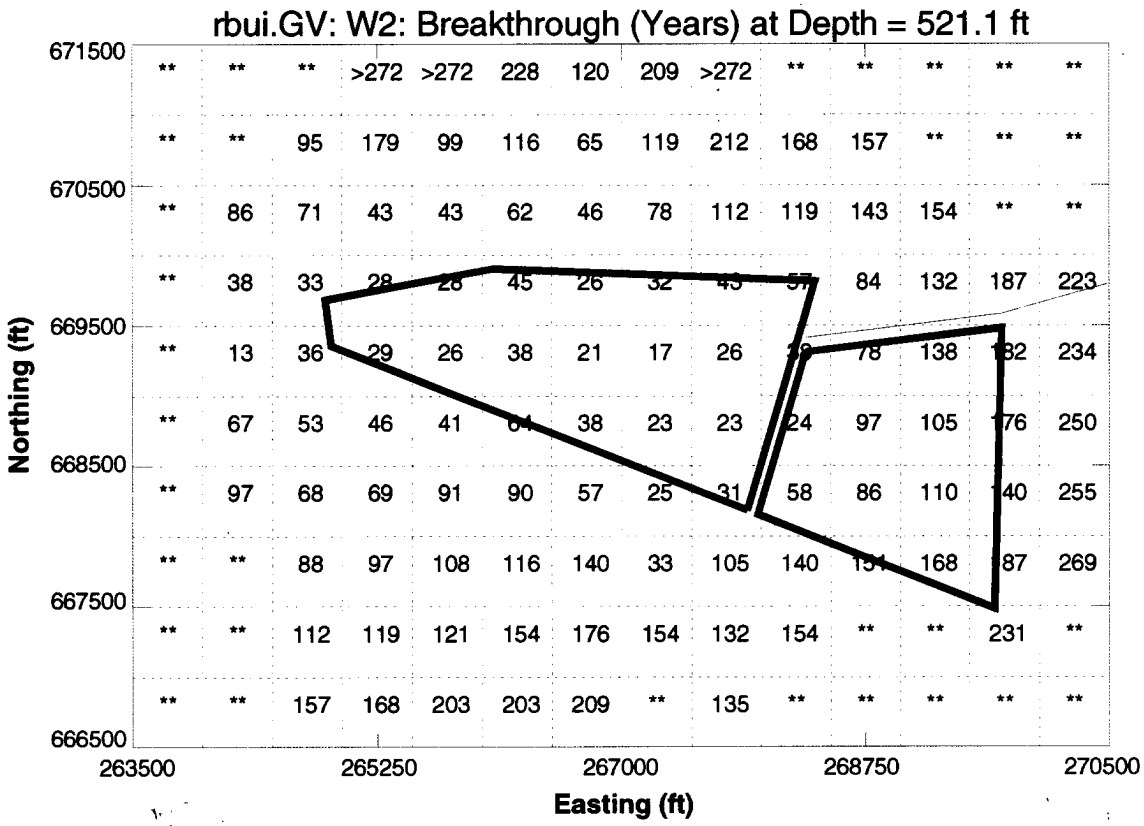

Figure 5-63. Simulated vadose zone water travel times (years) with a uniform infiltration rate of 8.5 cm/year (3.3 in./year) inside the Subsurface Disposal Area.

The second simulation set had a uniform infiltration rate of 23 cm/year (9 in./year) applied inside the SDA, which is equivalent to the total average annual precipitation infiltrating into the subsurface with no loss to evaporation. This infiltration rate was assigned beginning in 1952. This 23-cm/year (9-in./year) infiltration rate was approximately a factor of three times greater than that in the ABRA simulation and can represent the possible effect of a change in climate that resulted in three times as much precipitation at the INEEL. Yet another way to consider this simulation is as a surface treatment being applied that ensured that the total precipitation currently received on the INEEL infiltrated into the subsurface and no portion of that water evaportranspirated back into the atmosphere.

5.2.7 Simulation Nomenclature

Given the extensive number and types of simulations performed for the ABRA, development of a nomenclature to track the simulations was necessary. This nomenclature section is included to allow the reader to recognize headings in the simulation results figures.

The contaminants, as they were divided into seven groups for purposes of performing the simulations, are described in Section 5.1.4 and listed in Table 5-6. Table 5-22 provides the nomenclature for the leading character string in the run names. The first letter is always a "b" for a BRA-related simulation. Table 5-23 shows how these conventions were applied to define names for each of the simulation groups. The table gives the application that was being simulated and a detailed description of the simulation group. The "grp*" indicates Groups 1 through 7, as appropriate for each name.

Table 5-22. Run-naming nomenclature.

Run Nomenclature	Run Description
Leading b	Baseline risk assessment
kd	K_d
mf	Mobile plutonium fraction
us	Uranium solubility
nps	Neptunium solubility
nsa	No spreading area influence
2sa	Twice spreading area
ui	Uniform 8.5 cm/year infiltration rate
ui2	Uniform 23 cm/year infiltration rate
gap	B-C interbed gap

Table 5-23. Simulation group names and descriptions.

Simulation Group Name	Application	Description
	NO ACTION	
b_grp*	Baseline risk assessment (BRA) base case	Best-estimate inventories, average infiltration = 8.5 cm/year, plutonium K_d = 5,100 mL/g.
		No mobile fraction, uranium solubility = 5.9E-04 g/cc, neptunium solubility = 7.5E-08 g/cc.
		Spreading areas do have influence on transport.
	NO ACTION SENSITIVITY: Hold all values constant as in BRA base case except as noted:	
bub_grp*	Upper-bound inventories	Upper-bound instead of best-estimate inventories.
bkd1_grp*, bkd2_grp*,bkd3_grp*	Plutonium K_d	Three K_d values each for Groups 2 and 4 (K_d = 22, 320, and 1,700).
bmf1_grp*,bmf2_grp*,bmf3_grp*	Plutonium mobile fractions	Three mobile fractions each for Groups 2 and 4 (mobile fraction = 1E-02, 1E-04, and 1E-06).
bus1_grp*,bus2_grp*,bus3_grp*	Uranium solubility	Two masses for Group 5 (mass = 9.3E-07 g/cc and 9.3E-11 g/cc).
bnps1_grp*,bnps2_grp*	Neptunium solubility	Two masses for Group 1 (mass = 1.3E-11 g/cc and 1.2E-06 g/cc).
bnsa_grp*,b2sa_grp*	Spreading area influence	No influence and double the ABRA base case influence for Groups 1 through 7.
bui_grp*,bui2_grp*	Uniform Subsurface Disposal Area (SDA) infiltration	Uniform infiltration rates inside the SDA of 8.5 cm/year and 23 cm/year.
bgap_grp*	Gaps included in BC interbed	Gaps included in B-C interbed in grid blocks where any wells show zero thickness.
	Retrieval	Removal of all contaminant mass in surficial sediments, necessary for assessing potential contamination in the vadose zone.

5.3 Volatile Organic Compound Modeling

This section addresses VOCs, which have the added complication of being able to exist and be transported in a gaseous phase. Unlike dissolved-phase contaminants, which were simulated with an updated model since the IRA, no new modeling of VOCs has been performed for the ABRA. Instead, modeling for VOCs has been deferred to future activities planned for OU 7-08, the OCVZ Project. The IRA modeling results, with some adjustment to account for different inventories, were incorporated into this ABRA. Using the IRA results for VOCs is appropriate from the standpoint that modeling with new inventory estimates would not change the risks considerably. This section discusses the results of the IRA VOC modeling, the revised VOC COPC inventory estimates, and how both were used to estimate media concentrations for the ABRA.

5.3.1 Interim Risk Assessment Volatile Organic Contaminant Modeling and Results

The IRA VOC model is documented in Magnuson and Sondrup (1998). At its publication, it was the most comprehensive model developed for predicting water and contaminant movement in the SDA subsurface. The model included spatially variable lithology and time-dependent, spatially-variable infiltration in an integrated vadose zone-saturated zone (aquifer) representation. Contaminants were transported primarily by advection and diffusion in aqueous and gaseous phases. The model was implemented using the numerical simulation code TETRAD. Time-dependent releases of VOCs were calculated external to the TETRAD simulator using the DUST-MS code.

The vast majority of VOCs in the SDA subsurface were released from Rocky Flats Plant 743-series sludge. The sludge was prepared in an organic waste treatment processing facility at the Rocky Flats Plant by mixing lathe coolant (liquid carbon tetrachloride and Texaco Regal Oil) with calcium silicate. Small amounts of miscellaneous oils and other VOCs (e.g., tetrachlorethylene, trichloroethylene, and 1,1,1-trichloroethane) were also sometimes added. The resulting mixture was a very thick pasty substance devoid of free liquids. Because of the viscous nature of the 743-series sludge, it is unlikely that the VOCs were released or migrated as free liquids. Thus, VOC release by diffusion was simulated using DUST-MS. However, for computational convenience the VOCs were initially entered into the TETRAD model as free liquids, then quickly partitioned into aqueous- and vapor-phase components. Migration as a free liquid was not simulated, which is consistent with monitoring results because non-aqueous phase liquids have not been detected in vapor, perched water, or the aquifer.

The IRA VOC transport model was calibrated using carbon tetrachloride concentrations in soil gas, and aqueous concentrations in the aquifer and perched water. Calibration consisted of simulating the release and migration of VOCs until modeled concentrations matched actual concentrations within some specified tolerance. Initially, the HDT (LMITCO 1995) best-estimate carbon tetrachloride inventory value of 113,000 kg (250,000 lb) was used in the calibration. However, this inventory was insufficient to achieve adequate calibration despite relaxing other model parameters. To improve the calibration, the inventory was arbitrarily doubled to 226,000 kg (497,200 lb), and a much better match was obtained. However, it required that nearly all of the carbon tetrachloride be released in order to achieve calibration. Specifically, the IRA model assumed that 213,000 kg (468,600 lb) (94%) of the 226,000 kg (164,200 lb) of the carbon tetrachloride had been released by 1995, the end of the IRA calibration period. Of the 213,000 kg (468,600 lb) released by 1995, approximately 168,000 kg (369,600 lb) (79%) were predicted to have been lost to the atmosphere through vapor diffusion or advection, and 45,000 kg (90,000 lb) (21%) remained in the vadose zone.

In response to suspicions that the carbon tetrachloride inventory was too low, the inventories for the other organic COPCs (i.e., tetrachloroethylene and methylene chloride) also were doubled for the IRA. This made sense for tetrachloroethylene because it was codisposed with carbon tetrachloride in the

743-series sludge. Conversely, methylene chloride was not a component of 743-series sludge, but it did come from RFP as did the 743-series sludge. Therefore, doubling the methylene chloride seemed appropriate and fit with the intent of the IRA to be conservative.

The IRA model calibration was rather good in terms of agreement between modeled and measured concentrations of carbon tetrachloride. However, the model did not consider chemical degradation. Degradation is likely occurring based on detections of chloroform (a degradation byproduct). The IRA model did not include degradation because of uncertainty regarding the rate and mechanism. Neglecting degradation is conservative because byproducts of carbon tetrachloride degradation (i.e., chloroform, methylene chloride, and chloromethane) have transport properties similar to carbon tetrachloride, yet they all are less toxic (i.e., have higher risk-based concentrations).

Results of the IRA VOC model predicted VOC concentrations in soil and surface gas fluxes would peak shortly after burial. Soil concentrations and gas fluxes were used to calculate ingestion and inhalation risk. The VOC concentrations in groundwater were predicted to peak after the 100-year institutional control period at levels well above MCLs. Predicted maximum concentrations of VOCs in soil and groundwater as presented in the IRA are provided in Table 5-24 (Becker et al. 1998).

Table 5-24. Maximum predicted soil and groundwater concentrations for volatile organic contaminants of potential concern quantitatively evaluated in the Interim Risk Assessment.[a]

Contaminant of Potential Concern	Predicted Maximum Soil Concentration (mg/kg)	Year of Predicted Maximum Soil Concentration	Predicted Maximum Groundwater Concentration (µg/L)	Year of Predicted Maximum Groundwater Concentration
Carbon tetrachloride	1.65E+00	1967	304	2106
Methylene chloride	1.61E-02	1967	487	2187
Tetrachloroethylene	4.70E-01	1968	127	2138

a. Concentrations and dates were calculated from model results using a 30-year running average (Becker et al. 1998).

5.3.2 Revised Volatile Organic Compound Inventory Estimates

The IRA VOC modeling indicated that the best-estimate inventory as presented in the HDT was too low for carbon tetrachloride, which led to a two-part investigation that ultimately resulted in an estimate for carbon tetrachloride that was several times higher than the HDT value. The initial investigation by Miller and Navratil (1998) evaluated monthly shipping records rather than yearly records as had been done in the past. Miller and Navratil (1998) also used newly acquired information on the makeup of 743-series sludge and concluded that the carbon tetrachloride inventory could be approximately 4× the HDT value. The follow-on investigation by Miller and Varvel (2001) made use of other critical sources of information (e.g., RFP Building 664 waste disposal sheets and the RFP Building 774 Organic Waste Treatment Process Logbook) that were obtained as a result of inquiries made by Miller and Navratil (1998). These other sources of information allowed an even more accurate count of the 743-series sludge drums buried in the SDA. Miller and Varvel (2001) estimated that the carbon tetrachloride mass in the 743-series sludge was 8.2E + 05 kg, which is approximately 7.3× more than the best-estimate value in the HDT.

Miller and Varvel (2001) also estimated total VOC mass in 743-series sludge to be 1.0E + 05 kg. From that estimate, Varvel (2001) calculated the mass of the other VOCs in 743-series sludge: trichloroethylene, tetrachloroethylene, and 1,1,1-trichloroethane. Lacking any evidence to the contrary, Varvel (2001) assumed the VOC mass that was not carbon tetrachloride consisted of equal volumes of the other three VOCs. This resulted in an estimated mass of 9.8E + 04 kg of tetrachloroethylene, or about 3.9× more than in the HDT estimate. Varvel (2001) also investigated methylene chloride, which is not a component of 743-series sludge, and concluded that the methylene chloride inventory presented in the HDT was reasonable and appropriate.

Table 5-25 contains a summary of the VOC COPC inventories. The table shows that the revised best-estimate inventory for carbon tetrachloride and tetrachloroethylene is greater than the HDT inventory and even greater than the IRA inventories, which were double the HDT values. The current best-estimate inventory for methylene chloride, the other organic COPC, has not changed from the value used in the HDT. Therefore, the inventory for methylene chloride used in the ABRA is the same inventory reported in the HDT (LMITCO 1995a) value, or one-half the IRA value.

Table 5-25. Summary of volatile organic compound contaminant of potential concern inventories.

Contaminant of Potential Concern	Original Best-Estimate Inventory[a] (kg)	IRA Inventory[b] (kg)	Revised Best-Estimate Inventory (kg)	Ratio of Revised to Original[a] Best-Estimate Inventory	Ratio of Revised to IRA Inventory
Carbon tetrachloride	113,000	226,000	820,000[c]	7.3	3.6
Tetrachloroethylene	25,000	50,000	98,000[d]	3.9	2.0
Methylene chloride	14,000	28,000	14,000[d]	1 (no change)	0.5

a. Taken from *A Comprehensive Inventory of Radiological and Nonradiological Contaminants in Waste Buried in the Subsurface Disposal Area of the INEL RWMC During the Years 1952–1983* (LMITCO 1995).
b. Interim Risk Assessment (Becker et al. 1998) with modeling in Magnuson and Sondrup (1998). The IRA inventory is 2× the original best-estimate inventory.
c. *Reconstructing Past Disposal of 743 Series Waste in the Subsurface Disposal Area for Operable Unit 7-08, Organic Contamination in the Vadose Zone* (Miller and Varvel 2001).
d. Varvel (2001)

5.3.3 Implications of Revised Volatile Organic Compound Inventories

The IRA inventories and ABRA revised best-estimate inventories are different for the VOC COPCs; therefore, it is reasonable to assume that media concentrations (soil, groundwater) and surface gas fluxes would be different. Information from a previous modeling study was used (Sondrup 1998) to appropriately scale the IRA results to the new ABRA revised best-estimate inventory. Before completion of the carbon tetrachloride inventory investigation by Miller and Varvel (2001), Sondrup (1998) performed some preliminary modeling of carbon tetrachloride transport. At the time, Miller and Varvel (2001) were confident that the carbon tetrachloride inventory would be at least 5× greater than the best estimate reported in the HDT. Sondrup then evaluated potential groundwater impacts assuming a preliminary carbon tetrachloride inventory of 5× the HDT (LMITCO 1995a) value, or 2.5× greater than the IRA value. While complete details of the study are documented in Sondrup (1998), relevant information has been included here.

Sondrup (1998) modeled carbon tetrachloride using essentially the same model as the IRA VOC model documented in Magnuson and Sondrup (1998), with some modifications. The major modification used a smaller model domain and increased grid refinement in the vertical dimension. These changes

were enacted to speed simulation times and increase resolution in the vicinity of the SDA. The drawback was that the new domain did not extend to the INEEL boundary; therefore, concentrations at the boundary could not be predicted with the model.

Because of modifications to the IRA model and the larger source inventory of carbon tetrachloride, it was decided that the model should be recalibrated. To limit the effort required for recalibration, it was decided that all source-release parameters could be modified to make the release rate using the preliminary 5× inventory (i.e., 5× the HDT inventory) imitate the general release rate character of the IRA inventory (i.e., 2× the HDT inventory) during the period of IRA model calibration (1952 to 1995). The additional mass from the 5× inventory would then be released after the calibration period. Figure 5-64 illustrates a comparison of the release rate for the IRA and 5× sources. The IRA and 5× results are similar in trend with one major difference: A few years before the end of the calibration period, virtually nothing is being released from the IRA source, while the 5× source is still active. This can be seen more dramatically in Figure 5-65, which compares the cumulative release of the IRA and 5× sources. At approximately the year 2000, virtually nothing is left in the IRA source, while the cumulative release from the 5× source continues to increase.

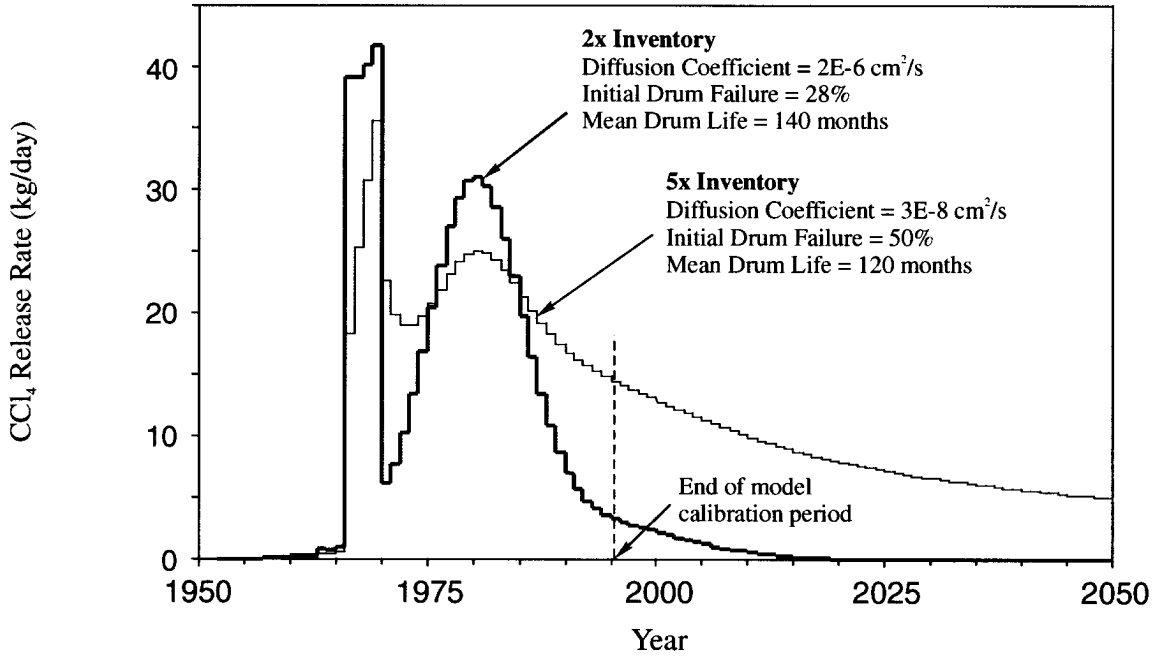

Figure 5-64. Comparison of carbon tetrachloride release rates using the Interim Risk Assessment inventory (2×) and the preliminary 5× inventory estimate.

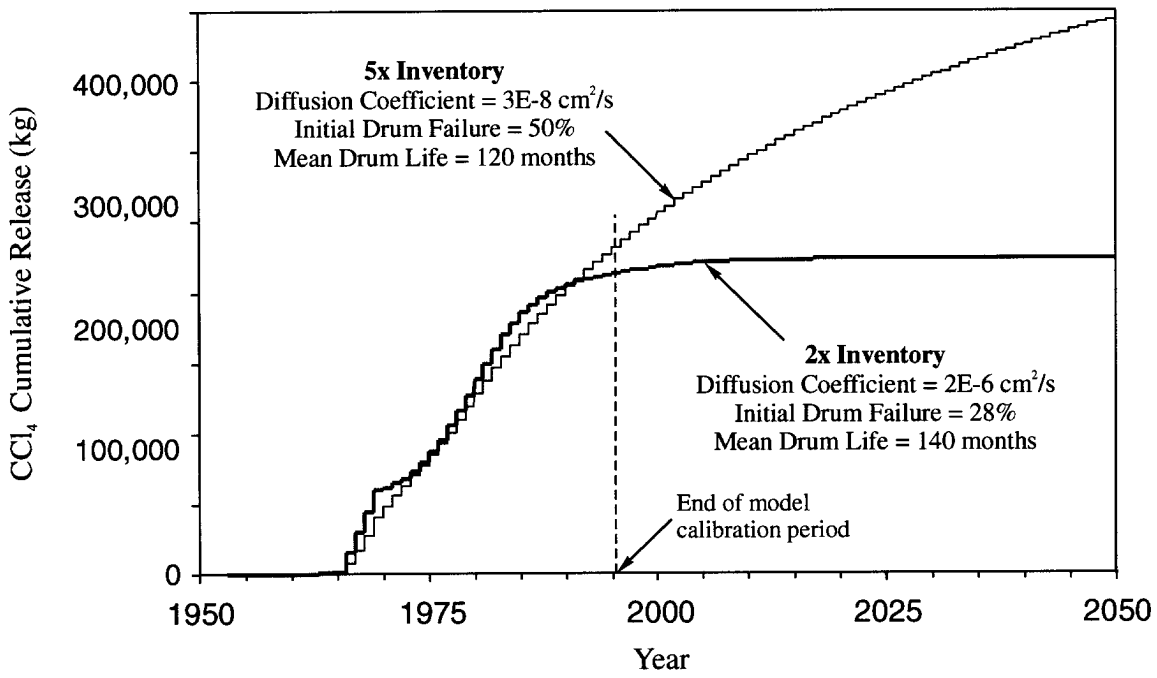

Figure 5-65. Comparison of carbon tetrachloride cumulative release using the Interim Risk Assessment inventory (2×) and the preliminary 5× inventory estimate.

Figure 5-66 compares carbon tetrachloride concentrations in groundwater at the southern boundary of the SDA for the IRA and 5× inventories, as predicted by the Sondrup (1998) model. The predicted peak concentration for the recalibrated model using the IRA inventory is 337 µg/L and occurs in calendar year 2110, while the peak concentration for the 5× inventory is 740 µg/L and occurs in calendar year 2165, over 50 years later. The recalibrated model using the IRA inventory is close to the result using the original IRA model (304 µg/L) published in Magnuson and Sondrup (1998). The difference is attributable to modifications made to the IRA model and to the new calibration of the VOC model from Sondrup (1998).

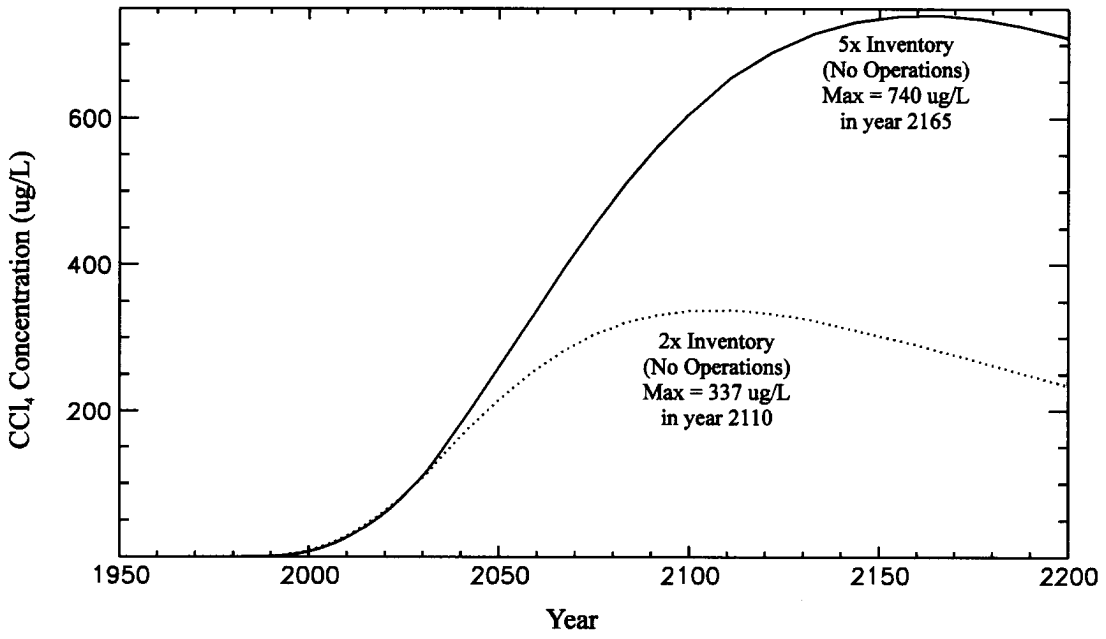

Figure 5-66. Comparison of simulated carbon tetrachloride concentrations in the aquifer near Well M10S for the Interim Risk Assessment and revised inventory estimates.

Results show that the 5× inventory (which is 2.5× larger than the IRA inventory) produced a peak groundwater concentration 2.2× larger than the IRA inventory. While the results are not a direct 1:1 correlation, they are close enough that a 1:1 correlation is reasonable and appropriate in light of the uncertainties. Therefore, because the ABRA revised best-estimate inventory is 3.6× larger than the IRA inventory, it is appropriate to assume that peak groundwater concentration from the ABRA revised best-estimate inventory could be 3.6× larger than the IRA peak concentration, or 1,094 µg/L (3.6 × 304 µg/L). This value should be thought of as an upper-bound estimate of peak concentration based on the following logic. The IRA inventory can be considered the minimum amount necessary to generate the carbon tetrachloride plume as observed in 1995. This is because it was necessary to release essentially all of the IRA inventory before 1995 and also use fairly extreme values for key model parameters to keep enough contamination in the subsurface to recreate the observed plume. When simulating the 5× inventory (Sondrup 1998), all additional mass above the minimum amount necessary to generate the plume was released after the calibration period because the release rate was essentially the same as the IRA model up to 1995. This additional mass, coupled with the model parameters designed to keep mass in the subsurface, produces high groundwater concentrations. These high groundwater concentrations can be considered upper-bound impacts to groundwater because if the same model parameters that were adjusted to keep mass in the subsurface were conversely relaxed, more mass would escape to the atmosphere, meaning a larger inventory could be tolerated by increasing the release rate. This, in turn, would reduce impact to groundwater.

Assuming a 1:1 correlation between inventory and peak groundwater concentration, groundwater impacts for the other VOC COPCs were estimated by scaling the IRA modeling results using a ratio of the ABRA revised best-estimate inventory to the IRA inventory. Table 5-26 contains estimated peak groundwater concentrations for the three VOC COPCs.

Table 5-26. Estimated peak groundwater concentrations for revised inventories of volatile organic compound contaminants of potential concern.

Contaminant of Potential Concern	Interim Risk Assessment[a] Peak Groundwater Concentrations (µg/L)	Ratio of Ancillary Basis for Risk Analysis Revised Best-Estimate Inventory to the Interim Risk Assessment[a] Inventory	Estimated Peak Groundwater Concentrations (µg/L)
Carbon tetrachloride	304	3.6	1094
Methylene chloride	487	0.5	244
Tetrachloroethylene	127	2.0	254

a. Interim Risk Assessment (Becker et al. 1998) concentrations were calculated using a 30-year running average.

Though the predicted peak groundwater concentration occurred later in time for the Miller and Varvel (2001) inventory simulation when compared to the IRA simulation, the ABRA simply used scaled IRA results without regard to timing.

Soil concentrations and surface gas fluxes used to calculate ingestion and inhalation risks also were scaled based on the inventory ratio. This is likely a more conservative approach than it was for groundwater because the surface soil concentrations and surface fluxes are very closely tied to release rates. Because the 5× release rate was made to look similar to the IRA release rate (see Figures 5-64 and 5-65), it can be expected that the soil concentrations and surface fluxes are also similar. However, given that the release rate could have been higher for a larger inventory, as discussed previously in this section, it is reasonable that soil concentrations and flux results also can be scaled using the inventory ratio.

5.3.4 Impact of Vapor Vacuum Extraction on Volatile Organic Compound Concentrations

In January 1996, OU 7-08 began operation of a multi-well VVE system inside the SDA to remove gas-phase VOCs from the subsurface. This system has operated on a nearly continuous basis since 1996 and removed more than 45,000 kg (99,000 lb) of total VOCs from the subsurface.

Estimated concentrations and fluxes discussed in the previous section are base case estimates, taking no account for remedial actions such as those performed for OU 7-08. Operation of the VVE system has reduced vadose zone soil gas concentrations and perched water concentrations considerably in many locations and will certainly reduce future impacts to groundwater; however, the full extent is not known at this time. Also, it appears that sufficient mass may be remaining in both the source and vadose zone (Sondrup 1998) to necessitate continued operation of the VVE system in order to meet the OU 7-08 ROD objectives. Therefore, OU 7-08 will continue to monitor VOC concentrations and predict plume development caused by operation of the VVE system and future releases.

5.4 Biotic Transport

The biotic pathway model predicts the transport of contaminants to the surface through plant intrusion or animal burrowing. Selection of DOSTOMAN for the biotic pathway model for the ABRA is detailed in Becker (1997). The following subsections describe how the DOSTOMAN code was used to predict surface concentrations of contaminants at the SDA.

Unlike other WAGs, the contaminants at WAG 7 are buried under an average of 1.5 m (5 ft) of soil cover. The contaminants must be brought to the surface to enable human contact with contaminants. One possible mechanism for the contaminants to be brought to the surface is biotic transport, which has been measured at the INEEL. The 1.5-m (5-ft) soil cover at WAG 7 is not deep enough to prevent intrusion into the waste by the deeper burrowing animals and rooting plants; therefore, biotic transport was modeled for WAG 7.

5.4.1 Biotic Model Methodology

The DOSTOMAN code was used to predict the amount of contaminants brought to the surface. Yearly average concentrations were computed for the SDA. Four successive phases have been addressed that describe transition from the current disturbed setting back to a native vegetation mixture. The processes modeled using DOSTOMAN include animal burrowing, burrow collapse, plant uptake, radioactive decay, and leaching of contaminants from infiltrating water. Loss caused by erosion or surface runoff was not modeled. Neglecting erosion and surface runoff is conservative because it leads to higher surface concentrations at the SDA. The effect of including erosion would be to remove contaminant mass from the surface and, thereby, reduce the soil concentration to which the receptor would be exposed. The effect would be offset by the reduced depth to the waste and the enhanced intrusion. However, the erosion scenario is not appropriate for the SDA because it is a depositional environment (Hackett et al. 1995).

The SDA has been used for shallow land disposal since 1952. The possibility exists that animals and insects on or adjacent to the SDA could serve as mechanisms of transport or accumulation of contaminants at the surface. The DOSTOMAN code was used to simulate the movement of contaminants by plant uptake, as well as animal and insect excavation, to evaluate the transport of contaminants through biota. Release of nonvolatile contaminants to the surface environment involves mechanical transport of waste to the surface. The mechanical transport can be simulated using a compartmentalized model that provides for flora to uptake waste and burrowing animals to burrow into the waste and deposit it at the surface. The compartmentalized modeling approach has been used (Shuman, Case, and Rope 1985) to model the movement of radionuclides at the INEEL with the DOSTOMAN code (Root 1981).

Subsurface contamination at the SDA can be moved to the surface and near-surface soil profile through root assimilation. Once transferred to aboveground plant structures, contamination may be transported by primary consumers through the food web or accumulate in the surface soil through plant death and decay. Most of the SDA has been seeded with crested wheatgrass (*Agropyron cristatum*) to reduce moisture infiltration and erosion. Russian thistle (*Salsola kali*) has invaded disturbed areas that have not been seeded successfully with grass. The vegetation surrounding the SDA is dominated by big sagebrush (*Artemisia tridentata*), green rabbitbrush (*Chrysothamnus viscidiflorus*), and bluebunch wheatgrass (*Pseudoroegneria spicata*).

Redistribution of soil by burrowing animals may impact mobility of buried waste through transport enhancement, intrusion and active transport, and secondary transport (Arthur and Markham 1982; Cline et al. 1982). Four rodent species account for more than 90% of the composition of small mammals inhabiting the crested wheatgrass and Russian thistle habitat types at the SDA. These are Townsend's ground squirrel (*Spermophilus townsendii*), 4%; Ord's kangaroo rat (*Dipodomys ordii*), 10%; montane

vole (*Microtus montanus*), 23%; and the deer mouse (*Peromyscus maniculatus*), 57% (Groves and Keller 1983).

Evidence exists that harvester ants (*Pogonomyrmex salinus*) are active at the INEEL. The sampling of harvester ant nests at TRA ponds suggests that the ants redistribute radionuclide concentrations in soil and the effect is seen mainly in the mound material (Blom, Johnson, and Rope 1991). In addition, harvester ants appear to have transported radioactive contaminants at the Boiling Water Reactor Experiment I site (Blom, Johnson, and Rope 1991) where a zone of surface contamination was covered with a layer of gravely soil at least 15 cm (6 in.) deep. Harvester ants also exhibit a preference for disturbed conditions similar to those found on the SDA (Fitzner et al. 1979; McKenzie et al. 1982).

The DOSTOMAN code mathematically simulates movement of contaminants from subsurface source compartments to overlying sink compartments by solving a system of differential equations at specified time steps. The general equation is shown below:

$$dQ_n / dt = \sum_{m=1}^{N} \lambda_{n,m} Q_m - \sum_{m=1}^{N} \lambda_{m,n} Q_n - \lambda_R Q_n \pm S_n \qquad (5\text{-}5)$$

where

Q_n = quantity of contaminant in compartment n (g)

Q_m = quantity of contaminant in compartment m (g)

$\lambda_{n,m}$ = rate constant for the transport of contaminants from compartment m to compartment n ($year^{-1}$)

$\lambda_{m,n}$ = rate constant for the transport of contaminants from compartment n to compartment m ($year^{-1}$)

λ_R = decay constant for the contaminant ($year^{-1}$)

S_n = source or sink term in compartment n (g/year)

N = total number of subsurface source compartments under consideration.

The first summation term in Equation (5-5) is the sum of all input rates to compartment n. The second summation term includes all rate-constant losses from compartment n. The remaining two terms include contaminant decay and the gain or loss in compartment n from sources or sinks.

At specified time increments, the system of differential equations presented by Equation (5-5) for n compartments can be solved to determine the contaminant inventory Q_n for each compartment. Details of the mathematical approach for determining a solution are given in Root (1981).

The DOSTOMAN model is represented graphically in Figure 5-67. Up to eight contaminants can be modeled in a single run. The figure shows only two components that are part of a single decay chain. This simplification was used to illustrate how the model was set up. The first contaminant mass is contained in the dotted blue box at the left of Figure 5-67. Waste zones are represented by the two red boxes at the bottom of the figure. Once mass is released from the waste by the source term model, the mass amount is input into the waste zones. Empty black boxes above the waste zone represent the

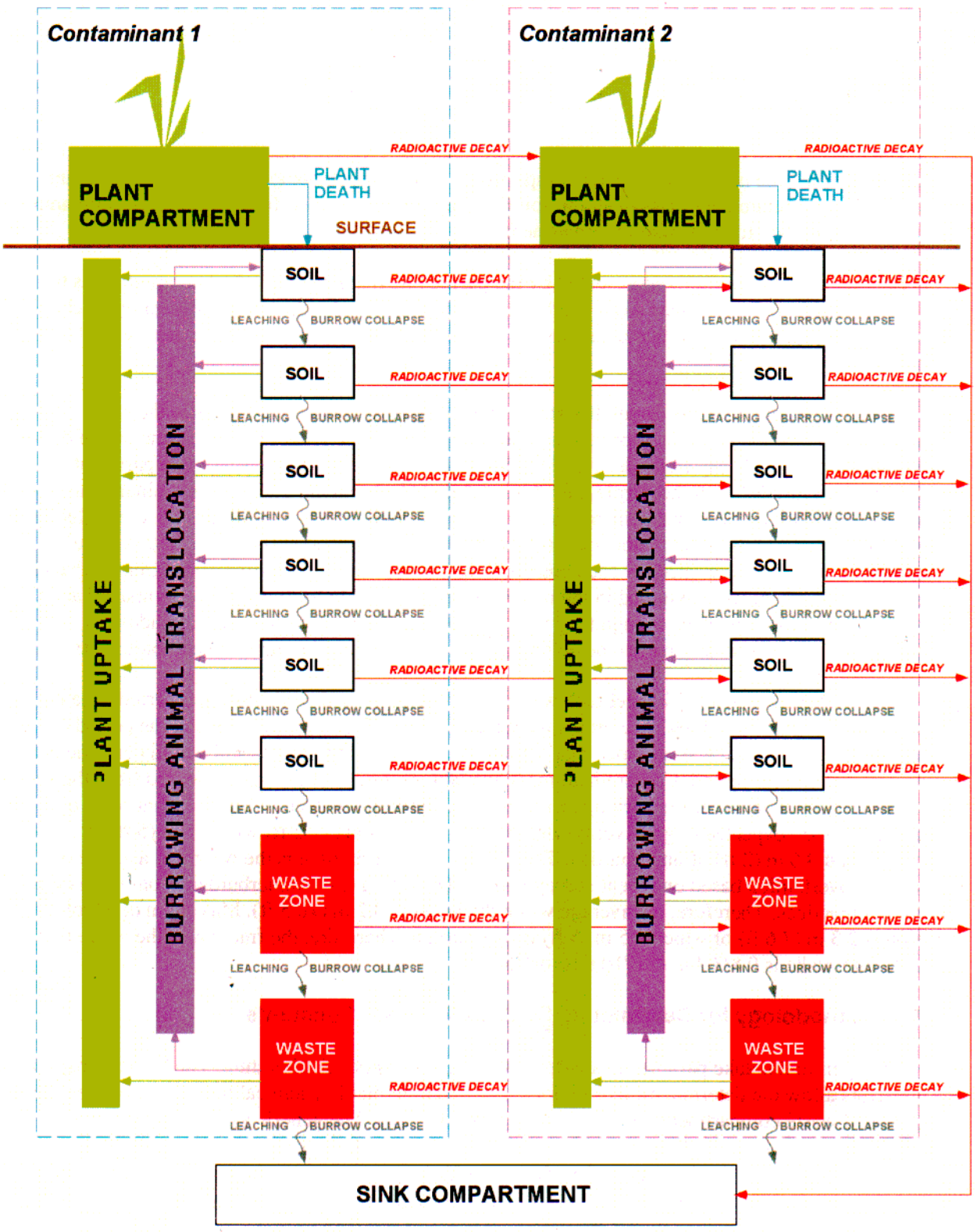

Figure 5-67. DOSTOMAN biotic modeling.

individual soil compartments. The green shaded box at the upper left corner is the plant compartment. Contaminant mass is assimilated by the plants and becomes part of the plant compartment, which is represented by the green lines that come from the waste zone and the individual soil zones to the plant compartment.

The mass of contaminant that is assimilated by plants is released when the plants die. Plant death is represented by the blue line from the plant compartment to the surface compartment. In reality, plant death contributes contaminant mass to all the soil compartments; however, for simplicity, the contaminant is shown as going only to the surface compartment.

Contaminant movement is represented by the purple line from the individual compartments to the surface compartment. Contaminant mass can be removed from an individual compartment by leaching or burrow collapse, which effectively moves mass to the next lower compartment and is represented by the gray lines in Figure 5-67.

Radioactive contaminants decay. If a stable isotope decays, the lost mass goes to the sink compartment; that is, the stable isotopes are not hazardous and are no longer tracked. However, if another radioactive isotope in a decay chain decays, then the mass is transferred to the set of compartments seen on the right of Figure 5-67 (in the purple dotted box labeled Contaminant 2). The contaminant mass can be transported by all the same mechanisms as the original isotope. The transport rates are controlled by the properties (e.g., plant uptake factors or soil-to-water partition coefficient) of each isotope. The contaminant blocks were repeated for each contaminant modeled in a single simulation. Contaminants in any given compartment were assumed in the modeling to be available for transport by animals that burrow into a compartment even though they may not burrow as deeply as the waste. In addition, shallow-rooted plants were assumed to be able to uptake contaminants in nonwaste compartments.

Uptake of contaminants by sagebrush was not modeled during the occupational period because it was assumed that current RWMC operations would inhibit growth of sagebrush during the period of institutional control. It also was assumed that maintenance of the SDA surface soil would continue during the institutional control period. Contaminant mass available is 23.2% of the mass released from the source term model. This accounts for the burying of much of the waste more deeply than the plant roots or animal burrows are expected to go. Average depth to basalt is 5.3 m (17.5 ft) with 1.5 m (5 ft) of overburden and 0.6 m (2 ft) of underburden. The 1.5-m (5-ft) overburden is the weighted average of thickness of overburden based on recent survey results. The 0.6-m (2-ft) underburden is based on current operational practices. Therefore, the average waste thickness is 3.2 m (10.5 ft). Maximum depth of biotic intrusion is 2.3 m (7.6 ft) of which 1.5 m (5 ft) is overburden. Therefore, the fraction of the waste that is available for uptake is 0.8/3.2 m (2.6/10.6 ft) or 25%.

5.4.2 Methodology for Determining DOSTOMAN Rate Constants

Transport and uptake parameters are determined using applicable literature. The biotic transport rate constants allow the determination of radionuclide and nonvolatile chemical movement between the contaminated waste compartment and overburden compartments. The generic symbol for the rate coefficient for compartment n to compartment m is $\lambda_{m,n}$. The specific coefficients for each process are defined below. A superscript is used to identify the coefficients for an individual process such as plant uptake. For example, the plant uptake rate coefficient for compartment n to compartment m is λ_{mn}^{PU}. These coefficients are then used as shown in Equation (5-1) to determine soil contaminant concentrations. The plant death-rate constant determines the rate at which biomass dies and decays in the soil of each compartment. The rate constant is given by the following expression:

$$\lambda_{m,n}^{PD} = \sum_{i=1}^{N}[(1 - FBAG_i) \times FD_i \times FP_{i,m} + (FBAG_i \times FD_i)_{surface}] \quad (5\text{-}6)$$

where

$\lambda_{m,n}^{PD}$ = death-rate constant for each plant in each compartment m ($year^{-1}$)

$FBAG_i$ = fraction of total biomass of plant species i that is aboveground

FD_i = fraction of belowground biomass of plant species i that dies annually ($year^{-1}$)

$FP_{i,m}$ = fraction of belowground mass of plant i in soil compartment m

N = number of plant species.

The second term in this expression is used only in the uppermost (surface) soil compartment. This term accounts for aboveground biomass that is assumed to enter the uppermost soil compartment (surface) at a rate equal to the annual death rate. The second term is deleted for all other soil compartments. The death-rate constant is calculated for each plant species, which is then summed to give an aggregate death-rate constant for each soil compartment.

Data for plant death and plant uptake were compiled from both INEEL-specific and outside literature. All source references, data reviews, and compilations have been summarized in Hampton and Benson (1995) and Hampton (2001).

The current scenario reflects plant production over a period of 100 years, during which time the current vegetation community is maintained. Community composition for future scenarios was modeled for four separate periods to replicate change in community structure over time (e.g., 100 to 130, 130 to 150, 150 to 200, and greater than 200 years).

Plant-age composition for current and future scenarios was assumed to remain constant over the modeled periods. Biomass calculations were based on a total community production and fractional contributions of individual plant species (NRCS 1981). Successional trends of the SDA from the current vegetation community were assumed to result in a natural community similar to sagebrush-grass communities surrounding the RWMC and other parts of the region (Anderson 1991; Anderson and Inouye 1988; NRCS 1981).

Where possible, best-estimate input values from studies conducted in disturbed soil were used for the current scenario and values from undisturbed studies for 100+-year scenarios. Average values from studies with the greatest sample size were given preference and the largest average was selected if there were no differences in sample sizes. If no average was reported, a median value was calculated from a published range. Otherwise, the smallest reported maximum value from all studies was selected. Data specific to the INEEL were selected over off-Site data unless the study was flawed or somehow less applicable; for example, plants grown in media other than native soil.

5.4.3 Flora—Current Scenario

The vegetation cover on the SDA comprises two species: crested wheatgrass (*Agropyron cristatum*) and Russian thistle (*Salsola kali*) (Arthur and Markham 1982). Biomass and rooting depths for these species are summarized in Table 5-27. The total average community biomass (aboveground and

belowground) was estimated as approximately 11,000 kg/ha (2.2 ton/ha) for current SDA conditions (Arthur and Markham 1982).

Table 5-27. Fractional root distribution for individual plant species for the current scenario.

Depth (cm)	Crested Wheatgrass[a]	Russian Thistle[a]
0 to 15	**0.35**	**0.22**
15 to 30	**0.25**	**0.21**
30 to 45	**0.10**	**0.21**
45 to 90	**0.23**	**0.23**
90 to 135	**0.04**	**0.10**
135 to 180	**0.03**	**0.03**
180 to 225	**0**	**0.02**
225 to 270	**0**	**0**

a. Reynolds (1990).
Note: Data in bold are specific to the Idaho National Engineering and Environmental Laboratory.

The composition was assumed to remain constant through 100 years of maintenance of current conditions. Rooting depths and root mass distribution are summarized on Table 5-28. The maximum rooting depth for crested wheatgrass is not expected to reach a depth sufficient to penetrate the waste matrix during the current scenario. However, Russian thistle can penetrate into the waste zone during the current occupational scenario. The establishment of sagebrush and other deeper rooting shrub species is controlled on the SDA; therefore, those species were not included as components for the current scenario.

5.4.4 Flora—100+-Year Scenario

The 100+-year scenario for vegetation consists of several phases in which transitional changes in the current SDA community composition result in reestablishment of a natural sagebrush and bunchgrass community (Anderson and Inouye 1988; Anderson et al. 1978; NRCS 1981). The composition of different species for communities modeled after 100 years is presented in Table 5-28, which summarizes the biomass and maximum rooting depth of the individual species for each transitional phase. Composition and percent biomass for successive increments are based on Arthur and Markham (1982), Anderson and Inouye (1988), Hull and Klomp (1974), Anderson et al. (1978), and Anderson (1991).

Table 5-28. Fractional root distribution for individual plant species for the 100+-year scenario.

Depth (cm)	Crested Wheatgrass[a]	Russian Thistle[a]	Sagebrush[a]	Green[b] Rabbitbrush	Bluebunch Wheatgrass[a]	Needle and Thread[a] Grasses	Other[a] Grasses	Forbs[a]	Other Shrubs[b]
0 to 15	0.35	0.22	0.21	0.125	0.35	0.35	0.35	0.22	0.12
15 to 30	0.25	0.21	0.20	0.10	0.25	0.25	0.25	0.21	0.10
30 to 45	0.10	0.21	0.20	0.07	0.10	0.10	0.105	0.21	0.07
45 to 90	0.30	0.23	0.23	0.45	0.23	0.20	0.23	0.23	0.45
90 to 135	0	0.10	0.13	0.20	0.04	0.05	0.065	0.10	0.20
135 to 180	0	0.03	0.015	0.04	0.03	0.05	0	0.03	0.04
180 to 225	0	0	0.015	0.015	0	0	0	0	0.02
225 to 270	0	0	0	0	0	0	0	0	0

a. Reynolds (1990). Adjusted for maximum depths given on Table 5-28.
b. McKenzie et al. (1982).

Biomass calculations for the three periods (130 to 150, 150 to 200, and greater than 200 years) are based on average yearly above land-surface estimates of 1,490, 2,030, and 1,000 kg/ha, respectively (see Table 5-27). Root mass distribution with depth for this scenario is contained in Table 5-29. Sagebrush and similar shrubs (e.g., gray rabbitbrush [*Chrysothamnus nauseosus*]) are expected to attain maximum rooting depths with maximum shrub density developing at 200 years.

The other plant-rate constant is plant uptake, which simulates uptake of contaminants into the plant biomass. The death of the plants returns the contaminants to the soil compartments. The equation describing the uptake constant is shown in Equation (5-7).

$$\lambda_{m,n}^{P^U} = \sum_{i=1}^{N} (B_V \times PP_i \times FP_{i,m}) / MS_m \qquad (5\text{-}7)$$

where

$\lambda_{m,n}^{P^U}$ = plant uptake rate constant ($year^{-1}$)

B_V = plant bioaccumulation factor ([mg/g plant]/[mg/g soil])

PP_i = annual plant productivity (g/year) for all plants of species i

$FP_{i,m}$ = fraction of root mass of all plant species i in soil compartment m

MS_m = mass of soil in compartment m (g)

N = number of species.

The annual plant productivity (PP_i) can be found by using Equation (5-8):

$$PP_i = SB_i \times (RS_i + 1) \times FN_i \times SA \qquad (5\text{-}8)$$

where

PP_i = annual plant productivity

SB_i = shoot biomass per unit area for species i (g/m^2)

RS_i = root-to-shoot ratio for species i

FN_i = fraction of total biomass produced each year (1/year)

SA = surface area of the SDA (m^2).

Table 5-29. Estimated parameters for the uptake of plant species for the Subsurface Disposal Area for current and 100- to 200+-year scenarios.

				Current Scenario		100+-Year Scenarios			
Plant Species	Root-to-Shoot Ratio	Fraction Litterfall ($Year^{-1}$)[a]	Fraction Root Death ($Year^{-1}$)[b]	Maximum Root Depth (cm)	Fraction of Total Biomass[c]	Maximum Root Depth (cm)	Fraction of Total Biomass 130 Years[d]	Fraction of Total Biomass 150 Years[d]	Fraction of Total Biomass 200+ Years[d]
Crested wheatgrass	8[e]	1	0.5	**150**[f]	**0.75**	75[g]	**0.55**	**0.30**	—
Russian thistle	1.4[b]	1	1	172[h]	**0.25**	172[h]	**0.15**	—	—
Sagebrush	1.3[e]	0.50[f]	0.5	—	—	220[f]	**0.05**	**0.10**	**0.20**
Green rabbitbrush	1.3[e]	0.85[f]	0.5	—	—	200[f]	**0.11**	**0.06**	**0.05**
Bluebunch wheatgrass	8[e]	1	0.5	—	—	150[j]	**0.03**	**0.05**	**0.10**
Needle and thread grasses	9[i]	1	0.5	—	—	139[j]	**0.02**	**0.09**	**0.10**
Other grasses	9[i]	1	0.5	—	—	100[f,j]	**0.05**	0.20	**0.29**
Forbs	1.5[b]	1	0.8[a]	—	—	145[h]	**0.02**	**0.10**	**0.15**
Other shrubs	1.5[b]	1	0.8[a]	—	—	183[k]	**0.02**	**0.10**	**0.11**
		Community aboveground biomass (kg/ha)		—	**1,490**	—	**1,490**	1,700	800
		Community root-to-shoot ratio		—	**6.35**	—	5.57	5.70	5.22

a. Estimate based on root-to-shoot and fractional root depths for grass and shrub species presented in Becker et al. (1994).

b. Becker et al. (1994).

c. Arthur (1982); Arthur and Markham (1982).

d. Composition and percent biomass based on successive increments based on data presented in Arthur (1982); Anderson and Inouye (1988); Anderson (1991).

e. Hull and Klomp (1974).

f. Reynolds and Fraley (1989).

g. Abbott, Fraley, and Reynolds (1991).

h. Klepper, Gano, and Caldwell (1985).

i. Pearson (1965).

j. McKenzie et al. (1982).

k. For gray rabbitbrush from Klepper et al. (1979).

Notes: Data in **bold** are specific to the Idaho National Engineering and Environmental Laboratory.

— = Plant species is not present for this scenario.

Mass of soil in compartment m (MS_m) can be found by using the following equation:

$$MS_m = VC_m \times \rho \quad (5\text{-}9)$$

where

MS_m = mass of soil in compartment m

VC_m = volume of compartment m (cm^3)

ρ = density of soil (1.5 g/cm^3).

Plant uptake constants are determined for each plant species in each compartment and then summed to produce the aggregate uptake rate constant for that compartment.

Movement of contaminants by burrowing animals and ants requires soil transport rate constants. The equation describing calculation of the soil transport rate constant is as follows:

$$\lambda^{\beta}_{m,n} = \sum_{i=1}^{N} (I_i \times MB_i \times FNB_i \times FB_{i,m}) / MS_m \quad (5\text{-}10)$$

where

$\lambda^{\beta}_{m,n}$ = soil transport rate constant ($year^{-1}$)

I_i = number of individual animals in species i

MB_i = mass of soil moved to the surface per individual by species i (g)

FNB_i = fraction of new burrows per year for species i ($year^{-1}$)

$FB_{i,m}$ = fraction of burrows of species i in soil compartment m

MS_m = mass of soil in compartment m (g)

N = number of species.

A soil transport rate constant is calculated for each compartment for each species that burrows in that compartment. Constants for each species are summed to produce the aggregate soil transport rate constant for each compartment. The predominant effect produced by this constant occurs when a burrowing animal digs directly into the waste and transports it to the surface.

Burrowing animals enhance waste transport through intrusion activities that move contaminants to the surface. The DOSTOMAN biotic transport model includes the contributions of both burrowing mammals and harvester ants. Data were compiled from SDA- and INEEL-specific and outside literature.

5.4.5 Fauna—Current Scenario

Composition of burrowing species, population density, burrow volumes, and average burrow depths reflecting estimated current burrowing activity at the SDA are shown in Table 5-30. Burrow distribution with depth for individual species is listed in Table 5-31. Burrow distributions with depth for the current scenario are based on average burrow depths and the soil profile was assumed to be disturbed. No animals are expected to attain burrow depths sufficient to exceed the current overburden thickness of 1.5 m (5 ft) (calculated average). The deepest average burrow depths are 1.4 m (4.5 ft) for harvester ants

and 1.3 m (4.3 ft) for Townsend's ground squirrels (see Table 5-30). Species densities (see Table 5-32) are based primarily on previous studies of the SDA by Groves (1981), Groves and Keller (1983), Koehler (1988), Boone (1990), and Boone and Keller (1993). Burrow volume, depth, composition, and average population densities were assumed to remain constant for 100 years, assuming institutional controls maintain current conditions over that period (see Tables 5-31 and 5-32).

5.4.6 Fauna—100+-Year Scenario

The composition of the animal community for the 100^{+}-year scenario was altered to reflect changes as the vegetation community is transformed to simulate conditions at the Site if institutional controls were discontinued. The composition, burrow depth, volume, and density of species for the 100^{+}-year modeled periods are summarized in Table 5-33. The fractional burrow distribution for each individual species is presented in Table 5-33. Burrow distributions with depth for the 100^{+}-year scenario are based on average burrow depths and undisturbed soil profiles. While rodent populations fluctuate widely from year to year (Boone and Keller 1993), the population densities presented are average species compositions and population levels over time.

Leaching from a compartment is computed using the following equation:

$$\lambda^{L}_{m,m+1} = \frac{P}{\theta R T_m} \qquad (5\text{-}11)$$

where

$\lambda^{L}_{m,m+1}$ = leach rate coefficient for compartment m ($year^{-1}$)

P = net infiltration (m/year)

θ = volumetric moisture content (unitless)

R = contaminant-specific retardation coefficient (unitless)

T = thickness of compartment m (m).

Table 5-30. Small-animal density and burrowing parameters for the current scenario.

Burrowing Animal Species[a]	Population (Individuals per Hectare)[a]	Maximum Depth (cm)	Burrow Volume (L)	Number of New Burrows (per Year)[b]
Townsend's ground squirrel	**5**	**130**[c]	**9.4**[c]	0.75
Ord's kangaroo rat	**5**	**90**[c]	**7.3**[c]	0.87
Deer mouse	**17**	**50**[c]	**1.3**[c]	0.87
Montane and sagebrush voles	**30**	**40**[c]	**2.1**[c]	0.87
Great Basin pocket mouse	**15**	77[d]	6.8[d]	0.75
Western harvester ant	**13**[e]	138[f]	2.4[g]	0.1[e]

a. Mammal species composition and populations are based on studies conducted on the SDA by Groves (1981), Groves and Keller (1983), Koehler (1988), Boone (1990), and Boone and Keller (1993).

b. McKenzie et al. (1982).

c. Reynolds and Laundre (1988).

d. Landeen and Mitchell (1981).

e. Blom, Clark, and Johnson (1991).

f. Gaglio et al. (1998).

g. Fitzner et al. (1979).

Note: Data in bold are specific to the Idaho National Engineering and Environmental Laboratory.

Table 5-31. Burrow volume and fraction of volume excavated at depth by small animals for the current scenario.

Depth of Disturbed Soil (cm)	Townsend's Ground Squirrel[a]	Ord's Kangaroo Rat[a]	Deer Mouse[a]	Voles[a]	Great Basin Pocket Mouse[b]
	Fraction of Volume				
0 to 15	0.06	0.16	0.38	0.46	0.24
15 to 30	0.18	0.13	0.29	0.46	0.24
30 to 45	0.34	0.23	0.25	0.08	0.24
45 to 90	0.24	0.47	0.08	0	0.29
90 to 135	0.18	0	0	0	0
135 to 180	0	0	0	0	0
180 to 225	0	0	0	0	0
225 to 270	0	0	0	0	0
Total burrow volume (L)	9.4	7.3	1.3	2.1	6.8

a. Reynolds and Laundre (1988); Reynolds and Wakkinen (1987).

b. McKenzie et al. (1982).

Table 5-32. Small-animal density and burrowing parameters for the Subsurface Disposal Area 100+-year scenario.

Species[a]	Number per Hectare[a] Current/100+ Years	Average Depth (cm)	Burrow Volume (L)	New Burrows ($Year^{-1}$)[b]
Badger	1/3	180[c]	318.0[b,d] (diameter =30 cm, length = 450 cm)	3
Deer mouse	**17/30**	**24**[e]	**1.7**[e]	0.87
Great Basin pocket mouse	**15/25**	44.4[f]	**5.6**[f]	0.75
Least chipmunk	**3/8**	**17.5**[g]	**5.5**[g]	0.75
Montane and sagebrush voles	**30/10**	**23**[c]	**1.5**[c]	0.87
Northern pocket gopher	**7/7**	13.4[h]	5.5[h,d]	0.75
Ord's kangaroo rat	**8/5**	**34**[i]	**7.2**[i]	0.87
Rabbits	8/20	150	87.0[d] (length = 170 cm)	0.75
Townsend's ground squirrel	**5/5**	**128**[e]	8.2[e]	0.75
Western harvester ant	20[j]/36[j]	138[k]	7.0[l,d]	0.1

a. Compiled from Groves (1981), Groves and Keller (1983), Koehler (1988), Boone (1990), and Boone and Keller (1993) unless otherwise noted.
b. Lindzey (1976).
c. McKenzie et al. (1982).
d. Calculated from data presented in reference.
e. Reynolds and Wakkinen (1987).
f. Landeen and Mitchell (1981).
g. Laundre (1989a).
h. Winsor and Whicker (1980).
i. Reynolds and Laundre (1988).
j. Blom, Clark, and Johnson (1991).
k. Gaglio et al. (1998).
l. Fitzner et al. (1979).
Note: Data in bold are specific to the Idaho National Engineering and Environmental Laboratory.

Table 5-33. Burrow volume and fraction of volume excavated at depth by small animals for the 100^{+}-year scenario in undisturbed soil.

Depth of Undisturbed Soil (cm)	Townsend's Ground Squirrel[a]	Ord's Kangaroo Rat[a]	Deer Mouse[a]	Voles[a]	Great Basin Pocket Mouse[b]	Northern Pocket Gopher[b]	Least Chipmunk[c]	Badger[b]	Rabbits[d]	Western Harvester Ant
	Fraction of Volume									
0 to 15	**0.08**	**0.21**	**0.32**	**0.46**	0.32	0.98	**0.48**	0.21	**0.17**	0.21
15 to 30	**0.18**	**0.29**	**0.68**	**0.54**	0.31	0.02	**0.52**	0.21	**0.17**	0.21
30 to 45	**0.08**	**0.14**	**0**	**0**	0.37	0	**0**	0.20	**0.17**	0.21
45 to 90	**0.11**	**0.36**	**0**	**0**	0	0	**0**	0.19	**0.17**	0.15
90 to 135	**0.55**	0	0	0	0	0.	**0**	0.10	**0.17**	0.12
135 to 180	**0**	0	0	0	0	0	**0**	0.09	**0.15**	0.10
180 to 225	**0**	0	0	0	0	0	**0**	0	**0**	0
225 to 270	**0**	0	0	0	0	0	**0**	0	**0**	0
Total burrow volume (L)[e]	**8.2**	**7.2**	**1.7**	**1.5**	5.6	5.5	**5.5**	170	**87**	2.4

a. Reynolds and Laundre (1988).
b. McKenzie et al. (1982).
c. Laundre (1989a; 1989b).
d. Wilde (1978).
e. Total burrow volumes from Appendix C, Table C-3.
Note: Data in bold are specific to the Idaho National Engineering and Environmental Laboratory.

Burrow collapse is computed using the burrow compartment mass excavation given in Equation (5-12). The lowest compartment receives mass from the middle compartment equal to the amount of soil moved to the surface from the lowest compartment. The middle compartment receives mass from the upper compartment equal to mass moved to the surface from both the first and second compartments. This way mass removed by burrowing is replaced by burrow collapse from the compartment above. Total mass moved into any compartment by burrow collapse is equal to mass removed from that compartment plus total mass moved to the surface from all compartments below. The equation for computing the burrow collapse for a compartment is shown in Equation (5-12):

$$\lambda^{c}_{m,n} = \sum_{i=1}^{nl} \lambda^{\beta}_{m,i} \frac{T_n}{T_i} \qquad (5\text{-}12)$$

where

$\lambda^{c}_{m,n}$ = burrow collapse rate constant ($year^{-1}$)

$\lambda^{\beta}_{m,i}$ = soil transport rate constant for compartment i ($year^{-1}$) for burrowing animals

T_n = thickness of compartment n (m)

T_i = thickness of compartment i (m)

nl = the number of compartments lower than compartment i.

5.4.7 Biotic Model Calibration.

The biotic model was not calibrated for two reasons. First, data from surface sampling are inconsistent and probably reflect past operational releases and flooding events rather than biotic uptake. In addition, ongoing recontouring efforts have made data for surface concentrations less useful for calibration purposes. Concentrations of Cs-137 and Co-60 decrease more rapidly than can be accounted for by decay or leaching. Rapid decrease is believed to be caused by the sampling of clean soil used in recontouring. Second, regardless of which potential remedy is selected, it is assumed that some form of recontouring and capping of the waste will be required. Any additional cover would tend to eliminate the potential for biotic intrusion into the waste. With this assumption, effort to calibrate to suspect data did not seem appropriate. If the assumption of additional cover is not appropriate in the future, then additional work on the biotic model would be warranted at that time.

5.4.8 Summary

The DOSTOMAN biotic model was used to predict surface soil concentrations for use in the exposure assessment. The concentrations are believed to be conservative for the processes modeled. However, operational releases and flooding releases were not simulated. The biotic model was not calibrated to measured soil concentrations because (a) soil data were inconsistent for many contaminants, (b) the surface of the SDA is routinely modified by subsidence repair and recontouring, and (c) some form of covering with additional material (i.e., a cap) will be implemented as a component of any remedial action at the SDA. An appropriately designed cover would eliminate the possibility of biotic intrusion into the waste.

5.5 Summary and Conclusions

Modeling presented in this section is the basis for analysis of risk, remedial alternatives, and remedial decisions for OU 7-13/14. Except for the VOC COPC analysis, modeling in the ABRA is improved compared to the IRA model. Improvements in the inventory and results of characterization activities have been successfully incorporated. Table 5-34 summarizes improvements in the ABRA models compared to the modeling implemented for the IRA. However, results must be considered in the context of uncertainties inherent in the modeling relative to conceptual models and parameterization of the conceptual model that was implemented. For discussion of uncertainties, see Section 6.

Table 5-34. Summary of improvements in the remedial investigation/feasibility study models compared to the Interim Risk Assessment models.

Topic	IRA Approach	Modifications for the Ancillary Basis for Risk Analysis	Bases for Improvement
Contaminant screening	Assessed 91 radioactive and chemical contaminants (53 quantitatively in 11 groups and 38 qualitatively)	• Simulated fate and transport for contaminants in seven groups. • Only surface pathway risks were assessed for C-137 and Sr-90 (human health) and ecological contaminants of potential concern (COPCs) using DOSTOMAN. • Risk estimates for the three volatile organic compound (VOC) COPCs were scaled from the IRA and not remodeled by Operable Unit (OU) 7-13/14. (Note: OU 7-08 remodeling is planned for calendar year 2003.)	Eliminated contaminants were shown in the IRA to be clearly outside of the cumulative risk ranges for all pathways. Several contaminants with 1E-07 or 0.1 order of magnitude risks or hazard quotients (HQs) were retained based on uncertainties (e.g., Ac-227, Pa-231, Pb-210, with groundwater concentrations still rising at the 10,000-year simulation period; methylene chloride and tetrachloroethylene because of uncertain VOC disposal quantities).
Source term inventory	Contaminant Inventory Database for Risk Assessment (CIDRA) best-estimate inventories through 1993 used for limited calibration, upper-bound inventories used for base case risk estimates, and projected inventories not assessed.	Corrected CIDRA best-estimate inventories were used to generate base-case risk estimates. Uncertainties in inventories were assessed by simulating corrected upper-bound quantities and the projected maximum limits on the facility disposal quantities.	CIDRA revisions: • Projected disposal data replaced with actual disposal quantities for 1994 to 1999 • Adjusted to include estimated historical Idaho National Engineering and Environmental Laboratory (INEEL) reactor operations waste.
Source discretization	Three time periods reflecting the types of disposal operations that were simulated are: 1950 to 1970, 1971 to 1983, and 1983 to 1993	The CIDRA inventories were proportioned into 13 discrete source areas based on shipping information in the WasteOScope database.	Revisions to CIDRA and development of WasteOScope database.

Table 5-34. (continued)

Topic	IRA Approach	Modifications for the Ancillary Basis for Risk Analysis	Bases for Improvement
C-14 risk	Based on CIDRA upper-bound inventories and release rates from literature reviews of corrosion data	Revised inventory, mobility (K_d), and site-specific corrosion rates were used.	Revised inventory (see above), mobility, and site-specific corrosion test data.
Volatile organic contaminant mass remaining in the waste	• The CIDRA best-estimate inventories were doubled for both model calibration and base-case risk • The VOC mass removed by the ongoing extraction was not accounted for • Conservative diffusion from the sludge was simulated.	Scaled concentrations and risks based on inventory corrections.	Disposal records showed actual number and weight of buried organic sludge.
Uranium risk	Unlimited solubility.	Unlimited solubility.	Addressed solubility limits in uncertainty based on Eh and pH combinations possible in waste.
Interbed hydrologic and transport properties	Used average values estimated from site-specific data where available and literature values in other cases.	Included spatial variability in hydrologic properties in the B-C and C-D interbeds.	• Cores collected in calendar year 2000 were analyzed to profile hydrologic properties • Cores collected in calendar year 2000 were analyzed to improve basis for site-specific uranium and neptunium partition coefficients.
Interbed lithology	Kriged available values.	Used updated kriging with additional information.	New well data (e.g., interbed tops and thicknesses from 22 vadose zone and aquifer wells installed in calendar year 2000).
Infiltration rates	Source term model used spatially averaged value of 8.5 cm/year.	A unique infiltration rate was implemented for each of the 13 source areas.	Model change allowing discrete infiltration rates for each of the areas.
Aquifer boundary conditions	Interpolated from 1994 to 1995 measured water levels.	Additional data were used to update the aquifer model.	Water level measurements from expanded monitoring network.
Upgradient contributions	Upgradient contribution assumed not to occur.	Looked for upgradient contributions but detected no discernable impact.	Ongoing work to help fingerprint isotopes and determine if upgradient impact exists.

Table 5-34. (continued)

Topic	IRA Approach	Modifications for the Ancillary Basis for Risk Analysis	Bases for Improvement
Sporadic low-level detections of actinides in aquifer	Assumed to be anomalous or related to upgradient influences.	Not included.	Isotopic analysis (thermal ionization mass spectrometry) of aquifer samples from across the INEEL delayed so results are not available to support this analysis.
Separation of vadose zone and aquifer simulation domains for dissolved-phase transport	Combined domains to consider downgradient off-gassing.	Separated domains for vadose zone and aquifer.	None necessary, simply a modeling change.
Calibration of vadose zone flow model	Used perched water locations and temporal behavior as targets (poor results).	Updated properties for the B-C and C-D interbeds.	New data from core collected from the 22 wells drilled in 1999 and 2000.
Calibration of aquifer flow model	Steady-state calibration using three values assigned to specific zones in the aquifer and a value developed by Waste Area Group 3 to the I-Basalt at depth.	Steady-state calibration to improved water-level data set and kriged aquifer permeabilities before calibration.	Additional water level data from expanded monitoring network (routinely measured during quarterly sampling).
Partition coefficient assignments	Used data from Dicke (1997), which included site-specific values when available and values from other literature.	Used data from Dicke (1997) except for revised value for C-14.	Site-specific 2000 core interbed sample analysis shows the K_d values in Dicke (1997) for uranium and neptunium are on the conservative end of the range. Dicke (1998) provides a site-specific C-14 value of 0.1 mL/g instead of 5 mL/g.
Facilitated transport	Assumed not to occur.	Three sensitivity cases implemented using 1E-02, 1E-04, and 1E-06 fractions of the plutonium mass.	Clemson column studies indicate less than 1% facilitated transport.
Spreading area influences	Assumed not to occur.	Included influence as part of base case and implemented sensitivity runs with no influence and with double the influence modeled in the base case.	1999 U.S. Geological Survey tracer test results and total chemistry sampling to include chlorine to bromine ratios.

In each case, best judgment was used in implementing the source-release model and the subsurface flow and transport model. Lack of data for calibrating the source-release model and the subsurface flow and transport model for strictly dissolved contaminants has resulted in an ongoing monitoring program representing considerable investment of time and expenditure of money. Eventually, results of these monitoring activities will improve the ability to simulate processes occurring in the subsurface.

Currently, results of these models are useful in estimating potential risks to human health and the environment and assessing appropriate remedial alternatives to mitigate unacceptable risk. However, results must be considered in light of uncertainties associated with this analysis. Existing data sets for dissolved-phase contaminants were inadequate for model calibration; therefore, model parameters were not adjusted in an attempt to achieve calibration by improving agreement between simulated and observed results. Comparisons were made to assess model predictions relative to observed results. Several sensitivity cases were completed that indicate the results of the modeling are generally conservative.

Future activities that would improve the overall ability of the ABRA model to represent the movement of contaminants in the subsurface include the following:

- Sensitivity of risk results to the infiltration regime through the waste was demonstrated in a sensitivity case. This result points out the importance of continuing the monitoring and interpretation of data being collected by the SDA Type A and B probes. Hydrologic conditions within the waste and leachate contaminant concentrations are particularly important.

- Monitoring data from the deep vadose zone monitoring network should be incorporated to update and improve the subsurface flow and transport model. The model used in the ABRA is inadequately calibrated. An influence appears to exist in observed aquifer concentrations from dissolved-phase nonsorbing transport of nitrate as well as a potential impact from hexavalent chromium. Monitoring and data interpretation to determine if these constituents are truly useful for model calibration should be continued. Monitoring of the vadose zone network also should be continued to improve the delineation of the extent of lateral influence from the spreading areas within the vadose zone.

- The low-permeability zone within the aquifer has previously been demonstrated to exert a large influence on predicted concentrations and risks. Continued monitoring and interpretation of ongoing tracer testing within the aquifer is necessary to improve understanding the extent of this low-permeability zone. The flat nature of the water table in the SDA vicinity has made determining direction of local water flow within the aquifer difficult. A proposed method to use existing isobaric wells at the SDA to more accurately measure water levels could also improve the state of knowledge regarding directions of groundwater flow.

- Evaluating the likelihood of fast pathways down through the interbeds should be continued. Part of this evaluation should include taking interbed samples for measuring hydrologic and transport properties, if any additional wells are drilled in the SDA vicinity. Spatially variable K_ds in the interbeds could not be included based on the currently available data. The data set resulting from the calendar year 1999 drilling campaign represents a good start, but spatial structure in the K_ds could not be identified.

- Another reason to make additional measurements of hydrologic and transport properties on interbed samples is to compare the K_ds used in the ABRA for uranium and neptunium to the distribution of measured values in Hull (2001). If the basis could be improved by increasing the number of samples on which analyses had been conducted, the assigned K_ds for the interbeds could

be justifiably increased, which would result in substantial changes in the time period within which concentration increases in the aquifer are simulated to occur.

- Modeling VOCs should be conducted with the improved ABRA model and should include or use (a) new inventory data, (b) estimates of VOC mass remaining in the pits, (c) information from the recently completed flux chamber and source-release studies, (d) updated mass removal data from operation of the VVE system, (e) updated monitoring data, and (f) all other improvements listed in this section (e.g., spreading area influences and aquifer flow analysis).

5.6 References

Abbott, M. L., L. Fraley Jr., and T. D. Reynolds, 1991, "Root Profiles of Selected Cold Desert Shrubs and Grasses in Disturbed and Undisturbed Soils," *Environmental & Experimental Botany* 31, pp. 165-178.

Adler Flitton, M. Kay, Carolyn W. Bishop, Ronald E. Mizia, Lucinda L. Torres, and Robert D. Rogers, 2001, *Long Term Corrosion/Degradation Test Third-Year Results*, INEEL/EXT-01-00036, Idaho National Engineering and Environmental Laboratory, Bechtel BWXT Idaho, LLC, Idaho Falls, Idaho.

Anderson, J. E., 1991, *Vegetation Studies to Support the NPR Environmental Impact Statement*, NPR-DEIS-SR-003, Environmental Science and Research Laboratory, U.S. Department of Energy Idaho Operations Office, Idaho Falls, Idaho.

Anderson, J. E., and R. Inouye, 1988, *Long-Term Dynamics of Vegetation in Sagebrush Steppe of Southeastern Idaho*, Final Report, Task Order 5, Modification 21, Contract No. C84130479, Department of Biological Sciences, Idaho State University, Pocatello, Idaho.

Anderson, J. E., R. J. Jeppson, R. J. Rjwilkosz, G. M. Marlette, and K. E. Holte, 1978, "Trends in Vegetation Development on the Idaho National Engineering Laboratory Site," ed. O. D. Markham, *Ecological Studies on the Idaho National Engineering Laboratory Site 1978 Progress Report*, IDO-12087, Environmental Science and Research Laboratory, U.S. Department of Energy Idaho Operations Office, Idaho Falls, Idaho.

Anderson, S. R., D. A. Ackerman, M. J. Liszewski, and R. M. Freiburger, 1996, *Stratigraphic Data for Wells at and near the Idaho National Engineering Laboratory, Idaho*, DOE/ID-22127, U.S. Geological Survey Open-File Report 96-248, U. S. Geological Survey.

Arnett, R. C., and R. P. Smith, 2001, "WAG 10 Groundwater Modeling Strategy and Conceptual Model," INEEL/EXT-01-00768 Rev. B, Idaho National Engineering and Environmental Laboratory, Bechtel BWXT Idaho, LLC, Idaho Falls, Idaho.

Arthur, W. J., and O. D. Markham, 1982, "Ecological Vectors of Radionuclide Transport at a Solid Radioactive Waste Disposal Facility in Southeastern Idaho," ed. M. A. Feraday, *Proceedings of the International Conference on Radioactive Waste Management, Winnipeg, Manitoba, Canada, September 12–15, 1982*, ISBN 0-919784-01-1, Canadian Nuclear Society, Toronto, Ontario, Canada.

Arthur, W. J. III, 1982, "Radionuclide Concentrations in Vegetation at a Solid Radioactive Waste-Disposal Area in Southeastern Idaho," *Journal of Environmental Quality*, Vol. 11, No. 3, pp. 394–399.

Baca, Robert G., Swen O. Magnuson, Hoa D. Nguyen, and Pete Martian, 1992, *A Modeling Study of Water Flow in the Vadose Zone Beneath the Radioactive Waste Management Complex*, EGG-GEO-10068, Idaho National Engineering and Environmental Laboratory, EG&G Idaho, Idaho Falls, Idaho.

Becker, B. H., J. D. Burgess, K. J. Holdren, D. K. Jorgensen, S. O. Magnuson, and A. J. Sondrup, 1998, *Interim Risk Assessment and Contaminant Screening for the Waste Area Group 7 Remedial Investigation*, DOE/ID-10569, U.S. Department of Energy Idaho Operations Office, Idaho Falls, Idaho.

Becker, B. H., 1997, *Selection and Development of Models Used in the Waste Area Group 7 Baseline Risk Assessment*, INEL/EXT-97-00391, Idaho National Engineering and Environmental Laboratory, Lockheed Martin Idaho Technologies Company, Idaho Falls, Idaho.

Becker, B. H., T. A. Bensen, C. S. Blackmore, D. E. Burns, B. N. Burton, N. L. Hampton, R. M. Huntley, R. W. Jones, D. K. Jorgensen, S. O. Magnuson, C. Shapiro, and R. L. VanHorn, 1996, *Work Plan for Operable Unit 7-13/14 Waste Area Group 7 Comprehensive Remedial Investigation/Feasibility Study*, INEL-95/0343, Idaho National Engineering and Environmental Laboratory, Lockheed Martin Idaho Technologies Company, Idaho Falls, Idaho.

Becker, B. H, C. A. Loehr, S. M. Rood, and J. A. Sondrup, 1994, *Risk Assessment of Remedial Objectives for Nontransuranic Waste in Pit 9*, EGG-ER-11093, Rev. 1, Idaho National Engineering and Environmental Laboratory, EG&G Idaho, Idaho Falls, Idaho.

Blom, P. E., W. H. Clark, and J. B. Johnson, 1991, "Colony Densities of the Seed Harvesting Ant *Pogonomyrmex salinus* (Hymenoptera: Formicidae) in Seven Plant Communities on the Idaho National Engineering Laboratory," *Journal of the Idaho Academy of Science*, Vol. 27, No. 1, pp. 28-36.

Blom, P. E., J. B. Johnson, and S. K. Rope, 1991, "Concentrations of ^{137}Cs and ^{60}Co in Nests of the Harvester Ant, Pogonomyrex Salinus, and Associated Soils near Nuclear Reactor Waste Water Ponds," *American Midland Naturalist*, Vol. 126, pp. 140-151.

Boone, J. D., 1990, *Ecological Characteristics and Preferential Edge Use of Small Mammal Populations Inhabiting a Radioactive Waste Disposal Area*, M.S. Thesis: Idaho State University, Pocatello, Idaho.

Boone, J. D., and B. L. Keller, 1993, "Temporal and Spatial Patterns of Small Mammal Density and Species Composition on a Radioactive Waste Disposal Area: the Role of Edge Habitat," *Great Basin Naturalist*, Vol. 53, No. 4, pp. 341-349.

Brooks, R. H., and A. T. Corey, 1966, "Properties of Porous Media Affecting Fluid Flow," *J. Irrig. Drain. Div.*, American Society of Civil Engineering, Vol. 92 (IR2), pp. 61-88.

Burgess, J. D., 1996, *Tritium and Nitrate Concentrations at the RWMC*, Engineering Design File EDF-ER-024, INEL-96/204, Idaho National Engineering and Environmental Laboratory, Lockheed Martin Idaho Technologies Company, Idaho Falls, Idaho.

Case, Marilyn J., Arthur S. Rood, James M. McCarthy, Swen O. Magnuson, Bruce H. Becker, and Thomas K. Honeycutt, 2000, *Technical Revision of the Radioactive Waste Management Complex Low-Level Waste Radiological Performance Assessment for Calendar Year 2000*,

INEEL/EXT-2000-01089, Idaho National Engineering and Environmental Laboratory, Bechtel BWXT Idaho, LLC, Idaho Falls, Idaho.

Cecil, L. D., J. R. Pittman, T. M. Beasley, R. L. Michel, P. W. Kubik, P. Sharma, U. Fehn, and H. Gove, 1992, "Water Infiltration Rates in the Unsaturated Zone at the Idaho National Engineering Laboratory Estimated from Chlorine-36 and Tritium Profiles, and Neutron Logging," *Proceedings of the 7th International Symposium on Water-Rock Interaction*, WRI-7, Park City, Utah.

Cline, J. F., F. G. Burton, D. A. Cataldo, W. E. Skiens, and K. A. Gano, 1982, *Long-Term Biobarriers to Plant and Animal Intrusion of Uranium Tailings*, DOE/UMT-0209, Pacific Northwest Laboratory, Richland, Washington.

Dicke, C. A., 1998, *Carbon-14 Distribution Coefficients Measured from Batch Experiments on SDA Sediments*, INEEL/INT-98-00068, Engineering Design File EDF-RWMC-1011, Idaho National Engineering and Environmental Laboratory, Lockheed Martin Idaho Technologies Company, Idaho Falls, Idaho.

Dicke, C. A., 1997, *Distribution Coefficients and Contaminant Solubilities for the Waste Area Group 7 Baseline Risk Assessment*, INEL/EXT-97-00201, Idaho National Engineering and Environmental Laboratory, Lockheed Martin Idaho Technologies Company, Idaho Falls, Idaho.

DOE-ID, 1998, *Addendum to the Work Plan for the Operable Unit 7-13/14 Waste Area Group 7 Comprehensive Remedial Investigation/Feasibility Study*, DOE/ID-10622, U.S. Department of Energy Idaho Operations Office, Idaho Falls, Idaho.

DOE-ID, 1994, *Track 2 Sites: Guidance for Assessing Low Probability Hazard Sites at the INEL*, DOE/ID-10389, Rev. 6, U.S. Department of Energy Idaho Operations Office, Idaho Falls, Idaho.

EPA, 1999, *Understanding Variation in Partition Coefficient, K_d Values*, EPA 402-R—99-004A&B, Office of Radiation and Indoor Air, U. S. Environmental Protection Agency.

Fabryka-Martin, J., A. Flint, G. Gee, "Peer Review Team Report on Conceptual Models and Field Verification of Radionuclide Transport through the Vadose Zone at INEEL," Final Report, November 5, 1998, prepared for Idaho National Engineering and Environmental Laboratory.

Fitzner R. E., K. A. Gano, W. H. Rickard, and L. E. Rogers, 1979, *Characterization of the Hanford 300 Area Burial Grounds, Task IV-Biological Transport*, PNL-6779, Pacific Northwest Laboratory, Hanford, Washington.

Freeze, R. A., and J. A. Cherry, 1979, *Groundwater*, Englewood Cliffs, New Jersey: Prentice-Hall.

Gaglio, M. D., W. P. Mackay, E. A. Osorio, and I. Iniguez, 1998, "Nest Populations of *Pogonomyrmex salinus* Harvester Ants (Hymenoptera: Formicidae)," *Sociobiology*, Vol. 332, pp. 459-463.

GE, 1989, *Nuclides and Isotopes Fourteenth Edition Chart of the Nuclides*, General Electric Nuclear Energy.

Gelhar, L. W., 1986, "Water Resources Research," Volume 22, No. 9, August 1986 Supplement, pp. 135S-145S.

Glover, P. A., F. J. Miner, and W. O. Polzer, 1976, "Plutonium and Americium Behavior in the Soil/Water Environment, I., 'Sorption of Plutonium and Americium by Soils,'" *Proceedings of Actinide-Sediment Reactions Working Meeting, Seattle, Washington*, BNWL-2117, pp. 225-254, Battelle Pacific Northwest Laboratories, Richland, Washington.

Grossman, Christopher J., Robert A. Fjeld, John T. Coates, and Alan W. Elzerman, 2001, *The Sorption of Selected Radionuclides in Sedimentary Interbed Soils from the Snake River Plain*, INEEL/EXT-01-01106, Clemson University, Clemson, South Carolina, Idaho National Engineering and Environmental Laboratory, Bechtel BWXT Idaho, LLC, Idaho Falls, Idaho.

Groves, C. R., and B. Keller, 1983, "Ecological Characteristics of Small Mammals on a Radioactive Waste Disposal Area in Southeast Idaho," *American Midland Naturalist*, Vol. 109, No. 2.

Groves, C. R., 1981, *The Ecology of Small Mammals on the Subsurface Disposal Area, Idaho National Engineering Laboratory Site*, M.S. Thesis: Idaho State University, Pocatello, Idaho.

Hackett, W. R., J. A. Tullis, R. P. Smith, S. J. Miller, T. V. Dechert, P. A. McDaniel, and A. L. Falen, 1995, *Geologic Processes in the RWMC Area, Idaho National Engineering Laboratory: Implications for Long Term Stability and Soil Erosion at the Radioactive Waste Management Complex*, INEL-95/0519, Idaho National Engineering and Environmental Laboratory, Lockheed Martin Idaho Technologies Company, Idaho Falls, Idaho.

Hampton, N. L., 2001, *Biological Data to Support Operable Unit 7-13/14 Modeling of Plant and Animal Intrusion at Buried Waste Sites,* INEEL/EXT-01-00273, Rev.0, Idaho National Engineering and Environmental Laboratory, Bechtel BWXT Idaho, LLC, Idaho Falls, Idaho.

Hampton, N. L., and T. A. Benson, 1995, *SDA Biotic Data Compilation*, Engineering Design File EDF-ER WAG7-76, INEL-95/139, Idaho National Engineering and Environmental Laboratory, Lockheed Martin Idaho Technologies Company, Idaho Falls, Idaho.

Hull, A. C., Jr., and G. J. Klomp, 1974, "Yield of Crested Wheatgrass Under Four Densities of Big Sagebrush in Southern Idaho," *Technical Bulletin No. 1483*, Agricultural Research Service, U.S. Department of Agriculture.

Hull, Larry, 2001, Interoffice Memorandum to Theodore J. Meyer, Doug Burns, Swen Magnuson, and James McCarthy, "Approach to Simulation of Actinides for the OU 7-13/14 Baseline Risk Assessment," Idaho National Engineering and Environmental Laboratory, Bechtel BWXT Idaho, LLC, Idaho Falls, Idaho, LCH-04-01, April 4, 2001.

INEEL, 2002a, *User's Manual for the WasteOScope Operable Unit 7-13/14 Mapping Software*, INEEL/EXT-01-01585, Rev. 0., Idaho National Engineering Laboratory, Bechtel BWXT Idaho, LLC, Idaho Falls, Idaho, March 2002.

INEEL, 2002b, *Waste Area Group 7 Geographic Information Systems WasteOScope Application*, INEEL/EXT-02-00292, Rev. 0., Idaho National Engineering and Environmental Laboratory, Bechtel BWXT Idaho, LLC, Idaho Falls, Idaho, March 2002.

Klepper, E. L., K. A. Gano, L. L. Cadwell, 1985, *Rooting Depth and Distributions of Deep-Rooted Plants in the 200 Area Control Zone of the Hanford Site*, PNL-5247, Pacific Northwest Laboratory, Battelle Memorial Institute, Hanford, Washington.

Klepper, E.L., L. E. Rogers, J. D. Hedlund, and R. G. Schreckhise, 1979, *Radioactivity Associated with Biota and Soil of the 216-A-24 Crib*, PNL-1948, Pacific Northwest Laboratory, Hanford, Washington.

Knobel, L. L., B. R., Orr, and L. D. Cecil, 1992, "Summary of Background Concentrations of Selected Radiochemical and Chemical Constituents in Groundwater from the Snake River Plain Aquifer, Idaho: Estimated from an Analysis of Previously Published Data," *Journal of the Idaho Academy of Science*, Vol. 28, X10.1, p. 48.

Koehler, D. K., 1988, *Small Mammal Movement Patterns Around a Radioactive Waste Disposal Area in Southeastern Idaho*, M.S. Thesis: University of Wyoming, Laramie, Wyoming.

Kudera, D. E., and B. W. Brown, 1996, *Volatile Organic Compounds Disposed of from 1952 Through 1983 at the Radioactive Waste Management Complex: Quantities Forms, Release Mechanisms and Rates*, ER-WAG7-90, Idaho National Engineering and Environmental Laboratory, Lockheed Martin Idaho Technologies Company, Idaho Falls, Idaho.

Landeen, D. S., and R. M. Mitchell, 1981, "Invasion of Radioactive Waste Burial Sites by the Great Basin Pocket Mouse (*Perognathus parvus*)," *International Symposium on Migration in the Terrestrial Environment of Long-lived Radionuclides from the Nuclear Fuel Cycle, Knoxville, Tennessee, July 27-31*, RHO-SA-211.

Laundre, J. W., 1989a, "Horizontal and Vertical Diameter of Burrows of Five Small Mammal Species in Southeastern Idaho," *Great Basin Naturalist*, 1989, Vol. 49, pp. 646–649.

Laundre, J. W., 1989b, "Burrows of Least Chipmunks in Southeastern Idaho," *Northwestern Naturalist*, Vol. 70, pp. 18–20.

Leecaster, Molly K., 2002, *Geostatistic Modeling of Subsurface Characteristics in the Radioactive Waste Management Complex Region, Operable Unit 7-13/14*, INEEL/EXT-02-00029, Rev. 0. Idaho National Engineering and Environmental Laboratory, Idaho Falls, Idaho, Bechtel BWXT Idaho, LLC, Idaho Falls, Idaho.

Lerman, A., 1988, "*Geochemical Processes Water and Sediment Environments*," Reprint ed., Melbourne, Florida: Krieger Publishing Company.

Lindzey, F. G., 1976, "Characteristics of the Natal Den of the Badger," *Northwest Science,* Vol. 50, No. 3, pp. 178–180.

LMITCO, 1995, *A Comprehensive Inventory of Radiological and Nonradiological Contaminants in Waste Buried in the Subsurface Disposal Area of the INEL RWMC During the Years 1952–1983*, INEL-95/0310 (formerly EGG-WM-10903), Rev. 1, Idaho National Engineering and Environmental Laboratory, Lockheed Martin Idaho Technologies Company, Idaho Falls, Idaho.

Magnuson, S. O., and A. J. Sondrup, 1998, *Development, Calibration, and Predictive Results of a Simulator for Subsurface Pathway Fate and Transport of Aqueous- and Gaseous-Phase Contaminants in the Subsurface Disposal Area at the Idaho National Engineering and Environmental Laboratory*, INEEL/EXT-097-00609, Idaho National Engineering and Environmental Laboratory, Lockheed Martin Idaho Technologies Company, Idaho Falls, Idaho.

Magnuson, S. O., 1995, *Inverse Modeling for Field-Scale Hydrologic and Transport Parameters of Fractured Basalt*, INEL-95/0637, Idaho National Engineering and Environmental Laboratory, Lockheed Martin Idaho Technologies Company, Idaho Falls, Idaho.

Magnuson, S. O. and D. L. McElroy, 1993, *Estimation of Infiltration from In Situ Moisture Contents and Representative Moisture Characteristic Curves for the 30-, 110-, and 240-ft Interbeds*, Engineering Design File RWM-93-001.1, EG&G Idaho, Idaho Falls, Idaho.

Maheras, S. J., A. S. Rood, S. O. Magnuson, M. E. Sussman, and R. N. Bhatt, 1994, *Radioactive Waste Management Complex Low-Level Waste Radiological Performance Assessment*, EGG-WM-8773, Idaho National Engineering and Environmental Laboratory, EG&G Idaho, Idaho Falls, Idaho.

Martian, P., 1995, *UNSAT-H Infiltration Model Calibration at the Subsurface Disposal Area, Idaho National Engineering Laboratory*, INEL-95/0596, Idaho National Engineering and Environmental Laboratory, Lockheed Martin Idaho Technologies Company, Idaho Falls, Idaho.

MathSoft, 2000, *S+SPATIALSTATS User's Manual Version 1.5*, Data Analysis Products Division, MathSoft, Seattle, Washington.

McCarthy, J. M., B. H. Becker, S. O. Magnuson, K. N. Keck, and T. K. Honeycutt, 2000, *Radioactive Waste Management Complex Low-Level Waste Radiological Composite Analysis*, INEEL/EXT-97-01113, Idaho National Engineering and Environmental Laboratory, Bechtel BWXT Idaho, LLC, Idaho Falls, Idaho.

McCarthy, J. M., R. C. Arnett, R. M. Neupauer, M. J. Rohe, and C. Smith, 1995, *Development of a Regional Groundwater Flow Model for the Area of the Idaho National Engineering Laboratory, Eastern Snake River Plain Aquifer*, INEL-95/0169, Rev. 1, Idaho National Engineering and Environmental Laboratory, Lockheed Martin Idaho Technologies Company, Idaho Falls, Idaho.

McKenzie, D. H., L. L. Caldwell, C. E. Cushing Jr., R. Harty, W. E. Kennedy Jr., M. A. Simmons, J. K. Soldat, and B. Swartzman, 1982, *Relevance of Biotic Pathways to the Long-Term Regulation of Nuclear Waste Disposal*, NUREG/CR-2675, U.S. Nuclear Regulatory Commission.

Merck, 1989, *An Encyclopedia of Chemicals, Drugs, and Biologicals*, 11th ed., Rahway, New Jersey: Merck & Co. Publishing.

Miller, Eric C., and Mark D. Varvel, 2001, *Reconstructing Past Disposal of 743 Series Waste in the Subsurface Disposal Area for Operable Unit 7-08, Organic Contamination in the Vadose Zone*, INEEL/EXT-01-00034, Rev. 0, Idaho National Engineering and Environmental Laboratory, Bechtel BWXT Idaho, LLC, Idaho Falls, Idaho.

Miller, E. C., and J. D. Navratil, 1998, *Estimate of Carbon Tetrachloride in 743 Series Sludges Buried in the Subsurface Disposal Area at the Radioactive Waste Management Complex*, INEEL/EXT-98-00112, Rev. 0, Idaho National Engineering and Environmental Laboratory, Lockheed Martin Idaho Technologies Company, Idaho Falls, Idaho.

Miner, F. J., P. A. Evans, and W. L. Polzer, 1982, "Plutonium Behavior in the Soil/Water Environment Part I. Sorption of Plutonium by Soils," RFP-2480, Rocky Flats Plant, Golden, Colorado.

Nagata, P. K., and J. Banaee, 1996, *Estimation of the Underground Corrosion Rates for Low-Carbon Steels: Types 304 and 316 Stainless Steels; and Inconel 600, 601, and 718 Alloys at the Radioactive Waste Management Complex*, INEL096/098, Idaho National Engineering and Environmental Laboratory, Lockheed Martin Idaho Technologies Company, Idaho Falls, Idaho.

Newman, M. E., and F. M. Dunnivant, 1995, *Results from the Large-Scale Infiltration Test: Transport of Radionuclide Tracers*, Engineering Design File EDF-ER-WAG7-77, INEL-95/146, Idaho National Engineering and Environmental Laboratory, Lockheed Martin Idaho Technologies Company, Idaho Falls, Idaho.

Nimmo, J. R., K. S. Perkins, P. A. Rose, J. P. Rousseau, B. R. Orr, B. V. Twining, and S. R. Anderson, 2002, "Rapid Transport of Naphthalene Sulfonate Tracer in the Unsaturated and Saturated Zones near the Big Lost River Flood-Control Areas at the Idaho National Engineering and Environmental Laboratory," Submitted to the *Vadose Zone Journal.*

NRCS, 1981, *NRCS Range Site Descriptions for MLRA*, BLM-BLMB-B11b, National Resource Conservation Service.

Orr, B. R., L. D. Cecil, and L. L. Knobel, 1991, *Background Concentrations of Selected Radionuclides, Organic Compounds, and Chemical Constituents in Ground Water in the Vicinity of the Idaho National Engineering Laboratory*, DOE/ID-22094, U.S. Department of Energy, Idaho Operations Office, Idaho Falls, Idaho.

Oztunali, O. I., and G. W. Roles, 1985, *Update of Part 61 Impacts Analysis Methodology,* NUREG/CR-4370, Vol. 1, U.S. Nuclear Regulatory Commission.

Pearson, L. C., 1965, "Primary Production in Grazed and Ungrazed Desert Communities of Eastern Idaho," *Ecology*, Vol. 46, pp. 278–285.

Reynolds, T. D., and L. L. Fraley Jr., 1989, "Root Profiles of Some Native and Exotic Plant Species in Southeastern Idaho," *Environmental and Experimental Botany*, Vol. 29, No. 2. pp. 241–248.

Reynolds, T. D., 1990, "Root Mass and Vertical Root Distribution of Five Semi-Arid Plant Species," *Health Physics*, Vol. 58, No. 2.

Reynolds, T. D., and J. W. Laundre, 1988, "Vertical Distribution of Soil Removed by Four Species of Burrowing Rodents in Disturbed and Undisturbed Soils," *Health Physics*, 1988, Vol. 54, No. 4, pp. 445-450.

Reynolds, T. D., and W. L. Wakkinen, 1987, "Characteristics of the Burrows of Four Species of Rodents in Undisturbed Soils in Southeastern Idaho," *American Midland Naturalist*, Vol. 118, No. 2, pp. 245–250.

Roback, R. C., T. M. Johnson, T. L. McLing, M. T. Murrell, S. Luo, and T. L. Ku, 2001, "Uranium isotopic evidence for groundwater chemical evolution and flow patterns in the eastern Snake River Plain aquifer, Idaho," *Geological Society of America Bulletin*, Vol. 113, pp. 1133-1141.

Robertson, J. B., 1974, *Digital Modeling of Radioactive and Chemical Waste Transport in the Snake River Plain Aquifer at the National Reactor Testing Station, Idaho,* IDO-22054, U.S. Geological Survey Open File Report, U.S. Geological Survey.

Robertson, J. B., R. Schoen, J. T. Barraclough, 1974, "The Influence of Liquid Waste Disposal on the Geochemistry of Water at the National Reactor Testing Station, Idaho: 1952-1970, IDO-22053," U.S. Geological Survey Open File Report, U.S. Geological Survey.

Rodriguez, R. R., A. L. Schafer, J. McCarthy, P. Martian, D. E. Burns, D. E. Raunig, N. A. Burch, and R. L. Van Horn, 1997, *Comprehensive RI/FS for the Idaho Chemical Processing Plant OU 3-13 at the INEEL—Part A. RI/BRA Report (Final),* DOE/ID-10534, U. S. Department of Energy Idaho Operations Office, Idaho Falls, Idaho.

Rood, A. S., 1999, *GWSCREEN: A Semi-Analytical Model for Assessment of the Groundwater Pathway from Surface or Buried Contamination, Theory and User's Manual Version 2.5,* INEEL/EXT-9800750, Idaho National Engineering and Environmental Laboratory, Lockheed Martin Idaho Technology Company, Idaho Falls, Idaho.

Root, R. W. Jr., 1981, *Documentation and User's Guide for "DOSTOMAN," A Pathways Computer Model f Radionuclide Movement,* DPST-81-549, Idaho National Engineering and Environmental Laboratory, EG&G Idaho, Idaho Falls, Idaho.

Shleien, B., ed., 1992, *The Health Physics and Radiological Health Handbook,* revised ed., Scinta, Silver Spring, Maryland.

Shuman, R. D., M. J. Case, and S. K. Rope, 1985, *Documentation of a Simple Environmental Pathways Model of the Radioactive Waste Management Complex at the Idaho National Engineering Laboratory,* EGG-WM-6916, Idaho National Engineering and Environmental Laboratory, EG&G Idaho, Idaho Falls, Idaho.

Sondrup, A. J., 1998, *Preliminary Modeling of VOC Transport for Operable Unit 7-08, Evaluation of Increased Carbon Tetrachloride Inventory,* INEEL/EXT-2000-00849, Rev. 0, Idaho National Engineering and Environmental Laboratory, Bechtel BWXT Idaho, LLC, Idaho Falls, Idaho.

Sullivan, T. M., 1993, *DUST Data Input Guide,* NUREG/CR-6041, U.S. Nuclear Regulatory Commission.

Sullivan, T. M., 1992, *Development of DUST: A Computer Code That Calculates Release Rates from LLW Disposal Unit,* BNL-NUREG-47118, Brookhaven National Laboratory, U.S. Nuclear Regulatory Commission.

USGS, 2001, "Science for a Changing World," http://water.usgs.gov/id/nwis, April 17, 2001.

USGS, 1998, "Significant Issues to Be Resolved to Support and Defend the Interim Risk Assessment and Additional Work Required to Resolve Those Issues," Letter report from J. P. Rousseau to K. E. Hain, U.S. Department of Energy, Idaho Operations Office, U.S. Geological Survey, Idaho Falls, Idaho.

van Genuchten, M. T., 1980, "A closed-Form Equation for Predicting the Hydraulic Conductivity of Unsaturated Soils," *Solo Science Society of America Journal,* Vol. 44, pp. 892-898.

Varvel, Mark D., 2001, *Mass Estimates of Organic Compounds Buried in the Subsurface Disposal Area for Operable Unit 7-08 and 7-13/14,* INEEL/EXT-01-00277, Engineering Design File EDF-ER-301, Rev. 0, Idaho National Engineering and Environmental Laboratory, Bechtel BWXT Idaho, LLC, Idaho Falls, Idaho.

Vigil, M. J., 1988, *Initial Estimate of Hazardous Waste Constituents in Pit 9*, Engineering Design File EDF-BWP-02, Idaho National Engineering and Environmental Laboratory, EG&G Idaho, Idaho Falls, Idaho.

Vinsome, P. K. W., and G. M. Shook, 1993, "Multi-Purpose Simulation," *Journal of Petroleum Science and Engineering*, Vol. 9, pp. 29-38.

Visual Numerics, 1996, PV-WAVE Version 6.0 User's Guide, Visual Numerics, Inc., 6230 Lookout Road, Boulder, Colorado.

Whitmire, D. L., 2001, *Summary Report: Simulation of Groundwater Flow near the Subsurface Disposal Area at the Idaho National Engineering and Environmental Laboratory*, INEEL/EXT-01-01643, Rev. 0, North Wind Environmental, Idaho National Engineering and Environmental Laboratory, Bechtel BWXT Idaho, LLC, Idaho Falls, Idaho.

Wilde, D. B., 1978, "A population Analysis of the Pygmy Rabbit (*Sylvilagus idahoensis*) on the INEL Site," Ph.D. Dissertation, Idaho State University, Pocatello, Idaho.

Winsor, T. F., and F. W. Whicker, 1980, "Pocket Gophers and Redistribution of Plutonium in Soil," *Health Physics*, Vol. 39, pp. 257–262.

Wood, T. R., 1989, Preliminary Assessment of the Hydrogeology at the Radioactive Waste Management Complex, Idaho National Engineering Laboratory, EGG-WM-8694, Idaho National Engineering and Environmental Laboratory, EG&G Idaho, Idaho Falls, Idaho.